YEAR-END TECHNICAL REPORT
September 29, 2018 to September 28, 2019

Environmental Remediation Science and Technology

Date submitted:

January 17, 2020

Principal Investigator:

Leonel E. Lagos, Ph.D., PMP®

Florida International University Collaborators:

Yelena Katsenovich, Ph.D.
Ravi Gudavalli, Ph.D.
Ashleigh Sockwell, Ph.D.
Angelique Lawrence, M.S., GISP
Yan Zhou, Ph.D.
DOE Fellows

Submitted to:

U.S. Department of Energy
Office of Environmental Management
Under Cooperative Agreement # DE-EM0000598

FIU | **Applied Research Center**
FLORIDA INTERNATIONAL UNIVERSITY

Addendum:

This document represents one (1) of four (4) reports that comprise the Year End Reports for the period of September 29, 2018 to September 28, 2019 prepared by the Applied Research Center at Florida International University for the U.S. Department of Energy Office of Environmental Management (DOE-EM) under Cooperative Agreement No. DE-EM0000598. Incremental funding under this cooperative agreement resulted in FIU having to execute carryover scope, which was completed in November 2019. The technical information for the carryover scope from FIU Performance Year 9 has therefore also been included in these reports.

The complete set of FIU's Year End Reports for this reporting period includes the following documents:

Project 1: Chemical Process Alternatives for Radioactive Waste
Document number: FIU-ARC-2018-800006470-04b-264

Project 2: Environmental Remediation Science and Technology
Document number: FIU-ARC-2018-800006471-04b-263

Project 3: Waste and D&D Engineering and Technology Development
Document number: FIU-ARC-2018-800006472-04b-253

Project 4: DOE-FIU Science & Technology Workforce Development Initiative
Document number: FIU-ARC-2018-800006473-04b-297

Each document will be submitted to OSTI separately under the respective project title and document number as shown above. In addition, the documents are available at the DOE Research website for the Cooperative Agreement between the U.S. Department of Energy Office of Environmental Management and the Applied Research Center at Florida International University: http://doeresearch.fiu.edu

TABLE OF CONTENTS

LIST OF FIGURES

LIST OF TABLES

PROJECT 2 OVERVIEW

This project is focused on environmental remediation of contaminated soil and groundwater at Hanford, SRS, and WIPP. The aim is to reduce the potential for contaminant mobility or toxicity in the surface and subsurface through the development and application of state-of-the-art environmental remediation technologies at DOE sites. This project is conducted in close collaboration between FIU, PNNL, SRNL, SREL, CBFO and LANL scientists in order to plan and execute research that is synergistic with the work being conducted at the sites, and supports the resolution of critical science and engineering needs which leads to a better understanding of the long-term behavior of contaminants in the subsurface. Research involves laboratory-scale studies which utilize novel analytical methods and microscopy techniques for characterization of various mineral and microbial samples. Tasks also include the implementation of hydrological models, which help to predict the behavior and fate of existing and potential contaminants in the surface and subsurface.

During FIU Performance Year 9 (2018-2019), FIU ARC worked on the following tasks:

Task 1: Remediation Research and Technical Support for the Hanford Site

The U.S. Department of Energy's Office of Environmental Management (DOE EM) faces a number of environmental challenges in addressing the cleanup of the legacy contamination left behind from previous nuclear weapons development and production of the Manhattan Project during the Cold War era, which has tremendous associated cleanup costs. FIU's support to Hanford includes contributing to the understanding of Tc-99 chemistry and the fate and transport mechanisms of co-mingled contaminants including Tc-99, U(VI), Cr(VI), and iodine (I).

During FIU Performance Year 9, FIU continued the investigation of ammonia (NH_3) gas injection as a potential remediation strategy for uranium (U) contamination via laboratory-scale experiments. Previous work has shown that the injection of NH_3 gas to the vadose zone can potentially decrease uranium mobility in the contaminated subsurface via pH manipulation and co-precipitation processes (Szecsody et al. 2012a, Zhong et al. 2015). There is a need for a better understanding of the formation processes leading to co-precipitation of uranium and the stability of the U-bearing precipitates. This information will help to accurately predict the fate of uranium in post-treatment vadose zone soil. Experiments were also focused on solids characterization in order to confirm both mineral transformations and U association via adsorption and co-precipitation processes.

Experiments also investigated technetium reduction in the presence of iron-bearing minerals that are present in the Hanford Site sediment. Two biotite and two ilmenite pure minerals were used in these experiments.

Historical [129]I releases have resulted in massive, dilute plumes spreading to the scale of greater than 50 km^2 in the subsurface of the Central Plateau at the Hanford Site. The largest [129]I plume is associated with the 200 West Area in the 200-UP-1 operable unit (OU). Currently, DOE has no approved treatment technologies for subsurface iodine plumes. The majority of [129]I concentration in the plumes is within the proximity of 10 pCi/L, which is above the drinking water standard (DWS) of 1 pCi/L. This task investigated the effect of vadose zone environmental conditions such as pH and porewater constituencies, particularly silica content, on the iodate colocated with

chromate co-precipitation process with calcium carbonate. This study also evaluated via dissolution experiments the stability of comingled iodine and chromate incorporated in calcite.

FIU also worked on a new subtask to support the Hanford Field Lysimeter Test Facility (FLTF) located in the 200-W area of the Hanford site. This facility is to be utilized by Pacific Northwest National Laboratory (PNNL) and Washington River Protection Solutions (WRPS) for testing of various waste forms expected, or possible candidates, to be produced during treatment and immobilization of low activity waste (LAW) at Hanford. The FLTF test was used to validate model predictions of long-term waste form behavior upon disposal in the Hanford site's integrated disposal facility.

Task 2. Remediation Research and Technical Support for Savannah River Site

There is a need for the Savannah River Site (SRS) to gather results to supplement permit requirements associated with the Area Completion Project (ACP), including the Phase 2 strategy to evaluate the performance of Phase 1 including "…downgradient of the F-Area inactive process sewer line and at Four Mile Branch". Per permitting requirements delineated in the corrective action plan, ^{129}I concentrations must be below groundwater standards in the Four Mile Branch by October 31, 2025 and in the F-Area plume in surface water at the seepline by October 31, 2030. Because the DOE has no approved technology for remediation of subsurface iodine, it is essential to understand its long-term fate in plumes at the Savannah River Site. The experimental results presented in this report contribute to our understanding of the interactions of U, Tc, and I with organic materials as well as the potential for remediation of U via injection of commercial humic materials providing essential data for fulfillment of the permitting requirements and goals for DOE-EM.

SRS is also conducting synergistic research, funded by DOE-EM's Office of Soil and Groundwater Remediation (EM-12), as part of the Attenuation-Based Remedies for the Subsurface Applied Field Research Initiative (ABRS AFRI). This applied research is geared towards developing science-based approaches to clean and close sites contaminated with combinations of metals, radionuclides, and other contaminants of concern. A primary objective of this program is to develop approaches for attenuation-based remedies, in this case, to investigate and validate the use of humate for subsurface stabilization of metals in contaminated groundwater plumes. SRS successfully conducted a field campaign that demonstrated the viability of dissolving and then injecting low cost agricultural humate into the subsurface and proposed it as a viable attenuation-based remedy for uranium and potentially I-129 as well. Humic acid, which carries a large number of functional groups, provides an important function in ion exchange and as a metal complexing ligand with a high complexation capacity being able to affect the mobility of radionuclides in natural systems. Different types of humic substances such as unrefined humic acid, modified humic acid, and commercial humic acid were used in this research to study their effects on uranium removal.

Task 3: Contaminant Fate and Transport Modeling in the Tims Branch Watershed

This research involves the development of an integrated, fully distributed hydrology and contaminant transport model, which will be used as a tool to address the knowledge gaps related to the fate and transport of dissolved contaminants at DOE EM sites. Implementation of a tin-based mercury rememdiation technology in the Tims Branch watershed has provided records of the quantity and timing of the tin released. This subsequently presented a unique opportunity for the tin to serve as a potential tracer for modeling sedimentation and particle transport processes

in the stream, making Tims Branch an ideal testbed for evaluating the effectiveness of wetland treatment and tin (II) - based mercury treatment at the SRS site. DOE EM has highlighted the need to track the tin and to understand the impact of frequent or extreme atmospheric events on its redistribution in Tims Branch. FIU intends to utilize the data available from the tin-based remediation technology to develop a hydrological and contaminant transport model that can in future be extended to investigate other heavy metal and radionuclide contaminants of concern (e.g., mercury, uranium and nickel). Knowledge acquired from this research will also assist in developing cost-effective remediation plans integrated into the SRS Area Completion Project (ACP) and accelerate progress of the DOE EM environmental restoration mission.

Task 5: Research and Technical Support for WIPP

There is a need to better understand the mobility of actinides and lanthanides in the presence of ligands under high ionic strength conditions in order to develop more accurate risk assessment models for the WIPP. The current performance assessment (PA) for the Waste Isolation Pilot Plant (WIPP) recommends a Kd range of $20 - 400$ mL/g for Pu(III) and Am(III) (Brush and Storz 1996). However, reliable measurements have not been reported for actinide and lanthanide sorption to relevant minerals, especially in the presence of relevant ligands like EDTA and cellulose degradation products such as isosaccharinic acid (Dunagan et al. 2007, Askarieh et al. 2000). In this study, FIU ARC collaborated with Dr. Donald Reed, a team leader of the Actinide Chemistry and Repository Science (ACRSP), in support of Los Alamos National Laboratory's field office located at the Carlsbad Environmental Monitoring and Research Center (CEMRC) in Carlsbad, New Mexico. The goal of this study is to generate accurate sorption data for the actinides to minerals and under conditions relevant to the Waste Isolation Pilot Plant as previous risk assessment models are based on conservative assumptions.

Task 6: Hydrology Modeling for WIPP

This task is a new research collaboration between researchers at FIU's Applied Research Center and DOE personnel at Pacific Northwest National Laboratory (PNNL) and the Carsbad Field Office (CBFO) to support research and development activities at the WIPP site. There is a need for an improved understanding of the regional water balance, particularly the relation between Culebra recharge and the intense, episodic precipitation events typical of the monsoon. This relationship is essential for understanding the rate of propagation of the shallow dissolution front, and the impact of land-use changes around the WIPP facility on water levels in compliance-monitoring wells. The ultimate goal of this research therefore is to develop a groundwater-basin model for the WIPP site using the DOE-developed Advanced Simulation Capability for Environmental Management (ASCEM) modeling toolset to improve the current understanding of regional and local groundwater flow at the WIPP site, compute the water balance, and derive estimates of groundwater recharge in the post-closure phase. These types of analyses require a revision of the current site conceptual model to couple surface water and groundwater processes, a high resolution digital elevation model including channels and sink holes to account for surface water routing, and the development of a new mathematical model. As ASCEM cannot currently account for land surface hydrology, which is essential for computing the water balance, it will require coupling with a state-of-the-art open-source land surface model (LSM) to simulate three-dimensional, unsaturated and saturated water flow. Therefore, during the first year, FIU's aim was to initiate work on this task by: 1) determining the appropriate methodology, software, data, and processing requirements to initiate development of a high-resolution digital elevation model (DEM) for the WIPP facility and surrounding groundwater basins; 2) collecting and compiling

existing information and data relevant to site hydrology, and 3) training of FIU research personnel and students on the selected LSM and ASCEM. FIU's collaboration with WIPP is projected to be a multi-year effort which will benefit DOE-EM by providing improved estimates of the spatial and temporal patterns of recharge, so that better predictions of halite dissolution and propagation of the shallow dissolution front can be made possible to assess and quantify the potential impact on the WIPP repository performance.

MAJOR TECHNICAL ACCOMPLISHMENTS

Task 1: Remediation Research and Technical Support for the Hanford Site

- Investigated phyllosilicate clay mineral alteration in variable redox conditions and alkaline treatments. Results showed significant dissolution occurs upon exposure of phyllosilicate clay minerals to highly alkaline (pH > 11) solutions with slightly greater dissolution under anaerobic conditions. These observations suggest secondary precipitation may be an effective method for sequestration of contaminants within newly formed, low solubility minerals.

- Studied technetium (Tc-99) reduction in the presence of ferrous iron-containing minerals relevant to Hanford Site, such as ilmenite ($FeTiO_3$), and biotite ($K(Mg,Fe)_3AlSi_3O_{10}(F,OH)_2$). The reduction of Tc-99 was found dependent on the amount of iron present in the mineral, which improved understanding on the effect of ferrous iron minerals to control Tc(VII) reduction thus helping to predict the potential for Tc(VII) migration in natural and engineered systems.

- Completed investigation on the effect of variable pH and silica concentrations on the incorporation of iodate co-located with chromate in calcium carbonate and evaluated the release of incorporated iodate and chromate during calcite dissolution. These findings can affect calcite-based iodate remediation strategies, indicating the preference of lower pH and higher Si concentrations on comingled iodate and chromium incorporation with calcite.

- Setup and validated experimental hardware for SPFT experiments at FIU. Completed q/S sweep for determination of necessary conditions for future studies of glass dissolution behavior with SPFT experiments.

- Initiated SPFT experiments using grout-contacted solution as leachate.

Task 2. Remediation Research and Technical Support for Savannah River Site

- Completed investigation on the removal of contaminants of concern such as Tc-99 and U by natural organic materials (NOM) using Savannah River wetland sediment.

- Investigated KW15 modified humics (known as modified humic acid) to facilitate uranium adsorption onto SRS sediment to control the mobility of uranium in acidic SRS groundwater. Results showed a significant increase in uranium removal in the presence of mod-HA.

Task 3: Contaminant Fate and Transport Modeling in the Tims Branch Watershed

- Developed and calibrated a fully integrated MIKE SHE/MIKE 11 hydrological model of the Tims Branch watershed that simulates surface and subsurface hydrologic processes and accounts for stream water hydraulics.

- Developed the contaminant transport component of the model by coupling the MIKE 11 stream hydrodynamic model with the MIKE 11 AD module that simulates solute transport through advection and dispersion, and the MIKE 11 ECO Lab module that accounts for both sediment transport and interactions with dissolved contaminants.

- Completed an extreme hydrological event analysis to determine hyetographs for return periods (TR) = 2, 5, 10, 25, 50, 100 and 200 years using data from 13 SRS weather

stations that will be used for future extreme rainfall scenario analysis, which provides a more spatially distributed analysis of the hydrological conditions in the Tims Branch study area.

- Conducted routine maintenance and calibration of remote monitoring devices deployed in Tims Branch and continued monitoring and download of water level timeseries data for hydrological model calibration and validation to increase confidence in the ability of the hydrology model being developed for Tims Branch to estimate flow depth and velocity, and contaminant spatial distribution over time.

Task 5: Research and Technical Support for WIPP

- Expanded dolomite dissolution batch experiments to investigate impact of ionic strength and EDTA on mineral dissolution behavior.
- Completed batch sorption investigation of the impact of EDTA and ionic strength on the sorption of Nd(III), Th(IV), and U(VI) to dolomite.
- Completed batch sorption experiments evaluating the sorption of Nd(III), Th(IV), and U(VI) to dolomite in WIPP-relevant brines, GWB and ERDA-6.

Task 6: Hydrology Modeling for WIPP

- Conducted a literature review of methodologies for development of a high-resolution digital elevation model (DEM) for the WIPP site and surrounding basins to better capture the ground surface topography and local features which will enable more accurate delineation and extraction of features such as drainage basins, brine lakes, channels, sink holes and discharge points for future development of a regional land surface model.
- Conducted a review of methodologies for vegetation removal from UAV-based photogrammetric digital surface models (DSMs) in addition to post processing methods for extracting significant topographical features such as sink holes from high resolution DEMs.
- Created an ArcGIS file geodatabase to serve as a central repository, and imported relevant spatial and temporal data of the New Mexico/WIPP region that was readily available for download from federal, state and local online resources for future use in development of regional land surface and groundwater models of the WIPP and surrounding basins.

TASK 1: REMEDIATION RESEARCH AND TECHNICAL SUPPORT FOR THE HANFORD SITE

Task 1: Executive Summary

DOE EM has a critical need to understand the biogeochemical processes influencing the behavior of contaminants (U, I, Tc, and Cr) in Hanford Site's deep vadose zone that can impact groundwater. This research studies solutions that may reduce the long-term costs of environmental stewardship at the Hanford site by transforming the more than 200,000 kg of mobile U released to the vadose zone into low solubility precipitates. It is directly applicable to plans to develop incremental technologies for treatment of subsurface contamination and 'gaining a better understanding of … biogeochemical processes that influence contaminant behavior' as outlined for 2017-2021 (DOE EM, 2016). Further, this effort is in alignment with DOE EM's plans to quantify the effect of co-mingled contaminant plumes (McCabe, D., *et al*., 2017) and targets Tc-99, uranium and comingled iodate and chromate, which are high priority contaminants.

Subtasks under Task 1 are performed with guidance from the Pacific Northwest National Laboratory. During FIU Performance Year 9, FIU completed the investigation of the Stability of Contaminants in Carbonate Precipitates; so, this activity will not continue in FIU Performance Year 10.

Subtask 1.1: Remediation Research of Ammonia Gas for Uranium Treatment

Subtask 1.1: Introduction

The dissolution and alteration of minerals under alkaline solutions is studied in a number of fields including geochemistry, hydrometallurgy, geopolymerization technology, materials science, and nuclear waste management, the latter being of interest to the Department of Energy's (DOE) Hanford Site in Washington State. During the years 1945 to 1987, plutonium production at the Site generated approximately 2.1×10^8 L of nuclear waste (Reynolds et al., 2018). Due to improper disposal or leakage, millions of liters of fluid waste was released and infiltrated into the deep Hanford vadose zone (up to 253 feet in depth) (Serne et al. 2008). Additional waste is currently stored in 177 underground tanks, containing a substantial quantity of radioactive elements (i.e., Cr, Cs, I, Tc, U, etc.) and large concentrations of hydroxyl ions and dissolved aluminum (Qafoku et al. 2003). These alkaline waste waters contained a high sodium concentration (5.2 to 13.4 M) resulting in dissolution of carbonates and aluminosilicates such as kaolinite, montmorillonite, and muscovite clay mineral (Szecsody et al. 2013). These wastes represent the most important scenarios impacting the local mineralogy of relevance to the Hanford Site including the potential for (1) release of alkaline waste from the tanks and (2) *in situ* subsurface treatment of contaminants with gaseous or liquid base injection.

The major aluminosilicate minerals in the Hanford Site sediment are muscovite (9%), illite (2.8%), and montmorillonite (1.2%) (Qafoku et al., 2004; Serne et al., 2008). Although the mica (e.g. illite and muscovite) and smectite (e.g. montmorillonite) minerals together constitute only 5 – 13% of the Hanford Site's total soil mass, they account for 40 – 60% of the total cation

exchange capacity (CEC) of the bulk sediments (Serne et al. 2008). Further, these minerals are members of the most abundant clays on the Earth's surface, phyllosilicates, and are categorized based on the layering of a tetrahedral $[TO_4]^{n-}$ and an octahedral $[MO_6]^{m-}$ structure. Because more than 75% of Earth's continental crust consists of silicates and aluminosilicates, they are of great importance worldwide (Dietrich and Skinner 1979). In fact, phyllosilicates are likely to sorb cations by (1) exchange in the interlayer planes and (2) specific sorption especially at the broken edges of clay particles (Charlet, Schindler et al. 1993, Charlet and Tournassat 2005). Because of their high sorption and ion exchange capacities, clays are often used for removal of contaminants (Casey, Westrich et al. 1993). Whether clays are naturally present such as at the Hanford Site or used as geochemical barriers such as in landfills, there is a need to understand their potential dissolution and alteration under highly alkaline conditions in order to predict the fate of contaminants.

Upon alkaline treatment, phyllosilicate dissolution is likely to result in incongruent, or non-stoichiometric, release of Al over Si (Lippert 1960, Oelkers 2001, Köhler, Dufaud et al. 2003, Miranda-Trevino and Coles 2003). Congruent dissolution occurs when no new phases are formed with stoichiometric release of ions, while incongruent dissolution occurs when new solid phases form with non-stoichiometric release (Crundwell 2014). The mechanism controlling Al release is expected to be primarily due to formation of monomeric silica, $Si(OH)_3$, reacting with aqueous Al and leading to low solubility Al precipitates (Iler 1979).

Although previous research has shown that incongruent dissolution occurs under alkaline conditions for many minerals and sediments (Köhler et al. 2003, Qafoku, et al. 2003, Mashal et al. 2004, Oda et al. 2014, Elert et al. 2015, Emerson et al. 2018), there is a need to systematically compare the effects of variable redox conditions and alkaline treatments on mineral dissolution and alteration (i.e., aiming to answer objectives #1 and 3 from subtask 1.1). Indeed, none of these studies focused on the combined effects of redox conditions, alkaline treatment, and pH on phyllosilicate dissolution trends. The objective of this research is to quantify the dissolution of phyllosilicate clays following alkaline treatments.

The present work aims to do so by (1) comparing treatments with weak and strong alkaline solutions and (2) quantifying the impact of redox conditions on mineral dissolution. In this report, results are presented for batch experiments conducted with similar free OH^- species (3.1 M NH_4OH and 0.01 M NaOH) exposed to illite, muscovite, or montmorillonite minerals. These experiments, conducted at room temperature and atmospheric pressure, were performed to closely monitor the release of cations (Al^{3+}, $Fe^{2+/3+}$, and Si^{4+}) into solution under anaerobic versus aerobic conditions. These minerals were chosen due to their abundance in the Earth's crust, relevance to the Hanford site, and representation of the weathering trend for phyllosilicate minerals (Hibbard 2002).

Subtask 1.1: Results and Discussion (Summary)

The focus of this study was to identify differences in dissolution for phyllosilicate minerals following alkaline treatment under variable redox conditions. As Figure 1 shows below, removal of Al and Si to the aqueous phase upon treatment was used to observe mineral dissolution. Illite, muscovite, and montmorillonite demonstrated a steady increase in Si throughout the 60-day contact-time. Contrary to Si, there was a preferential release of Al over Si at the first sampling time followed by a decrease in aqueous Al (Figure 2). Both trends were generally observed throughout all experimental conditions, regardless of redox or alkaline condition. The significant

change in dissolution of minerals at elevated pH and likely secondary mineral formation was observed in previous studies (Buck and McNamara, 2004; Chermak, 1992; Egashira and Kang, 1997; Fernandez-Jimenez et al., 2006; Qafoku et al., 2004; Szecsody et al., 2013; Wan et al., 2004). This conclusion is also supported by the poor correlation of first and second order models with dissolution results.

Further, all studied minerals present non-stoichiometric dissolution regardless of treatment or redox condition. However, Figure 3 distinctly displays incongruent behavior particularly for anaerobic conditions, although it is unclear if this is due to incongruent dissolution or secondary precipitation. Qafoku *et al*., observed both dissolution and precipitation processes controlling the dissolution of Si and Fe after 1000 hrs (Qafoku et al., 2003).

When comparing alkaline treatments, the strong base NaOH dissolved more of the mica minerals, illite and muscovite. This is likely due to ion-pairing between Si tetrahedra and Na cations in solution. Montmorillonite, however, dissolved moreso with NH_4OH treatment. This is because of its interlayer basal spacing, which has been shown to intercalate the NH_4^+ polycation into the expandable layer causing greater dissolution due to greater available surface area interacting with solutions. ORP measurements were significantly different when compared by treatment with a 100 mV higher measurement for NaOH than in NH_4OH solution. Although it is still unclear whether it is due to an unidentified interaction of solutions and mineral structures, it was noted that the ORP measurements of the alkaline solutions in contact with montmorillonite did not shift as significantly in anaerobic conditions (Figure 4). We suggest that this was due to removal of the redox sensitive element Fe as it increased in solution up to 240 hours followed by a sharp decrease (not shown) likely due to secondary precipitation. For all investigated phyllosilicate minerals, montmorillonite exhibited the most Al and Si dissolution at the first and last sampling event, respectively. On the contrary, illite dissolved the least, especially for aerobic conditions similar to previous observations (Jozefaciuk and Bowanko, 2002; Szecsody et al., 2013; Szecsody et al., 2012).
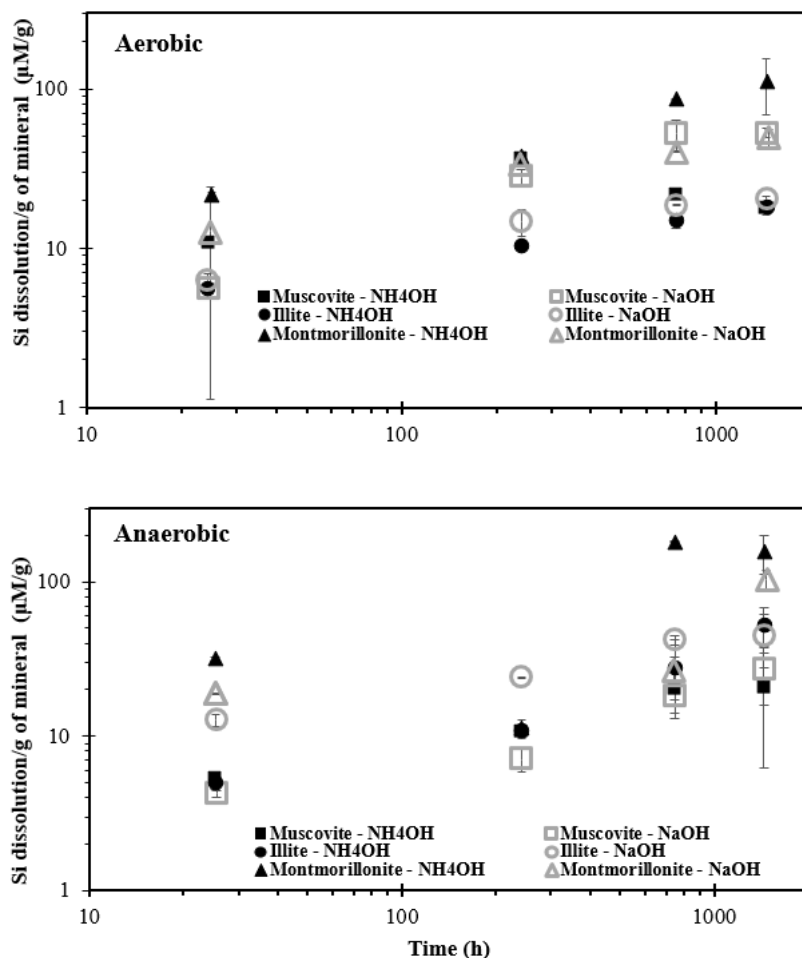
Figure 1. Aqueous Si, in µM/g, with time for batch experiments with 33 g/L minerals, including: montmorillonite (triangles), muscovite (squares), and illite (circles) with exposure to 3.1 M NH₄OH (closed black) and 0.01 M NaOH (open gray) under aerobic (top) and anaerobic (bottom) conditions, Note: error is based on analysis of triplicate samples.
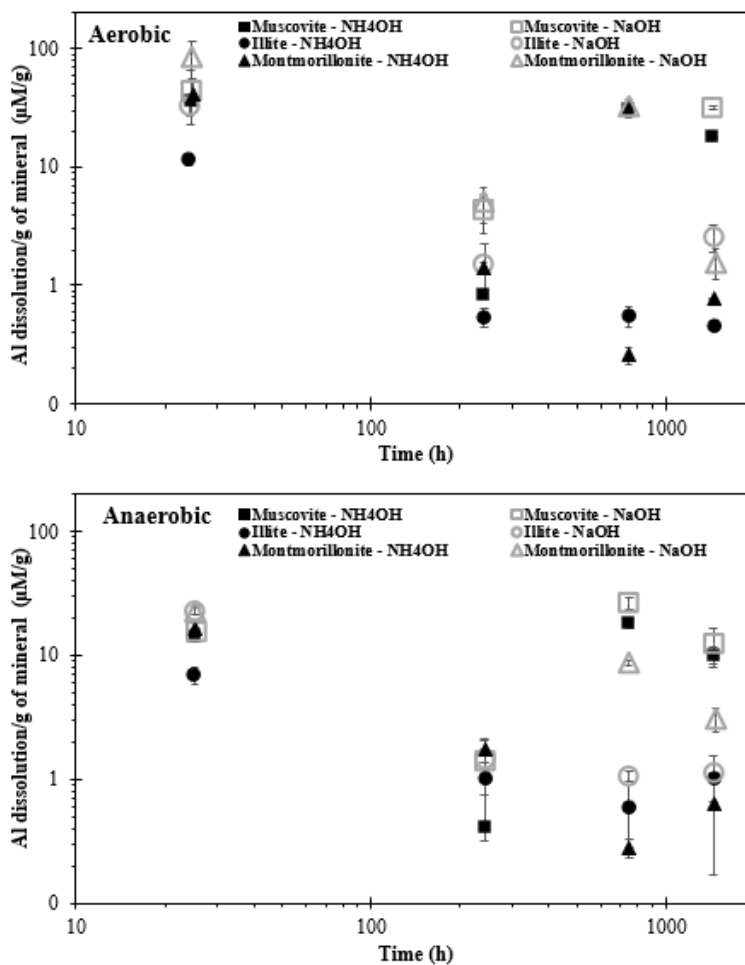
Figure 2. Aqueous Al, in μM/g, with time for batch experiments with 33 g/L minerals, including: montmorillonite (triangles), muscovite (squares), and illite (circles) with exposure to 3.1 M NH₄OH (closed black) and 0.01 M NaOH (open gray) under aerobic (top) and anaerobic (bottom) conditions, Note: error is based on analysis of triplicate samples.
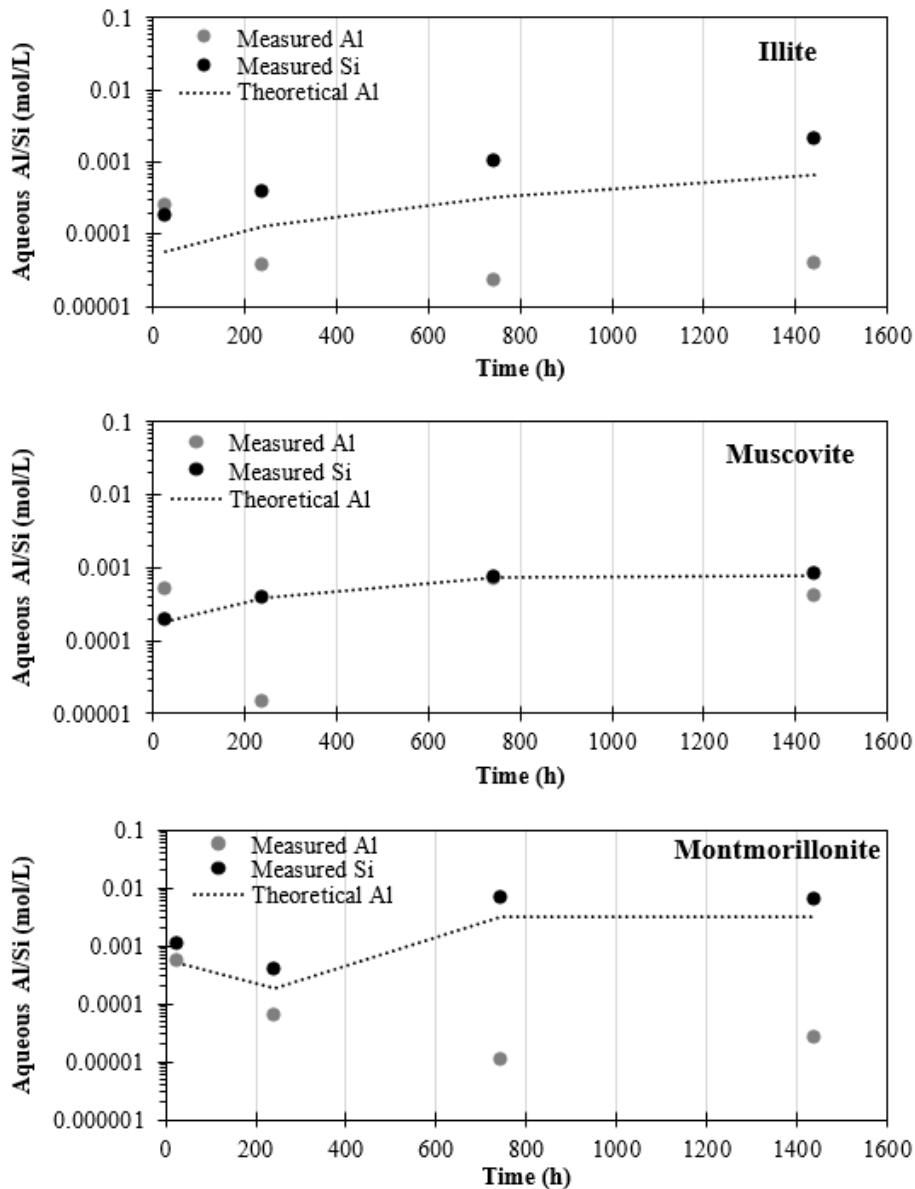
Figure 3. Aqueous Si (black) and Al (gray), in mol/L after reaction of 33 g/L suspension of minerals [illite (top), muscovite (middle) and montmorillonite (bottom)] over time (24-, 240-, 745- and 1440-h) with 3.1 M NH₄OH under anaerobic conditions. Dashed lines represent congruent Al dissolution based on measured Si in the aqueous phase.
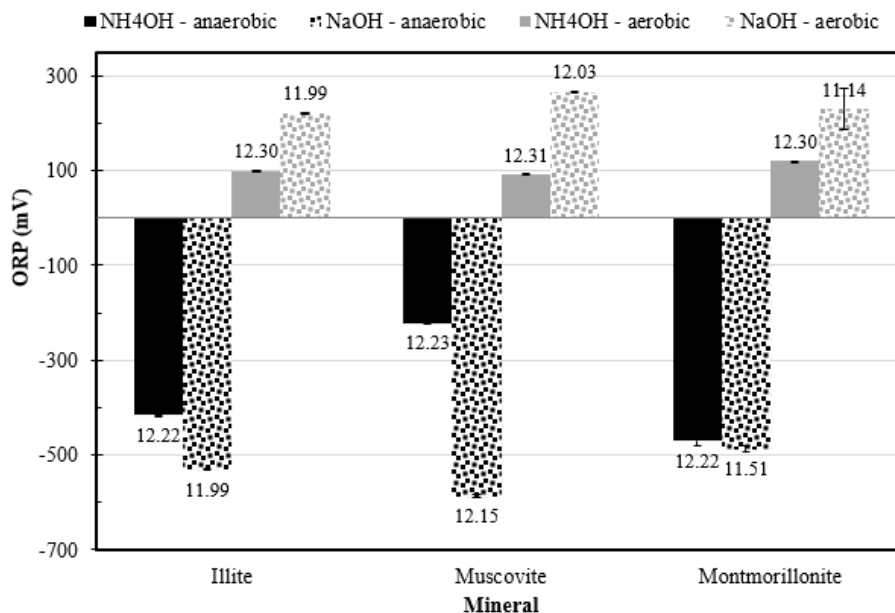
Figure 4. ORP, in mV, measurements for investigated minerals under anerobic (black) and aerobic (gray) conditions exposed to alkaline treatments (NaOH – pattern and NH₄OH – solid) after two months of reaction. Note: values printed above and below bars correspond to pH measurements and error bars are based on analysis of triplicate samples.

Subtask 1.1: Conclusions and Future Work

This unique study considered variable redox conditions and alkaline treatments in parallel for the first time for a series of phyllosilicate clay minerals. Results showed significant dissolution occurs upon exposure to highly alkaline (pH > 11) solutions with slightly greater dissolution under anaerobic conditions. More details on the experimental work are presented in the draft manuscript inlcuded in Appendix 1 that is under review by the *Applied Clay Science Journal*.

Future work should focus on identification of secondary minerals by using thermodynamic predictions and determination of their ability to incorporate contaminants.

Subtask 1.1: Acknowledgements

Funding for this research was provided by U.S. DOE Cooperative Agreement DE-EM0000598. We truly appreciate Drs. Jim Szecsody, Nik Qafoku, Hilary P. Emerson, Daria Boglaienko, and Vicky Freedman for their invaluable feedback and training of Silvina Di Pietro.

Subtask 1.1: References

Buck, E.C. and McNamara, B.K. (2004) Precipitation of Nitrate: Cancrinite in Hanford Tank Sludge. Environmental Science & Technology 38, 4432-4438.

Chermak, J. (1992) Low temperature experimental investigation of the effect of high pH NaOH solutions on the Opalinus Shale, Switzerland. Clays and Clay Minerals 40, 650-658.

Crundwell, F.K. (2014) The mechanism of dissolution of minerals in acidic and alkaline solutions: Part II Application of a new theory to silicates, aluminosilicates and quartz. Hydrometallurgy 149, 265-275.

Dietrich, R.V. and Skinner, B.J. (1979) Rocks and rock minerals. Elert, K., Pardo, E.S. and Rodriguez-Navarro, C. (2015a) Alkaline activation as an alternative method for the consolidation of earthen architecture. Journal of Cultural Heritage 16, 461-469.

Egashira, K. and Kang, S.-J. (1997) Modification of different grades of Korean natural zeolites for increasing cation exchange capacity. Applied Clay Science 12, 131-144. Emerson, H.P., Di Pietro, S., Katsenovich, Y. and Szecsody, J. (2018) Potential for U sequestration with select minerals and sediments via base treatment. Journal of environmental management 223, 108-114.

Fernandez-Jimenez, A., De la Torre, A.G., Palomo, A., Lopez-Olmo, G., Alonso, M.M. and Aranda, M.A.G. (2006) Quantitative determination of phases in the alkaline activation of fly ash. Part II: Degree of reaction. Fuel, 1960.

Hibbard, M.J. (2002) Mineralogy: a geologist's point of view. McGraw-Hill College.

Jozefaciuk, G. and Bowanko, G. (2002) Effect of acid and alkali treatments on surface areas and adsorption energies of selected minerals. Clays and Clay minerals 50, 771-783.

Köhler, S.J., Dufaud, F. and Oelkers, E.H. (2003) An experimental study of illite dissolution kinetics as a function of pH from 1.4 to 12.4 and temperature from 5 to 50 C. Geochimica et Cosmochimica Acta 67, 3583-3594.

Lippert, E. (1960) The Strengths of Chemical Bonds, von TL Cottrell. Butterworths Publications Ltd., London 1958.

Mashal, K., Harsh, J.B., Flury, M., Felmy, A.R. and Zhao, H. (2004) Colloid formation in Hanford sediments reacted with simulated tank waste. Environmental Science & Technology 38, 5750-5756.

Miranda-Trevino, J.C. and Coles, C.A. (2003) Kaolinite properties, structure and influence of metal retention on pH. Applied Clay Science 23, 133-139.

Oda, C., Walker, C., Chino, D., Ichige, S., Honda, A., Sato, T. and Yoneda, T. (2014) Na-montmorillonite dissolution rate determined by varying the Gibbs free energy of reaction in a dispersed system and its application to a coagulated system in 0.3 M NaOH solution at 70° C. Applied clay science 93, 62-71.

Qafoku, N.P., Ainsworth, C.C. and Szecsody, J.E. (2003a) Aluminum Effect on Dissolution and Precipitation under Hyperalkaline Conditions: II. Solid Phase Transformations. Journal of Environmental Quality 32, 2364-2372.

Qafoku, N.P., Ainsworth, C.C., Szecsody, J.E. and Qafoku, O.S. (2003b) Aluminum Effect on Dissolution and Precipitation Under Hyperalkaline Conditions I. Liquid Phase Transformations. Journal of environmental quality 32, 2354-2363.

Qafoku, N.P., Ainsworth, C.C., Szecsody, J.E. and Qafoku, O.S. (2004) Transport-controlled kinetics of dissolution and precipitation in the sediments under alkaline and saline conditions11Associate editor: D. J. Rimstidt. Geochimica et Cosmochimica Acta 68, 2981-2995.

Reynolds, J. G., G. A. Cooke, J. S. Page and R. W. Warrant (2018). "Uranium-bearing phases in Hanford nuclear waste." Journal of Radioanalytical and Nuclear Chemistry 316(1): 289-299.

Serne, R.J., Last, G.V., Gee, G.W., Schaef, H.T., Lanigan, D.C., Lindenmeier, C.W., Lindberg, M.J., Clayton, R.E., Legore, V.L. and Orr, R.D. (2008) Characterization of vadose zone sediment: Borehole 299-E33-45 near BX-102 in the B-BX-BY waste management area. Pacific Northwest National Lab.(PNNL), Richland, WA (United States).

Szecsody, J.E., Truex, M.J., Qafoku, N.P., Wellman, D.M., Resch, T. and Zhong, L. (2013) Influence of acidic and alkaline waste solution properties on uranium migration in subsurface sediments. Journal of contaminant hydrology 151, 155-175.

Szecsody, J.E., Truex, M.J., Zhong, L., Johnson, T.C., Qafoku, N.P., Williams, M.D., Greenwood, W.J., Wallin, E.L., Bargar, J.D. and Faurie, D.K. (2012) Geochemical and Geophysical Changes during Ammonia Gas Treatment of Vadose Zone Sediments for Uranium Remediation. Vadose Zone Journal 11, 0.

Subtask 1.2: Effect of Bicarbonate Ions on Tc Interactions with Iron Minerals

Subtask 1.2: Introduction

The Hanford Site in Washington State is the most contaminated nuclear site in the United States. Chemical separations for plutonium extraction resulted in the production of hazardous liquid and radioactive solid wastes stored in underground storage tanks. Leakages of mixed contaminant streams from some of these tanks, ponds, cribs and trenches, has caused widespread subsurface contamination. Common co-mingled contaminants in the vadose zone and groundwater include U, ^{99}Tc, ^{3}H, ^{129}I, NO_3^- and CCl_4, all present in concentrations exceeding the drinking water standards. Clean up of technetium contamination is a high-priority activity for the U.S. Department of Energy (DOE) Office of Environmental Management (EM) complex. Remediation efforts are being carried out to greatly reduce its migration and diminish risk to human health and the environment (McCabe et al. 2017). In oxic environments technetium exists as the weakly sorbing anionic pertechnetate species, TcO_4^-. Pertechnetate (TcO_4^-) is highly soluble, does not sorb onto sediments and migrates at the same velocity as groundwater (Kaplan et al., 1998). In the reduced form, Tc(IV) is expected to either sorb onto the sediments or precipitate as insoluble $TcO_2 \cdot n H_2O$ (Icenhower et al. 2008). The Columbia River, adjacent to the Hanford Site, exhibits large stage variations causing fluctuations in the water table, which in turn create an oxic-anoxic interface in this region directly affecting the fate and transport of technetium. Technetium migration is also affected by pore water and groundwater chemical composition, soil mineralogy and presence of low permeability zones in the field (Szecsody et al. 2015). The development of long-term remediation strategies requires a better understanding of Tc retention mechanisms in the sediments in order to predict its future migration in the subsurface. Fe(II)-bearing minerals are ubiquitous in natural systems, and due to their high reduction capacity and sorption properties, are able to affect Tc biogeochemistry (Peretyazhko et al. 2008, 2012). Ferrous iron containing minerals could potentially reduce and precipitate Tc(VII) (+7 oxidation state) as TcO_2 (+4 oxidation state) (Cui et al. 1996; Jaisi et al. 2009). The presence of bicarbonates in Hanford porewater and iron minerals in Hanford soil may affect technetium's fate in the environment.

Subtask 1.2: Objectives

Biotite and ilmenite are Fe-bearing minerals found in the Hanford Site sediment, and due to their high ferrous iron content, could potentially provide the necessary electrons for the reduction of pertechnetate (+7 oxidation state) to TcO_2 (+4 oxidation state). The objective of this research is to explore the effect of iron minerals on redox transformations of Tc-99, specifically, by pure minerals relevant to the Hanford Site, such as ilmenite and biotite. The existence of soluble Tc(IV)-carbonate complexes under circumneutral conditions has been recorded (Alliot et al. 2009) and therefore, the fate of Tc-99 in soil containing ferrous iron minerals needs to be studied in the presence of bicarbonates. Ferrous iron minerals may provide the necessary electrons for the reduction of pertechnetate to amorphous TcO_2, but the presence of bicarbonates may act antagonistically and retain Tc-99 in the aqueous phase.

The specific objectives of this subtask are to investigate the behavior of Tc in the presence of ferrous iron minerals. Another parameter for consideration is the presence of high concentrations of bicarbonate in pore and groundwater compositions at Hanford that might affect Tc reduction:

a) Characterize site-specific ferrous iron materials for morphology, particle size and surface area.

b) Study the reduction of Tc-99 in the presence of pure minerals, ilmenite and biotite, with and without bicarbonates under identical pH conditions. With the bicarbonate-free samples serving as controls, compare the kinetics of Tc(VII) reduction with and without bicarbonate for the minerals used in the study.

Subtask 1.2: Methodology

1. Iron minerals, stock and working solutions

Two minerals (ilmenite and biotite) were used in these experiments. Two biotite mineral specimens with a sheet-like structure were obtained from Eisco labs (designated as Biotite 1) and Carolina Biological Supply (designated as Biotite 2). A mortar and pestle were used to break down these specimens into smaller particles before use in the experiments. However, this technique proved to be ineffective and a blender was then used to obtain a smaller particle size.

Two ilmenite minerals were obtained from Fisher Scientific and Ward Scientific. The ilmenite mineral from Fisher Scientific (designated as Ilmenite 1) was received as a powder that was sieved to obtain a uniform size. The ilmenite specimen obtained from Ward Scientific (designated as Ilmenite 2) came in large chunks, which were crushed to smaller sized particles and then sieved to obtain uniform size for characterization studies and subsequent use in the experiments. Pertechnetate stock solution was provided by Pacific Northwest National Laboratory (PNNL) as an 18-mL solution of NH_4TcO_4 with an initial concentration of 1000 mg L^{-1} of Tc-99 (10.2 mM). The stock solution was stored at $4^{o}C$ and diluted to the desired final concentration for each experiment using a degasser with high purity N_2 deionized water with continuous stirring for 2h. In all experiments, the initial concentration of pertechnetate was 25µM unless stated otherwise.
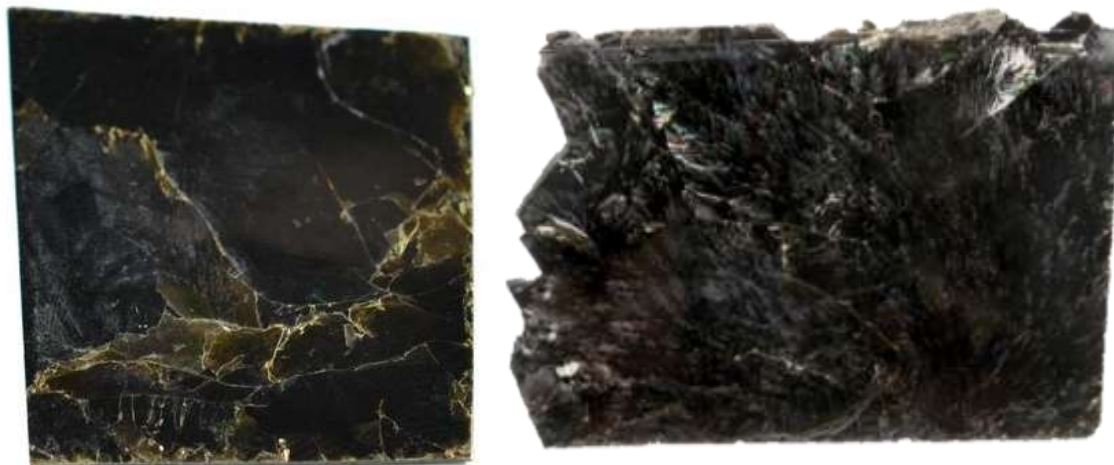
Figure 5. Biotite specimen from Escio labs (left) and Carolina Biological Supply Co. (right).

Figure 6. Ilmenite specimen from Fishersci (left) and Ward Scientific (right).

2. Iron minerals characterization

The specific surface area and the pore volume of the ferrous iron minerals were determined by the nitrogen adsorption method (BET) at FIU's Department of Mechanical Engineering. Samples were analyzed by an X-ray diffractometer (XRD) (Bruker GADD/D8 X-ray with Apex Smart CCD detector) from the Advanced Materials and Engineering Research Institute (AMERI) at FIU's Engineering Campus. XRD measurements were conducted by step-size scanning at 0.02 2θ intervals from 5∘ to 75∘ using CuKα radiation at 40 kV. The XRD data analysis was performed using *MATCH!* Software. SEM analysis was performed using a JSM-5900-LV low vacuum scanning electron microscope at 15kV. The composition of the particles was analyzed using a Noran System Six Model 200SEM energy dispersive X-ray spectroscope (EDS).

3. Batch experiments

Batch experiments were performed using iron minerals in the presence and absence of technetium at pH 8. DI water previously degassed with nitrogen was kept in the anaerobic chamber in 98% N_2:2% H_2 atmosphere (Figure 7) until an ORP less than -100 mV was reached. The pH of the DI water was adjusted to pH 8 using 0.01 M HCl. 300mg of iron minerals were measured and introduced into an anaerobic chamber where it was equilibrated for at least 24 hours prior to addition of pH-adjusted DIW. A Tc solution with an initial concentration of 1

mg/L was prepared by adding 0.4 mL of 1000 mg/L Tc to 399.60 mL of pH adjusted DIW. The solution was then distributed between 12 vials containing biotite and ilmenite minerals in triplicate. Eh and pH of the samples were monitored periodically by using a Hannah Instruments redox electrode and an Orion 9110D pH electrode, respectively. The pH of the mixture was monitored and adjusted as needed to maintain a pH of 8. 100 µL sub-samples were collected at regular time intervals and diluted with 4,900 µL of 2% HNO_3 prior to measuring the concentration of Tc and Fe via ICP-MS. Additional batch experiments with Tc-free control samples were prepared similar to the samples with Tc-containing samples to study the release of Fe from ferrous iron minerals.

Figure 7. Anaerobic glovebox with 98% N_2: 2% H_2 atmosphere where pertechnetate reduction experiments are currently taking place.

Subtask 1.2: Results and Discussion

1. Characterization of iron minerals

All iron samples were sieved through a 300 µm sized mesh to ensure a uniform particle size distribution prior to characterization and use in the experiments (Figure 8).
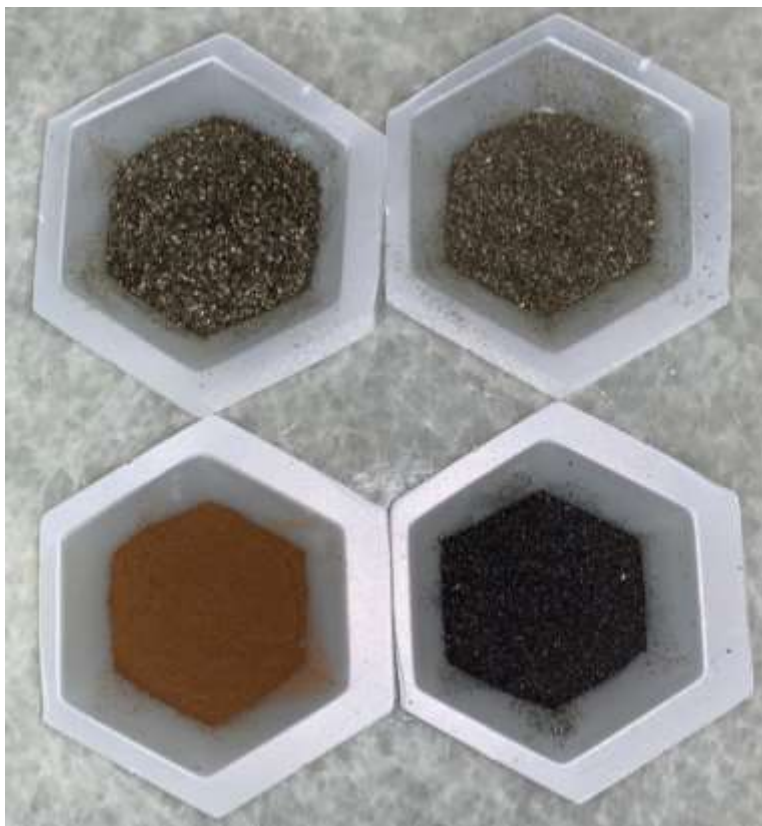
Figure 8. Biotite and ilmenite minerals used in the experiments after sieving through a 300 µm mesh.

Approximately 0.456 g, 0.469 g, 1.892 g and 3.148g of Biotite 1, Biotite 2, Ilmenite 1 and Ilmenite 2, respectively, were placed inside the glass tubes and degassed for at least 24 hours prior to measuring the surface area. Table 1 shows the results obtained from the surface area analysis. Biotite 1 and Biotite 2 surface areas were measured as 1.2 and 1.9 m^2/g, respectively, while Ilmenite 1 was 0.6 m^2/g and Ilmenite 2 showed the lowest surface area of 0.12 m^2/g compared to all tested minerals. Similarly, Biotite 2 had a higher pore volume while Ilmenite 2 had the lowest pore volume while having highest pore size.

Table 1. Surface Area and Pore Size Analysis of Iron Minerals

Mineral	BET Surface Area (m^2/g)	Pore Volume (cm^3/g)	Pore Size (A)
Biotite 1	1.4286	0.005826	163.1253
Biotite 2	1.9227	0.007035	146.3603
Ilmenite 1	0.6154	0.002003	130.1658
Ilmenite 2	0.1204	0.000604	200.6978

XRD analysis on iron minerals was performed by placing a small amount of sample onto a sample holder and flushing the surface of the sample. The resulting XRD patterns were analyzed using *MATCH!* Software to identify the minerals present in the samples. Both Biotite samples had similar patterns; the XRD pattern for Biotite is shown in Figure 9 matching 90% with (K,

Na) (Fe, Al, Mg)$_2$(Si, Al)$_4$O$_{10}$(OH)$_2$. The Ilmenite 1 pattern matched 82% with Fe$_2$Ti$_3$O$_{10}$ (Figure 10) and Ilmenite-2 matched 80% with Cu$_3$Ti$_{0.96}$Fe$_{0.98}$O$_{9.12}$ (Figure 11).
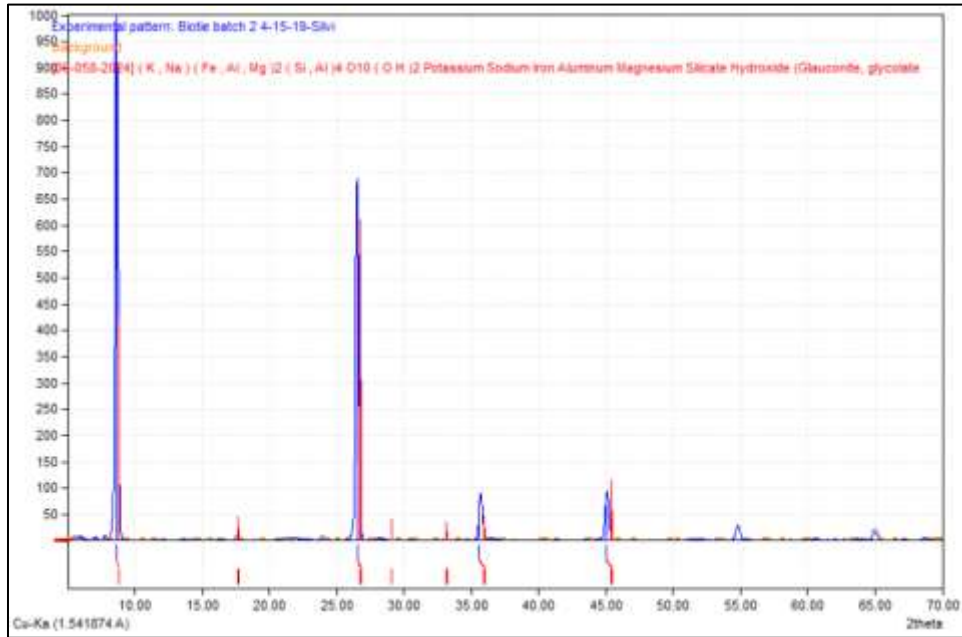
Figure 9. XRD pattern of Biotite 2 comparing with (K, Na) (Fe, Al, Mg)$_2$ (Si, Al)$_4$ O$_{10}$ (OH)$_2$.
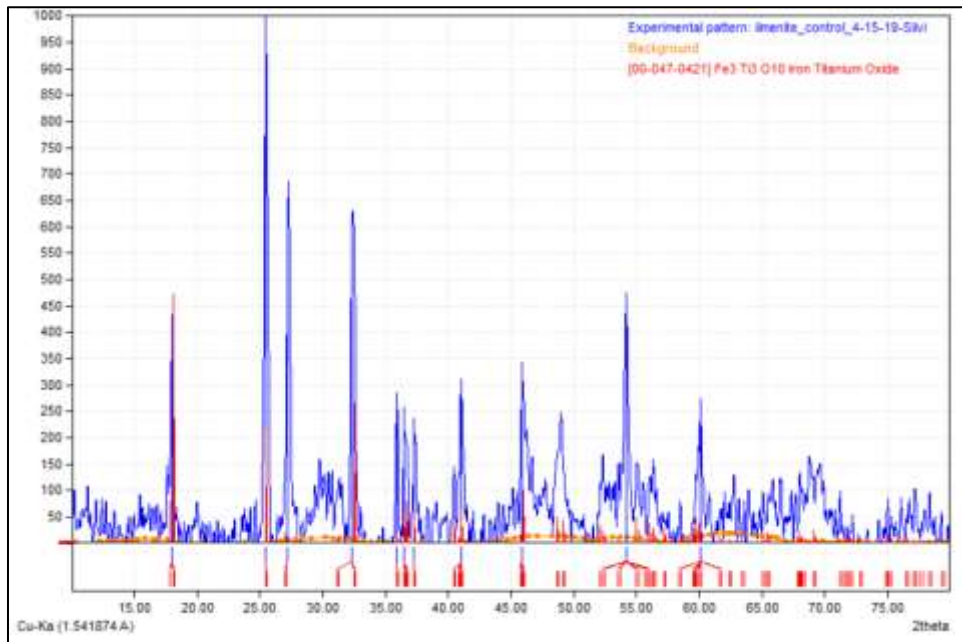
Figure 10. XRD pattern of Ilmenite-1 comparing with Fe$_3$ Ti$_3$ O$_{10}$.
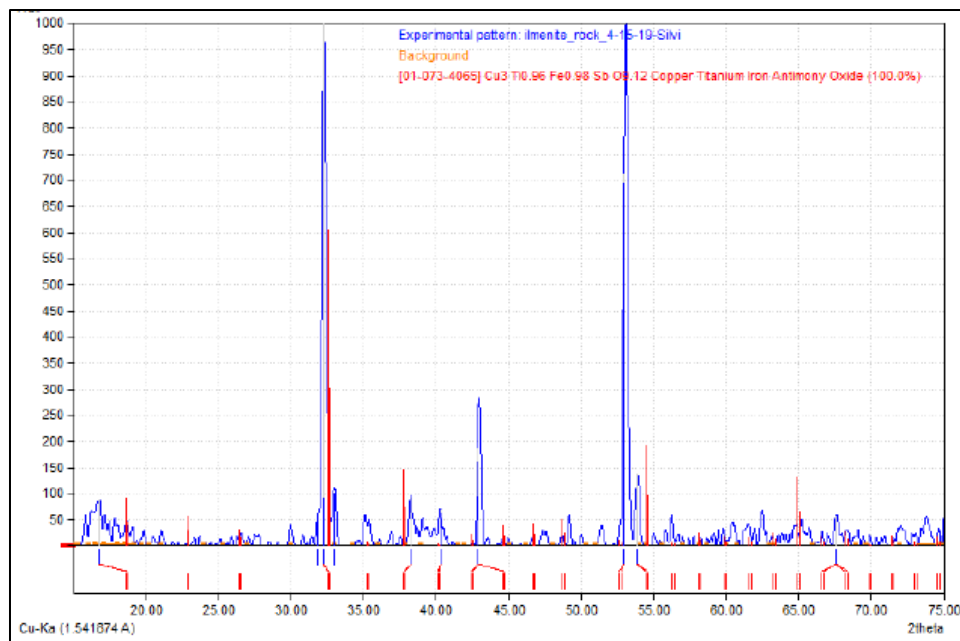
Figure 11. XRD pattern of Ilmenite-2 comparing with $Cu_3 Ti_{0.96\ Fe0.98}\ Sb\ O_{9.12}$.

The SEM image of Biotite minerals show a sheet-like structure while Ilmenite minerals have a rock-like structure (Figure 12). Table 2 and Table 3 show the percentage by weight of elements obtained via EDS analysis for Biotite and Ilmenite minerals, respectively. Biotite 1 and 2 have shown to have 15 − 20% by weight of iron, while Ilmenite had approximately 20% iron with Ilmenite 2 having a higher iron percentage by weight of approximately 55%, which is a much higher iron content compared to the rest of the minerals.
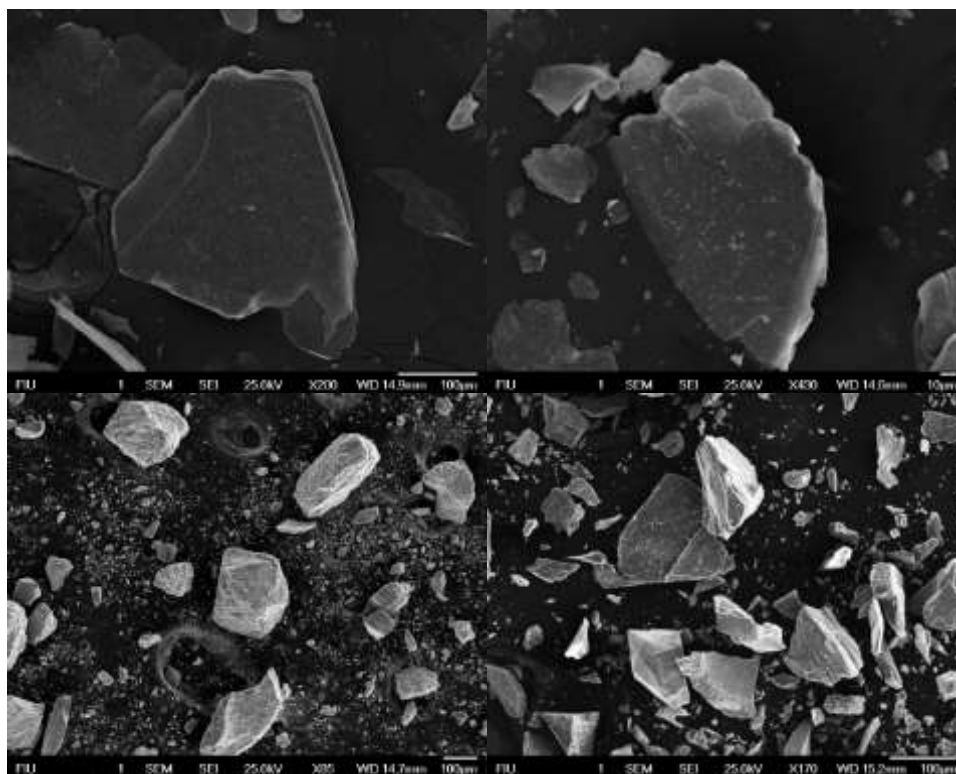
Figure 12. SEM images of biotite and ilmenite samples.

Table 2. Weight Percent of Elements in Biotite Samples

	C	O	Mg	Al	Si	K	Fe
Biotite 1	0	28.04	8.20	6.44	23.08	10.54	20.37
Biotite 2	13.87	24.39	8.88	4.32	21.40	11.33	14.48

Table 3. Weight Percent of Elements in Ilmenite Samples

	O	Ti	Fe
Ilmenite 1	32.63	41.86	19.57
Ilmenite 2	18.29	24.57	54.23

2. Technetium reduction in the presence of iron minerals

Triplicate samples were prepared, as described in the materials section, with biotite and ilmenite minerals in the presence of technetium. Samples were placed on a drum rotator at a 75 degree angle at 100 rpm, and aliquot samples were collected and analyzed via ICP-MS for Fe and Tc. Figure 13 shows the reduction of technetium with change in time. The reduction of Tc was observed on the level of 20-30% in the case of the two biotite minerals, while Ilmenite 1 showed slightly higher Tc reduction (~50%) compared to the biotite minerals. Ilmenite 2 minerals were shown to reduce technetium approximately 100% within one day. Presumably Tc^{7+} is reduced to Tc^{4+} and precipitated as low aqueous soluble $TcO_2 \cdot xH_2O$. Figure 14 shows the dissolution of iron, it was observed that around 20-40 ppm of iron was released from biotite minerals, while only about 1-5 ppm of iron was released from the ilmenite minerals.
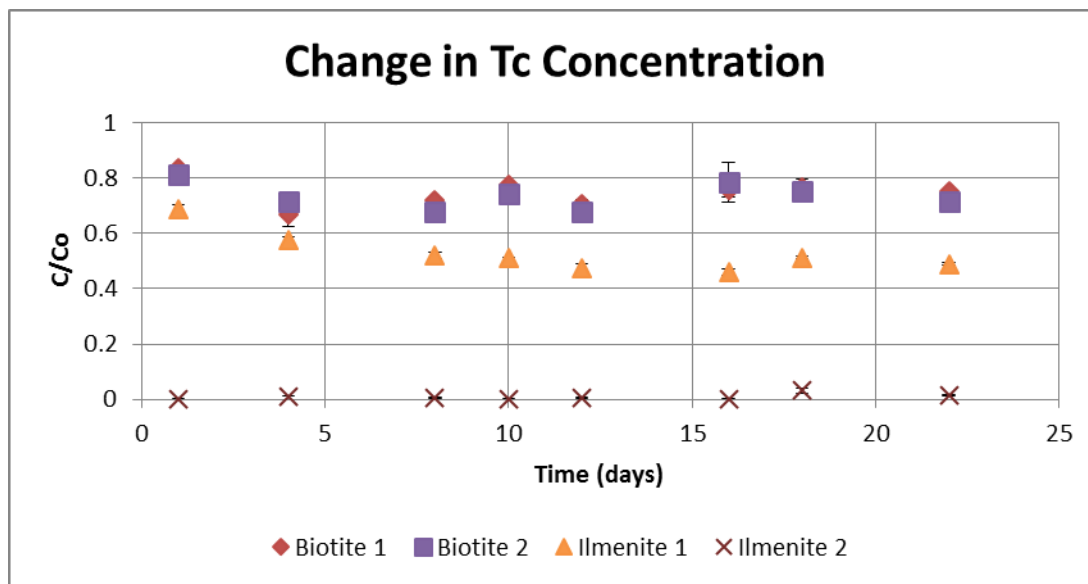
Figure 13. Reduction of Tc over time.
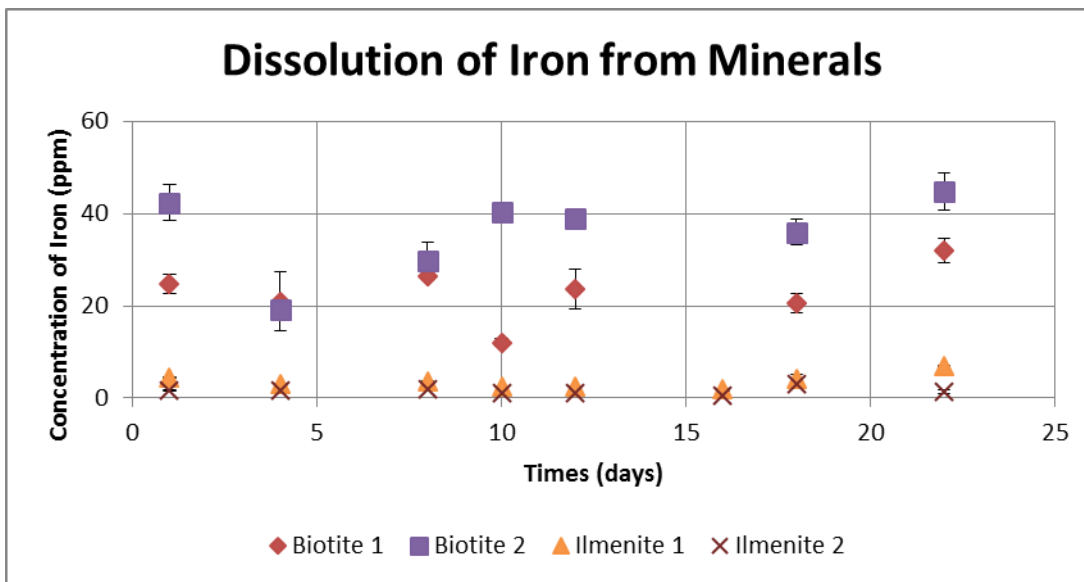
Figure 14. Dissolution of iron from minerals.

3. Dissolution of iron from minerals

A control dissolution experiment was performed with iron minerals (biotite and ilmenite) in the absence of technetium to study the release of ferrous iron from the minerals. Figure 15 shows an increase in iron concentration from the minerals as the time increases. The release of iron from the biotite minerals was shown to increase over time in the absence of technetium. In contrast, the release of iron from the minerals in the presence of technetium was constant. In addition, the maximum iron concentration observed in the presence of technetium was around 50 mg/L, and in the absence of technetium was less at 35 mg/L. In the case of the ilmenite minerals, the iron release was noted to be similar in both instances.
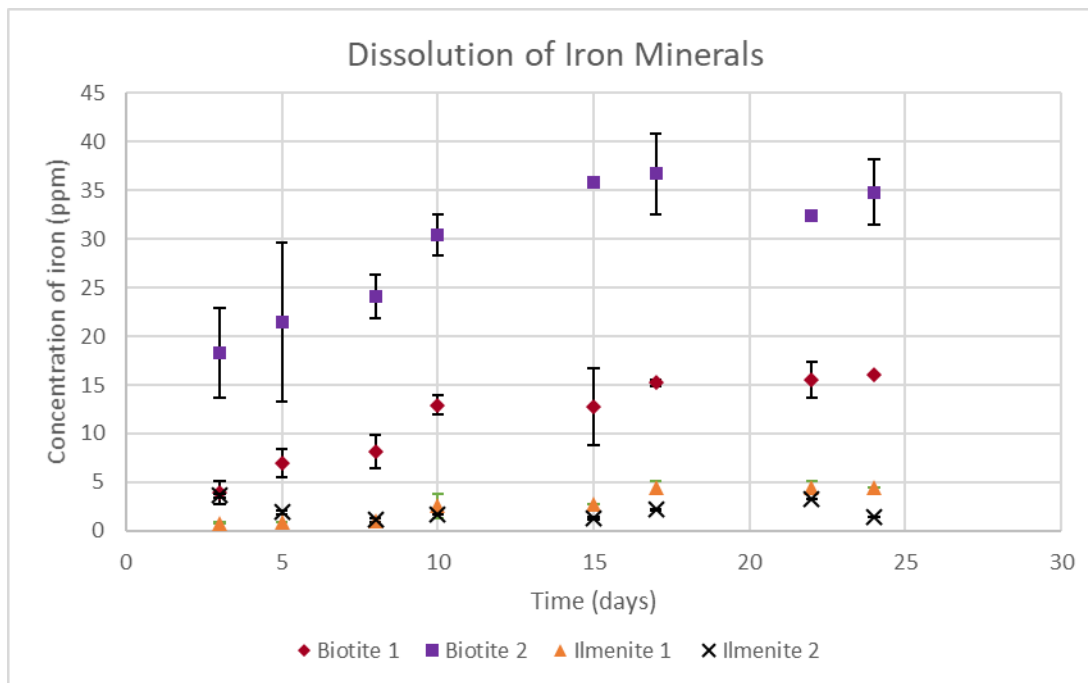
Figure 15. Dissolution of iron minerals in the absence of Tc.

Subtask 1.2: Conclusions and Future Work

Experimental data showed that technetium reduction occurs in the presence of ferrous iron containing minerals under anaerobic conditions. The reduction of technetium is dependent on the amount of iron present in the mineral. Ilmenite 2 has significantly higher iron content (50% iron by weight compared to 15%-20% iron by weight in other tested minerals) that resulted in completed reduction of technetium.

This task will not continue in FIU year 10.

Subtask 1.2: Acknowledgements

Subtask 1.2: References

Alliot, I., C. Alliot, P. Vitorge & M. Fattahi (2009) Speciation of technetium (IV) in bicarbonate media. *Environmental science & technology,* 43**,** 9174-9182.

Cui D., Eriksen T.E. (1996). Reduction of pertechnetate by ferrous iron in solution: influence of sorbed and precipitated Fe(II), *Environmental Science and Technology*, 30, 2259-2262

Icenhower, J. P., W. J. Martin, N. P. Qafoku & J. M. Zachara. 2008. The geochemistry of technetium: a summary of the behavior of an artificial element in the natural environment. Richland, WA: PNNL.

Jaisi D.P., Dong H.L., Plymale A.E., Fredrickson J.K., Zachara J.M., Heald S., Liu C.X. (2009). Reduction and long term immobilization of technetium by Fe(II) associated with clay mineral nontronite. *Chemical Geology* 264, 127-138

Kaplan, D. I., K. E. Parker & I. Kutynakov. 1998. Radionuclide Distribution Coefficients of Sediments Collected from Borehole 299-E17-21: Final Report for Subtask 1a. Pacific Northwest National Lab.(PNNL), Richland, WA (United States).

McCabe, D., B. Wilmarth, N. Machara, R. Bonczek, S. Chamberlain, M. Cline, M. Denham, M. Freshley, B. Harp, H. Lee, T. Levitskaia, R. Peterson & P. Suggs. 2017. *Technetium Management Program Plan*, SRS. Proceedings for the 2017 Waste Management Symposia. SRNL-STI-2016-00712.

Peretyazhko T., Zachara J.M., Heald S.M., Jeon B.-H., Kukkadapu R.K., Liu C., Moore D., Resch C.T., (2008). Heterogeneous reduction of Tc(VII) by Fe(II) at the solid–water interface. *Geochimica et Cosmochimica Acta*, 72, 1521–1539.

Peretyazhko, T., Zachara J.M., Kukkadapu R.K., Heald S.M., Kutnyakov I.V., Resch C.T., Arey B.W., Wang C.M., Kovarik L., Phillips J.L., Moore D.A. (2012). Pertechnetate (TcO_4^-) reduction by reactive ferrous iron forms in naturally anoxic, redox transition zone sediments from the Hanford Site, USA. *Geochimica et Cosmochimica Acta*, 92, 48-66

Szecsody, J. E., M. J. Truex, L. Zhong, T. C. Johnson, N. Qafoku, M. D. Williams, W. J. Greenwood, E. L. Wallin, J. Bargar & D. K. Faurie (2012) Geochemical and geophysical

changes during ammonia gas treatment of vadose zone sediments for uranium remediation. *Vadose Zone Journal,* 11.

Szecsody, J. E., M. J. Truex, L. R. Zhong, J. P. McKinley, N. P. Qafoku, B. D. Lee, and S. D. Saurey. 2015. "Remediation of Technetium in Vadose Zone Sediments Using Ammonia and Hydrogen Sulfide Gases." Vadose Zone Journal 14 (7). doi: 10.2136/vzj2014.09.0134.

Zachara, J. M., S. M. Heald, B.-H. Jeon, R. K. Kukkadapu, C. Liu, J. P. McKinley, A. C. Dohnalkova & D. A. Moore (2007) Reduction of pertechnetate [Tc (VII)] by aqueous Fe (II) and the nature of solid phase redox products. *Geochimica et Cosmochimica Acta,* 71**,** 2137-2157.

Subtask 1.3: Stability of Contaminants in Carbonate Precipitates

Subtask 1.3: Introduction (Summary)

Iodine-129 (^{129}I) is one of the top risk drivers at the radiological waste disposal sites in the United States due to its fast mobility in the subsurface, high toxicity, high bioaccumulation in the body's thyroid and extremely long half- life of 15.7 M year (Denham et al., 2009; Kaplan et al., 2010). ^{129}I was anthropogenically produced through the fission of uranium and plutonium at nuclear reactors. Large quantities of iodine-129 have been released to the environment during nuclear weapons testing and nuclear accidents (Gómez-Guzmán et al., 2014; Reithmeier et al., 2010). Accidental releases of ^{129}I to the subsurface at the U.S. Department of Energy (DOE) Hanford Site, Washington State, have resulted in large dilute plumes that cover an area of over 50 km^2 (Wan et al., 2004; Zhang et al., 2013). The largest ^{129}I plume is associated with the 200 West Area in the 200-UP-1 operable unit (OU). The primary concern for this plume is a potential discharge to the nearby Columbia River, which is a route for public exposure to contamination.

Iodine-129 is a beta-emitting radionuclide that has an extremely low maximum contaminant level (MCL) of 1 pCi L^{-1} in drinking water. The radioiodine (^{129}I) concentrations in Hanford Site plumes are in the proximity of 10 pCi/L, which is above the federal drinking water standard (Zhang et al., 2013). The aquifer also contains natural stable iodine (^{127}I), which has a similar chemical behavior as ^{129}I but is present at much larger concentrations in the groundwater, with ^{127}IO$_3^-$ /^{129}IO$_3^-$ ratios ranging from 100 to 1000 (Levitskaia et al., 2017; Truex et al., 2017a). The total iodine (^{127}I and ^{129}I) concentrations are < 100 ppb (Saslow et al., 2019; Zhang et al., 2013). The mobility of iodine depends on many factors, including chemical speciation, presence of other competitive contaminants, pH, redox conditions, sedimentary organic matter, calcium carbonate mineral content and microbial activity. Speciation measurements have suggested that the majority of the groundwater iodine at the Hanford Site, regardless of isotope, exists as IO$_3^-$ (Zhang et al., 2013), followed by organo-iodine and then a small amount of iodide species with averages of 76%, 22% and 2%, respectively (Xu et al., 2015). The radioactive iodine isotope (^{129}I) is very toxic to human and wildlife and accumulates in the thyroid. Currently, DOE has no approved treatment technologies for subsurface iodine plumes to control its mobility in the vadose zone and groundwater.

Remediation efforts at contaminated sites are generally complicated due to the presence of multiple contaminants with widely varying geochemical behavior. Hexavalent chromium [Cr(VI)] is a groundwater contaminant at numerous U.S. DOE sites and one of the major contaminants of concern at the Hanford Site where chromium persists as a co-contaminant in the current ^{129}I plume. At Hanford, chromium was used as a corrosion inhibitor in the reactor cooling water and was released to the environment as a result of planned and unplanned discharges from reactors during plutonium production. Chromate in the form of Cr(VI) is a highly mobile oxyanion in oxic oligotrophic environments typical of Hanford's vadose zone. Previous studies suggested that CrO_4^{2-} adsorption on soil minerals was suppressed when chromate co-located with other anions such as NO_3^-, HCO_3^-, and SO_4^{2-} (Zachara et al., 1988; Zachara et al., 1987). Hexavalent chromium concentration at the Hanford Site persists less than 0.5 mg/L (Hartman, 2019; Saslow et al., 2019).

Calcium carbonate minerals are abundant in nature and exist primarily as calcite, aragonite and vaterite, with calcite being the most thermodynamically stable form under ambient conditions and vaterite the least stable (Meldrum, 2003). The crystallization of $CaCO_3$ usually proceeds through a multi-step pathway involving intermediate phase sequences from amorphous $CaCO_3$ (ACC) to vaterite and then calcite (Kellermeier et al., 2008; Rieger et al., 2007). In nature, calcium carbonate may physically incorporate impurities within the solid during crystal growth (Morse et al., 2007). (Kitano et al., 1975) found that calcium carbonate can incorporate sulfate, chloride and sodium. Calcium carbonate can also incorporate magnesium depending on the nature of the co-anion present in the system (Kontrec et al., 2004). This mineral is also the dominant host of inorganic iodine and is important for the retention and removal of the radioactive iodine isotope (^{129}I) from contaminated waters (Podder et al., 2017). Studies confirmed that iodine removal from the aqueous phase can occur through incorporation into calcium carbonate, which is assumed to be mainly as the IO_3^- group substituting for CO_3^{2-}. Sequestration of iodate with calcium carbonate minerals is being considered as a potential passive *in situ* treatment approach such as monitored natural attenuation for immobilization of ^{129}I (Truex et al., 2017a; Zhang et al., 2013). Extensive research has been published on chromate (CrO_4^{2-}) incorporation with calcite (Hua et al., 2007; Sánchez-Pastor et al., 2011; Tang et al., 2007); however, these studies investigated iodate and chromate co-precipitation separately and did not consider their competitive effect on incorporation with other radionuclides. Saslow and team evaluated the effect of chromate on the iodine incorporation into calcite and noted a decrease in iodate removal from > 60 % to < 40 % upon chromate addition with less than 11 % of the chromate removal (Saslow et al., 2019).

Silica is one of the most abundant elements in nature and can have an impact on chemical weathering of alkaline-earth carbonates in the environment (Daval et al., 2009). Silica is one of the major elements both in minerals and in the porewater composition, and polymerization of silica at specific conditions can result in a transition of the solution to the solid phase (Iler, 1979; Kellermeier et al., 2013). There is limited data in the literature on how environmental conditions, specifically pH and silica concentrations in pore water compositions, affect the contaminant-calcium carbonate incorporation process. In previous studies, Si was effective in the removal of uranium from the synthetic bicarbonate and calcium bearing solutions mimicking pore water compositions at the Hanford Site vadose zone after pH manipulation via ammonia gas injections (Katsenovich et al., 2018). The presence of silica can affect the precipitation kinetics of calcium carbonate that would control iodate incorporation into calcium carbonate phases.

The focus of this task was to: (1) Study incorporation of iodate co-located with chromate in calcium carbonate at variable pH from 6.5 to 9 and Si concentrations from 0mM to 20mM; (2) conduct characterization of the precipitated solids via microscopy and x-ray diffraction analysis; and (3) investigate the stability of comingled iodine and chromate incorporated in calcite in the presence of silica via dissolution experiments.

The detailed description of the methodology and results is presented in the draft manuscript inlcuded in Appendix 2. This draft manuscript is currently under preparation for submission to a peer-reviewed journal.

This task was completed in FIU Year 9 and will not continue in FIU Year 10.

Subtask 1.3: Acknowledgments

Subtask 1.4: Experimental Support of Lysimeter Testing

Subtask 1.4: Introduction

The Hanford Field Lysimeter Test Facility (FLTF) is located in the 600 Area of the Hanford site (near the 200-W Area). This facility is being utilized by Pacific Northwest National Laboratory (PNNL) and Washington River Protection Solutions (WRPS) for field testing of various waste forms expected, or possible candidates, to be produced during treatment and immobilization of low activity waste (LAW) at Hanford. The FLTF test will be used to validate model predictions of long-term waste form behavior upon disposal in the Hanford site's integrated disposal facility.

One of the planned configurations of the lysimeter units described in the Implementation Plan (Bacon et. al., 2018) is to place cementitious waste forms (also termed grout waste forms) above glass waste forms. This waste form arrangement was modeled; however, limited laboratory data is available regarding the dissolution of glass in the presence of water which has contacted a cementitious material but then been buffered through sediment. Laboratory-scale experiments were conducted to investigate the impact of grout on the dissolution behavior of a borosilicate glass designed for the immobilization of LAW, ORLEC28 (Muller et al. 2016, Muller et al. 2017). The results of these experiments will provide information to support the design of future FTLF units to investigate the dissolution of waste forms at the Hanford Site Integrated Disposal Facility (IDF).

Borosilicate glass dissolution reportedly occurs through pH-dependent mechanisms. Primarily, glass dissolution occurs through the hydrolysis of the Si-O bonds within the glass network (or other network formers). In the PA rate model used by Hanford, the dissolution rate is controlled by the [Si] in the near-field solution. The addition of grout to the environment has the potential to alter the glass dissolution behavior through either the increased concentration of aqueous Si or an alteration of the pH environment from the presence of grout components.

Subtask 1.4: Objectives

This task was initiated during FIU Year 9 to conduct a series of laboratory-scale single-pass flow-through experiments to investigate the impact of grout on the dissolution behavior of a borosilicate glass designed for LAW immobilization. Three phases of experiments were designed for this study:

- Phase 1 (Baseline performance): Buffered pH solutions (pH 9/10: TRIS, pH 11/12: LiCl/LiOH) of equal ionic strength will be used to contact the glass. Experiments will be conducted at pH 9, 10, 11, and 12 and temperatures 25°C, 40°C, and 70°C.

- Phase 2 (Grout contacted solutions): The grout-contacted solution will be used directly in SPFT experiments at 25°C, 40°C, and 70°C.

- Phase 3 (Grout + sediment contacted solution): The grout-contacted solution will be passed through a column filled with sediment, provided by PNNL. The resulting solution will not be pH adjusted before using for the SPFT experiments. The SPFT experiments will be conducted at temperatures 25°C, 40°C, and 70°C.

During FIU Year 9, a q/S sweep was completed to determine the necessary conditions for the SPFT experiments. Agreement of the q/S results with literature led to the decision to begin with Set 2 experiments. These experiments were conducted and the results are discussed below, along with explanations of issues experienced during the experiments that will require further study. This work will be continued in FIU Year 10.

Subtask 1.4: Methodology

This task aims to conduct a series of experiments utilizing the single-pass flow-through (SPFT) method to determine the effect of grout material on the dissolution behavior of a borosilicate glass wasteform provided by PNNL (ORLEC28).

Glass preparation

Bulk glass samples were prepared in the manner described in ASTM C1285-14. The glass was crushed with an agate mortar and pestle then sieved to the desired size fraction (149 − 74 μm). The samples were washed with alternating DI water (>18 MΩ) and ethanol to remove fine particulate material formed during the crushing step. The glass was dried in an oven overnight before use in experiments.

Glass characterization

The crushed glass samples were characterized by scanning electron microscopy/energy dispersive X-ray spectroscopy (SEM/EDS) and BET analysis. The SEM/EDS results will allow for comparison of the glass size and structure before and after dissolution. The lack of fine particulates after cleaning the glass is also observable.

SEM/EDS

SEM/EDS samples were collected on a JEOL JSM-5900LV at 25.0 kV and a takeoff angle of 35.0°. The uncoated samples were analyzed in variable pressure (30 Pa). Samples were placed on carbon tape on a steel sample holder.

Surface area analysis

The glass surface area was determined using three methods, Brunauer-Emmett-Teller (BET) analysis, and geometric calculations based on the sieve mesh size and the SEM results. BET analysis was performed on a Micrometrics TriStar II 3020 instrument.

Solution analysis

All samples collected during the SPFT experiments were analyzed by inductively coupled plasma mass spectrometry (ICP-MS) or inductively coupled plasmas optical emission spectrometry (ICP-OES) following dilution in 2% nitric acid (HNO$_3$, Fisher Chemicals). A ThermoFisher Scientific iCAP RQ ICP-MS was used to analyze aqueous concentrations of Al, B, Ca, Mg, Fe, and Re. A Perkin Elmer 7600 ICP-OES was used to analyze aqueous concentrations of Ca, Mg, Na, and Si.

An estimated quantification limit (EQL) was determined by the lowest calibration standard that could be reproducibly measured within 10% error of the certified concentration. Calibration standards were measured a minimum of five times for this determination. ICP-MS EQL values for Al, B, Fe, and B were determined to be 3.4 µg/L, 9.2 µg/L, 0.46 µg/L, and 0.13 µg/L, respectively. The EQL values for Na and Si on the ICP-OES were determined to be 21.5 µg/L and 50 µg/L, respectively. The EQL values for Mg and Ca were not calculated, though the data is available.

Single-pass flow-through (SPFT)

SPFT experiments allow for determination of the dissolution behavior through the continuous flow of solution into a vessel containing the glass samples and subsequent collection and characterization of the effluent for monitoring the release of the target analytes. This method is reported by ASTM C1662-17.
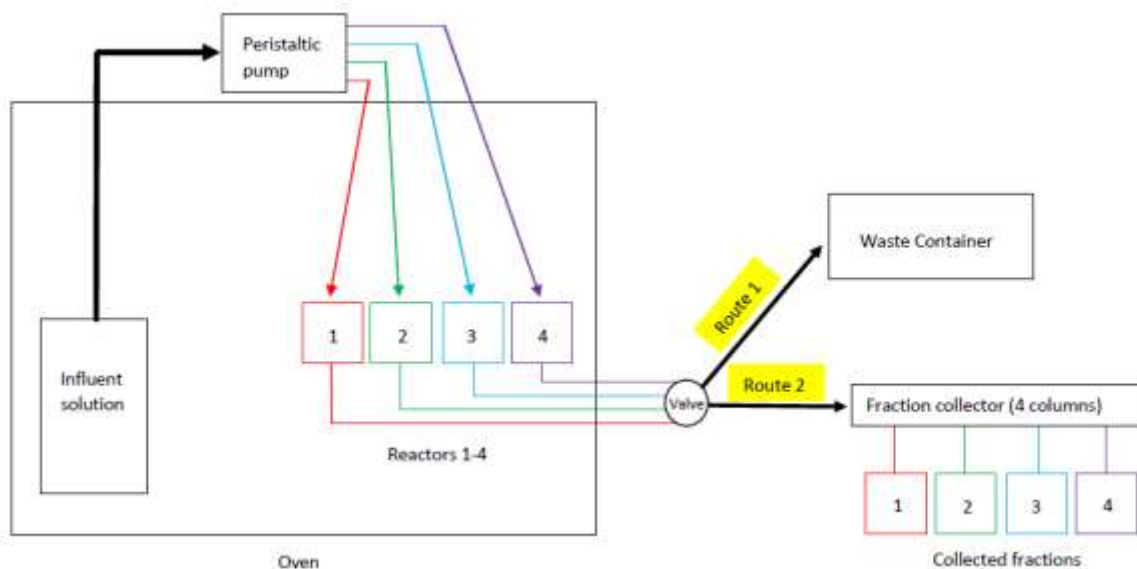
Figure 16. Experimental setup of SPFT experiments in a temperature-controlled environment.

The experimental setup is shown in Figure 16. The influent solution is kept inside an oven to maintain better control of the overall experimental temperature. The influent solutions are comprised of either Tris HCl/LiOH (pH 9-10) or LiOH/LiCl (pH 11-12). A peristaltic pump (Cole-Parmer, Wertheim, Germany, Ismatec IPC model) outside of the oven pumps the influent solution through the reactor vessels and into the collection containers. The primary tubing in the system is Tygon and the connections are Norprene (Cole-Parmer). The reactor vessels are 60-mL Teflon reactors (Savillex).

A Spectrum IS-95 interval collector (Figure 17) with four 3-way diverter valves is used to allow for intermittent sampling of the SPFT experiments while also collecting the bulk of the pass through solution into individual containers. This system will allow for multiple experiments to be carried out simultaneously, decreasing the overall time requirement for each set of experiments.

Figure 17. Spectrum IS-95 interval collector for SPFT experiments.

Buffer solution preparation

Buffered solutions were prepared for pH-controlled experiments. The solutions comprised of either Tris HCl/LiOH (pH 9-10) or LiOH/LiCl (pH 11-12). Tris(hydroxymethyl) aminomethane hydrochloride (Tris HCl) (Calbiochem, CAS: 1185-53-1), anhydrous lithium hydroxide (LiOH), and lithium chloride (Fisher Chemicals, CAS: 7447-41-8) were obtained from Fisher Scientific (Acros Organics, CAS: 1310-65-2). All prepared solutions were stored capped in a refrigerator.

Tris HCl/LiOH buffer (pH = 9): 2 L of 0.05 M Tris HCl was prepared by dissolving 15.76 g Tris HCl in 2 L DI water (> 18 MΩ) in a volumetric flask. The pH was then adjusted to 9.00 with 1.0 M LiOH.

LiOH/LiCl buffer (pH = 12): 2 L of 0.01 M LiOH/LiCl was prepared by dissolving 0.5124 g LiOH and 0.850 g LiCl in 2 L DI water (> 18 MΩ) in a volumetric flask. The pH was recorded. The pH of this solution should be monitored for changes as the solution interacts with the air.

q/S Sweep

Prior to investigating the impact of grout on glass dissolution, a series of experiments were carried out to determine the necessary conditions required to reach the forward rate of dissolution. The experimental matrix employed with these experiments was based on the matrix provided in PNNL-27098 (Neeway, *et al.* 2018) and is presented in Table 4. The matrix allows for a broad sweep of q/S (flow rate/glass surface area) values for determination of the forward

rate of dissolution. These experiments were carried out at the lowest and highest temperatures so that will be used in future experiments (25°C and 70°C). The data was used to extrapolate the necessary conditions for experiments at 40°C. All experiments were in a pH 9 Tris-buffered solution. The resulting fractions from each trial were analyzed by ICP-OES for Si, Na, and Ca, and ICP-MS for Al, B, Fe, Mg and Re.

Table 4. Experimental matrix for q/S Sweep for determination of forward rate of dissolution in SPFT experiments with ORLEC28 glass (Neeway, et al. 2018)

Temperature (°C)	pH	Glass mass (g)	Flow rate (mL/d)	q/S (m/s)
25	9	3.00	25	4.8×10^{-9}
		0.50	40	5.0×10^{-8}
		0.25	80	2.0×10^{-7}
		0.10	130	7.0×10^{-7}
70	9	1.50	40	1.5×10^{-8}
		0.15		1.5×10^{-7}
		0.015		1.5×10^{-6}
		1.50	80	3.0×10^{-8}
		0.15		3.0×10^{-7}
		0.015		3.0×10^{-6}

Determination of analyte release rates

The normalized release rates (r_i) were determined using

Equation 1, where $C_{i,s}$ is the steady-state concentration of the analyte i (g/m^3), $C_{i,b}$ is the background concentration of the analyte i (g/m^3), Q is the measured flow rate (m^3/d), S is the surface area of the glass powder (m^2), and f_i is the normalization factor for analyte i for the ORLEC28 glass. The values for f_i were calculated from the mass fraction of the glass (Neeway, *et al.* 2018).

$$r_i = \frac{(C_{i,s} - C_{i,b}) \times (Q)}{S \times f_i}$$

Equation 1. Formula for determination of normalized release rates of analytes.

SPFT experiments with grout-contacted solution

The test matrix (Table 5) to investigate the impact of grout on glass dissolution behavior was developed from previous literature (Neeway, et al. 2018). The matrix covers three temperatures, 25°C, 40°C, and 70°C and includes a control experiment using a pH 12 buffered solution as the inlet solution. Each experiment with the grout-solution was performed in duplicate.

Table 5. Test matrix for grout-contacted SPFT experiments with ORLEC28 glass

Temp (°C)	pH	Glass Mass (g)	Flow rate mL/d	q/S m/s

25	Grout	0.1	40	2.30×10^{-7}
	Grout	0.1	40	2.30×10^{-7}
	12	0.1	40	2.30×10^{-7}
40	Grout	0.05	40	4.70×10^{-7}
	Grout	0.05	40	4.70×10^{-7}
	12	0.05	40	4.70×10^{-7}
70	Grout	0.04	40	5.90×10^{-7}
	Grout	0.04	40	5.90×10^{-7}
	12	0.04	40	5.90×10^{-7}

Grout-contacted solution preparation

A grout-contacted solution was used as the inlet solution in SPFT experiments investigating the impact of grout on glass dissolution behavior. A sample of grout was provided to FIU by Matthew Asmussen at PNNL. The grout was crushed and sieved to <2 mm in size. The grout (250 g) was then kept in contact with DI water (1 L) while shaking for 7 days. After the contact time, the solution was filtered and then used in the SPFT experiments. The pH of the grout-contacted solution was 12.5.

Powder X-ray diffraction

Solid samples from from the grout-contacted solution were characterized by powder XRD. XRD analysis was performed on a Bruker D2 Phaser with a Cu K-alpha wavelength source (10 mA, 30 kV) from 3° to 90° (2θ) with a step size of 0.05° and a dwell time of 1.0 second using the continuous PSD scan mode. Pattern matching was performed with Bruker DIFFRAC.SUITE Eva V5.1 and the Crystallography Open Database. Solid samples were prepared by drying in a vacuum oven for 48 hours at 40°C.

Subtask 1.4: Results and Discussion

Glass characterization

Glass samples from PNNL were compared to the samples crushed by an agate mortar and pestle to investigate any discrepancies between size and EDS results.
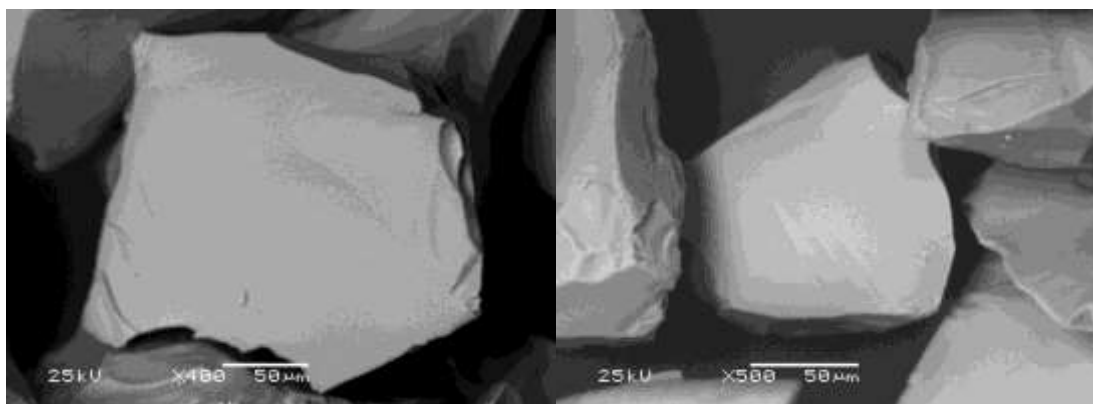
Figure 18. PNNL glass sample (149 µm -74 µm) (left) and FIU crushed glass sample (149 µm -74 µm) (right). Both samples show an absence of fines.

Both samples in Figure 18 represent the desired size fraction and were washed and dried to remove fines. EDS results from both samples (Table 6) showed comparable elemental concentrations, demonstrating a lack of contaminants from the in-house preparation method.

Table 6. EDS Analysis Results from PNNL Glass Sample and FIU Glass Sample

Element	PNNL sample (%)	FIU sample (%)
B	0.000	0.000
O	42.522	42.134
Na	16.776	16.649
Mg	0.670	0.671
Al	6.048	6.090
Si	18.298	18.626
S	0.158	0.177
Cl	0.222	0.219
K	2.178	2.199
Ca	1.310	1.321
Ti	0.279	0.333
Cr	0.277	0.229
Fe	0.345	0.337
Zn	1.593	1.552
Zr	5.240	5.317
Sn	3.361	3.471
Re	0.723	0.674
Total	100.000	100.000

The surface area (S) of the glass samples used in the SPFT experiments were calculated as the product of the specific surface area (S_p) and the mass of glass (m). Previous publications have shown the benefits of geometrically calculating the specific surface area of glass particles, rather than the use of Brunauer-Emmett-Teller (BET) analysis (McGrail et al. 1997, Icenhower et al. 2013). Geometric determination of the surface area of glass particles requires the assumption that the particles are spherical in shape, which is contradicted in Figure 19, and that cracks and dips in the glass do not significantly contribute to surface area. Isenhower et al. (2013) determined that despite these assumptions, the geometrically-calculated surface area provided more similar dissolution rates to monolithic samples of known surface area, than the BET determined surface area.

The surface area was determined through three methods, which are summarized in Table 7. BET analysis using nitrogen as the adsorbing gas determined the glass sample (149 μm to 74 μm) to be $2.035 \times 10^2 \pm 0.005$ m^2 g^{-1}. The density for quartz was used in the BET program. Two values for the specific surface area were calculated using Equation 2 (McGrail et al. 1997) and the

estimated particle radius from the average mesh opening (- 100 + 200) or the average measured radius from SEM. All three surface area values were similar, providing support for the geometric determination method.

$$S_p = \frac{3}{\rho \times r}$$

Equation 2. Geometric determination of specific surface area (S_p)

Table 7. Surface Area of FIU Glass (149 µm - 74 µm) Determined by BET Analysis and Geometric Calculation from Mesh Size Average or SEM-Measured Particle Size Average

Method	Density ρ (g cm^{-2})	Average particle radius r (m)	Specific surface area (m^2 g^{-1})
BET analysis	2.6500 (quartz)		2.04 x 10^{-2} $\pm$ 0.005
Geometric (mesh)	2.6979[†]	5.63 x 10^{-5}	1.98 x 10^{-2}
Geometric (SEM)	2.6979[†]	5.86 x 10^{-5}	1.90 x 10^{-2}

[†]Neeway et al. 2018

Figure 19. Measurement of particle size using SEM data: PNNL glass sample (149 µm -74 µm) (left) and FIU-crushed glass sample, crushed by agate mortar and pestle (149 µm - 74 µm) (right).

Interestingly, the average particle size of the FIU crushed glass samples (117.2 µm) was much smaller than the PNNL samples (170.3 µm) (Figure 19), suggesting a beneficial outcome from the additional preparation step of crushing the glass with a mortar and pestle.

q/S sweep

The q/S sweep experiments were carried out between October 2018 and April 2019. The experimental conditions are listed in Table 8. The normalized steady-state release rates for Al, B, Si, and Na in experiments at 25°C are presented in

Table 9. The normalized steady-state release rates for experiments at 70°C with a flow rate of 40 mL/day or 80 mL/day are presented in Table 10 and Table 11, respectively.

The q/S sweep included a wide range of flow rates and glass masses to investigate the necessary conditions for the dissolution behavior to reach steady-state. These conditions also required the

aqueous concentration of analytes to be above the limits of detection for the ICP-MS and ICP-OES. The results for the experiments at 25°C with flow rates < 80 mL/day were below detection limits. The release rates were calculated from the detection limit values.

Table 8. Experimental conditions used in q/S sweep for ORLEC28 glass

Experiment ID	Temperature (°C)	q (mL/d)	Glass mass (g)	S (m^2)	q/S (m/s)
QS.25.9.130	25	134	0.1013	2.06×10^{-3}	7.32×10^{-7}
QS.25.9.80	25	88.5	0.2553	5.18×10^{-3}	1.79×10^{-7}
QS.25.9.40	25	41.8	0.5168	1.05×10^{-2}	4.41×10^{-8}
QS.25.9.25	25	24.7	2.0055	4.07×10^{-2}	7.11×10^{-9}
QS.70.9.40.A	70	30.7	0.0145	2.94×10^{-4}	1.57×10^{-6}
QS.70.9.40.B	70	22.9	0.1480	3.00×10^{-3}	1.54×10^{-7}
QS.70.9.40.C	70	22.2	1.5092	3.06×10^{-2}	1.51×10^{-8}
QS.70.9.80.A	70	111	0.0176	3.57×10^{-4}	3.56×10^{-6}
QS.70.9.80.B	70	82.4	0.1504	3.05×10^{-3}	3.07×10^{-7}
QS.70.9.80.C	70	78.6	1.5030	3.05×10^{-2}	2.96×10^{-8}

Table 9. Results from q/S sweep at 25°C and pH 9 for ORLEC28 glass. The rates were normalized to account for the glass normalization factor (fi) for each analyte.

Steady-state q/S	Al Normalized Release Rate	B Normalized Release Rate	Si Normalized Release Rate	Na Normalized Release Rate
(m/s)	(g/m^{2}d)	(g/m^{2}d)	(g/m^{2}d)	(g/m^{2}d)
7.40E-07	5.64×10^{-2}	2.91×10^{-2}	1.64×10^{-2}	1.04×10^{-2}
1.96E-07	1.26×10^{-2}	7.87×10^{-3}	7.06×10^{-3}	2.80×10^{-3}
4.53E-08	2.79×10^{-3}	1.75×10^{-3}	4.87×10^{-3}	1.24×10^{-3}
6.71E-09	3.38×10^{-3}	1.43×10^{-3}	2.50×10^{-3}	1.60×10^{-3}

Table 10. Results from q/S Sweep at 70°C and pH 9 for ORLEC28 Glass with a target flow rate of 40 mL/day. (The rates were normalized to account for the glass normalization factor (fi) for each analyte.)

Steady-state q/S	Al Normalized Release Rate	B Normalized Release Rate	Si Normalized Release Rate	Na Normalized Release Rate
(m/s)	(g/m^{2}d)	(g/m^{2}d)	(g/m^{2}d)	(g/m^{2}d)
1.19E-06	2.75×10^{-1}	1.62×10^{-1}	---	2.65×10^{-1}
8.64E-08	2.10×10^{-1}	8.62×10^{-2}	---	1.56×10^{-1}
8.11E-09	4.44×10^{-2}	1.66×10^{-2}	---	3.06×10^{-2}

Table 11. Results from q/S Sweep at 70°C and pH 9 for ORLEC28 Glass with a target flow rate of 80 mL/day. (The rates were normalized to account for the glass normalization factor (fi) for each analyte.)

Steady-state q/S	Al Normalized Release Rate	B Normalized Release Rate	Si Normalized Release Rate	Na Normalized Release Rate
(m/s)	(g/m²d)	(g/m²d)	(g/m²d)	(g/m²d)
3.72×10^{-6}	2.80×10^{-1}	1.16×10^{-1}	1.70×10^{-1}	1.49×10^{-1}
4.34×10^{-7}	1.93×10^{-1}	1.01×10^{-1}	2.00×10^{-1}	1.33×10^{-1}
3.01×10^{-8}	6.41×10^{-2}	2.44×10^{-2}	3.65×10^{-2}	3.52×10^{-2}

Increased temperature or flow rate led to an increased dissolution rate of the glass. One accepted theory for this is based on the Transition State Theory, which assumes the overall reaction rate is dependent on the rate-limiting step. In this case, the release of the glass former Si is the accepted rate limiting step. This assumption allows for the determination of kinetic parameters, such as the rate constant, as demonstrated in *Equation 3*. (Aagaard and Helgeson 1982, Grambow 1985)

$$r = \overrightarrow{k_0} 10^{\eta pH} exp\left(\frac{-E_a}{RT}\right)\left[1 - \left(\frac{Q}{K_a}\right)\right]^{\sigma}$$

r = dissolution rate (g/m²d)

k_0 = forward rate constant (g/m²d)

E_a = apparent activation energy (kJ/mol)

R = gas constant (8.314 J/mol•K)

Q = ion activity product of rate-limiting reaction (unitless)

K_g = pseudo-equilibrium constant for the rate controlling reaction (unitless)

σ = Temkin coefficient

Equation 3. Relationship between dissolution rate (r) and pH, temperature, the saturation state of the system, and the activities of species.

The B release rates are considered the best representation of glass dissolution behavior. Na can be released by two mechanisms, glass dissolution and ion-exchange (IEX). IEX release of Na can affect the results, leading to misrepresented glass dissolution. Si and Al are both capable of forming secondary alteration layers due to solubility limitations. While the SPFT experimental setup is designed to prevent these alteration layers from occurring, the possibility prevents the use of Si and Al to determine glass dissolution behavior.
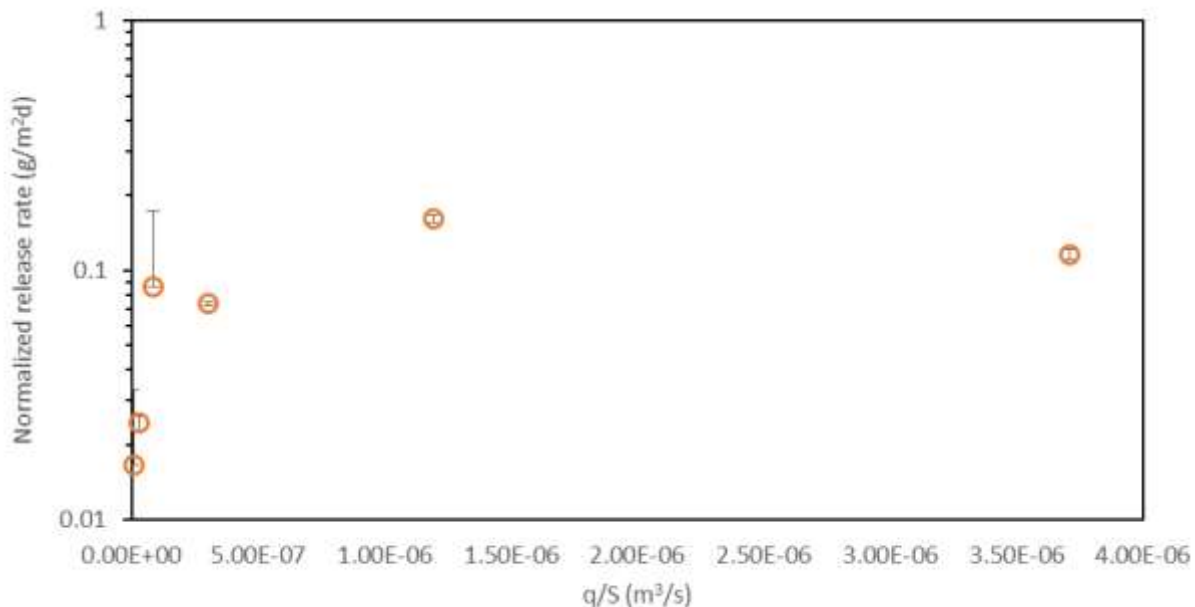
Figure 20. Normalized release rates for B from the q/S sweep at 70°C and pH 9 for ORLEC28 glass. The x-axis represents the steady-state q/S (m³ s⁻¹) values and the y-axis represents the steady-state release rate (g m⁻² d⁻¹).

The results from the q/S sweep were in agreement with those presented in PNNL-27098 (Neeway, *et al.* 2018), validating the experimental method and providing the necessary conditions for future experiments. Due to the agreement with literature results, the decision was made to move forward with the test matrices presented in PNNL-27098 (Neeway, *et al.* 2018), which investigated the baseline dissolution behavior of ORLEC28 glass in varying pH and temperature. While the baseline behavior will be determined by FIU in future experiments, the next set of experiments performed in FIU Year 9 focused on investigating the impact of grout on the dissolution behavior.

SPFT experiments with grout-contacted solution

During the last half of FIU Year 9, SPFT experiments using grout-contacted solution as the leachate were initiated. Table 5 shows the test matrix that was employed for these experiments. The grout-solution experiments were run in duplicate alongside a control using a pH 12 buffered solution (LiOH/LiCl) for comparison to the literature baseline behavior (Neeway, et al. 2018).

Initial results show a significant impact from the presence of grout on the release of B from the glass (Figure 21). The samples labeled A-25 and A-40 designate experiments where the leachate was a pH 12 LiOH/LiCl buffer. These were carried out in addition to duplicate experiments with the grout-contacted solution for comparison of dissolution behavior due to the pH of the grout solution being between 12-12.5. The presence of grout appears to significantly slow dissolution of the glass. The B dissolution rates of the grout-contacted experiments (B-25, B-40, C-25, C-40) are more similar to the rates observed when a buffered pH 9 solution was used. However, the controls (C-25 and C-40), which used a buffered pH 12 solution (LiOH/LiCl) solution as leachate, were lower than the literature values. A small amount of white solid was observed in the grout-contacted solution and inside the related reactors during the 40°C experiments.
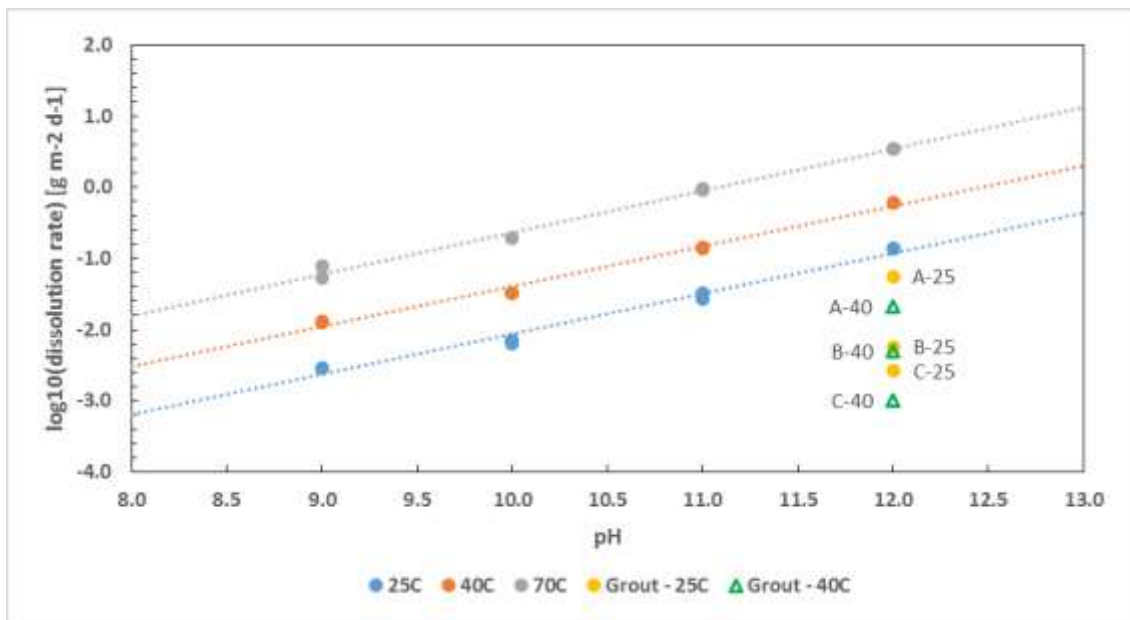
Figure 21. Baseline B dissolution behavior of ORLEC28 glass in varying pH and temperature as reported in PNNL-27098 (Neeway, et al. 2018) is shown in gray, orange, and blue. The preliminary results from experiments at 25°C and 40°C utilizing grout-contacted water as the leachate are shown in yellow and green.

The SPFT experiments at 70°C were unsuccessful due to blockages throughout the tubing that prevented even flow of the grout solution. A white solid formed inside the tubing between the stock bottle and pump and between the pump and reactor. The affected areas of tubing were outside of the oven. The white solid was not present in the stock solution, indicating formation occurred inside the tubing. The white solid was also found inside the reactors.

This white solid was observed in smaller amounts in the experiments at 25°C and 40°C; however, the flow remained even, so the experiments were continued. Additionally, in these experiments, the white solid was found in the stock solution bottle. This white solid appears to form in the grout solution after filtration. The lack of solid in the stock bottle at 70°C suggests the high temperature allowed the solid to remain in solution due to the higher solubility of the solution, but the solid precipitated once outside the oven and in the room temperature tubing and did not go back into solution once inside the reactor.

Precipitation issues

The white solid observed in the experiments with the grout-contacted solution were analyzed by powder XRD. A solid was collected from within the grout-solution stock bottle (Solid A) and a second solid was collected from inside the reactor (Solid B, Figure 22).

Figure 22. Suspension of white solid observed inside reactor from SPFT experiment at 70°C. The circle in the bottom left indicates where the suspension has held shape from the presence of the tubing.

Figure 23 shows a comparison of the XRD patterns for Solid A (C and D) and Solid B (A and B) from 5° to 50° (2θ). No peaks were observed past 50° (2θ). Both solids have peaks near 5.5°, 9.0°, 29°, 36°, 39°, and 43° (2θ). Both solids also have peaks indicative of an amorphous phase at 20° and 23° (2θ). However, pattern matching of the two solids indicated little similarities between them, with only $AlPO_4$ matching both solids.

The results of the pattern matching of both solids are presented in Table 12. Pattern matching percentages were calculated based on peak area and ignored the presence of amorphous phases. Solid A appears to be primarily comprised of aluminum phosphate mineral ($AlPO_4$, 36.3%), while Solid B is primarily comprised of nitratine ($NNaO_3$, 61.3%). Both solids contain Al, Ca, Na, P, and Si; however, Solid A also contains S while Solid B contains N. The difference in relative elemental composition is shown in Table 13.
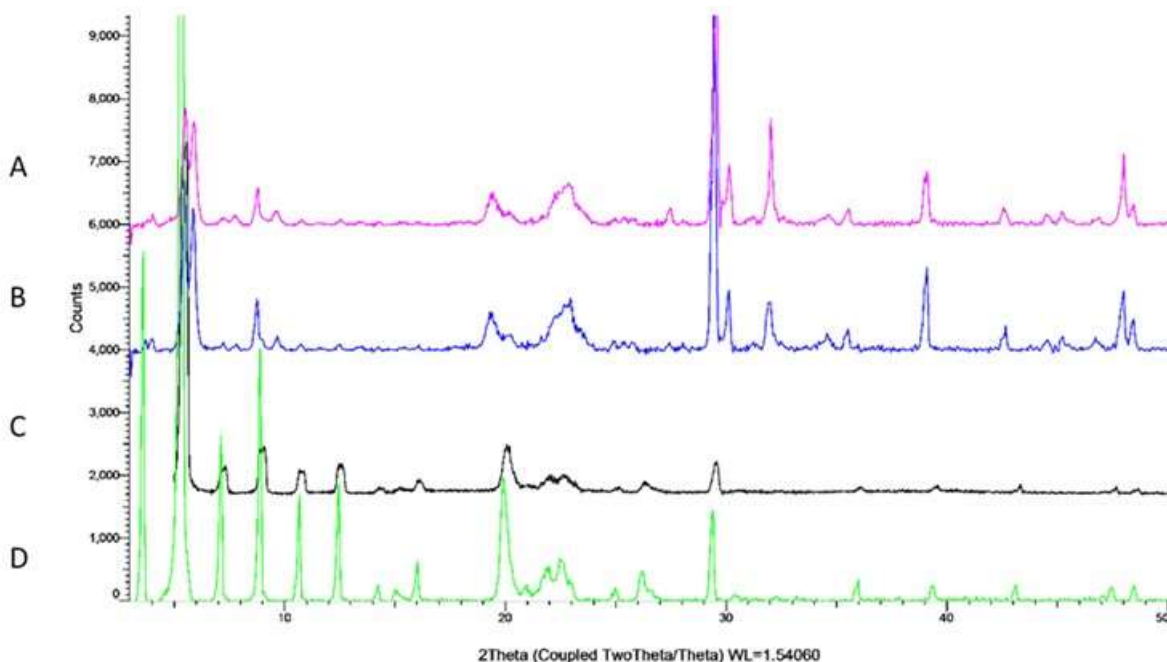
Figure 23. Comparison of powder XRD patterns of Solid A (C and D) and Solid B (A and B). No peaks were

observed past 50° (2θ) in any scans. Each solid was analyzed in duplicate.

Table 12. XRD pattern matching for Solid A and Solid B from Diffrac.Eva software. All percentages are semi-quantitative and calculated by the software based on peak area.

Solid	Compound Name	Formula	Compound Number	Percentage (semi-quant)
Grout Solution (Solid A)	---	$AlPO_4$	COD 1537021	36.3%
	---	$CCaO_3$	COD 2310543	16.6%
	---	$C_4H_{12}SiO_4$	COD 5900021	10.8%
	Quartz	SiO_2	COD 9007378	5.0%
	---	$Al_{12}Ca_4Na_4Si_{12}O_{48}$	COD 2310483	6.6%
	---	SO_3	COD 9011063	24.6%
Reactor Solid (Solid B)	Nitratine	$NNaO_3$	COD 9009659	61.3%
	---	$AlPO_4$	COD 1537021	28.98%
	---	$Al_2CaSi_4O_{12}$	COD 1101054	27.0%
	Darapskite	$H_2NNa_3SO_8$	COD 9012765	10.45%
	Diaspore	AlO_2	COD 9014565	14.1%
	---	$CCaN_2$	COD 1010503	13.51%

Table 13. Element composition of Solid A and Solid B calculated by Diffrac.Eva based on XRD pattern matching

Element	Solid A	Solid B
Hydrogen	0.9%	0.1%
Carbon	5.4%	1.2%
Nitrogen	---	13.5%
Oxygen	52.0%	50.9%
Sodium	0.4%	19.2%
Aluminum	9.3%	8.5%
Silicon	5.7%	0.6%
Phosphorus	9.2%	0.6%
Sulfur	9.9%	1.2%
Calcium	7.3%	4.3%

Table 14. Quantitative XRD characterization of Cast Stone samples. Adapted from Table S1 (supplementary material) (Asmussen, et al. 2018)

Compound Name	Formula	Percentage (wt%)
Hydrocalumite	$Ca_2Al(OH)_{6.5}Cl_{0.5} \cdot 3H_2O$	1.3 - 2.8%
Hemicarbonate	$(Ca_2Al(OH)_6)_2 \cdot \frac{1}{2}CO_3 \cdot OH \cdot nH_2O$	0.8 - 2.6%
Hydrotalcite	$Mg_6Al_2(CO_3)(OH)_{16} \bullet 4(H_2O)$	1.4 - 2.7%
Calcite	$CaCO_3$	0.7 - 3.2%
Larnite	Ca_2SiO_4	1.0 - 3.0%
Tobermorite	$Ca_5Si_6O_{16}(OH)_2 \cdot 4H_2O$	2.7 - 5.6%
Burtite	$Ca(Sn(OH)_6)$	0.0 - 0.06%
Quartz	SiO_2	1.4 - 2.8%
Amorphous	---	83 – 90%

Pattern matching was performed assuming a similar chemical makeup of the grout as the Cast Stone used in previous studies

Table 14 shows the quantitative XRD results for Cast Stone samples previously studied by Asmussen *et al.* in leaching studies (Asmussen, *et al.* 2018). Attempts to match the same minerals to Solid A and B were unsuccessful. However, similarities between Solid A and B and the Cast Stone samples were present (e.g. calcite and quartz).

Additional analysis is necessary to fully determine the chemical makeup of Solid A and Solid B. Currently, XRD data suggests the solids differ in composition. More accurate pattern matching may be achieved once the exact composition of the grout material has been provided by PNNL.

The formation of two different solids during the SPFT experiments was concerning due to the significant change in solution chemistry that must occur. When Solid A forms in the grout-solution stock bottle, the solution that later contacts the glass is significantly different from what was previously assumed. The most noteworthy difference between solids is the percentage of Si, 5.7% and 0.6%, for Solid A and B, respectively. The change in composition of these two solids prevents accurate interpretation of SPFT results from previous experiments.

To prevent the formation of solid in the SPFT experimental setup, the grout solution will be diluted (1:10). One possible cause of this precipitation is the saturated nature of the grout solution. By diluting the stock solution, precipitation should not occur and the solution chemistry will remain stable.

Subtask 1.4: Conclusions and Future Work

During FIU Year 9, SPFT experiments were initiated to investigate the impact of grout on glass dissolution behavior. As a new direction of research for FIU, this task required method

development and validation. The work was initiated through a series of q/S experiments to determine necessary conditions for future SPFT experiments as well as to validate the experimental setup through comparison with literature precedence. SPFT experiments using a grout-contacted solution as the leachate were performed. These experiments were halted after the formation of solids in the grout solution and reactor. Efforts toward identifying the solids were made and will continue in the following year. Strategies to prevent precipitation of the grout solution were devised and will be tested in future experiments.

Investigations into the impact of grout on the dissolution behavior of ORLEC28 glass will be continued with the dilute grout-contacted solution. Additional experiments may be performed to determine if impacts from the presence of grout arise from the increased Si concentration or from a change in pH from the grout components. The baseline glass dissolution behavior will also be determined by FIU to further validate this work with the literature values.

Subtask 1.4: Acknowlegements

Subtask 1.4: References

Aagaard, P.; Helgeson, H. C. Thermodynamic and Kinetic Constraints on Reaction Rates among Minerals and Aqueous Solutions. I. Theoretical Considerations. *American Journal of Science* **1982**, *282*, 237–285.

Amussen, R. M., *et al.* "Getters for improved technetium containment in cementitious waste forms." Journal of Hazardous Materials, 341(2018): 238-247.

ASTM International. C1285-14 Standard Test Method for Determining the Chemical Durability of Nuclear Waste Glasses: The Product Consistency Test (PCT). ASTM International, West Conshohocken, PA.

ASTM International. C1662-17 Standard Practice for Measurement of the Glass Dissolution Rate Using the Single-Pass Flow-Through Test Method. ASTM International, West Conshohocken, PA.

Bacon, D. H., Meyer, P. D., Neeway, J. J., Fang, Y., Asmussen, R. N., Strickland, C. E. 2018. Field-Scale Lysimeter Studies of Low-Activity Waste Form Degradation. PNNL-27394, Pacific Northwest National Laboratory, Richland, Washington.

Grambow, B. A General Rate Equation for Nuclear Waste Glass Corrosion. *MRS Proceedings* **1985**, *44*, 15–27.

Icenhower JP and CI Steefel (2013) Experimentally determined dissolution kinetics of SON68 glass at 90°C over a silica saturation interval: Evidence against a linear rate law. *J. Nucl. Mater.* **439**, 137-147.

McGrail, B. P.; Ebert, W. L.; Bakel, A. J.; Peeler, D. K. Measurement of Kinetic Rate Law Parameters on a Na-Ca-Al Borosilicate Glass for Low-Activity Waste. *Journal of Nuclear Materials* **1997**, *249*, 175–189.

Muller IS, KS Matlack and IL Pegg. (2016) Enhanced LAW Glass Correlation – Phase 1. VSL-16R4000, Vitreous State Laboratory, The Catholic University of America, Washington, DC.

Muller IS, KS Matlack and IL Pegg. (2017) Enhanced LAW Glass Correlation – Phase 2. VSL-17R4140-1, Rev. A, Vitreous State Laboratory, The Catholic University of America, Washington, DC.

Neeway JJ, RM Asmussen, EA Cordova, CE Lonergan, BD Williams, II Leavy and EM McElroy. (2018) FY2017 ILAW Glass Corrosion Testing with the Single-Pass Flow-Through Method. PNNL-27098, Rev. 0, Pacific Northwest National Laboratory.

TASK 2: REMEDIATION RESEARCH AND TECHNICAL SUPPORT FOR SAVANNAH RIVER SITE

Task 2: Executive Summary

Iodine-129, technetium-99, and uranium represent the major radiological risk drivers from contaminants released at the Savannah River Site. Radionuclides previously disposed of through unlined seepage basins as a constituent of acidic, aqueous waste are moving towards Four Mile Branch and Tims Branch wetland with natural groundwater flow, where they may subsequently be interacting with natural organic materials present in the wetland or with humic materials injected for remediation purposes. The fate and transport of uranium, technetium, and iodine in the subsurface are controlled by their oxidation state as it directly correlates to solubility as well as sorption and complexation affinity. A better understanding of the environmental conditions that affect these processes is critical to a more realistic risk assessment.

During FIU Performance Year 9, FIU completed experiments to investigate the impact of reductive oxygen species on the fate of Tc, I, and U in wetlands at the Savannah River Site. The following subtasks were developed during FIU Performance Year 9.

Subtask 2.1: Impact of Reductive Oxygen Species on the Fate of Tc, I, and U in Wetlands at the Savannah River Site

Subtask 2.1: Introduction

The F-Area at the Savannah River Site contained three unlined seepage basins that received low-level, radioactive wastewater from plutonium processing. These disposal operations resulted in a groundwater plume that is moving towards Four Mile Branch, where contaminants have been interacting with wetland soils rich in natural organic matter (NOM, Figure 24). The waste contained non-radioactive metals (Hg, Pb, Cd, Cr, and As) and various radionuclides (U, Pu, Am, Sr, Cs, Ce, I, ^{3}H) dissolved in dilute nitric acid. The conditions of the waste and subsequent remediation activities led to mobilization of some radionuclides depending on their speciation. Uranium isotopes (U), iodine-129 (I-129), and technetium-99 (Tc-99) released during operations are the major radiological risk drivers at Savannah River Site.
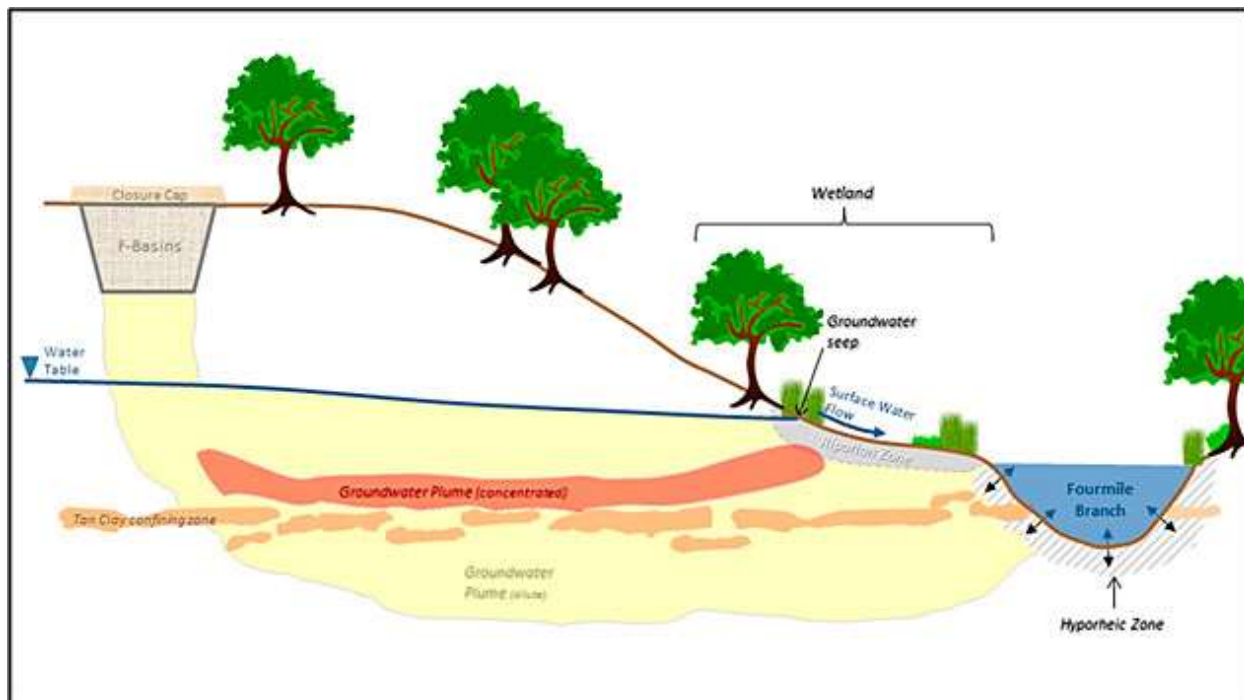
Figure 24. Schematic of F-Area Seepage Basins, wetlands, and Fourmile Branch (Eddy-Dilek, Kostelink, and Denham 2016).

The fate, transport and natural attenuation of contaminants in the subsurface are controlled by many variables including their oxidation state, pH, soil minerals and organic content. Strong interactions were observed for I-129 and Tc-99 with NOM, especially in the acidic pH range (Icenhower et al. 2008, Emerson et al. 2013, Kaplan et al. 2014). Strong interactions have also been reported for U with NOM with nearly complete removal across the pH range 4-10 (Wan, Dong, and Tokunaga 2011). The interactions of Tc, U, and I with organic matter in a natural wetland environment will change depending on many different factors including redox conditions, water content, temperature, and organic matter degradation with time.

In surface waters in a wetland, reactive oxygen species (ROS) will form due to solar irradiation of nitrate and organic matter (Brezonik and Fulkerson-Brekken 1998, Gligorovski et al. 2015). Further, the high concentrations of nitrate released with acidic waste may elevate ROS above expected concentrations in natural conditions due to their strong photochemical reactions (Brezonik and Fulkerson-Brekken 1998, Gligorovski et al. 2015). Associated redox changes can degrade NOM and directly change the valence state of radionuclides and metals, leading to increased or decreased mobilization of these elements in the subsurface. The objective of this study is to understand light induced changes on NOM in the presence of nitrate and to evaluate the effect on the attenuation/sequestration of contaminants such as I-129, Tc-99, and U in the F-Area wetland.

This effort is in alignment with the DOE Office of Environmental Management (EM) plans to quantify the effect of co-mingled contaminant plumes (McCabe et al. 2017) and is relevant to SRS remediation needs including the generation of data that will supplement ongoing activities at SRS pertaining to the Area Completion Project (ACP).

Subtask 2.1: Objectives

To understand I, Tc, and U interactions with reactive oxygen species (ROS) and NOM impacted

by ROS due to nitrate and UV interactions. This is applicable due to the high concentrations of nitrates released to the basins, which may impact interactions of Tc/I/U with NOM in the F-Area wetland. Previous work has shown that nitrate is a major contributor to hydroxyl radical formation caused by photochemical reactions in natural environments. The presence of hydroxyl radicals may alter NOM or directly participate in redox reactions with contaminants of concern (Brezonik and Fulkerson-Brekken, 1998; Gligorovski et al., 2015). This research will determine whether these interactions affect the fate of Tc, I, and U and which processes are controlling their behavior (i.e. direct interaction with free radicals or interactions with altered NOM).

Subtask 2.1: Methodology

Materials

Everglades and Savannah River Site samples were included to investigate light-induced alterations of organic matter. The Everglades peat sample was included for comparison as it represents a different system with high NOM. Table 15 summarizes the water content and total organic carbon in these samples as measured via ASTM D2973-13.

Table 15. Total Water Content (θ) and Total Organic Carbon (TOC) in Soil Samples

Sample ID	θ	TOC
SRS	0.19 ± 0.01	0.06 ± 0.00
Everglades	0.90 ± 0.01	0.09 ± 0.02

Batch Experimental Design

Batch experiments were conducted in triplicate with autoclaved soil samples in 8-mL quartz vials under the following general conditions: 1.0 g/L peat, 11,475 mg/L (135 mM) $NaNO_3$, 100 µg/L $^{99}TcO_4^-$, $^{238}UO_2^{2+}$ and $^{127}IO_3^-$. Each experiment then included a set of samples with and without exposure to light (light flux of approximately 18,000 lux as measured by a Reed instruments R8120 lux meter which is representative of full daylight but not direct sunlight). Previous research has shown that IO_3^- is the primary species entering the Four Mile Branch wetland, although I^- and IO_3^- reach similar equilibrium sorption to wetland samples in batch experiments due to transformation to organo-iodine species which has important implications to the SRS ACP (Emerson et al. 2013, Otosaka et al. 2011). In order to eliminate the potential microbial impact, the soil samples were autoclaved and then spiked with contaminants.

One set was prepared with and without Tc, U, and I so that UV-vis analysis could be conducted in quartz cuvettes without contaminating the cuvettes. Further, one set both with and without the radionuclides of concern were exposed to full light in the environmental chamber (25°C and 18,000 lux) for approximately 24 hours while the others were placed into 50-mL black centrifuge tubes and carried through the same analysis. Another set was prepped to test the impact of contaminant addition before or after the 24-hour exposure in the environmental chamber.

Analytical Measurements

The dissolved fraction was separated by centrifugation (20 minutes at 8000 rpm, 4659 rcf). This centrifugation step is expected to remove particles >100 nm according to the Stoke's law. Analysis for total organic carbon was conducted by UV-vis spectroscopy. Each sample was prepared in 0.001 M NaOH to keep organics soluble for analysis at the following wavelengths: 254 (E2), 280, 365 (E3), 465 (E4), and 665 (E6) nm. Then, comparisons were made for the E2/E3 and E4/E6 ratios as previous researchers have shown these wavelengths suggest

alterations in photooxidation (E2/E3) and aromaticity (E4/E6 ratio and 280 nm wavelength) (Dobbs, Wise, and Dean 1972, Helms et al. 2008, Amador, Alexander, and Zika 1989, Sharpless et al. 2014, Chin, Aiken, and Oloughlin 1994). For analysis of Tc and U, samples were prepared in 2% HNO_3 and analyzed by inductively coupled plasma-mass spectrometry (ICP-MS, ThermoFisher Scientific iCAP RQ). Iodine samples were diluted with 0.1% tetramethylammonium hydroxide (25% w/w aq. soln., 99.9999% purity, Fisher Scientific) and analyzed by ICP-MS with a helium collision cell.

Subtask 2.1: Results and Discussion

Results for SRS and Everglades soils both indicated a significant removal of U (76 ± 2 and 80 ± 2% removal, respectively, at pH 6 with UV-light exposure). Although a slightly greater removal of U was observed in the Everglades peat as compared to SRS soils, these differences were not significantly different (Figure 25). Furthermore, greater removal was observed in the dark for Everglades peat as compared to light conditions, although a significant effect of light was not observed for any other samples potentially due to the short exposure time (24 hours). However, it is possible that UV-light degradation of NOM in the Everglades peat led to formation of small organic compounds, which complexed U leading to less U available for sorption.

Further, similar U removal was observed at pH 4.5 and 6 with 80 ± 2% removal (Figure 26) while Tc-99 removal (Figure 27) was slightly higher at pH 4.5 (89 ± 0%) compared to pH 6 (80 ± 1%). Because Tc-99 is primarily present in the aqueous phase as TcO_4^-, sorption generally increases with decreasing pH due in part to electrostatic interactions as potential sorption sites become more positive (due to greater H^+). Tc-99 also showed significantly more variable behavior between the two soil samples as compared to U with relatively more Tc-99 removed by SRS soils compared to Everglades peat (Figure 25 and Figure 28).
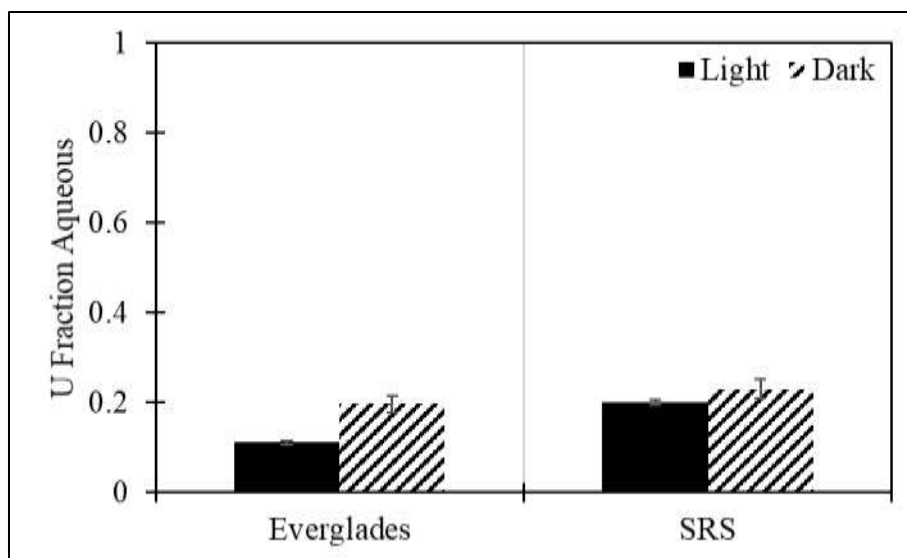
Figure 25. Comparison of remaining aqueous fraction of 100 µg/L U after 24 hours of exposure to 1.0 g/L SRS and Everglades samples prepared with 135 mM $NaNO_3$ at pH 6 in the presence or absence of UV light. Note: error bars are based on one standard deviation of triplicate samples.
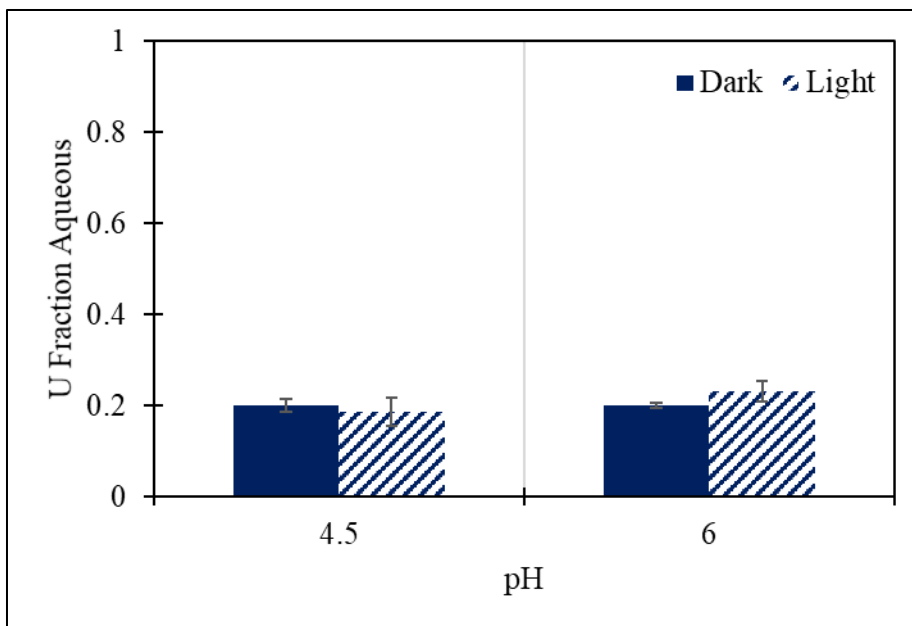
Figure 26. Comparison of remaining aqueous fraction of 100 μg/L U after 24 hours of exposure to 1.0 g/L SRS samples prepared with 135 mM NaNO₃ at pH 4.5 and 6 in the presence or absence of UV light. Note: error bars are based on one standard deviation of triplicate samples.
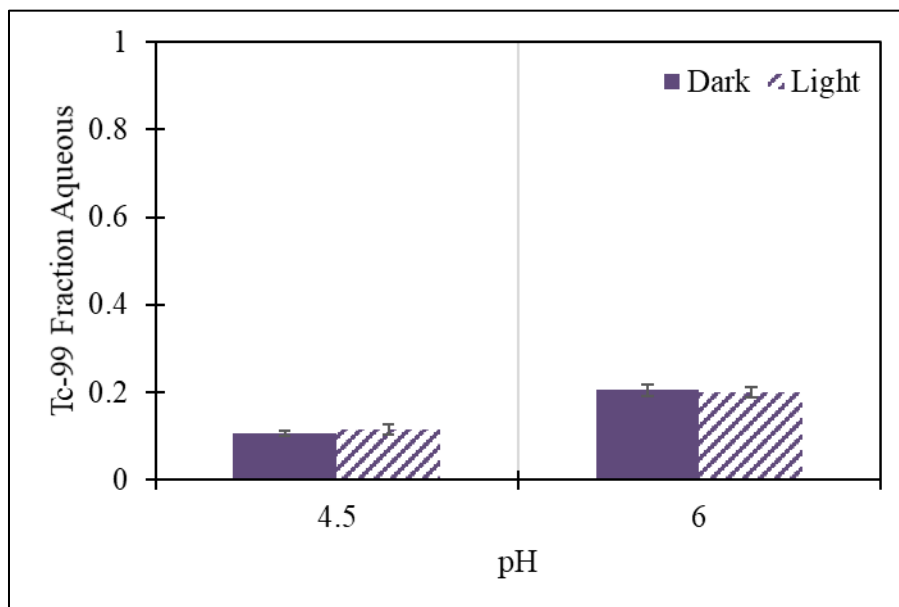
Figure 27. Comparison of remaining aqueous fraction of 100 μg/L Tc after 24 hours of exposure to 1.0 g/L SRS samples prepared with 135 mM NaNO₃ at pH 4.5 and 6 in the presence or absence of UV light. Note: error bars are based on one standard deviation of triplicate samples.
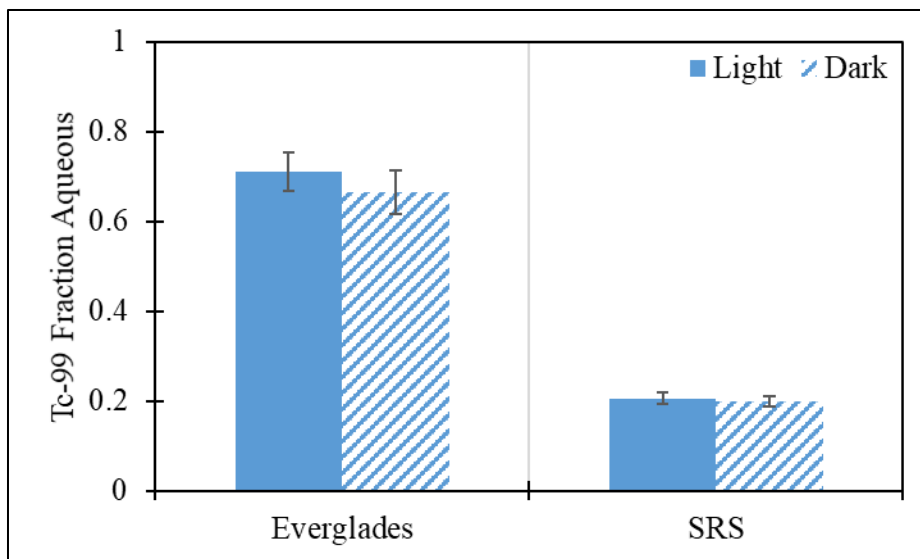
Figure 28. Comparison of remaining aqueous fraction of 100 µg/L Tc after 24 hours of exposure to 1.0 g/L SRS and Everglades samples prepared with 135 mM NaNO₃ at pH 6 in the presence or absence of UV light. Note: error bars are based on one standard deviation of triplicate samples.

NOM characterization before and after light exposure showed that significantly greater organic matter is dissolved at pH 6 as compared to pH 4.5. These results are consistent with previous research (Gonzalez-Raymat et al. 2018). Further, greater dissolution of organic matter occurs for SRS soils vs. Everglades peat highlighting that the two samples have widely different behavior. E2/E3 ratios are decreased in the presence of light for Everglades' peat, suggesting a change in aromaticity and E2/E3 ratios are significantly lower for SRS soils versus Everglades' peat, suggesting presence and formation of different organic compounds (Table 16).

Table 16. Comparison of dissolved NOM fraction and E2:E3 ratios measured after 24 hours of exposure of 1.0 g/L suspensions to 135 mM NaNO3 in two surface soil samples with gray shading for light exposure and white shading for dark exposure. Note: error is based on one standard deviation of triplicate samples.

Soil	Treatment	pH	E2/E3	Fraction Dissolved
SRS	Light	4.5	1.99 ± 0.04	18 ± 3
	Dark	4.5	2.07 ± 0.11	14 ± 2
	Light	6	1.74 ± 0.01	37 ± 2
	Dark	6	1.73 ± 0.01	36 ± 3
Everglades	Light	6	9.66 ± 0.75	19 ± 3
	Dark	6	15.53 ± 2.06	18 ± 2

Effect of pH data for technetium, uranium and iodine are shown in Figure 29, Figure 30 and Figure 31 respectively. The removal of contaminants was not influenced by light as seen in the figures. Technetium and uranium removal was around 80-85% between pH 3-6 while highest removal of 98% was observed at pH 7. Whereas in the case of iodine, lowest removal of up to 92% was observed at pH 4.5. Between 77% - 80% iodine removal was observed at the rest of the pH values.
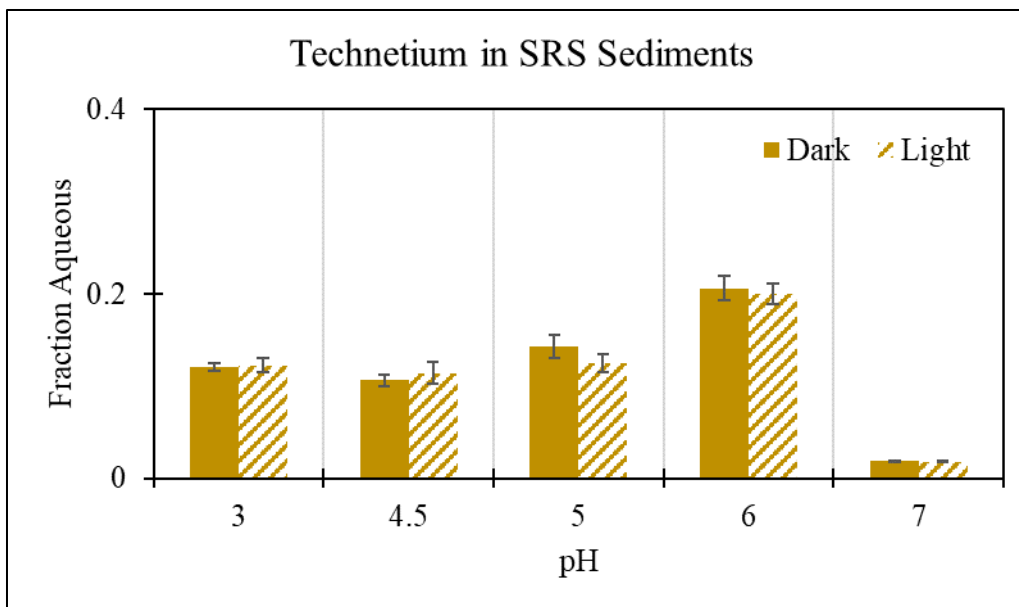
Figure 29. Comparison of remaining aqueous fraction of 100 µg/L Tc after 24 hours of exposure to 1.0 g/L SRS samples prepared with 135 mM NaNO$_3$ at pH 3-7 in the presence or absence of UV light. Note: error bars are based on one standard deviation of triplicate samples.
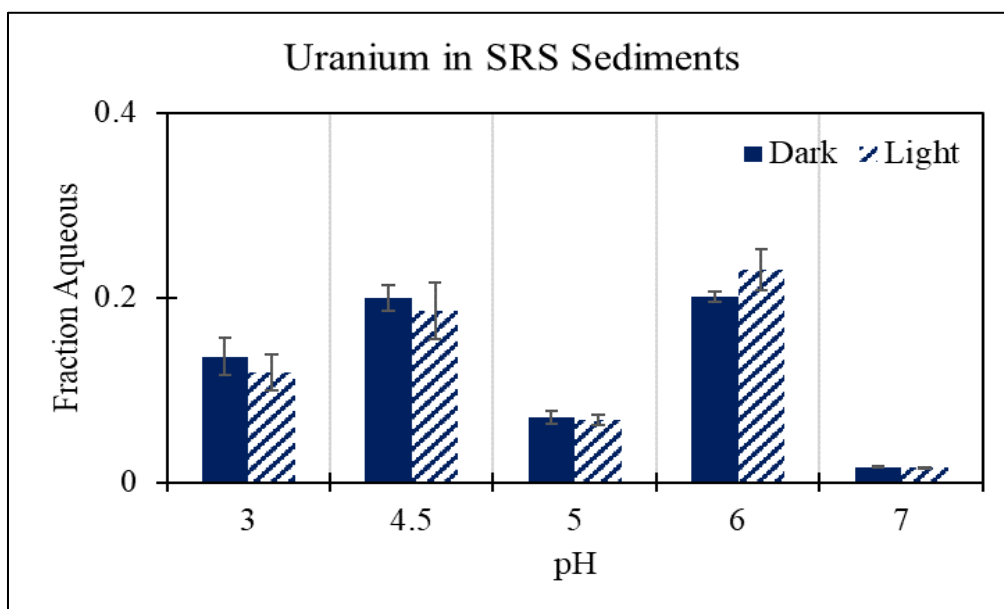
Figure 30. Comparison of remaining aqueous fraction of 100 µg/L U after 24 hours of exposure to 1.0 g/L SRS samples prepared with 135 mM NaNO$_3$ at pH 3-7 in the presence or absence of UV light. Note: error bars are based on one standard deviation of triplicate samples.
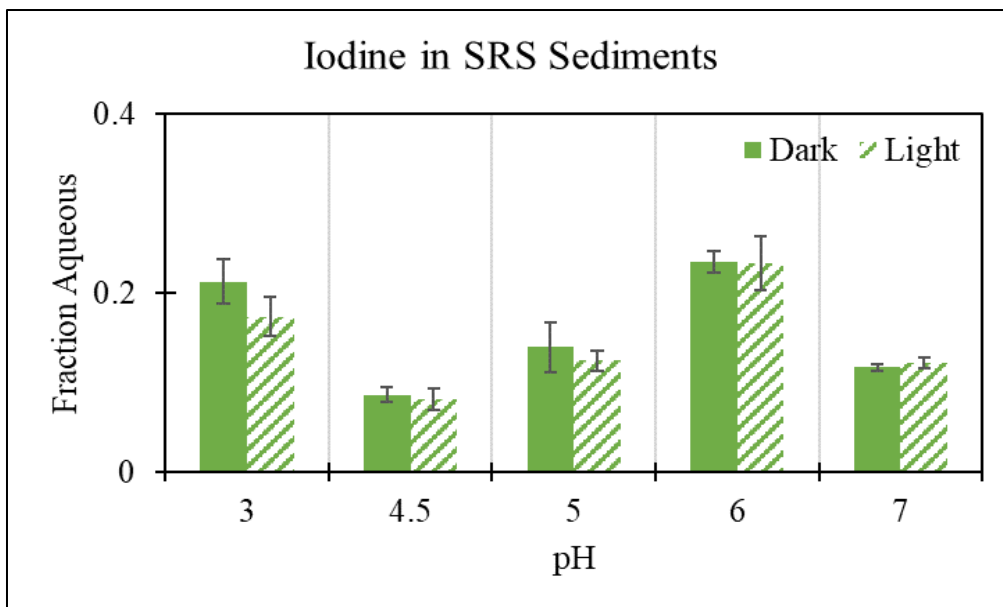
Figure 31. Comparison of remaining aqueous fraction of 100 µg/L I after 24 hours of exposure to 1.0 g/L SRS samples prepared with 135 mM NaNO$_3$ at pH 3-7 in the presence or absence of UV light. Note: error bars are based on one standard deviation of triplicate samples.

Subtask 2.1: Conclusions and Future Work

These experimental results indicate that contaminants can be removed by NOM with Tc-99 and U exhibiting different behavior for each soil and opposite trends with pH. Moreover, the evidence as to the interaction of Tc-99, I-129, and U behavior specifically in the Four Mile Branch wetland has important implications to the SRS ACP due to its association with specific regulatory requirements for contaminants of concern near the wetland. The short term (24 hour) light exposure had a negligible effect on contaminant removal with the exception of U in the Everglades peat at pH 6, although different behavior was observed at different pH and between the two soils. Greater organic matter was dissolved at pH 6 as compared to pH 4.5 and more dissolution of organic matter occurred for SRS soils versus Everglades peat. Future experiments will focus on further characterization of NOM in variable conditions in order to identify compounds that may be interacting with the contaminants to potentially compare with different NOM samples across SRS wetlands. This task will not continue in FIU year 10.

Subtask 2.1: Acknowledgements

Subtask 2.1: References

Amador, J. A., M. Alexander, and R. G. Zika. 1989. "Sequential Photochemical and Microbial-Degradation of Organic-Molecules Bound to Humic-Acid." *Applied and Environmental Microbiology* 55 (11):2843-2849.

Brezonik, P. L., and J. Fulkerson-Brekken. 1998. "Nitrate-induced photolysis in natural waters: Controls on concentrations of hydroxyl radical photo-intermediates by natural scavenging agents." *Environmental Science & Technology* 32 (19):3004-3010. doi: DOI 10.1021/es9802908.

Chin, Y. P., G. Aiken, and E. Oloughlin. 1994. "Molecular-Weight, Polydispersity, and Spectroscopic Properties of Aquatic Humic Substances." *Environmental Science & Technology* 28 (11):1853-1858. doi: DOI 10.1021/es00060a015.

Dobbs, R.A., R.H. Wise, and R.B. Dean. 1972. "use of ultra-violet absorbance for monitoring the total organic carbon content of water and wastewater."

Eddy-Dilek, C., K. Kostelink, and M. Denham. 2016. "The Challenge of Moving Science into Practice: Lessons Learned and New Approaches." Waste Management Symposium, Phoenix, Arizona, March 6 -10.

Emerson, Hilary, Chen Xu, Y. Feng, M. Lilley, Daniel Kaplan, Peter Santschi, and Brian Powell. 2013. "Geochemical controls of iodine transport in Savannah River Site subsurface sediments." *Chemical Geology* (Submitted).

Gligorovski, S., R. Strekowski, S. Barbati, and D. Vione. 2015. "Environmental Implications of Hydroxyl Radicals (center dot OH)." *Chemical Reviews* 115 (24):13051-13092. doi: 10.1021/cr500310b.

Gonzalez-Raymat, H., V. Anagnostopoulos, M. Denham, Y. Cai, and Y. P. Katsenovich. 2018. "Unrefined humic substances as a potential low-cost amendment for the management of acidic groundwater contamination." *Journal of Environmental Management* 212:210-218. doi: 10.1016/j.jenvman.2018.02.017.

Helms, J. R., A. Stubbins, J. D. Ritchie, E. C. Minor, D. J. Kieber, and K. Mopper. 2008. "Absorption spectral slopes and slope ratios as indicators of molecular weight, source, and photobleaching of chromophoric dissolved organic matter." *Limnology and Oceanography* 53 (3):955-969. doi: DOI 10.4319/lo.2008.53.3.0955.

Icenhower, Jonathan P., Nikolla Qafoku, Wayne J. Martin, and John M. Zachara. 2008. The Geochemistry of Technetium: A Summary of the Behavior of an Artificial Element in the Natural Environment. United States.

Kaplan, D. I., M. E. Denham, S. Zhang, C. Yeager, C. Xu, K. A. Schwehr, H. P. Li, Y. F. Ho, D. Wellman, and P. H. Santschi. 2014. "Radioiodine Biogeochemistry and Prevalence in Groundwater." *Crit Rev Environ Sci Technol* 44 (20):2287-2335. doi: 10.1080/10643389.2013.828273.

McCabe, D., B. Wilmarth, N. Machara, R. Bonczek, S. Chamberlain, M. Cline, M. Denham, M. Freshley, B. Harp, H. Lee, T. Levitskaia, R. Peterson, and P. Suggs. 2017. "TECHNETIUM MANAGEMENT PROGRAM PLAN." United States, 2017-03-05.

Otosaka, S., K. A. Schwehr, D. I. Kaplan, K. A. Roberts, S. Zhang, C. Xu, H. P. Li, Y. F. Ho, R. Brinkmeyer, C. M. Yeager, and P. H. Santschi. 2011. "Factors controlling mobility of 127I and 129I species in an acidic groundwater plume at the Savannah River Site." *Sci Total Environ* 409 (19):3857-65. doi: 10.1016/j.scitotenv.2011.05.018.

Sharpless, C. M., M. Aeschbacher, S. E. Page, J. Wenk, M. Sander, and K. McNeill. 2014. "Photooxidation-Induced Changes in Optical, Electrochemical, and Photochemical Properties of Humic Substances." *Environmental Science & Technology* 48 (5):2688-2696. doi: 10.1021/es403925g.

Wan, J., W. Dong, and T. K. Tokunaga. 2011. "Method to attenuate U(VI) mobility in acidic waste plumes using humic acids." *Environ Sci Technol* 45 (6):2331-7. doi: 10.1021/es103864t.

Subtask 2.2: Humic Acid Batch Sorption Experiments with SRS Soil

Subtask 2.2: Introduction

U.S. government-owned defense nuclear production facility, Savannah River Site (SRS), is located 13 miles south of Aiken in South Carolina and was constructed during the 1950s. During its operation, SRS produced a large amount of radioactive and hazardous acidic waste from the production of plutonium and irradiated fuel (Dong et al. 2012). Approximately 1.8 billion gallons of acidic waste solutions containing low-level radioactivity from numerous isotopes were discharged into a series of unlined seepage basins in the F/H Area. It was believed that most of the radionuclides present in the waste solution would bind to the soil, precluding the migration of the radionuclides. The acidic nature of the plumes, however, caused mobilization of several constituents of concern (COC) such as H-3, U-238, I-129, and Sr-90 for the F-Area. Groundwater contaminated by operation of the F-Area Seepage Basins remains acidic with a pH as low as 3.2 near the basins, increasing downgradient to pH 5. The concentrations of uranium and other radionuclides exceed the Environmental Protection Agency (EPA) Maximum Contaminant Levels (Wan, Dong, and Tokunaga 2011).

A pump-and-treat and re-injection system constructed in 1997 was initially used for removal of contaminants from the polluted groundwater. Downgrade groundwater within the system would be pumped to the water treatment facility and then re-injected upgrade within the aquifer. Decline in effectiveness and sustainability of this process over time resulted in discontinuation and ultimately replacement with a funnel-and-gate process in 2004. Sodium hydroxide was injected directly into the gates of the F-Area groundwater to effectively raise pH levels by creating a treatment zone reversing the acidic nature of the contaminated sediments and producing a negative net charge on the surface of sediment particles. As a result, the adsorption of cationic contaminants is expected to be enhanced. So far, this process has resulted in a decrease of Sr-90 and U-238 concentrations, though the concentration of iodine has been unaffected by this treatment. The solution used for the injections contains high carbonate alkalinity in order to overcome acidic conditions of the groundwater system. To maintain the neutral pH in the treatment zone, systematic injections are required. However, the continuous use of high concentrations of a carbonate solution to raise pH could re-mobilize uranium previously adsorbed within the treatment zone, though this has not been observed in the monitoring data.

Humic substances (HS) are major components of soil organic matter. HS are polyfunctional organic macromolecules formed by the chemo-microbiological decomposition of biomass or dead organic matter. These substances are usually divided into three main fractions: humin

(insoluble at all pH values), humic acid (soluble at pH greater than 3.5), and fulvic acid (soluble at all pH values) (Choppin 1992).

Humic acid carries a large number of functional groups such as aromatic rings, carboxyl groups, phenols, aliphatic chains, etc. (Tipping 2005). Humic acid is an important ion exchange and metal complexing ligand with a high complexation capacity. The ability of humic acid to chemically bind to metals influences their migration behavior and fate in natural systems (Davis 1982, Plancque et al. 2001). Various studies have suggested that the retention of U(VI) via sorption in the presence of humic acid is a complex process. For instance, humic acid can form an organic coating at the surface of minerals, which can enhance the sequestration of metals (Davis 1984, Zachara, Resch, and Smith 1994, Perminova, Hatfield, and Hertkorn 2002, Wall, Moulin, and Vilarem 1997). (Ivanov et al. 2012) studied the sorption of U(VI) onto bentonite in the presence and absence of humic acid. The study found that uranium sorption in the presence of humic acid was enhanced at low pH (below 3.8) while at moderate pH (from pH 3.8 and to pH 6.5) uranium sorption is reduced compared to the absence of humic acid. At high pH (from pH 7 and to pH 9), uranium sorption is reduced for both conditions with and without the presence and absence of humic acid [11]. Furthermore, (Krepelova, Sachs, and Bernhard 2011) not only found that U(VI) sorption onto kaolinite is influenced by pH, U(VI) concentration, the presence of inorganic carbon species, and humic acid, but also that U(VI) prefers to be adsorbed onto kaolinite as a uranyl-humate complex (Krepelova et al. 2007).

A blended material, humate (HA), that contains both humic and fulvic acids is the initial/raw product of an alkaline extraction of natural substances that are rich in organic matter. Based on desirable properties, various humate materials, specifically raw potassium humate (referred to as Huma-K) and a chemically modified humate (KW15 modified humics or mod-HA), are being tested for remediation purposes to reduce the mobility of uranium (VI) and other radionuclides in the subsurface at SRS. Injecting humate into the contaminated plumes augment sorption of uranium, Sr-90 and I-129 by increasing ion exchange and increasing/stabilizing pH. This report focuses on batch experiments to understand the impact of mod-HA as an amendment for uranium removal.

Subtask 2.2: Objectives

The objective of this study is to determine if the KW15 modified humics, which contain humic/fulvic acids of different molecular weights, can be used to facilitate uranium adsorption to SRS sediment to control the mobility of uranium in acidic SRS groundwater.

Subtask 2.2: Methodology

This study used sediment samples (FAW1 70-90 ft.) collected from the F-Area. This particular background sediment was selected because of similarities in mineral composition with the uranium contaminated aquifer layer. The SRS sediment was sieved (U.S. Standard Testing Sieves, Fisher Scientific), and the sediment fraction with diameter $\leq$ 2 mm was retained and used throughout the experiments. A commercial 1000 ppm uranyl nitrate stock solution in 2% nitric acid (Fisher Scientific) was used as a source of U(VI). Sorption experiments were conducted by using humate stock solution prepared by dissolving 1000 mg of mod-HA in 1000 ml of deionized water from Barnstead Nanopure Diamond Water Purification System (resistivity $\geq$ 18 MΩ·cm). All experiments were performed under atmospheric ($P_{CO2} = 10^{-3.5}$) and ambient temperature (25°C) conditions. A blended material, humate (HA), containing both humic and

fulvic acids and a chemically modified humate (KW15 modified humics or Mod-HA) was used as a humate source.

Experimental Procedure

Humate Sorption Experiments on SRS Sediment

Batch sorption experiments were conducted in triplicate using 20 mL of aqueous suspension in DI water in 50 mL polypropylene centrifuge tubes, containing 1 g of SRS sediment (49 g L^{-1}) spiked with initial mod-HA. Samples were vortex mixed for 30 sec and then rotated for 5 days on a platform shaker at 100 rpm throughout the sorption period. Equilibrated samples were centrifuged for 30 minutes at 2700 rpm, and the residual humate in the aqueous phase was measured spectrophotometrically at 254 nm using UV-Vis spectrophotometer.

Effect of pH: The effect of pH on the removal of mod-HA by SRS sediment as a result of sorption and/or precipitation was studied at a pH range of 4-8 with a reaction time of 5 days and an initial mod-HA concentration of 50 ppm. The pH was adjusted with 0.1 M HCl or 0.1 M NaOH during the reaction period. Also, control experiments using sediment-free batches of mod-HA (50 ppm) were conducted to estimate the precipitated fraction of mod-HA at pH range 4-8. The fraction attributed to sorption was calculated from the difference between the total removal and the homogeneous precipitation fraction.

Kinetics of humate removal: The kinetic studies were conducted with a mod-HA concentration of 50 ppm, where humate was allowed to equilibrate with SRS sediment for different time intervals of 30 minutes to 10 days at pH 4. The pH was monitored and adjusted daily by 0.1 M HCl or 0.1 M NaOH.

Equilibrium studies: For the equilibrium studies, the initial mod-HA concentration ranged from 10-500 ppm, and the samples were reacted at pH 4 for a period of 5 days (past equilibrium time based on the kinetic study). Control experiments using sediment-free batches of mod-HA (10-500 ppm) were also conducted to estimate the precipitated fraction of mod-HA at pH 4.

Sorption of U(VI) Onto SRS Sediment

In order to study the sorption of uranium, SRS sediment amended with mod-HA samples were prepared by adding sediment and mod-HA into a vial and allowing it to equilibrate. 200 mg of SRS sediment was spiked with a fixed mod-HA concentration of 20 ppm at constant ionic strength (I = 0.01 M $NaClO_4$) at pH 4. The samples were mixed and placed on a rotary shaker for 5 days at 100 rpm. All samples were centrifuged for 30 min at 2700 rpm (Thermo Scientific Sorvall ST 16R centrifuge), and the supernatant was removed and spiked with U(VI). Samples were then mixed and placed on a platform shaker followed by centrifugation. Aqueous U(VI) concentration was measured by ICP-MS. Kinetic studies were performed by using an initial U(VI) concentration of 0.5 ppm that was allowed to equilibrate with the sediment for different time periods at pH 4. For the equilibrium studies, the initial U(VI) concentration ranged from 0.025 to 1 ppm, and samples were kept at pH 4 for a period of 7 days. The pH was adjusted with 0.1 M HCl or 0.1 M NaOH during the reaction period.

Subtask 2.2: Results and Discussion

Effect of pH on Mod-HA Sorption on SRS Sediment

Batch experiments in a pH range of 4-8 were performed in identical conditions in the presence or absence of SRS sediment to determine the percent of mod-HA removed from the aqueous phase. Sediment-free samples acted as a control to provide information on the precipitation of humate substances with change in pH, while sediment-amended samples provided total removal due to precipitation and sorption; sorption of humate was estimated from the difference between values obtained in two sets of experiments. As shown in Figure 32, humate removal was observed to be 75% at pH 4 and then decreased to 40% with an increase in pH to pH 8. The sedimen-free samples prepared to study the effect of pH on precipitation of humate showed that 50% of humate precipitates at pH 4. Similar to sediment bearing samples, the humate removal due to precipitation decreases reaching 40% at pH 8. The amount of sorbed humate was calculated by subtracting the amount of precipitation from humate removal experiments at each pH value; the resulting sorption on the level of 25% at pH 4 was decreased to 0.6% at pH 8.
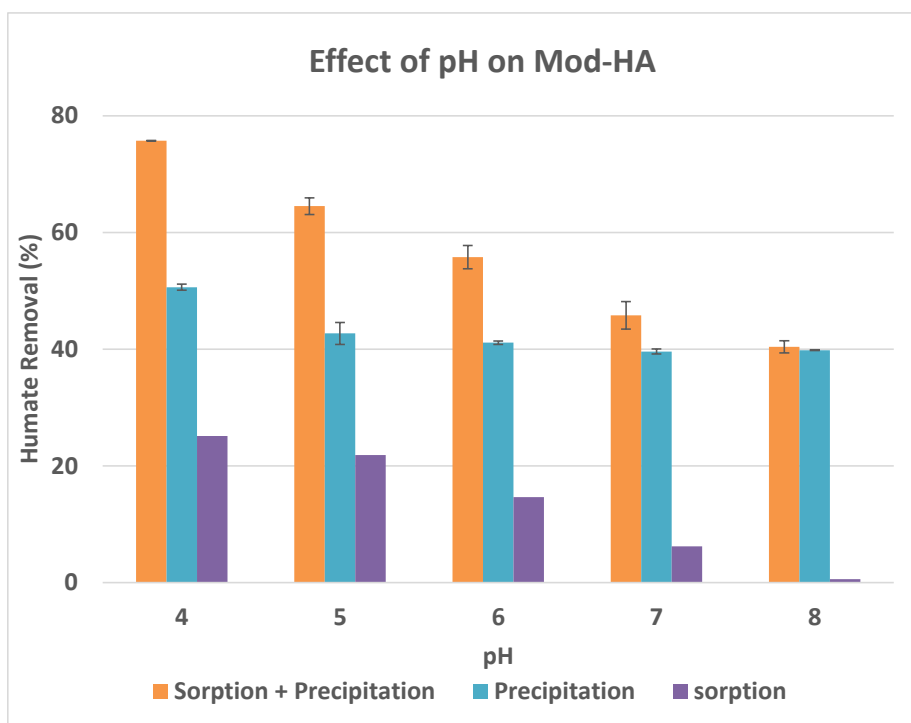
Figure 32. Percent of mod-HA removal from the aqueous phase as a function of pH.

Kinetic Studies of Humate Sorption on SRS Sediment

Kinetic studies were conducted at different time intervals (30 minutes, 1 hour, 2 hours, 4 hours, 8 hours, 24 hours, 48 hours, 72 hours, 4 days, 5 days, 7 days, and 10 days) by preparing triplicate samples. Each sample had 1 g of SRS sediment, 50 ppm of modified humic acid (mod-HA), and 19 mL of deionized water. Samples were prepared as described in the methodology section and placed on a platform shaker for the specific time. Samples were centrifuged at 2700 rpm for 30 minutes and immediately the aliquot was taken and analyzed via UV-vis for aqueous humate concentration. Humate sorption was calculated using the following equation:

$$q_t = (C_i - C_t)\, \frac{V}{w}$$

Where:

qt = amount of humate adsorbed to the sediments at time t

Ci = initial concentration of Humate

Ct = concentration of Humate at any time

V = total volume of solution used in the sample

w = weight of SRS sediment in the sample

Figure 33 shows the results obtained from the kinetics of humate sorption onto SRS sediments. Results indicate fast uptake of mod-HA with equilibrium achieved within 24 hours.
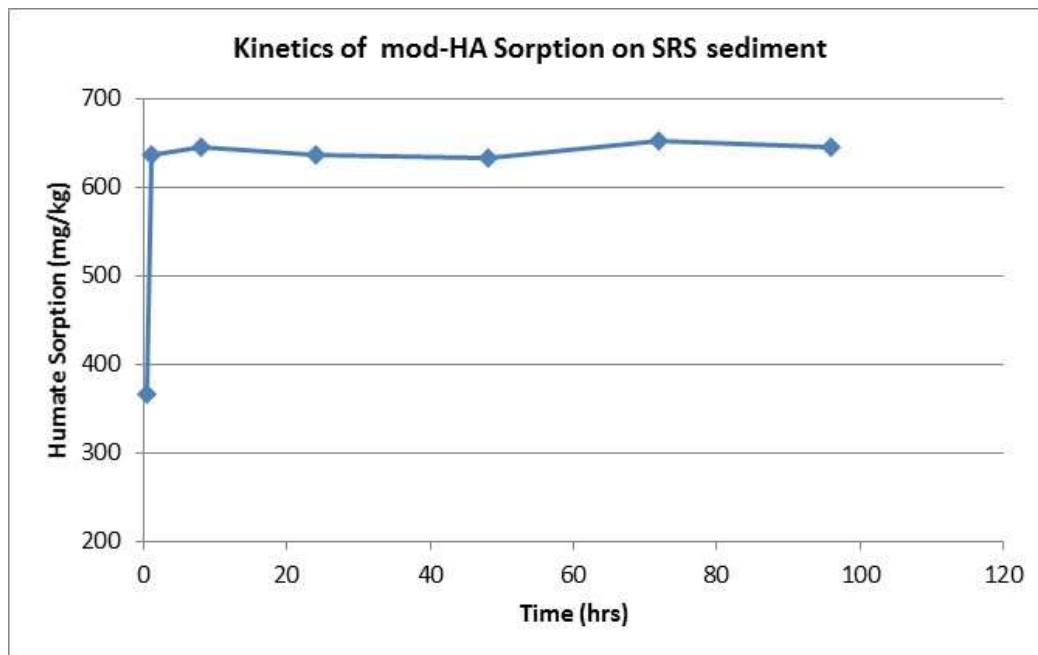
Figure 33. Kinetics of mod-HA sorption on SRS sediment.

Equilibrium Studies of Mod-HA Sorption

The control mod-HA isotherm experiment in the absence of SRS sediment was performed to determine the removal of mod-HA due to precipitation as concentration increases from 10 ppm to 500 ppm. Control sediment-free batch samples were prepared in 50-ml centrifuge tubes spiked with an appropriate amount of mod-HA to reach the desired concentration at a pH of 4. The pH of these samples was monitored and adjusted as described in the methodology section. After reaching equilibrium, samples were centrifuged for 30 mins at 2700 rpm. Aqueous solutions were analyzed using the UV-Vis in order to determine the mod-HA concentrations. Figure 34 shows that mod-HA precipitation increased with an increase in concentration to 150 ppm. At this point there was a decrease in precipitation until the concentration reached 250 ppm. Further increase in humate concentration resulted in an increase in precipitation of humate. Some samples in the range of 150 ppm to 350 ppm will be repeated to confirm these results. Figure 34 shows that mod-HA removal increased with an increase in concentration to 200 ppm. At this point there was a decrease in precipitation with a slight increase at around 325 ppm that dropped back down to the continuous decreasing pattern.
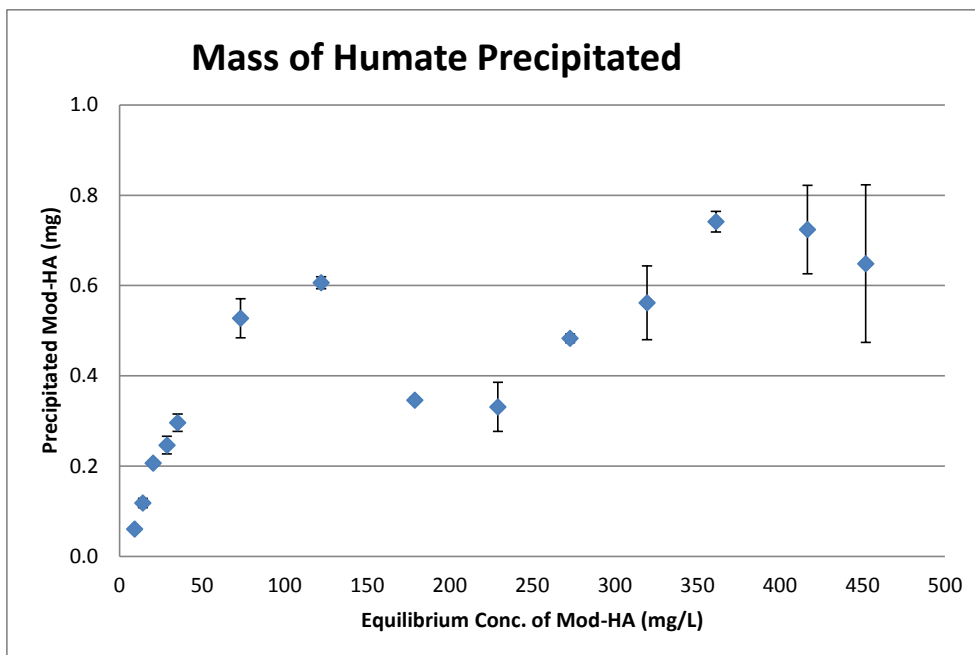
Figure 34. Precipitation of mod-HA without SRS sediment.
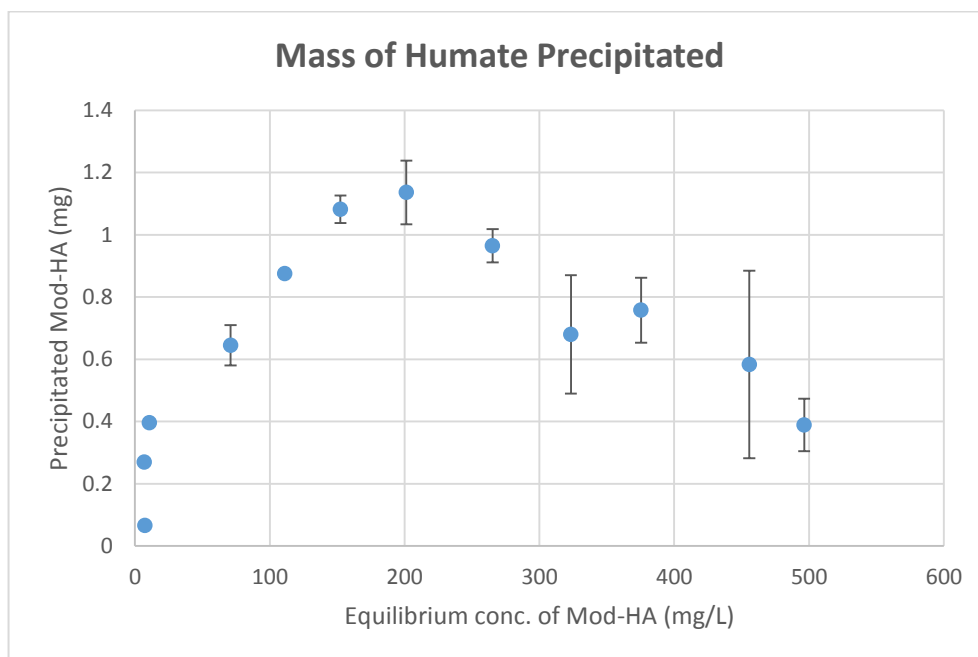
Figure 35. Removal of mod-HA with SRS sediment.

Kinetic Studies of U(VI) Sorption onto SRS Sediment with Mod-HA Amendment

Uranium sorption kinetics using SRS sediment amended with mod-HA was studied by preparing samples with 20 ppm of modified humic acid, 200 mg of SRS sediment, and 19.5 mL of DIW. This was followed by replacement of the supernatant with 0.5 ppm of U(VI), and 0.1 ml of 0.01 M perchlorate, after which the pH was adjusted to 4. Figure 35 and Figure 36 show sorption of mod-HA onto SRS sediments and the kinetics of uranium sorption onto humate-coated sediment, respectively. Sorption of mod-HA was observed to be around 4,500 mg/kg for the samples

tested. The sorption of uranium onto the mod-HA-amended SRS sediment increased sharply at 30 mins to 20 mg/kg, and reached equilibrium in about 2 days with 30 mg/kg sorption. The steady state sorption of uranium onto mod-HA is similar to the sorption of uranium onto Huma-K-coated sediments (not shown in the report); however, in the case of mod-HA, equilibrium was reached in 2 days vs, 7 days as in the case of Huma-K.
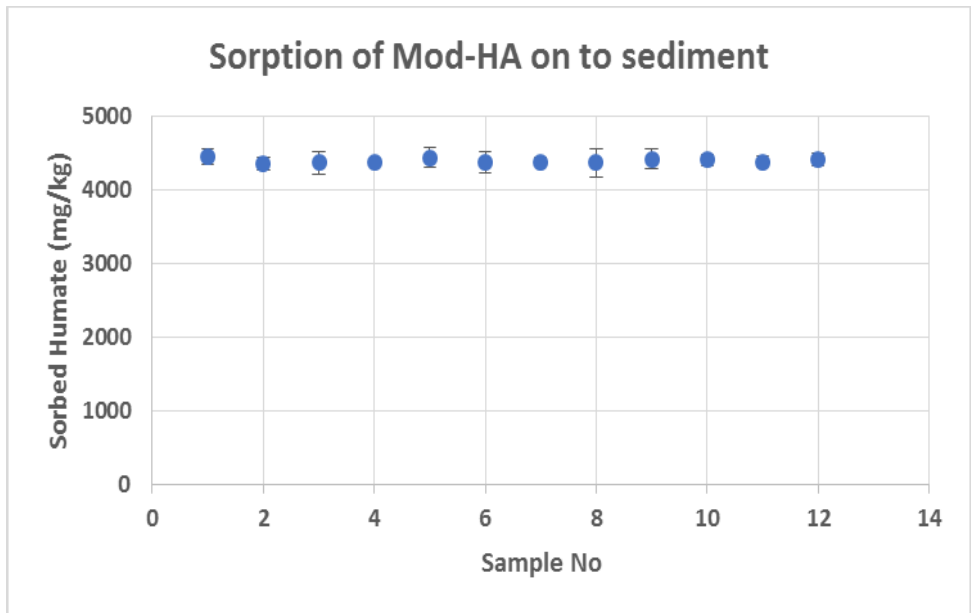
Figure 36. Sorption of mod-HA onto SRS sediment.
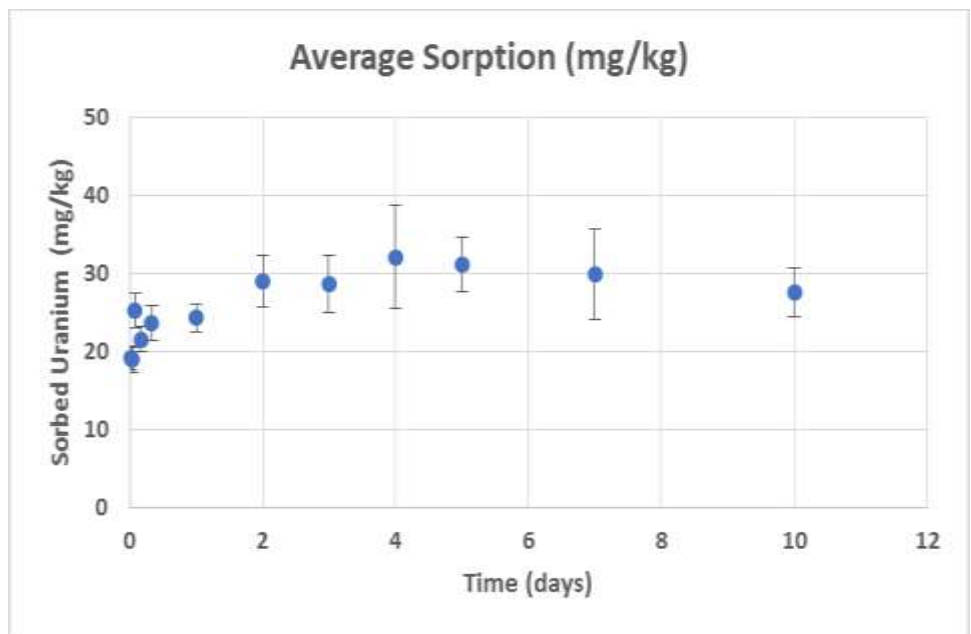
Figure 37. Kinetics of uranium sorption onto SRS sediment amended with mod-HA.

Equilibrium Studies of U(VI) Sorption onto SRS Sediment with Mod-HA Amendment

Sorption capacity of SRS sediment amended with mod-HA was studied by conducting equilibrium studies of U(VI) sorption onto SRS sediment amended with mod-HA. Experimental data shown in

Figure **37** revealed that the sorption of uranium increased with an increase in uranium concentration measured at equilibrium conditions. Also as shown in

Figure **38**, SRS sediment amended with mod-HA has a significantly higher sorption capacity compared to plain SRS sediment with similar sorption capacity to SRS sediments coated with Huma-K.
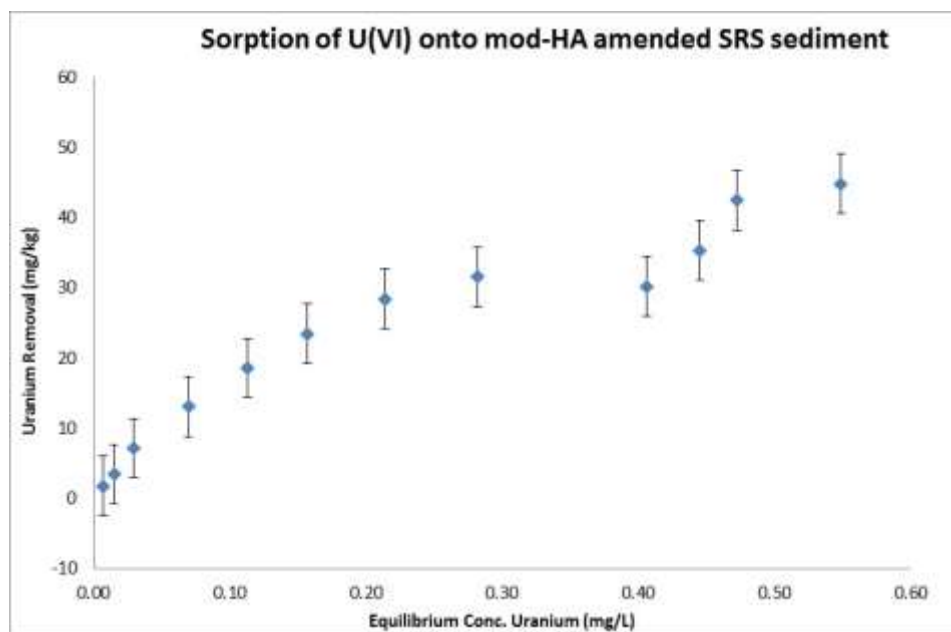
Figure 38. Sorption isotherm of uranium on SRS sediment amended with mod-HA

Figure 39 exhibits uranium sorption onto SRS sediment for all tested conditions.
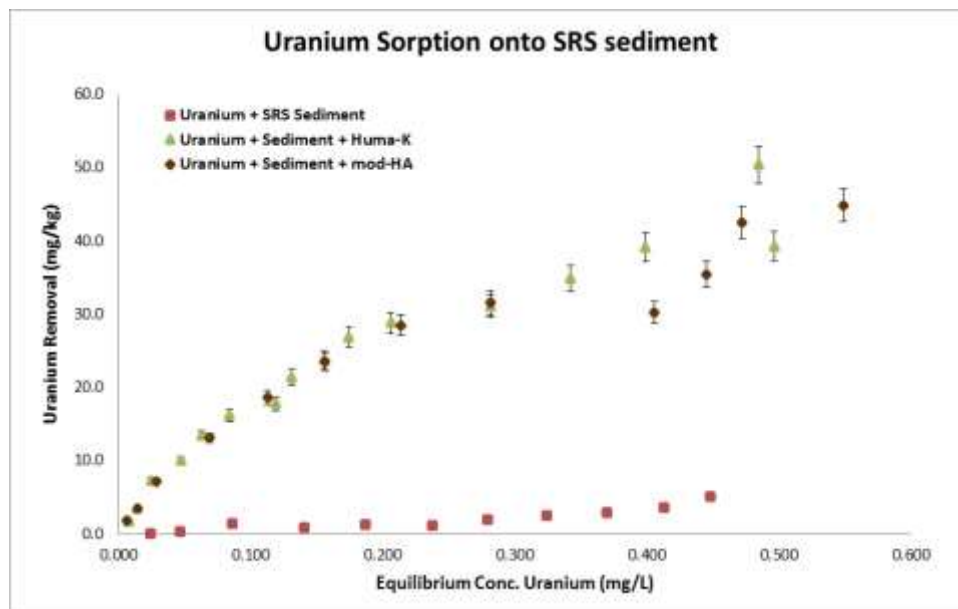
Figure 39. Sorption isotherm of uranium on SRS sediment with and without humate amendment.

Subtask 2.2: Conclusions and Future Work

These experiments show proof that amendment of sediment with mod-HA results in a significant increase of uranium removal. Future work will focus on finalizing mod-HA sorption studies and initiating desorption experiments to study the effect of pH on mod-HA. Future experiments will also study the effect of pH on uranium sorption onto SRS sediments coated with mod-HA.

Subtask 2.2: Acknowledgements

Subtask 2.2: References

Choppin, G. R. 1992. "The role of natural organics in radionuclide migration in natural aquifer systems." *Radiochimica Acta* 58-59 (pt1):113-120.

Davis, James A. 1982. "Adsorption of natural dissolved organic matter at the oxide/water interface." *Geochimica et Cosmochimica Acta* 46 (11):2381-2393. doi: 10.1016/0016-7037(82)90209-5.

Davis, James A. 1984. "Complexation of trace metals by adsorbed natural organic matter." *Geochimica et Cosmochimica Acta* 48 (4):679-691. doi: https://doi.org/10.1016/0016-7037(84)90095-4.

Dong, W., T. K. Tokunaga, J. A. Davis, and J. Wan. 2012. "Uranium(VI) adsorption and surface complexation modeling onto background sediments from the F-Area Savannah River Site." *Environ Sci Technol* 46 (3):1565-71. doi: 10.1021/es2036256.

Ivanov, P., T. Griffiths, N. D. Bryan, G. Bozhikov, and S. Dmitriev. 2012. "The effect of humic acid on uranyl sorption onto bentonite at trace uranium levels." *J Environ Monit* 14 (11):2968-75. doi: 10.1039/c2em30512g.

Krepelova, A., V. Brendler, S. Sachs, N. Baumann, and G. Bernhard. 2007. "U(VI)-kaolinite surface complexation in absence and presence of humic acid studied by TRLFS." *Environ Sci Technol* 41 (17):6142-7. doi: 10.1021/es070419q.

Krepelova, A., S. Sachs, and G. Bernhard. 2011. "Influence of humic acid on the Am(III) sorption onto kaolinite." *Radiochimica Acta* 99 (5):253-260. doi: 10.1524/ract.2011.1829.

Perminova, I., K. Hatfield, and N. Hertkorn, eds. 2002. *Use of humic substances to remediate polluted environments: from theory to practice*, *In the proceedings of the NATO Advance Research Workshop*: Springer.

Plancque, Gabriel, Badia Amekraz, Valérie Moulin, Pierre Toulhoat, and Christophe Moulin. 2001. "Molecular structure of fulvic acids by electrospray with quadrupole time-of-flight mass spectrometry." *Rapid Communications in Mass Spectrometry* 15 (10):827-835. doi: 10.1002/rcm.307.

Tipping, Edward. 2005. *Cation Binding by Humic Substances*.

Wall, Nathalie, Valérie Moulin, and J. Vilarem. 1997. "Retention Properties of Humic Substances onto Amorphous Silica: Consequences for the Sorption of Cations." *Radiochimica Acta* 79:37-49. doi: 10.1524/ract.1997.79.1.37.

Wan, J., W. Dong, and T. K. Tokunaga. 2011. "Method to attenuate U(VI) mobility in acidic waste plumes using humic acids." *Environ Sci Technol* 45 (6):2331-7. doi: 10.1021/es103864t.

Zachara, J. M., C. T. Resch, and S. C. Smith. 1994. "Influence of humic substances on Co2+ sorption by a subsurface mineral separate and its mineralogic components." *Geochimica et Cosmochimica Acta* 58 (2):553-566. doi: https://doi.org/10.1016/0016-7037(94)90488-X.

TASK 3: SURFACE WATER MODELING OF TIMS BRANCH

Task 3: Executive Summary

This task involves the development of an integrated, fully distributed hydrology and contaminant transport model to be used as a tool for assessment, evaluation and long-term monitoring of the fate and transport of sediment and contaminants in the Tims Branch watershed at SRS in Aiken, SC. Contamination in Tims Branch was derived from direct discharges of wastewater from on-site process and laboratory facilities in the A/M Area which, at various times, has contained uranium, nickel, aluminum, mercury, other metals and radionuclides, as well as organic solvents. Innovative treatment methods were deployed which effectively eliminated all local anthropogenic mercury inputs to Tims Branch; however, the tin-based treatment resulted in the controlled discharge of low-levels of inorganic tin oxide into the ecosystem. DOE EM has highlighted the need to track the tin and to understand the impact of frequent or extreme atmospheric events on its redistribution in Tims Branch. Records of the quantity and timing of the tin released has provided a unique opportunity for the tin to serve as a potential tracer for modeling sedimentation and particle transport processes in the stream, making Tims Branch an ideal testbed for evaluating the effectiveness of wetland treatment and tin (II) - based mercury treatment at the SRS site. FIU intends to utilize the data available from the tin-based remediation technology to develop a hydrological and contaminant transport model that can in future be extended to investigate other heavy metal and radionuclide contaminants of concern (e.g., mercury, uranium and nickel), and that can also be applied to other nearby watersheds.

In previous research, most of the hydrologic modeling efforts focused on other areas of Savannah River Site and South Carolina rather than Tims Branch. Conrads, Roehl, Daamen, & Kitchens, (2006) developed a three-dimensional model of the Savannah River estuary to simulate changes in water levels and salinity in the marsh by coupling a 3D hydrodynamic river-estuary model and the marsh-succession empirical model. In recent years, Feaster et al.(2010) investigated the relationship between hydrological, geochemical, and ecological processes on mercury concentration in fish tissue where they applied two watershed hydrology models to the Mc Tier Creek watershed in South Carolina: a topography-based hydrological model, TOPMODEL (Beven & Kirkby, 1979) to simulate surface flow hydrology, and a grid-based mercury model, GBMM (Dai et al., 2005) to simulate the fate and transport of mercury. However, due to a complex hydrologic connection, none of the existing hydrological modeling efforts were directly transferable to Tims Branch. Therefore, there is a need to develop a site-specific flow and transport model to better understand the fate and transport of contaminants in Tims Branch watershed.

This research addresses the knowledge gaps related to the fate and transport of dissolved contaminants at DOE EM sites as affected by the interactions with sediment movement. Results from this study are a key to evaluating the effectiveness of tin (II)-based mercury treatment of wetlands at the SRS site, and are also relevant to evaluating the potential of using this type of novel remediation technology in other mercury-contaminated stream systems at SRS and possibly other DOE sites to accelerate site closure. Knowledge acquired from this research will support model development for other heavy metal and radionuclide contaminants of concern (U, Ni, and Hg) in the future, and interpretation of historical data on the trends of contaminant distribution in Tims Branch, particularly considering the effect of extreme hydrological events

on the stream flow and consequent mobilization and sedimentation of contaminants that adsorbed on sediment. This research will also assist in developing cost-effective remediation plans integrated into the SRS Area Completion Project (ACP) and accelerate progress of the DOE EM environmental restoration mission.

Subtask 3.1: Modeling of Surface Water Flow and Contaminant Transport in the Tims Branch Ecosystem

Subtask 3.1: Introduction

A MIKE SHE/MIKE 11 hydrology model of the Tims Branch watershed has been developed by FIU and over the past year (FIU Performance Year 9), FIU has focused on the calibration of this model and development of the contaminant transport component. Coupling of the hydrology and contaminant transport components will, in future, provide SRS and DOE EM's Office of Soil and Groundwater Remediation with a tool to monitor the fate and transport of sediment and major contaminants of concern (e.g., mercury, uranium, nickel) in Tims Branch, particularly during extreme hydrological events. This will assist DOE-EM in examining the response of the Tims Branch ecosystem to innovative EM-developed remediation treatment technologies that have eliminated anthropogenic mercury sources from this watershed, and determine the potential applicability of these technologies in other contaminated stream systems at SRS and possibly other DOE sites.

Subtask 3.1: Objectives

The principal objective is to develop and test a comprehensive transport model using available hydrology software and geographical information systems (GIS) tools to examine the response of Tims Branch to historical discharges and environmental management remediation actions. The following steps were identified to achieve the principal objective: i) development of the integrated hydrologic watershed model by coupling the MIKE SHE that simulates surface/subsurface hydrologic processes with MIKE 11 stream hydrodynamic model that accounts for stream water hydraulics; ii) calibration and validation of the integrated hydrologic model; iii) development of the contaminant transport model by coupling the MIKE 11 stream hydrodynamic model with the MIKE 11 AD module that simulates solute transport through advection and dispersion, and MIKE 11 ECO Lab module that accounts for both sediment transport and interactions with dissolved contaminants, and iv) verification of the coupled contaminant transport model.

Subtask 3.1: Methodology

The Tims Branch model development is being executed in phases. The preliminary phase has involved the development of an integrated surface water/groundwater model capable of simulating the Tims Branch watershed hydrology and examining its response to extreme hydrological events. Subsequent phases involve development and integration of the contaminant transport component in order to create a fully comprehensive, distributed contaminant fate and transport model that can be used as a tool to estimate the potential movement and redistribution of contaminants of concern in the Tims Branch watershed.

In March 2019, Dr. Noosha Mahmoudi who was leading the hydrology model development announced her departure from FIU. A new post-doctoral fellow, Dr. Yan Zhou, joined the

hydrology modeling team in April 2019 and has continued the modeling work initiated by Dr. Mahmoudi. FIU has maintained communication with SRNL collaborators regarding this transition and any milestones or deliverables that may have potentially been impacted. In April, Dr. Zhou began working with the DOE Fellow students to implement recommendations for improvement of the model performance in its inherited state provided by an external reviewer, Lagos Consulting, who conducted a complete in-depth review of the Tims Branch hydrology model. The following provides a brief summary of the research area, the input data used in the model and the current status of the model development.

Research Area

Tims Branch is a second-order stream within the Savannah River basin (Seaman, Arey, & Bertsch, 2001) that drains an area of 45 km^2 (Figure 40). It originates from the north of SRS, flows for approximately 15 km to the south, passes through Beaver Ponds 1 to 5 and Steed Pond until reaching to the confluence with the Upper Three Runs which flows into the Savannah River (Fig. 1). Hydrologic conditions of Tims Branch vary spatially due to difference in aquifer depth. Upstream of A-014 tributary, groundwater is deep below land surface, thus Tims Branch is disconnected from the aquifer and considered a losing stream. This segment of Tims Branch never receives groundwater discharge and stays dry most of the year except for flash flow during precipitation events. Downstream of the A-014 tributary, groundwater elevation is high enough for Tims Branch to receive groundwater discharge seasonally. Streamflow in this segment of Tims Branch responds to both precipitation and changes in groundwater depth. The climate in Tims Branch is heavily influenced by the Appalachian Mountains and Atlantic coast. As a result, the watershed rarely experiences snow or icing conditions and features humid subtropical climate with a mean temperature of 18 °C and a mean annual precipitation of 1,225 mm (Kilgo, 2005).
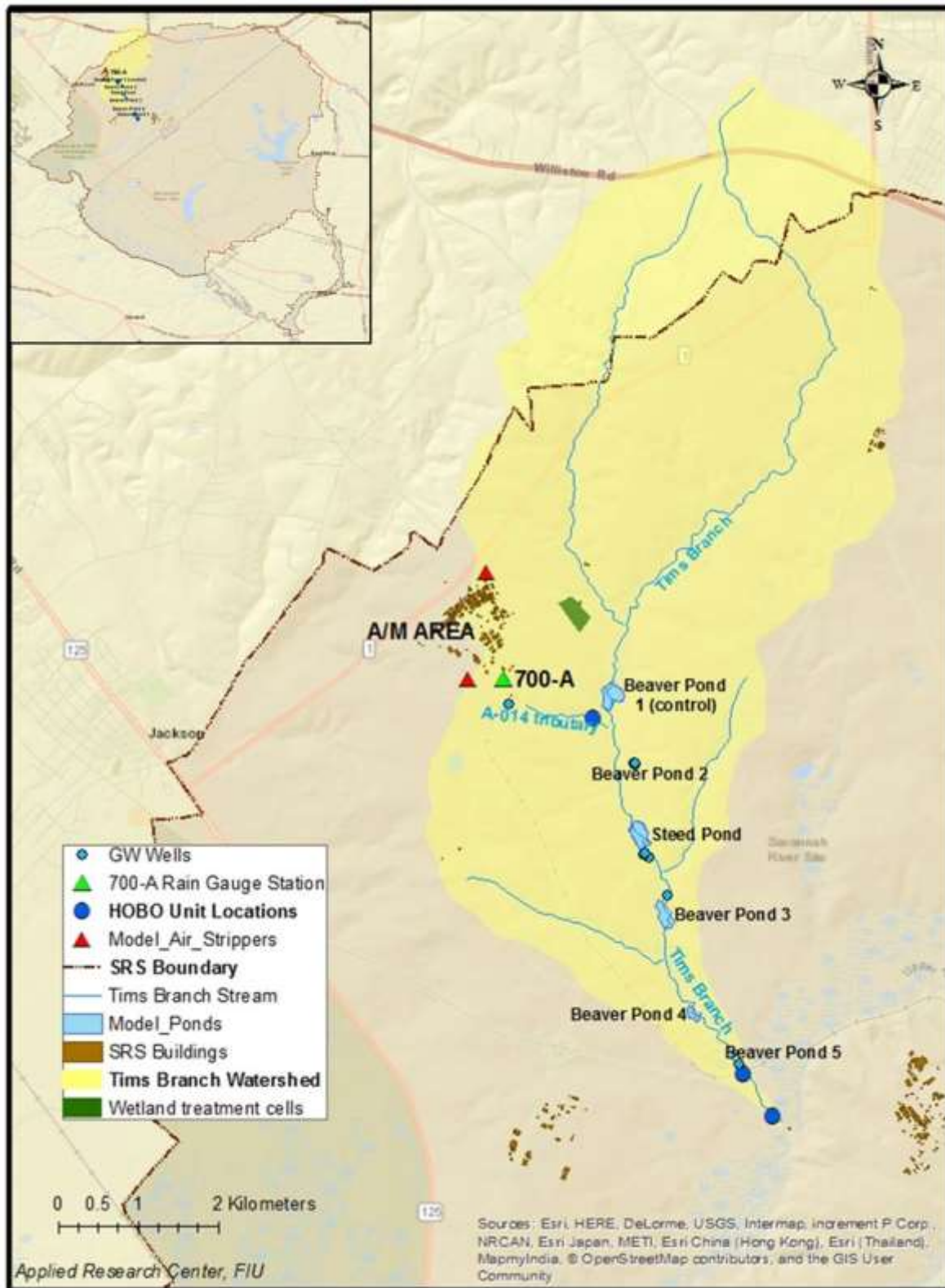
Figure 40. Tims Branch watershed study area within the Savannah River Site, showing significant features including: watershed boundary (model domain), ponded areas, A-014 tributary, A/M Area, precipitation gauge, groundwater wells and stream stages.

Data Source

Topography of the Tims Branch watershed was represented by a 3-m resolution digital elevation model (DEM) of South Carolina derived from LiDAR data, obtained from the South Carolina Department of Natural Resources (SCDNR), with the elevation ranging from approximately 130 m to 460 m above mean sea level. The DEM was clipped to the model domain and resampled to the grid of the model to represent the topography of the research area.

The climatic condition of Tims Branch watershed was assumed to be uniformly distributed because of its spatial extent and represented by time series of precipitation and reference evapotranspiration (ET_0). Precipitation data was obtained from a rain gauge located within the SRS (700-A station, Figure 40) and managed by the Savannah River National Laboratory's (SRNL's) Atmospheric Technologies Group (ATG). Cumulative precipitation was measured in 15-minute increments, which is considered adequate to represent storm events. ET_0 was estimated from pan evaporation measurements taken adjacent to the SRS CLM station, Figure 40). Daily averaged ET_0 was calculated from daily pan evaporation based on a constant pan coefficient of 0.7, an averaged pan coefficient found for five major lakes in the Savannah River Basin (Phillips, Saylor, Kaye, & Gibert, 2016).

Land cover and soil type were represented by spatially distributed categorical maps derived from federal databases, as their influence on the hydrological response of the watershed is critical in model certainty. Land cover was represented by vegetation/land use categories based on land use data of 2016 obtained from the Multi-Resolution Land Characteristics (MRLC) consortium National Land Cover Database (NLCD). The land cover map included 15 vegetation/land use categories where the most dominant land cover type is evergreen forest, covering approximately 62% of the Tims Branch watershed. The soil map was represented by soil types and associated soil physical properties, based on the soil map of 2016 and the associated soil metadata obtained from the Soil Survey Geographic Database (SSURGO) provided by the Natural Resources Conservation Service (NRCS) United States Department of Agriculture (USDA) including 44 soil types. Similar to the DEM, both land cover and soil type maps were clipped to the model domain and resampled to the grid of the model.

Groundwater elevation and discharge records were represented by time series at monitoring points and used in generating initial conditions and model calibration. Groundwater elevation time series were obtained from South Carolina Department of Natural Resources at multiple locations within SRS (Figure 40). Streamflow records are scarce in this restricted watershed. Therefore, in order to collect a consistent and detailed timeseries dataset of flow rate, three HOBO RX3000 remote monitoring stations were installed onsite at SRS to collect water level data at strategic locations along the Tims Branch stream and the A-014 outfall tributary (Figure 40). The water depth is recorded every 15 minutes and downloadable every 4 hours from its cloud-based storage. More information could be found in Subtask 3.3. The recorded water depth was then used to calculate flow rate based on measured cross-sectional geometry and other hydraulic conditions of the transect.

Integrated Hydrologic Model

The integrated hydrologic watershed model for Tims Branch watershed was developed by coupling the MIKE SHE land model that simulates surface/subsurface hydrologic processes (such as overland flow, evapotranspiration, unsaturated and saturated flow) and the MIKE 11

stream hydrodynamic model that accounts for stream water hydraulics (such as cross-sections and stream network).

The MIKE SHE land model (MSHE) is a deterministic, physically-based, fully distributed numerical model designed for simulating various processes of the hydrologic cycle on the land surface as well as the subsurface. These hydrologic processes include evapotranspiration (ET), overland flow (OL), and flow in both the unsaturated zone (UZ) and saturated zone (SZ). Based on governing partial differential equations of mass, momentum, and energy conservation, MSHE numerically solves for water movement among model grids using a finite difference scheme and provides an estimate for various water budget components (Figure 41).
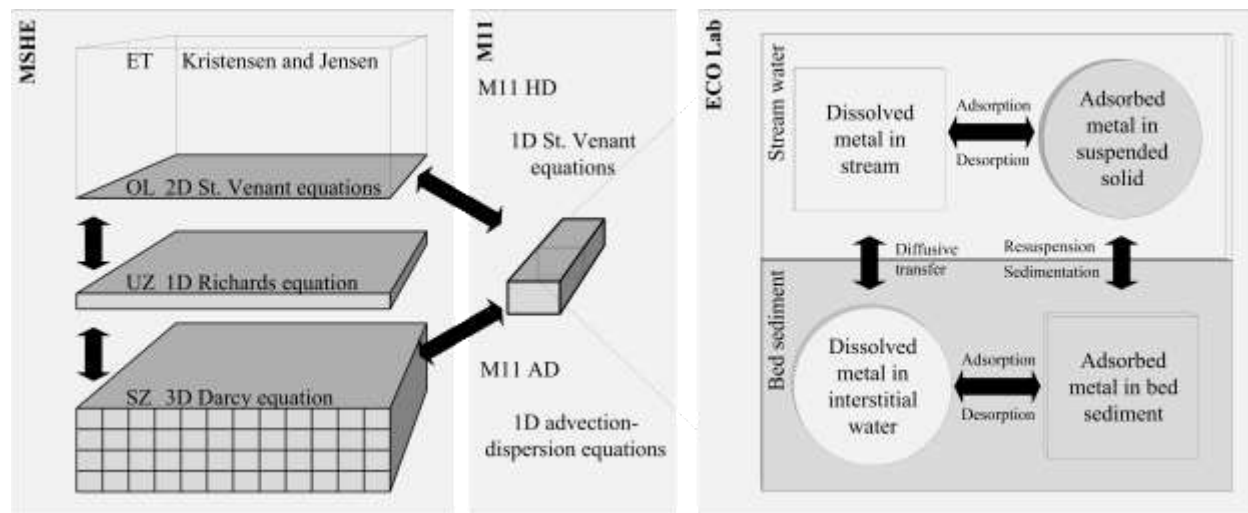
Figure 41. Diagram of an integrated hydrologic model showing the MIKE SHE land model including evapotranspiration (ET), overland flow (OL), and flow in the unsaturated zone (UZ) and saturated zone (SZ), MIKE 11 stream hydrodynamic model (M11 HD), and contaminant transport components including the MIKE 11 Advection Dispersion (M11 AD) and MIKE 11 Ecological Laboratory (ECO Lab) modules.

The Tims Branch watershed boundary, defined by the 12-digit hydrologic unit code (HUC) 030601060504, was specified as the computational model domain. The Tims Branch watershed hydrologic model with a total area of 45 km^2 was represented in MIKE SHE by 18,105 grid cells with a size of 50 by 50 m (Figure 40).

A modeling period of 2/20/2018 to 7/30/2018 was selected dependent on the overall availability of model input. Initial condition of the OL, UZ and SZ is obtained by iteratively running the model after initial setup using measured values (e.g., groundwater elevation) until steady state is reached. The spatially distributed initial condition includes overland water depth (OL) initial water content (UZ) and initial head (SZ).

To properly account for the hydraulics feature of streams, such as stream networks and cross sections, MIKE 11 stream hydrodynamic model (M11 HD) was used to simulate streamflow and coupled with MSHE land model. The stream network was delineated from a 3-m DEM using the MIKE HYDRO tool. Since the 3-m DEM was derived from LiDAR data generally collected during low flow season, most of the channels and tributaries were exposed and captured. To balance model performance and runtime efficiency, branches with a length shorter than 200 m or stream order lower than 2 were manually removed using ArcGIS tools with the assumption that simulation of these branches can be simplified as overland flow in MSHE with negligible impact on the overall performance of the integrated hydrologic model. The completed stream network of

the Tims Branch watershed consists of five stream branches outlined by 517 control points. Cross section profiles were derived from field survey results with the addition extracted from the DEM for inaccessible locations. Field surveys were conducted at steam gauge to properly develop a depth-flow rate rating curve and other locations of interests such as ponds and known contaminated sites in June 2016 and 2017. Using MIKE HYDRO tools, additional cross sections were also extracted from the 3-m DEM at other locations where accessibility is limited, achieving an overall resolution of approximately 250 meters per cross section. A process of manual modification was applied to cross sections extracted from 3-m DEM using MIKE 11 cross section editor, where irregular cross section profiles were corrected to a trapezoidal shape while maintaining the overall dimension of the profile, elevation of the stream bank and bottom.

The MSHE and the M11 HD were coupled through both lateral inflows originating from OL in MSHE and exchange between stream water and aquifer in the SZ. If a river link, locator of the connection between M11 HD and MSHE, is present in the grid of the OL, overland flow will be intercepted by the river link and added to the water balance of the M11 HD. The exchange flow between river link and a SZ grid is computed as the product of conductance and head difference.

Model calibration including parameters from both MSHE and M11 HD was conducted using an auto-calibration tool based on the Population Simplex Evolution (PSE) method. Model components included in the calibration are evapotranspiration, overland flow, and the saturated zone module in MIKE SHE and hydrodynamic components in MIKE 11. Calibration parameters, their initial values and boundaries were summarized in Table 17.

Table 17. Summary of the calibration parameters from both MIKE SHE land model (MSHE) and MIKE 11 stream hydrodynamic model (M11 HD), including initial values and boundaries.

		Unit	Initial	Calibrated
OL	Detention storage	mm	15.00	25.91
	Overland leakage coefficient	/s	5.00E-05	9.89E-04
	Manning's M	$m^{1/3}$/s	25.00	29.10
SZ	Horizontal hydrological conductivity	m/s	5.00E-05	1.20E-08 to 1.90E-04
	Storage coefficient	/m	5.00E-05	4.52E-08 to 9.91E-04
	Specific yield		0.20	0.04 to 0.23
ET	C1		0.30	0.44
	C2		0.20	0.49
	C3	mm/day	20.00	24.45
	Interception coefficient	mm/day	0.05	0.02
	Root coefficient	/m	0.25	3.42

To evaluate the calibration result, the FITEVAL program was used to quantify the fit between predicted and monitored discharge. FITEVAL is a software tool for standardized model evaluation that accounts for data and model uncertainty based on procedures presented by Ritter and Muñoz-Carpena (2013), and has been applied to many hydrologic (Kisekka et al., 2014; Leitman & Kiker, 2015; Zhou, Fox, Miller, Mollenhauer, & Brewer, 2018) and ecological studies (Kihumba, Longo, & Vanclooster, 2016). FITEVAL evaluates and visualizes model performance using a combination of normalized statistics (Nash–Sutcliffe Efficiency coefficient, NSE), absolute value error statistics (root mean square error, RMSE), and graphical illustrations. To reduce subjectivity in the interpretation of the model performance, FITEVAL calculates bias corrected confidence intervals based on approximated probability distributions derived from bootstrapping and performs hypothesis tests of the indicators.

Contaminant Transport Model

A 2-day (16 hr) training workshop on the implementation of the MIKE 11 ECO Lab and advection/dispersion modules was conducted in November 2018 at FIU ARC's DOE Modeling, Simulation and GIS Research Laboratory in order to improve the software proficiency of the students so they can effectively support the development of the contaminant transport component of the hydrological model of the Tims Branch watershed. Five DOE Fellows as well as several ARC researchers participated in the training (Figure 42). The MIKE SHE/MIKE 11 hydrology model of the A-014 outfall tributary was used as a case study for the training.

Figure 42. DOE Fellows and ARC researchers being trained on MIKE 11 ECO Lab in the DOE Modeling, Simulation and GIS Research Laboratory at FIU.

After achieving satisfactory performance of the integrated hydrologic model through calibration, the contaminant transport component was developed by coupling the M11 HD with the MIKE 11 Advection Dispersion (M11 AD) and MIKE 11 Ecological Laboratory (M11 ECO Lab) modules (Figure 41). The coupled model structure accounted for the full transport processes within the stream channel including 1D advective-dispersive transport (M11 AD) with subsurface transfer (M11 HD-MSHE) and interactions with suspended/bed sediment (M11 ECO Lab). The M11 AD module simulates transport of dissolved or suspended material based on the 1D equation of conservation of mass. Based on the assumption that substance is well-mixed over the cross-section and that dispersive transport is proportional to the concentration gradient (Fick's law), M11 AD numerically solves the 1D advection-dispersion equation with an implicit finite difference scheme using output from M11 HD (e.g., flow velocity, cross-sectional area and hydraulic radius) at each temporal and spatial step. The M11 ECO Lab module is an open and generic tool for customized transport processes within aquatic ecosystems. In this research, the heavy metal template of M11 ECO Lab was used that can simulate adsorption/desorption of metals to suspended and bed sediment, sedimentation/resuspension of sediment, and diffusive exchange of metal in dissolved form in the water column and in the interstitial waters (Figure 41). The list of transport parameters is summarized in Table 18 with values representing transport of Sn.

Table 18. Summary of the transport parameters used in MIKE 11 Advection Dispersion module (M11 AD) and MIKE 11 Ecological Laboratory module (M11 ECO Lab).

	Parameter	Unit	Preliminary testing
ECO Lab	Organic-carbon partitioning coefficient	l/kg	50000
	Desorption rate in water (suspended solids)	/day	1
	Desorption rate in sediment (bed sediment)	/day	0.1
	Fraction of organic carbon in suspended solids		0.1
	Fraction of organic carbon in bed sediment		0.2
	Factor for diffusion due to bioturbation		1

	Density of dry sediment	kg/m^3	250
	Porosity of bed sediment		0.8
	Settling velocity	m/day	0.1
	Resuspension rate	g/m^2/day	1000
	Particle production rate	g/m^2/day	1
	Critical current velocity	m/s	0.4
AD	Dispersion factor	m^2/s	5
	Dispersion exponent		0

Subtask 3.1: Results and Discussion

Work for this year (FIU Performance Year 9) has been focused on calibration of the fully coupled 1-D stream flow and 2-D overland flow hydrology models, and coupling of the hydrology and contaminant transport components. The main activities in Year 9 have included the following:

- Calibration of the coupled MIKE SHE/MIKE 11 hydrology model.

- Development of the contaminant transport model by coupling with the MIKE 11 AD module and MIKE 11 ECO Lab module.

- Preliminary testing of the coupled contaminant transport model.

Calibration of the coupled hydrology model will remain a continuous process, utilizing historical as well as recently acquired field observation timeseries data. In FIU Performance Year 10, FIU plans to complete the calibration of the fully coupled flow and transport model and implement specific rainfall scenarios in each model to understand the models' behavior under various atmospheric conditions. Atmospheric scenarios will be determined based upon historical rainfall events and data provided by federal/state online databases or data provided by SRNL/SRNS. MIKE and ArcGIS tools will be used for data analysis and visualization of model results.

Integrated Hydrologic Model

At the current stage, model calibration is completed based on discharge records measured at the outlet of Tims Branch (Figure 43). The results from FITEVAL also indicated an acceptable model performance with a RMSE of 0.039 m^3/s within the range of (0.028, 0.05) m^3/s and an NSE of 0.764 within the range of (0.513, 0.879) (Figure 44). According to FITEVAL, the probability of model performance within the category of very good (NSE>0.9) is 0.3%, 33.1% for good (0.8<NSE<0.9), 50.2% for acceptable (0.65<NSE<0.8) and 16.4% for unsatisfactory (NSE<0.65).
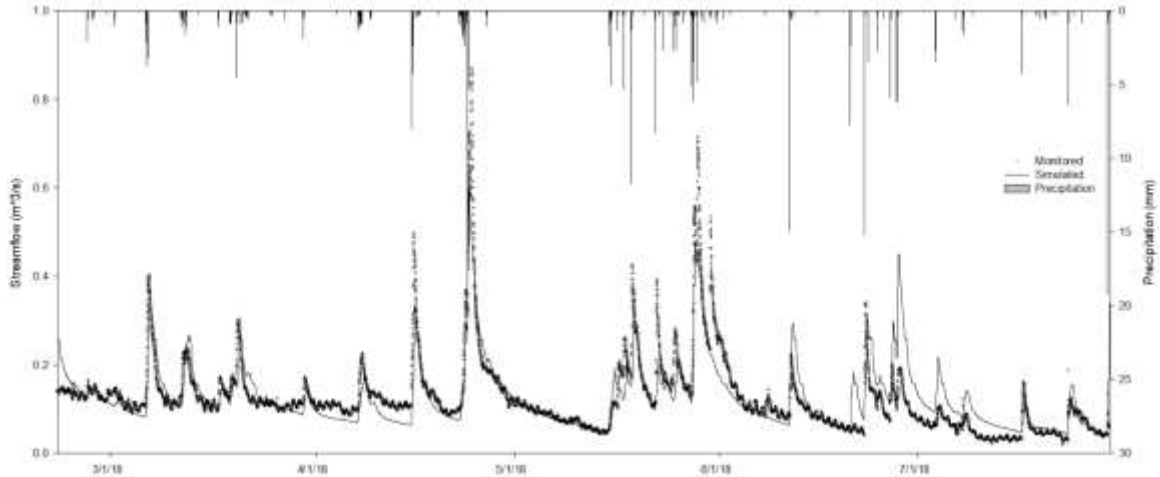
Figure 43. Model calibration result showing precipitation (bar from top), simulated (markers) and monitored discharge time series (solid line).
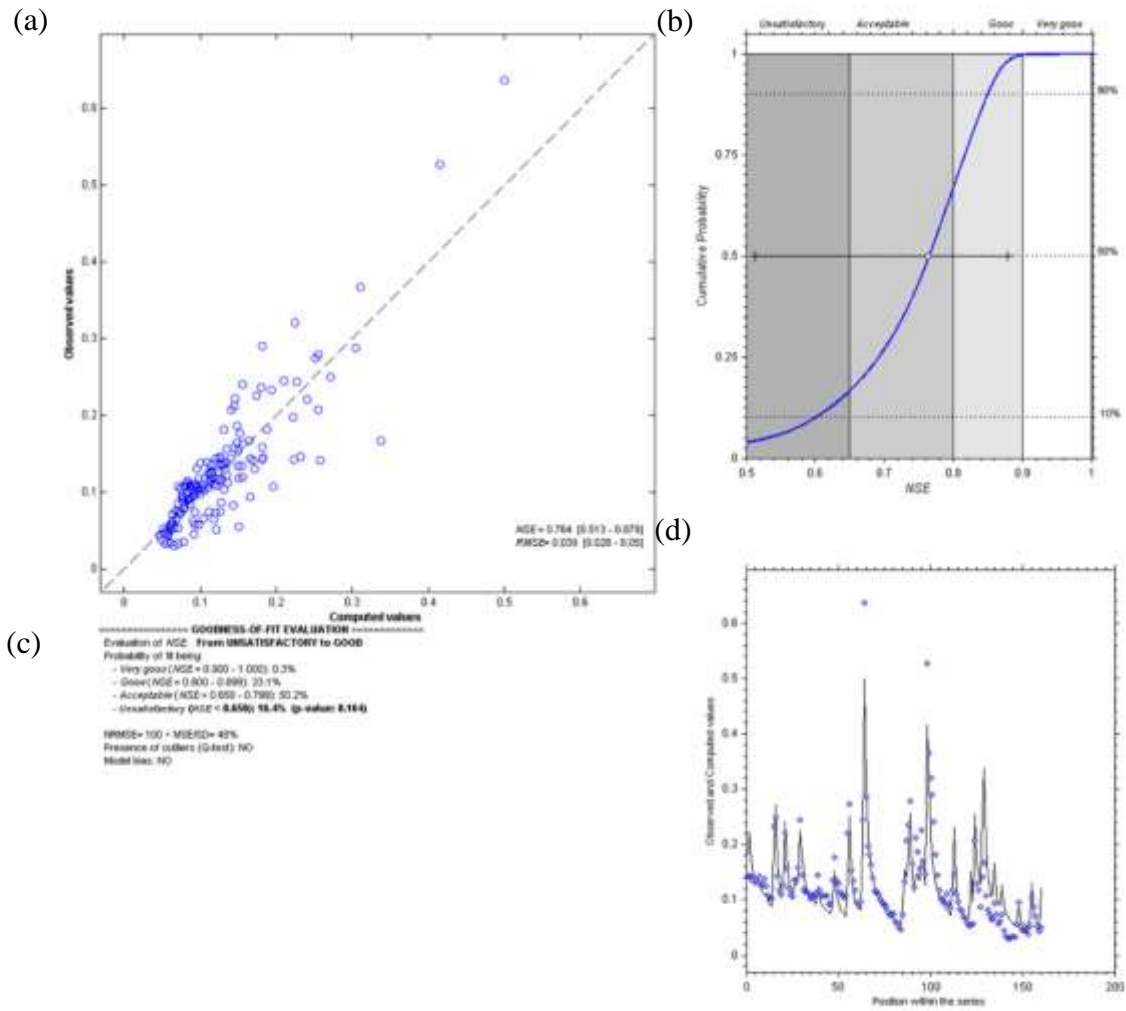
Figure 44. Model calibration evaluated using FITEVAL showing (a) regression of computed vs observed discharge, (b) FITEVAL plot of cumulative probability of NSE and its median, (c) FITEVAL goodness of fit evaluation including hypothesis test results, outliers, and the sensitivity of the indicators to model bias, and (d) scatter plot showing fit between computed vs observed discharge in order of the series.

Predictions of groundwater elevation were visualized in Figure 45. Due to lack of continuous monitored groundwater elevation time series, the groundwater elevation time series predicted for different wells were contrasted with the boxplot of observations at the same location. Figure 45 indicates that predicted groundwater elevation fits the range of observations for all five computational layers that represent five stratigraphic units, Hawthorn, Barnwell, McBean, Ellenton and Tuscaloosa at the depths of 9.1, 48.8, 88.4, 143.3 and 200 meters, respectively.
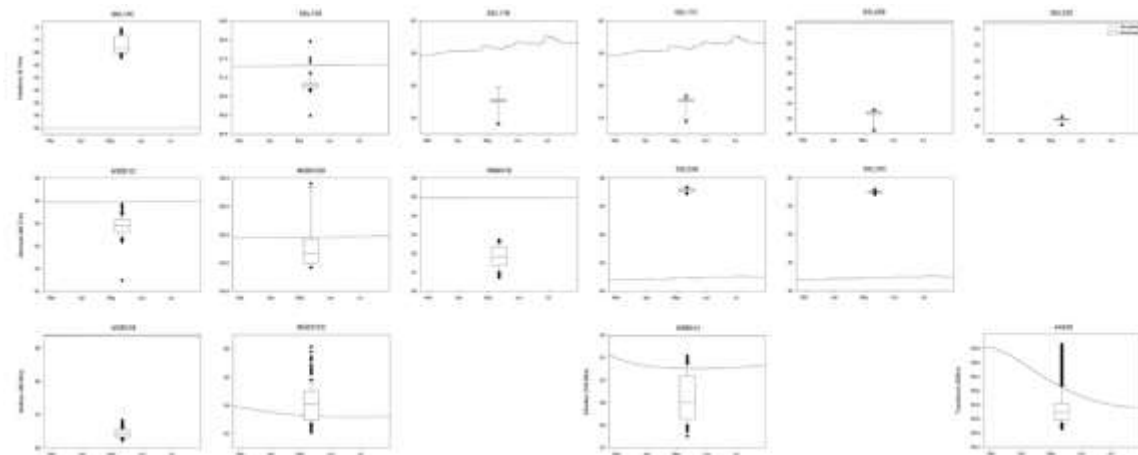
Figure 45. Predicted groundwater elevation time series represented by solid line contrasted against historical records represented as boxplots for five stratigraphic units, Hawthorn, Barnwell, McBean, Ellenton and Tuscaloosa at the depth of 9.1, 48.8, 88.4, 143.3 and 200 meters, respectively.

Contaminant Transport Model

The contaminant transport model is tested with a hypothetical release of Sn from the upstream boundary of A-014 branch (Figure 40) during a storm event from 4/20/2018 to 5/10/2018, which includes both a continuous release and a pulse release. Breakthrough curves of dissolved and adsorbed Sn concentration were visualized in Figure 46 respectively for a series of downstream locations within A-014 and after it reaches the confluence with Tims Branch, showing the spreading of dissolved contaminant peak and delayed peak moment due to advective-dispersive transport and its impact on adsorbed concentration. The transport of sediment was illustrated by temporal variation of bed sediment at the confluence of A-014 with Tims Branch (Figure 47) and by spatial variation of bed sediment (Figure 48). Figure 47 shows the process of resuspension during a storm event and sedimentation during base flow and recession period. Figure 48 shows the result of sediment migration from narrower riffles where flow velocity is high to pools where velocity is low.
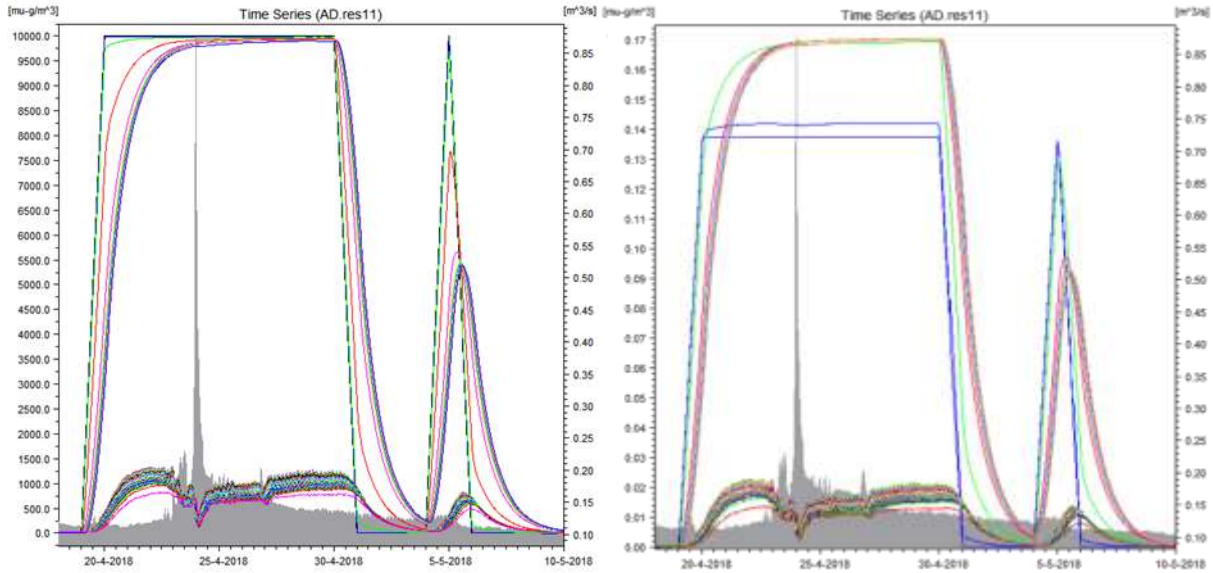
Figure 46. Breakthrough curves of dissolved (left) and adsorbed (right) Sn concentration, showing dissolved and adsorbed Sn concentration (colored lines) for a series of downstream locations within A-014 (upper group of curves) and after the confluence with Tims Branch (lower group of curves).
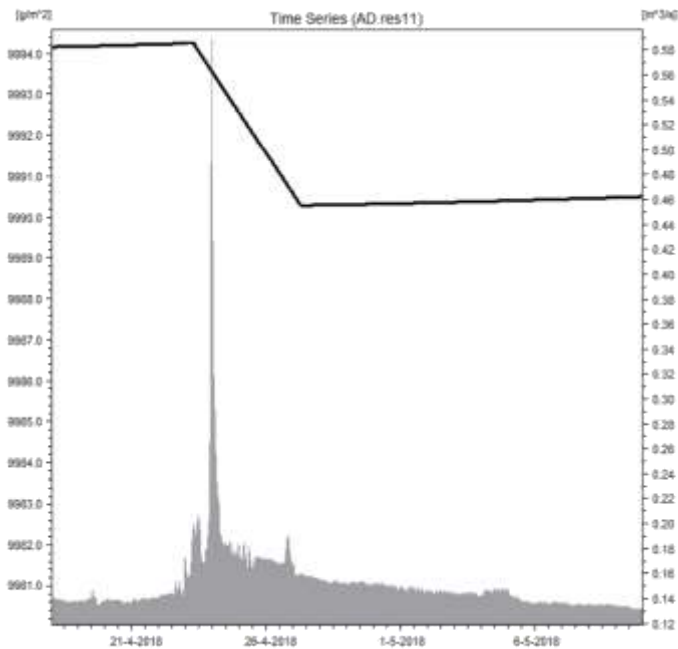
Figure 47. Temporal variation of bed sediment at the confluence of A-014 with Tims Branch showing the process of resuspension during a storm event and sedimentation during base flow period.
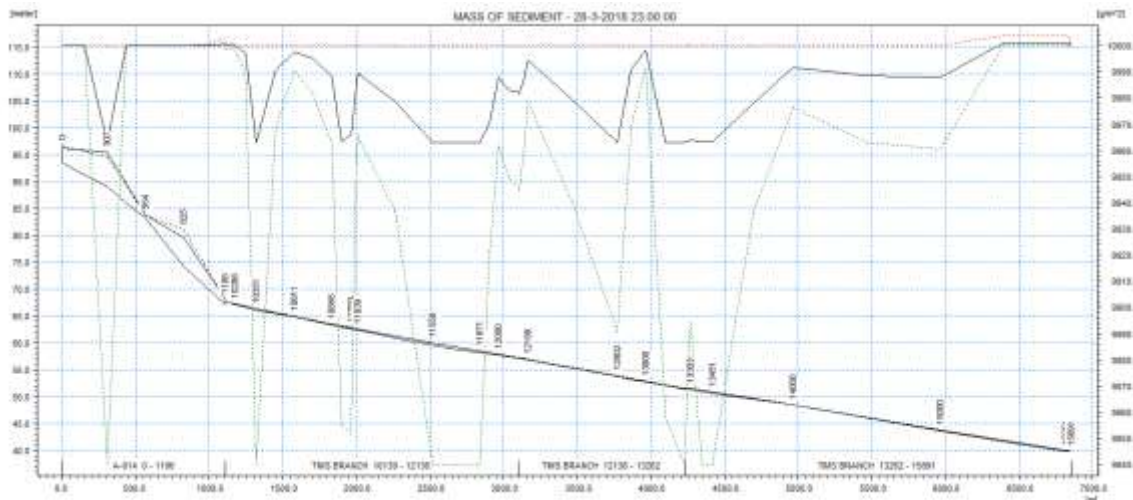
Figure 48. Spatial variation of bed sediment as the model equilibrates after storm events. The top group of curves show maximum mass of bed sediment (red), current mass of bed sediment (black) and minimum mass of bed sediment (green). The lower group of curves show the elevation of each cross-section.

Subtask 3.1: Conclusions and Future Work

The integrated hydrologic and contaminant transport model developed in this research was proved applicable to simulate the water movement and coupled transport of a heavy metal contaminant as affected by its interactions with sediment transport in Tims Branch. With in situ data collected during the tin (II)-based mercury treatment at the SRS site, this model could be used to evaluate the effectiveness of the applied remediation technology at the SRS site, and is also relevant to evaluating the potential of using water treatment and novel remediation technologies in other mercury-contaminated stream systems at SRS and possibly other DOE sites to accelerate site closure. The fully coupled contaminant transport model addresses the knowledge gaps related to the fate and transport of heavy metal contaminants at DOE EM sites as affected by the interactions with sediment movement. The model also serves as a basis upon which the fate and transport of other heavy metal and radionuclide contaminants of concern (U, Ni, and Hg) can be simulated in the future, and supports interpretation of historical data on the trends of contaminant distribution in Tims Branch, particularly considering the effect of extreme hydrological events on the stream flow and consequent mobilization and sedimentation of contaminants that have adsorbed on sediment.

Model calibration will continue as more monitoring data become available and other heavy metals of interest will also be simulated using coupled contaminant transport model in scenario runs. Detail of this research will be presented on Waste Management Symposia 2020 and summarized as peer-reviewed publication in the following year.

Subtask 3.2: Application of GIS Technologies for Hydrological Modeling Support

Subtask 3.2: Introduction

Application of GIS technology is a key component in hydrological modeling that helps to prepare data, display results and conduct further spatial analyses. The use of GIS technology has supported the MIKE SHE and MIKE 11 hydrology model development. In addition, the ArcGIS platform has provided a geodatabase to store and manage model-specific geospatial and timeseries data, as well as GIS modeling tools to prepare, analyze and visualize model input data and model results.

Subtask 3.2: Objectives

The aim of this subtask is to support the hydrological model development by using state-of-the-art geoprocessing tools to pre-process geospatial and tabular data for input into the MIKE model. The ArcGIS platform will be used to prepare maps for visualization of the study area and the spatiotemporal distribution of contaminants in the Tims Branch watershed based on large timeseries datasets. The development of process flow models using ArcGIS ModelBuilder will also help to accelerate the hydrological model development by automating the repetitive geoprocessing tasks. The following outlines the GIS-related work conducted over the past year in support of the Tims Branch hydrological model development.

Subtask 3.2: Methodology

In FIU Performance Year 9, FIU continued the utilization of ArcGIS tools to pre-process the geospatial data used in the Tims Branch hydrology model. Advanced geospatial and statistical analyses were also conducted for the Tims Branch watershed. This included an extreme hydrological event analysis to determine hyetographs for Tr = 2, 5, 10, 25, 50, 100 and 200 years for use in the integrated surface water model in future to simulate the spatiotemporal distribution of flow depth and velocity in Tims Branch under extreme hydrologic scenarios. FIU graduate and undergraduate DOE Fellow students were mentored and trained on how to perform geoprocessing tasks, conduct geospatial analyses and generate maps and graphs for reporting purposes.

In July 2018, FIU initiated communication with Dr. Richard Koehler to discuss a methodology he developed using GIS for visualization of large timeseries datasets, which FIU was considering for further analysis of the precipitation and flow data being used for the Tims Branch model. Through this collaboration, Dr. Koehler agreed to host a free webinar related to this topic as part of the ARC Lecture Series entitled "Using GIS to Visualize and Analyze Environmental Time-Series Data as Raster Maps" on October 24, 2018. This methodology enables large temporal datasets to be more easily reviewed and interpreted. Plotting the environmental timeseries datasets as raster hydrographs or "time maps" using a GIS-based methodology, provides an alternative technique for examining time-based data. Timeseries values from various sources such as specific observation points, model output data, or other time-based data can be integrated and summarized in a manner that allows multi-scale temporal pattern identification and quantification, data quality checks, delta value plots or image filtering. The raster hydrographs can provide a highly illustrative approach to examining and interpreting the large hydrologic timeseries datasets that FIU has used in developing the Tims Branch hydrology model, including

rainfall, water levels and stream flow/discharge, which is important in the era of "big data" for long-term monitoring and conducting scenario-based studies.

In December 2018 FIU initiated activities to identify the best applicable method for determining the spatial and temporal variability in spectral-based surface energy evapotranspiration (ET) across the SRS as an indicator of the environmental response to disturbances to the landscape and the effect that these changes can have on the energy and water budget. A preliminary literature review on remote sensing techniques used in monitoring hydrological conditions such as evapotranspiration and soil moisture content was conducted, however, after discussion with collaborators at SRNL following Dr. Mahmoudi's departure from FIU, it was agreed to discontinue this subtask and instead focus all resources on the Tims Branch modeling effort which was a higher priority to the site. As such, milestone 2018-P2-M5, "Literature Review of Remote Sensing Techniques for Monitoring Hydrological Conditions in the Tims Branch Study Area" was not completed during this performance year.

Subtask 3.2: Results and Discussion

Rainfall Analysis

This year FIU completed an extreme hydrological event analysis to determine hyetographs for return periods (TR) = 2, 5, 10, 25, 50, 100 and 200 years using data from 13 SRS weather stations. This task was initiated in FIU Performance Year 8, where hyetographs were generated for stations 700-A, SRTC and BARR2. In FIU Performance Year 9, FIU completed the task, generating hyetographs for the remaining stations: BARR3, BARR5, 100-C, 400-D, 200-F, 200-H, 100-K, 100-L, MOX and 100-P. The Log-Pearson Type III distribution was used for fitting frequency distribution data and predicting the design storm. Statistical parameters such as mean values, standard deviations, skewness, probabilities and recurrence intervals were calculated from the daily rainfall data. The maximum rainfall data for the various return periods will be used for future extreme rainfall scenario analysis, and using data derived from more than one location will provide a more spatially distributed analysis of the hydrological conditions in the Tims Branch study area.

Station 700A; Lat= 33.33431; Lon= -81.73379							Station SRTC; Lat= 33.34789; Lon= -81.73878					
TR (years)	LogTR (log year)	K1 (0.5)	K1 (0.6)	Slope	K1 (0.5053)	MaxRain (mm)	TR (years)	LogTR (log year)	K1 (0.8)	K1 (0.9)	Slope	K1 (0.8762)	MaxRain (mm)
1.0101	0.00	-1.96	-1.88	0.75	-1.95104	41.54	1.0101	0.00	-1.73	-1.66	0.73	-1.6774	47.89
2	0.30	-0.08	-0.10	-0.16	-0.08384	76.27	2	0.30	-0.13	-0.15	-0.16	-0.14419	81.05
5	0.70	0.81	0.80	-0.08	0.80758	101.93	5	0.70	0.78	0.77	-0.11	0.771622	110.98
10	1.00	1.32	1.33	0.05	1.32326	120.56	10	1.00	1.336	1.339	0.03	1.338285	134.80
25	1.40	1.91	1.94	0.29	1.91153	145.99	25	1.40	1.993	2.018	0.25	2.012041	169.87
50	1.70	2.31	2.36	0.48	2.31353	166.39	50	1.70	2.453	2.498	0.45	2.487274	199.96
100	2.00	2.69	2.76	0.69	2.68964	188.05	100	2.00	2.891	2.957	0.66	2.941269	233.67
200	2.30	3.04	3.13	0.91	3.0458	211.15	200	2.30	3.312	3.401	0.89	3.379787	271.62
Station BARR2; Lat= 33.38023; Lon= -81.6851							Station BARR3; Lat= 33.35702 ; Lon= -81.48763					
TR (years)	LogTR (log year)	K1 (0.2)	K1 (0.3)	Slope	K1 (0.2908)	MaxRain (mm)	TR (years)	LogTR (log year)	K1 (0.1)	K1 (0.2)	Slope	K1 (0.1298)	MaxRain (mm)
1.0101	0.00	-2.18	-2.10	0.74	-2.11078	46.30	1.0101	0.00	-2.252	-2.178	0.74	-2.22998	40.83
2	0.30	-0.03	-0.05	-0.17	-0.04844	81.50	2	0.30	-0.017	-0.033	-0.16	-0.02176	75.99
5	0.70	0.83	0.82	-0.06	0.82455	103.54	5	0.70	0.836	0.830	-0.06	0.834215	96.67
10	1.00	1.301	1.309	0.08	1.308267	118.22	10	1.00	1.292	1.301	0.09	1.294678	110.03
25	1.40	1.818	1.849	0.31	1.84616	137.00	25	1.40	1.785	1.818	0.33	1.794819	126.65
50	1.70	2.159	2.211	0.52	2.206237	151.22	50	1.70	2.107	2.159	0.52	2.122473	138.88
100	2.00	2.472	2.544	0.72	2.537405	165.59	100	2.00	2.400	2.472	0.72	2.421424	151.06
200	2.30	2.763	2.856	0.93	2.847481	180.28	200	2.30	2.670	2.763	0.93	2.697673	163.27
Station BARR5; Lat= ; Lon=							Station 100-C; Lat= 33.25247 ; Lon= -81.67722					
TR (years)	LogTR (log year)	K1 (0.4)	K1 (0.5)	Slope	K1 (0.4805)	MaxRain (mm)	TR (years)	LogTR (log year)	K1 (0.4)	K1 (0.5)	Slope	K1 (0.4306)	MaxRain (mm)
1.0101	0.00	-2.029	-1.955	0.74	-1.9694	45.51	1.0101	0.00	-2.029	-1.955	0.74	-2.00638	41.56
2	0.30	-0.066	-0.083	-0.17	-0.07969	80.10	2	0.30	-0.066	-0.083	-0.17	-0.0712	72.09
5	0.70	0.816	0.808	-0.08	0.809557	104.51	5	0.70	0.816	0.808	-0.08	0.813554	92.73
10	1.00	1.317	1.323	0.06	1.321832	121.82	10	1.00	1.317	1.323	0.06	1.318834	107.08
25	1.40	1.880	1.910	0.3	1.90416	145.00	25	1.40	1.880	1.910	0.3	1.889171	125.95
50	1.70	2.261	2.311	0.5	2.301267	163.30	50	1.70	2.261	2.311	0.5	2.276286	140.63
100	2.00	2.615	2.686	0.71	2.672179	182.46	100	2.00	2.615	2.686	0.71	2.636706	155.82
200	2.30	2.949	3.041	0.92	3.023091	202.66	200	2.30	2.949	3.041	0.92	2.977126	171.67

Station 400D; Lat= ; Lon=							Station 200F; Lat= 33.28569 ; Lon= -81.679141					
TR (years)	LogTR (log year)	K1 (0.4)	K1 (0.5)	Slope	K1 (0.4269)	MaxRain (mm)	TR (years)	LogTR (log year)	K1 (0.8)	K1 (0.9)	Slope	K1 (0.8762)	MaxRain (mm)
1.0101	0.00	-2.029	-1.955	0.74	-2.00908	43.04	1.0101	0.00	-2.326	-2.252	0.74	-2.27693	42.84
2	0.30	-0.066	-0.083	-0.17	-0.07058	76.84	2	0.30	0.000	-0.017	-0.17	-0.01127	80.85
5	0.70	0.816	0.808	-0.08	0.813846	100.09	5	0.70	0.842	0.836	-0.06	0.838021	102.58
10	1.00	1.317	1.323	0.06	1.318615	116.40	10	1.00	1.282	1.292	0.1	1.288631	116.39
25	1.40	1.880	1.910	0.3	1.888076	138.00	25	1.40	1.751	1.785	0.34	1.773545	133.33
50	1.70	2.261	2.311	0.5	2.274461	154.90	50	1.70	2.054	2.107	0.53	2.089143	145.66
100	2.00	2.615	2.686	0.71	2.634114	172.48	100	2.00	2.326	2.400	0.74	2.375068	157.82
200	2.30	2.949	3.041	0.92	2.973768	190.91	200	2.30	2.576	2.670	0.94	2.63833	169.90

Station 200H; Lat= 33.28810 ; Lon= -81.64255						
TR (years)	LogTR (log year)	K1 (-0.2)	K1 (-0.1)	Slope	K1 (-0.1171)	MaxRain (mm)
1.0101	0.00	-2.472	-2.400	0.72	-2.41234	39.40
2	0.30	0.033	0.017	-0.16	0.019742	81.45
5	0.70	0.850	0.846	-0.04	0.846686	104.26
10	1.00	1.258	1.270	0.12	1.267943	118.24
25	1.40	1.680	1.716	0.36	1.70983	134.92
50	1.70	1.945	2.000	0.55	1.990573	146.72
100	2.00	2.178	2.252	0.74	2.239316	158.03
200	2.30	2.388	2.482	0.94	2.465888	169.09

Station 100K; Lat= 33.21237 ; Lon= -81.66567							Station 100L; Lat= 33.20833 ; Lon= -81.62500						
TR (years)	LogTR (log year)	K1 (0.2)	K1 (0.3)	Slope	K1 (0.2790)	MaxRain (mm)	TR (years)	LogTR (log year)	K1 (0)	K1 (-0.1)	Slope	K1 (-0.0672)	MaxRain (mm)
1.0101	0.00	-2.178	-2.104	0.74	-2.11955	42.08	1.0101	0.00	-2.400	-2.326	0.74	-2.3757	36.73
2	0.30	-0.033	-0.050	-0.17	-0.04643	80.74	2	0.30	0.017	0.000	-0.17	0.011418	81.17
5	0.70	0.830	0.824	-0.06	0.825261	106.19	5	0.70	0.846	0.842	-0.04	0.844687	107.06
10	1.00	1.301	1.309	0.08	1.307319	123.57	10	1.00	1.270	1.282	0.12	1.27394	123.46
25	1.40	1.818	1.849	0.31	1.842486	146.21	25	1.40	1.716	1.751	0.35	1.727493	143.53
50	1.70	2.159	2.211	0.52	2.200073	163.61	50	1.70	2.000	2.054	0.54	2.017732	158.06
100	2.00	2.472	2.544	0.72	2.52887	181.42	100	2.00	2.252	2.326	0.74	2.276299	172.24
200	2.30	2.763	2.856	0.93	2.836458	199.84	200	2.30	2.482	2.576	0.94	2.512867	186.32
Station MOX; Lat= 33.29158 ; Lon= -81.67787							Station 100P; Lat= 33.23133 ; Lon= -81.58177						
TR (years)	LogTR (log year)	K1 (-0.6)	K1 (-0.5)	Slope	K1 (-0.5181)	MaxRain (mm)	TR (years)	LogTR (log year)	K1 (-0.5)	K1 (-0.4)	Slope	K1 (-0.4582)	MaxRain (mm)
1.0101	0.00	-2.755	-2.686	0.69	-2.69848	51.53	1.0101	0.00	-2.686	-2.615	0.71	-2.65632	29.72
2	0.30	0.099	0.083	-0.16	0.085893	85.93	2	0.30	0.083	0.066	-0.17	0.075893	76.66
5	0.70	0.857	0.856	-0.01	0.856181	99.00	5	0.70	0.856	0.855	-0.01	0.855582	100.46
10	1.00	1.200	1.216	0.16	1.213107	105.71	10	1.00	1.216	1.231	0.15	1.222271	114.08
25	1.40	1.528	1.567	0.39	1.559949	112.66	25	1.40	1.567	1.606	0.39	1.583304	129.30
50	1.70	1.720	1.777	0.57	1.766694	117.02	50	1.70	1.777	1.834	0.57	1.800829	139.43
100	2.00	1.880	1.955	0.75	1.94144	120.84	100	2.00	1.955	2.029	0.74	1.985936	148.67
200	2.30	2.016	2.108	0.92	2.091366	124.21	200	2.30	2.108	2.201	0.93	2.146879	157.20

Figure 49. Maximum rainfall values calculated for each SRS rainfall station for return periods (TR) = 2, 5, 10, 25, 50, 100 and 200 years using the Log-Pearson Type III distribution method.
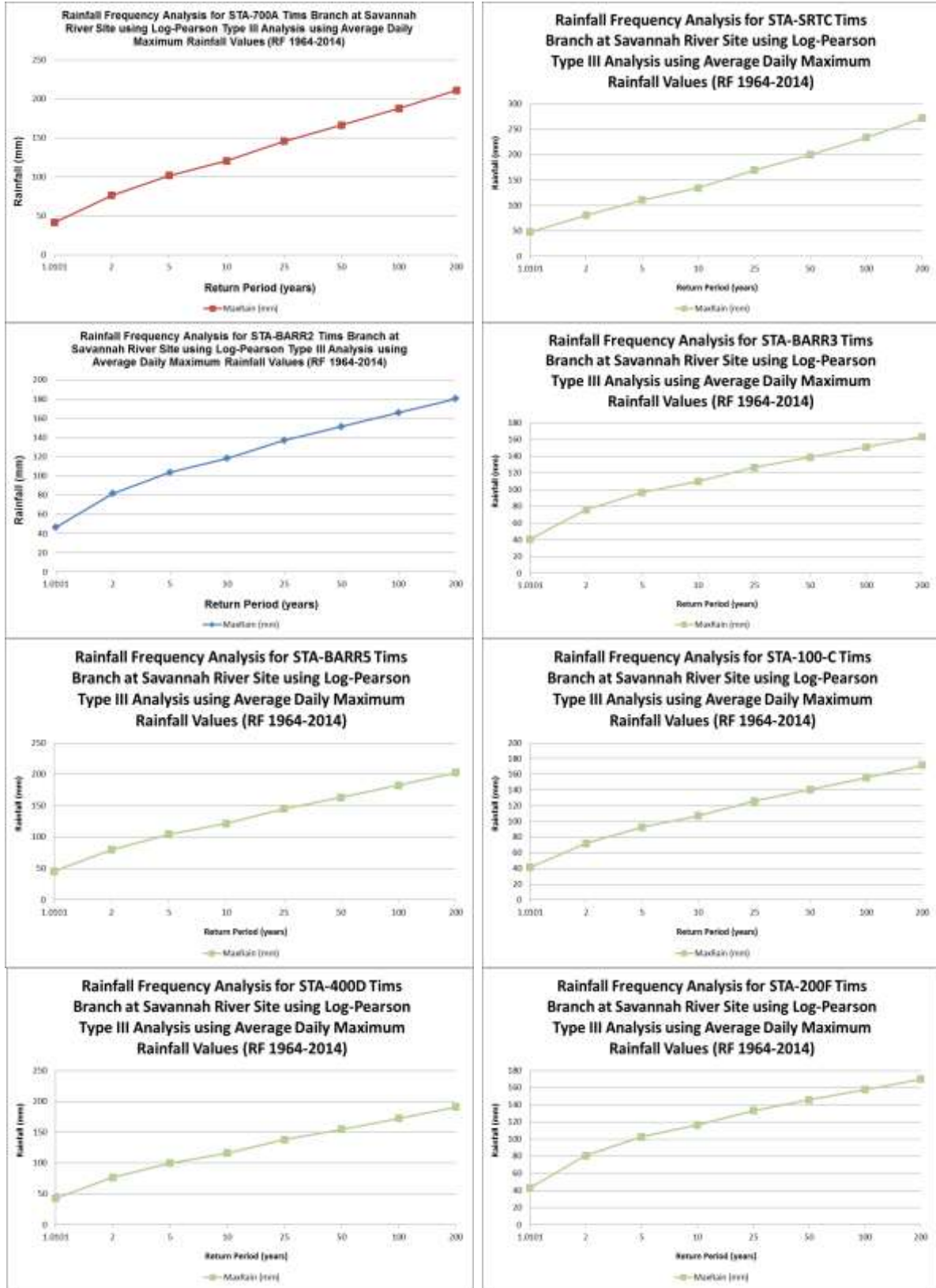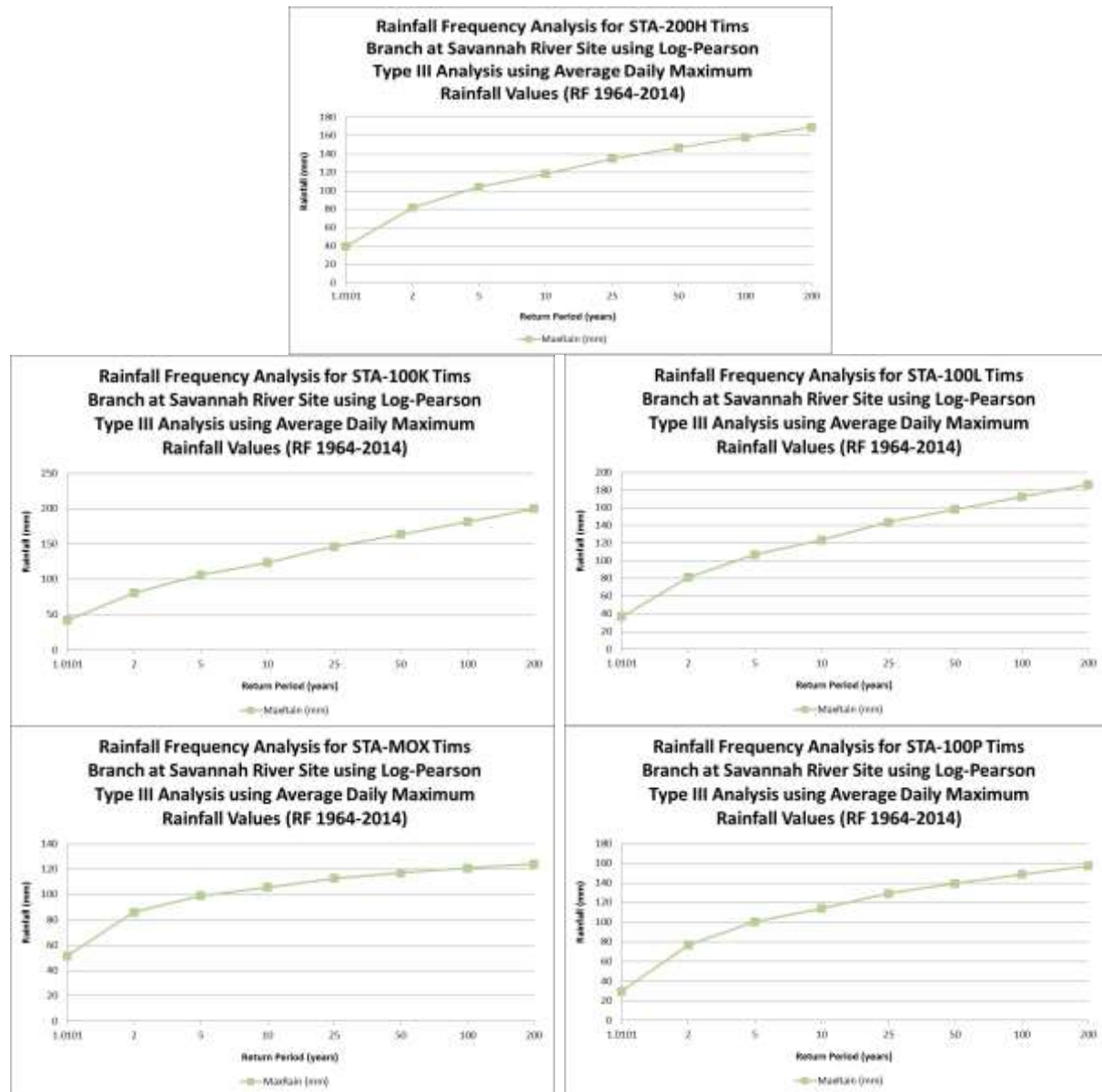
Figure 50. Hyetographs generated for each SRS rainfall station for return periods (TR) = 2, 5, 10, 25, 50, 100 and 200 years using the Log-Pearson Type III distribution method.

Data Pre-Processing

Following FIU's model review by Lagos Consulting, an effort was initiated by DOE Fellow Juan Morales to expand the A-014 model domain to include more of the A/M Area's paved surface and thus more accurately account for storm run-off. Although the former model domain was based on the sub-catchment basin, this was further refined to obtain a more accurate representation of the natural environment near the A-014 outfall and to incorporate approximately 1/3 of the A/M area facilities.
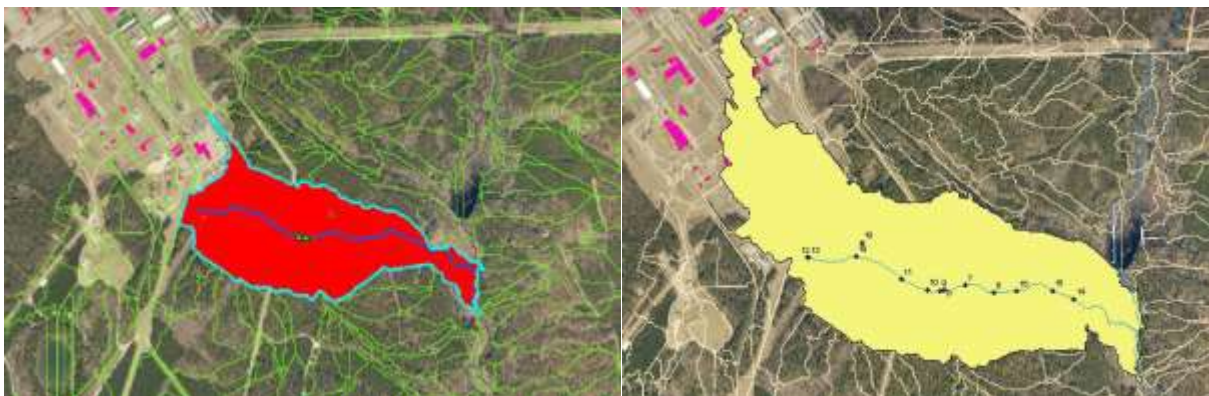
Figure 51. Current A-014 model domain (left). Revised A-014 model domain incorporating a larger portion of the A/M Area's paved surface (right).

In addition a new stream network file was generated using a 3-meter resolution digital elevation model (DEM) for comparison with the current river network file being used, which was derived from a 10-meter resolution DEM. A river bathymetry toolkit was then used to ensure an accurate network centerline was generated. The river bathymetry toolkit was also used to delineate other hydrological features from the 3-meter DEM which could be exported either as GIS shapefiles or MIKE 11 network files.

With a newly delineated stream network, modification of the sample location shapefile was subsequently necessary, as the points were no longer accurately overlaying atop the stream centerline. During an edit session in ArcGIS all of the sample locations were revised to show proper alignment as seen in the figure below.
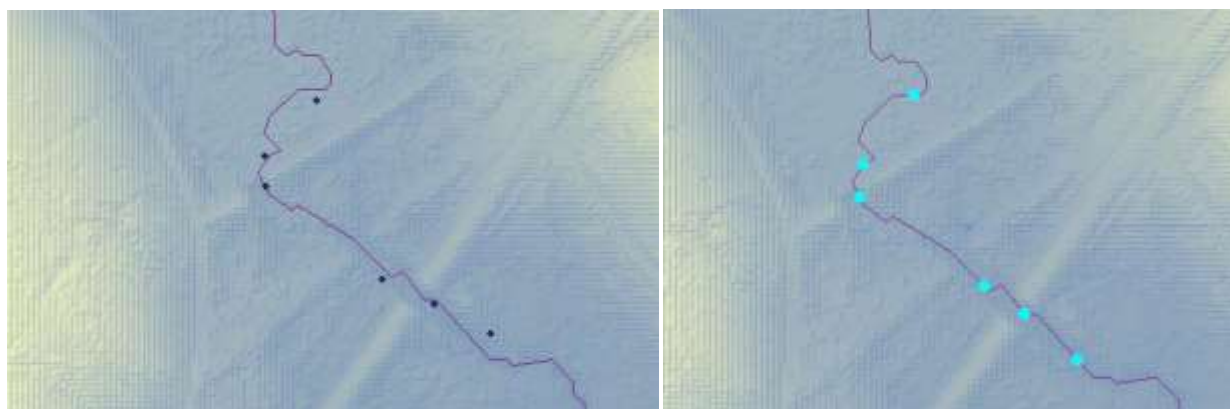
Figure 52. Sample locations from 2016 not accurately overlaying the new stream centerline (left). Revised sample location shapefile showing proper alignment with newly delineated river network (right).

The sample locations were also numbered according to coordinate locations following USGS standard operating procedures as seen in the figure below.
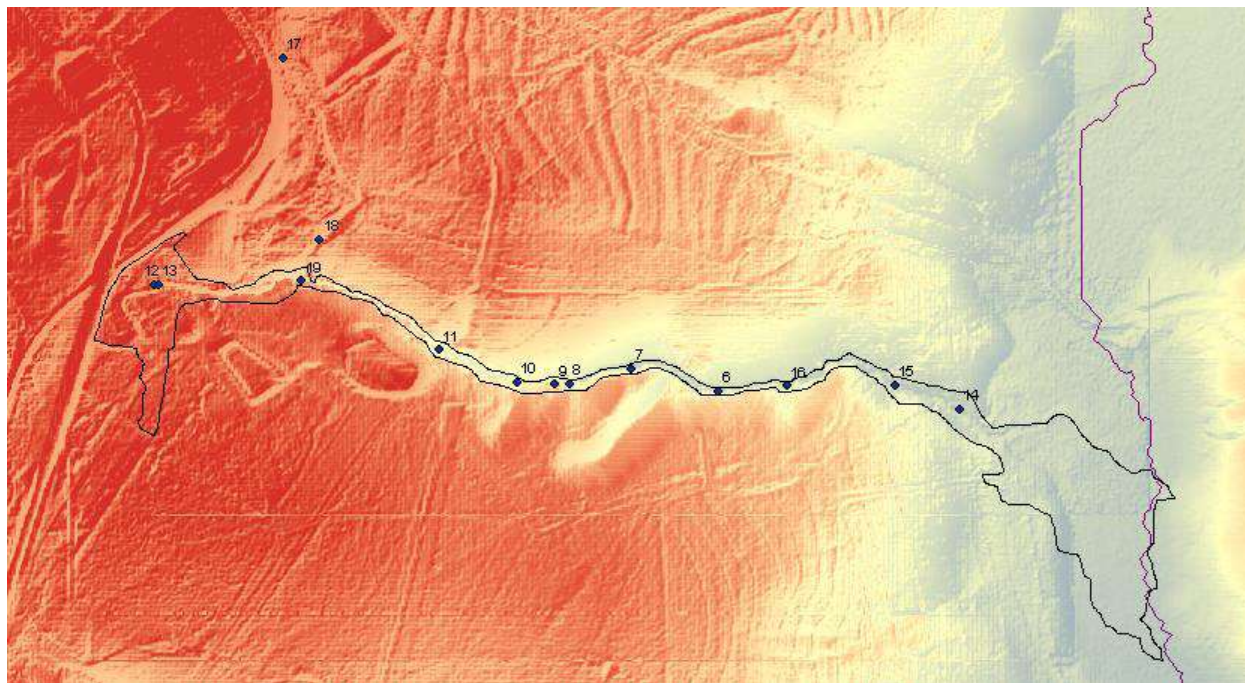
Figure 53. Sample locations accurately aligned with the stream centerlines and numbered according to USGS standard operating procedures.

FIU has updated several model grid inputs (i.e., land cover) with the most recently available data acquired from the federal online databases. In this process, many of the shapefiles were also resampled using ArcGIS tools to more accurately align with the grid in MIKE SHE rather than letting the model interpret the misaligned grid inputs, which greatly improved the model's representativeness. Geospatial tools were also used to simplify the stream network to reduce the model runtime.

These shapefiles were modified according to the following procedure:

1. Creation of dataset domain: Model domain was prepared by converting the MIKE domain grid .dsf2 file to a raster file using built-in MIKE toolbox.

2. Resample (Image 1):

   a. Polygon: The ArcGIS Polygon to Raster conversion tool was used to convert the polygons to raster grids using proper assignment type (e.g., majority for categorical data and average for numerical data).

   b. Raster: The ArcGIS Resample tool was then used to resample the input rasters to grids with a 50 m grid size. During this process, the prepared model domain raster layer was used as a snap feature (Environmental Settings→Processing Extent) that serves as a reference to provide the exact location of model grids, in additional to the size of the grids.

3. Creating ASCII file: The Raster to ASCII conversion tool was used to convert the raster files to .asc files

4. Creating MIKE input: The MIKE Zero toolbox Grid2Mike tool was used to convert the .asc files to NONUTM .dsf2 files. An example of the clipped and resampled soil parameters can be seen below in Figure 54.
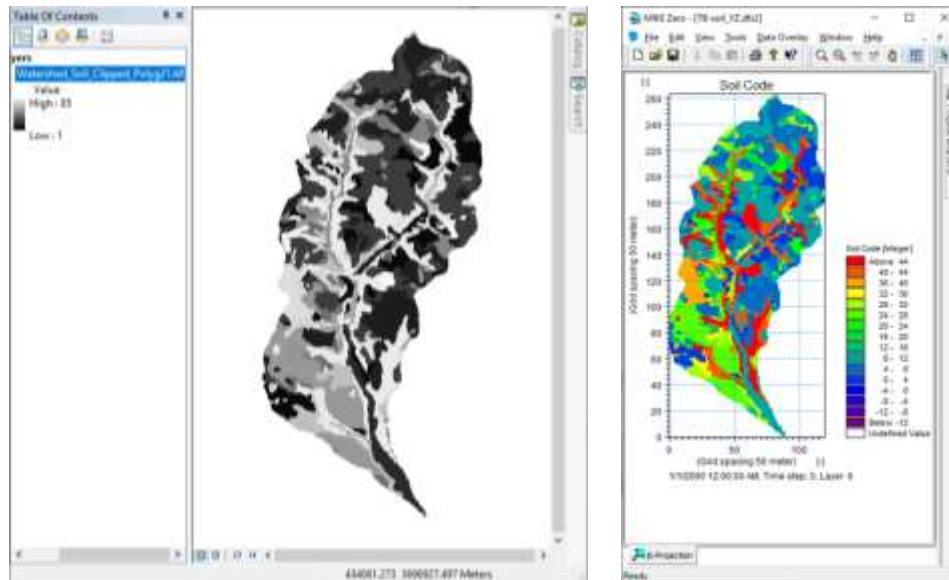
Figure 54. Clipped and resampled soil parameters as viewed in ArcMap (*left*) and MIKE SHE (*right*).

These modified grid files were incorporated into the MIKE models and currently the simulation results, after implementation of these changes, are being reviewed and analyzed.

ArcGIS tools were also used to develop shapefiles of head elevations from well data provided by the site which will be used as internal boundary conditions.

Subtask 3.2: Conclusions and Future Work

GIS data can be used for spatial representation of hydrologic features, particularly because it can be integrated with timeseries data attributes such as flow rates and directions, contaminant concentrations, water levels, precipitation, etc. Availability of data in this format shortens the time for model-specific data preparation and ultimately model development. GIS tools have also assisted in the analysis of hydrological model data and production of maps for visualization of the surface water hydrology of the Tims Branch watershed. The extreme hydrological event analysis using the Log-Pearson Type III distribution method provides projected maximum rainfall values and the hyetographs for return periods (TR) = 2, 5, 10, 25, 50, 100 and 200 years, can be used for future extreme event scenario analyses. Throughout the year, FIU graduate and undergraduate DOE Fellow students have been mentored and trained on how to perform geoprocessing tasks, conduct geospatial analyses and generate maps and graphs for reporting purposes.

Subtask 3.3: Data Collection, Sampling and Analysis in Tims Branch Watershed

Subtask 3.3: Introduction

A rigorous calibration and validation exercise is necessary to increase confidence in the ability of the hydrology model being developed for Tims Branch to estimate flow depth and velocity, and contaminant spatial distribution over time. Calibrating a numerical model of stream flow requires real-time data of rainfall and flow velocity/depth. As such, collection of field data to support model calibration and validation, particularly where data gaps have been found, is required. It is also important to collect real-time data as part of post remediation monitoring. Conducting numerical simulations with real-time data will provide a better understanding of the system's response to clean-up activities.

Collecting real-time data in Tims Branch, however, has been challenging due to the removal of historical monitoring stations and various field constraints, such as physical inaccessibility due to dense vegetation or other environmental conditions, or restricted areas which require site permits and adherence to specific safety protocols before they can be accessed. For this reason, FIU teamed with researchers at SRNL and SREL to deploy 3 remote monitoring devices in Tims Branch to assist in collecting real-time water level data at strategic locations in the watershed. One device was placed along the A-014 outfall tributary just before its confluence with the main Tims Branch stream. A second was installed downstream in Tims Branch at the watershed outlet just before the stream's confluence with Upper Three Runs, and the third data logger was placed just downstream of Beaver Pond 5 near the railroad. During FIU Performance Years 6 – 8, DOE Fellow students from FIU were mentored and trained on field data collection techniques, particularly the operation of the HOBO RX3000 Remote Monitoring System which is essentially a stage gauge/data logger that records water depth timeseries data which can be used to calculate flow rate. The remote monitoring device transmits the data in customized time intervals via a wireless network to a cloud-based storage where it can then be downloaded at FIU via the HOBOlink web-enabled software platform. Data collection, sampling and analysis activities identified under this task have been conducted with support from SRNL/SREL for site-required permitting and oversight activities, and access to their facilities for fieldwork preparation.

Subtask 3.3: Objectives

The purpose of this task is to collect detailed water level and precipitation timeseries data in the Tims Branch watershed, particularly where data gaps have been found. This data will be used for hydrological model calibration and validation to increase confidence in the ability of the hydrology model being developed for Tims Branch to estimate flow depth and velocity, and contaminant spatial distribution over time.

Subtask 3.3: Methodology

During FIU Performance Year 9, data collection activities were limited to monitoring and downloading of the data from the remote monitoring devices deployed by FIU in the Tims Branch watershed. FIU continuously monitored and periodically downloaded the water level data from the HOBOlink website for implementation in the hydrology model. The raw data was converted to the appropriate SI units (i.e., from ft to m) and several algorithms were implemented to convert the water level data to flow rates for model input.

Figure 55. Screenshot of the graphed water level data and battery performance for the Lower Tims Branch HOBO data logger for a 1-week time period viewed through the HOBOlink website. Graphs can be generated for recorded data on a daily, weekly or monthly basis.

Travel to SRS to conduct routine maintenance and calibration of the HOBO data loggers was postponed to allow Dr. Zhou to focus all his attention on the Tims Branch modeling effort after Dr. Mahmoudi's departure in order to further progress the task, particularly with respect to development of the contaminant transport component, which was a higher priority to the site. As such, the field trip to SRS was rescheduled to December 2019. To support the field work, DOE Fellow Ron Hariprashad who assisted with the deployment of the HOBO stage gauges, developed a manual for the installation and operation of the remote monitoring stations.

Subtask 3.3: Results and Discussion

Dr. Yan Zhou and DOE Fellows Amanda Yancoskie and Juan Morales visited SRS between 12/16/2019 to 12/18/2019. The purpose of this trip was to 1) re-install the HOBO remote monitoring station furthest downstream in Tims Branch that was removed due to culvert repairs that took place over the summer of 2019; 2) perform routine maintenance on the other 2 stations; and 3) meet with SRNL and SREL collabrators and tour the SRS study areas (A/M Area and Tims Branch). During the site visit, the device located furthest downstream in Tims Branch was successfully reinstalled and calibrated as the culvert repairs were completed. The images below show Drs. Brian Looney, Mike Paller and Hansell Gonzalez Raymat from SRNL assisting the FIU team with the reinstallation of the Lower Tims Branch HOBO unit..

Figure 56. SRNL collaborators (Drs. Brian Looney, Mike Paller and Hansell Gonzalez-Raymat) assisting Dr. Yan Zhou and DOE Fellows Juan Morales and Amanda Yancoskie with the re-installation of the HOBO RX3000 3G Remote Monitoring Stations located just upstream of the confluence of Tims Branch with Upper Three Runs.

In addition, the device located in the A-014 outfall tributary was cleaned and calibrated. In August of 2018, unusual flow oscillations were observed from the graphed cloud data recorded from this device. After field inspection of the unit, it was noted that the pressure transducer/sensor was covered by sediment. After several subsequent observations, it became apparent that during high flow periods the suspension of sediment in the stream was causing temporary fouling of the sensor. During the site visit by FIU in December 2019, measures were taken to counteract this issue by securing a wire mesh to the protective PVC pipe that houses the transducer cables. This mesh as seen in the figure below will serve to protect the sensor from potential fouling by sediment or debris such as leaves or biofilm during high flow periods.

Figure 57. Protective wire mesh installed to prevent fouling of the water level sensor by sediment or debris.

Lastly, during the December site visit, the station located downstream of Beaver Pond 5 was discovered to be malfunctioning and was unable to be repaired in the field. The station was therefore removed and brought back to FIU for troubleshooting. It was also determined that once the device is repaired, it should be relocated downstream of Steed Pond at the point where Tims Branch starts to receive groundwater discharge.

During FIU's visit to SRS, measurements were also taken of hydraulic parameters including flow velocity, cross-section geometry and water depth. The FIU team was also given a tour of the SRNL facilities and other areas of SRS, and held discussions regarding FIU's modeling work and other potential areas of research interest.

Subtask 3.3: Conclusions and Future Work

Watershed models are employed to understand dynamic interactions between climate and land-surface hydrology and are fundamental for the assessment and management of water resources. Hydrologists develop models to study catchments and use field measurements and observation data to better understand the dominant hydrological processes. Utilization of observed timeseries data such as precipitation and flow is important for model calibration and determining the model's ability to accurately estimate flow depth and velocity, and contaminant spatial distribution over time. Analysis of these field measurements can also aid modellers in evapotranspiration (ET) parameterization, estimation of the vertical drainage threshold and behaviour, depth and water holding capacity of the active soil zone, unsaturated and saturated zone model architecture and groundwater flow behavior as well. The water level data recorded by the HOBO data logger located farthest downstream of Tims Branch was downloaded via the HOBOlink website and is being used for calibration of the Tims Branch hydrology model. Data from the other two devices will be used in future for model validation.

FIU's deployment of the remote monitoring devices in Tims Branch will not only assist FIU with hydrological model development by providing much needed timeseries model calibration data, but will also provide DOE scientists with real-time water level/stream flow data, reducing the frequency of in situ field data collection needed by DOE personnel for long-term monitoring of hydrological conditions in the watershed. Tims Branch has served as an ideal test bed for the development of a numerical modeling tool which can evaluate the impacts of extreme hydrological conditions on the fate and transport of major contaminants of concern (e.g., Hg, U, Ni, radionuclides). This tool will particularly be beneficial to SRS, by expanding its application to other contaminated streams at SRS and possibly other DOE EM sites.

FIU will continue to monitor and download data from the remote monitoring devices deployed in Tims Branch and conduct routine maintenance and calibration of the devices as needed. The data will be used for continuous calibration and validation of the integrated hydrology model of the Tims Branch watershed. Specific rainfall scenarios will also be implemented in each model to understand the model's behavior under various atmospheric conditions. Atmospheric scenarios will be determined based upon historical rainfall events and data provided by federal/state online databases or data provided by SRNL/SRNS.

Task 3: Acknowledgements

Task 3: References

Beven, K. J., & Kirkby, M. J. (1979). A physically based, variable contributing area model of basin hydrology. *Hydrological Sciences Bulletin*, *24*(1), 43–69. https://doi.org/10.1080/02626667909491834

Conrads, P. A., Roehl, E. A., Daamen, R. C., & Kitchens, W. M. (2006). *Simulation of water levels and salinity in the rivers and tidal marshes in the vicinity of the Savannah National Wildlife Refuge, coastal South Carolina and Georgia*. U. S. Geological Survey.

Dai, T., Ambrose, R. B., Alvi, K., Wool, T., Manguerra, H., Chokshi, M., … Kraemer, S. (2005). Characterizing spatial and temporal dynamics: development of a grid-based watershed mercury loading model. In *Managing Watersheds for Human and Natural Impacts: Engineering, Ecological, and Economic Challenges* (pp. 1–12).

Evans, A. G., Bauer, L. R., Haselow, J. S., Hayes, D. W., Martin, H. L., McDowell, W. L., & Pickett, J. B. (1992). *Uranium in the Savannah River Site Environment*. Westinghouse Savannah River Co., Aiken, SC (United States).

Feaster, T. D., Golden, H. E., Odom, K. R., Lowery, M. A., Conrads, P. A., & Bradley, P. M. (2010). *Simulation of streamflow in the McTier Creek watershed, South Carolina*. U. S. Geological Survey.

Kihumba, A. M., Longo, J. N., & Vanclooster, M. (2016). Modelling nitrate pollution pressure

using a multivariate statistical approach: the case of Kinshasa groundwater body, Democratic Republic of Congo. *Hydrogeology Journal*, *24*(2), 425–437.

Kilgo, J. (2005). *Ecology and management of a forested landscape: fifty years on the Savannah River Site*. Island Press.

Kisekka, I., Migliaccio, K. W., Muñoz-Carpena, R., Schaffer, B., Boyer, T. H., & Li, Y. (2014). Simulating water table response to proposed changes in surface water management in the C-111 agricultural basin of south Florida. *Agricultural Water Management*, *146*, 185–200.

Leitman, S., & Kiker, G. A. (2015). Development and comparison of integrated river/reservoir models in the Apalachicola–Chattahoochee–Flint basin, USA. *Environment Systems and Decisions*, *35*(3), 410–423.

Mathews, T. J., Looney, B. B., Bryan, A. L., Smith, J. G., Miller, C. L., Southworth, G. R., & Peterson, M. J. (2015). The effects of a stannous chloride-based water treatment system in a mercury contaminated stream. *Chemosphere*, *138*, 190–196. https://doi.org/10.1016/j.chemosphere.2015.05.083

Phillips, R. C., Saylor, J. R., Kaye, N. B., & Gibert, J. M. (2016). A multi-lake study of seasonal variation in lake surface evaporation using MODIS satellite-derived surface temperature. *Limnology*, *17*(3), 273–289. https://doi.org/10.1007/s10201-016-0481-z

Pickett, J. B. (1990). *Heavy metal contamination in Tims Branch sediments*. Westinghouse Savannah River Co., Aiken, SC (United States).

Ritter, A., & Muñoz-Carpena, R. (2013). Predictive ability of hydrological models: objective assessment of goodness-of-fit with statistical significance. *J. Hydrol*, *480*(1), 33–45.

Seaman, J. C., Arey, J. S., & Bertsch, P. M. (2001). Immobilization of nickel and other metals in contaminated sediments by hydroxyapatite addition. *Journal of Environmental Quality*, *30*(2), 460–469. https://doi.org/10.2134/jeq2001.302460x

Zhou, Y., Fox, G. A., Miller, R. B., Mollenhauer, R., & Brewer, S. (2018). Groundwater flux estimation in streams: a thermal equilibrium approach. *Journal of Hydrology*, *561*, 822–832.

TASK 5: REMEDIATION RESEARCH AND TECHNICAL SUPPORT FOR THE WASTE ISOLATION PILOT PLANT

Task 5: Executive Summary

FIU ARC collaborates with research scientists within Los Alamos National Laboratory's Actinide Chemistry and Repository Science (ACRSP) team located at the Carlsbad Environmental Monitoring and Research Center (CEMRC) and the DOE Carlsbad Field Office (DOE-CBFO) including Dr. Andy Ward and Mr. Russ Patterson by providing experimental support toward the WIPP performance assessment needs. Experimental work targeting the fate and transport of actinides and lanthanides in systems with high ionic strength will provide better insight into contaminant behavior in systems similar to the WIPP environment. These experiments are expected to reduce uncertainty in the behavior of actinides in the WIPP environment and may lead to the development of more accurate performance assessment models of the actinide-mineral interaction at the WIPP.

During FIU Performance Year 9, batch experiments were finalized to investigate the impact of EDTA on the sorption of lanthanides and actinides to dolomite under WIPP conditions, including variable ionic strength systems (0.1 – 5.0 M) and two WIPP-relevant brines, GWB and ERDA-6. Additional batch experiments were conducted to better understand the impact of ionic strength and EDTA on the dissolution of dolomite. DOE Fellow Frances Zengotita earned a position in the Seaborg Institute Nuclear Science and Security Summer Internship Program at LLNL where she worked with Dr. Enrica Balboni to better understand the migration of plutonium at Ravenglass, UK. Zengotita graduated with her Bachelor's degree in Chemistry and English during Fall 2019. She was honored as an FIU World's Ahead Undergraduate. DOE Fellow Alexis Vento spent ten weeks at SRNL working with the Hydrology team to develop a density profile of well H-6bR. Vento also graduated with his Bachelor's degree (Environmental Engineering) during Fall 2019 and began working toward his Master's degree (Environmental Engineering) at FIU.

This work has been published in two peer-reviewed articles, including work performed by Zengotita during a summer internship with the ACRSP team. Two additional papers are in preparation from the work performed in FIU Year 9 to be submitted for publication in peer-reviewed journals. During Year 9, this work was presented at multiple conferences by students and staff. In addition, this work will be presented by two posters at the Waste Management 2020 Symposium. This work was supported by DOE Fellows Frances Zengotita (BS 2019, Chemistry and English) and Alexis Vento (BS 2019, Environmental Engineering, MS ongoing, Environmental Engineering).

Subtask 5.1 Sorption of Neodymium to Dolomite in Variable Ionic Strength Systems
This research subtask was finalized during FIU Performance Year 8 and was published in the *Journal of Environmental Radioactivity* with the following title "Retention of neodymium by dolomite at variable ionic strength as probed by batch and column experiments". This subtask was not part of the Year 9 research.

Subtask 5.2: Fate of actinides in the presence of ligands in high ionic strength systems

Subtask 5.2: Introduction

This task provides support to LANL researchers in the basic science required for risk assessment models for the 5-year WIPP re-certification. The overall objective of this task is to update the experimental sorption data for the actinides to develop more realistic performance assessment models for the WIPP. These data will improve our basic understanding of the interactions of actinides in these complex systems at the WIPP and reduce uncertainty in future performance assessment models.

The WIPP's deep geologic location is characterized by high ionic strength systems due to the high concentration of salts from the evaporite deposits (up to 7.4 M). Previous studies did not fully include conditions representative of the WIPP environment (Brady, et al., 1999; Brush and Storz, 1996; Perkins, et al., 1999). To support the development of more robust models, FIU investigates the fate and transport of lanthanides and actinides in high ionic strength systems.

This work focused on the impact of EDTA, a strong chelator found in high concentrations at the WIPP site (up to 0.08 mM), on the sorption of contaminants to dolomite, a calcium magnesium carbonate mineral found within the Culebra Member of the Rustler Formation above the WIPP (Brush and Xiong, 2003; Van Soest, 2018). The highly transmissive nature of the Rustler Formation may provide a mode of transport of the contaminants following intrusion of porewaters and the subsequent dissolution of minerals and formation of soluble metal species (Stein, 1985; Brush and Storz, 1996; Perks, et al., 1998).

Subtask 5.2: Objectives

The overall objective of this task is to update the experimental sorption data for the actinides to develop more realistic performance assessment models for the WIPP. These data will improve our basic understanding of the interactions of actinides in these complex systems at the WIPP and reduce uncertainty in future performance assessment models.

Research Questions:

1. *How do relevant ligands/chelators impact sorption of the actinides at ionic strengths relevant to the WIPP?*
2. *Is there potential for ternary complexation of actinides, ligands, and mineral phases in the near field of the WIPP repository and how will they impact the fate of actinides? (e.g. dolomite)*
3. *What is the potential effect of ligands on the fate of intrinsic actinide colloids versus dissolved species? (i.e. saturated versus unsaturated actinide systems)*

Subtask 5.2: Methodology

During FIU Performance Year 9, batch sorption experiments were conducted with dolomite in variable ionic strength solutions of NaCl with 10 or 1000 µg/L of U, Nd, and Th and with or without ethylenediaminetetraacetic acid (EDTA). Experiments with 10 µg/L of the contaminants investigated the removal of contaminants from solution via an expected sorption mechanism, while the experiments with 1000 µg/L of the contaminants investigated the removal of contaminants from solution via precipitation due to solubility limits. Additionally, three size

separation methods were employed during sample collection to evaluate the formation of intrinsic colloids in the systems. The expected particle size remaining in solution after size separation are listed in Table 19.

Table 19. Expected Particle Size Remaining in Solution After the Size Separation Step for Batch Sorption Experiments

Separation method	Particle size (nm)
Settling (15 min)	$<6 \times 10^4$
Centrifugation (20 min, 8000 rpm)	<80
10k MWCO centrifugal filtration	<5

The most recent Performance Assessment Inventory Report estimates a concentration of EDTA at the WIPP site to be up to 0.08 mM (Van Soest, 2018). Batch sorption experiments were performed with 50 mg/L EDTA to investigate the impact of the ligand at excess concentrations.

Two WIPP-relevant brines were used to better understand the impact of EDTA on contaminant sorption to dolomite under WIPP conditions. These brines included the U.S. Energy Research and Development Administration Well 6 (ERDA-6, ionic strength of 5.3 M) and generic weep brine (GWB, ionic strength of 7.4 M). The ERDA-6 brine is representative of the fluids in the Castile brine reservoirs, while the GWB brine is a representative MgO-impacted brine.

Batch sorption experiments were conducted for 28 days to allow for the system to reach equilibrium. Experiments were sampled at 15 min, 60 min, 180 min, 24 hours, 48 hours, 7 days, and 28 days. Samples were analyzed by ICP-MS (ThermoFisher Scientific iCAP RQ) in 2% nitric acid. Estimated quantification limits (EQL) for the target contaminants were Nd 0.0057 µg/L, Th 0.0053 µg/L, and U 0.0052 µg/L.

Subtask 5.2: Results and Discussion

Batch experiments were conducted to investigate the impact of EDTA on the sorption of Nd(III), Th(IV), and U(VI) to dolomite in variable ionic strength systems (0.1 − 5.0 M) and two WIPP-relevant brines, GWB and ERDA-6. The potential for intrinsic colloid formation was also investigated with batch experiments under near-saturated conditions of the contaminants. The WIPP brine work (GWB and ERDA) has been included in conference proceedings for the Waste Management 2020 Symposium. The EDTA impact on actinide and lanthanide sorption to dolomite is currently being prepared for submission to a peer-reviewed journal. The results for both sets of experiments are summarized below.

Impact of EDTA and ionic strength on sorption of actinides and lanthanides to dolomite (in preparation)

A wide range of concentrations of NaCl solutions were used for batch experiments to analyze the effect of EDTA on the sorption of Nd, Th, and U onto dolomite. Preliminary results from this sweep are presented in Figure 58. EDTA has a significant impact on the solubility of Nd and Th, but does not appear to significantly alter the solubility of U. At 48 hours, the ionic strength does not appear to have a large impact on the aqueous concentrations of the contaminants.
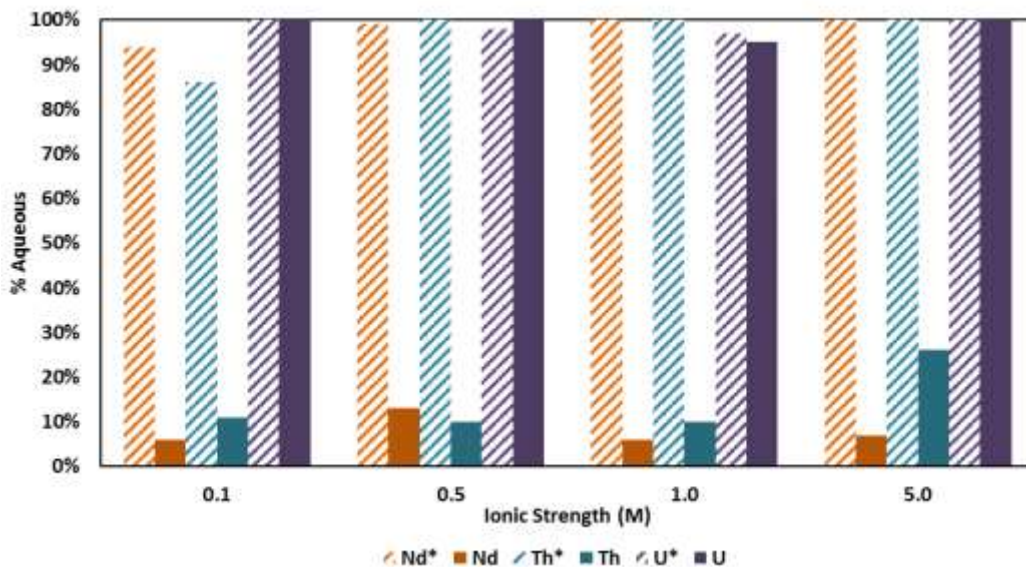
Figure 58. Aqueous fractions of 10 ppb Nd(III), Th(IV), and U(VI) in variable ionic strength (NaCl) with (Nd*, Th*, U*) and without (Nd, Th, U) EDTA after 48 hours.

Experiments were sampled at 15 min, 60 min, 180 min, 24 hours, 48 hours, and 28 days to better understand changes in the system over time. U consistently remained in solution in all systems over time. The presence of highly soluble U-carbonate species is the most likely explanation for the lack of change in the aqueous U concentration.

However, a significant change in aqueous concentration of Th and Nd was observed. Figure 59 and Figure 60 show the aqueous fractions of Nd and Th, respectively, over 7 days with and without EDTA in 0.1 and 5.0 M NaCl. In both cases, the aqueous concentration of Nd and Th decreases over time when EDTA is not present. The addition of EDTA appears to keep Nd and Th in solution. In addition, the only significant difference between low and high ionic strength is observed for Th when EDTA is present. In the 0.1 M system, after 48 hours, the aqueous concentration of Th began to decrease, but in the higher ionic strength system, this decrease did not occur.
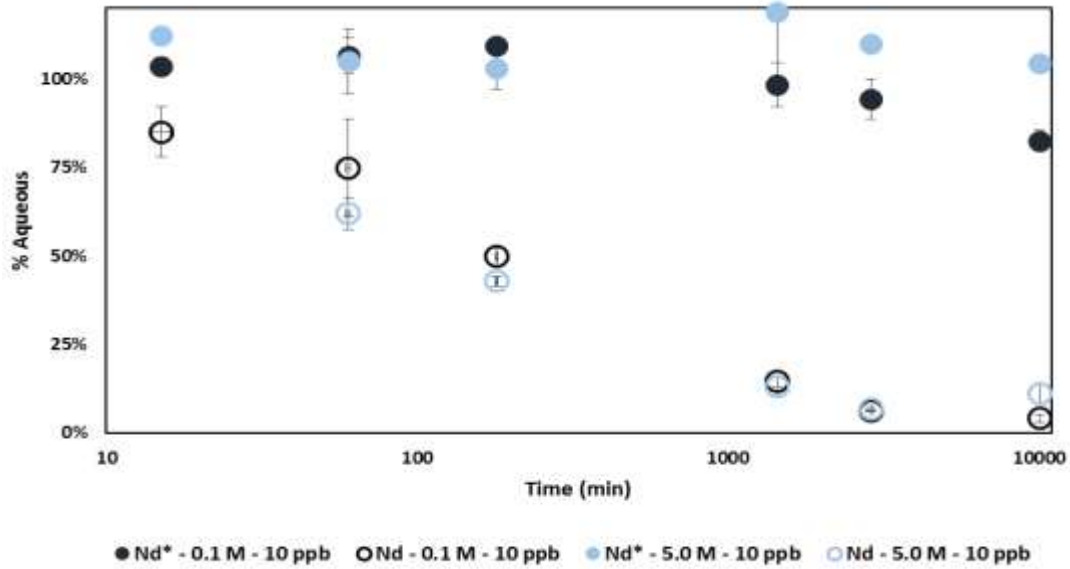
Figure 59. Aqueous fractions of 10 ppb Nd in 0.1 M and 5.0 M NaCl with dolomite (5 g/L) and with (Nd*) and without (Nd) EDTA (50 mg/L).
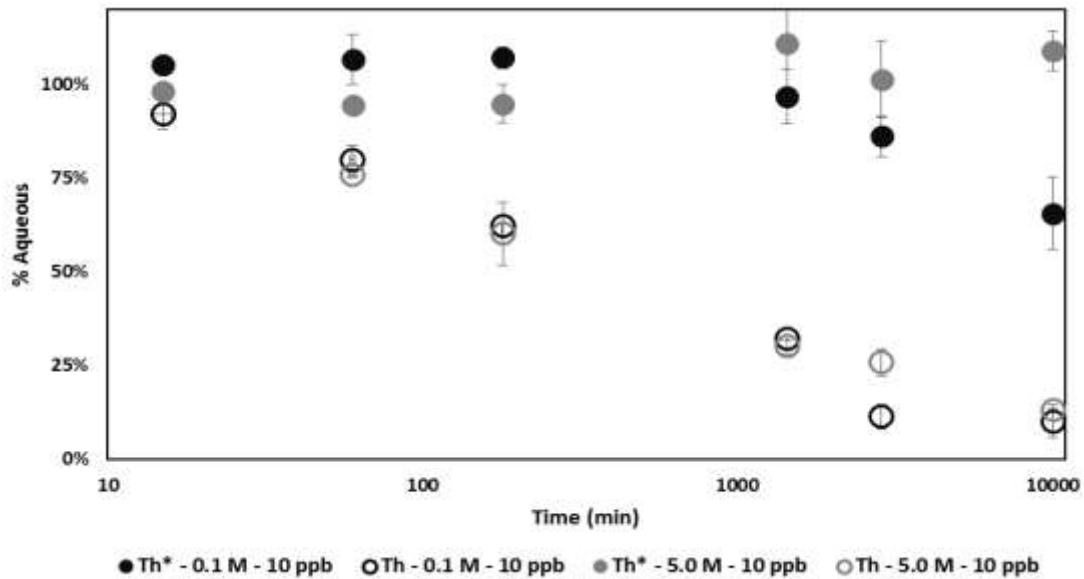
Figure 60. Aqueous fractions of 10 ppb Th in 0.1 M and 5.0 M NaCl with dolomite (5 g/L) and with (Th*) and without (Th) EDTA (50 mg/L).

The impact of EDTA on the sorption of Nd(III), Th(IV), and U(VI) onto dolomite in WIPP-relevant brines, GWB and ERDA-6

Batch experiments were conducted to investigate the behavior of Nd, Th, and U in the presence of EDTA and dolomite when in WIPP-relevant conditions. Two brines that were designed to mimic the WIPP environment were the focus of this task, the Generic Weep Brine (GWB) and the U.S. Energy Research and Development Administration Well 6 brine (ERDA-6). The GWB brine simulates a high Mg environment, similar to the environment expected in the Salado brines. The ERDA-6 brine simulates the environment of the Castile brine, which consists of high sodium concentrations. The compositions of each brine are listed in Table 20 (Borkowski, 2008; Lucchini, 2013). Magnesium oxide (MgO) in solution is expected to scavenge carbonate, potentially decreasing the concentration of highly soluble U-carbonate complexes (Snider, 2003; Xiong and Lord, 2008; Papenguth, 2000; Wall and Mathews, 2005).

Table 20. Composition of GWB and ERDA-6 Simulated WIPP Brines (Borkowski, 2008)

Component	GWB (M)	ERDA-6 (M)
NaCl	2.874	4.254
$MgCl_2$	0.953	0.018
Na_2SO_4	0.166	0.159
NaBr	0.025	0.010
$Na_2B_4O_7$	0.037	0.015
KCl	0.437	0.092
$CaCl_2$	0.013	0.011
LiCl	0.004	-

The results from batch experiments in GWB and ERDA-6 for aqueous U are presented in Figure 61 and Figure 62, respectively. As was observed in the NaCl systems, the aqueous concentration of uranium was not significantly impacted by the addition of EDTA in either of the brines. Additionally, little change was observed after 7 days. The behavior of uranium in both brines was similar. However, the aqueous concentration in GWB was slightly lower for the 10 ppb system (with EDTA) than the 1,000 ppb system (without EDTA).
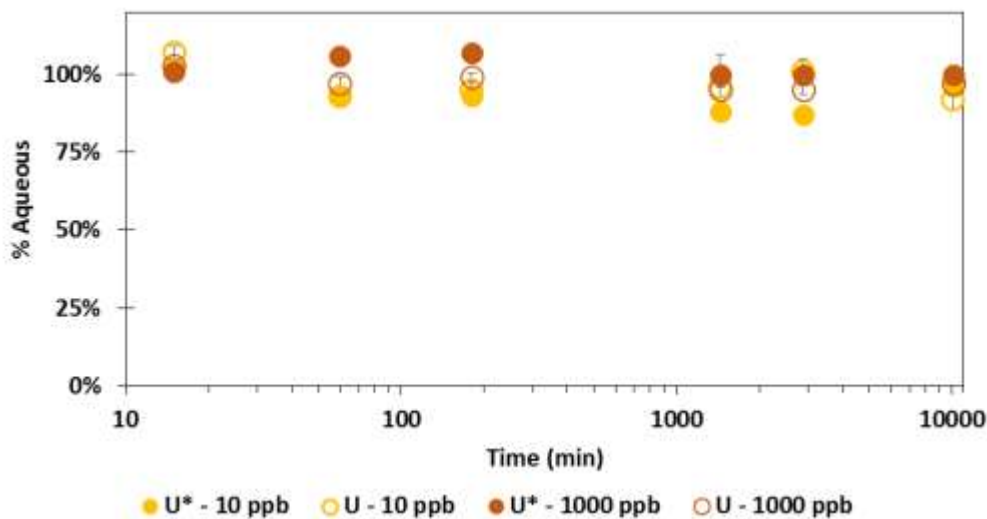
Figure 61. Aqueous fraction of U in GWB with dolomite (5 g/L) and with (U*, closed circles) and without (U, open circles) EDTA. Yellow data points denote [U]initial of 10 ppb and red data points denote [U]initial of 1,000 ppb. The 10 ppb data was collected after centrifuging (20 min, 8,000 rpm). The 1,000 ppb data was collected after filtration through 10k MWCO filters (20 min, 8,000 rpm).
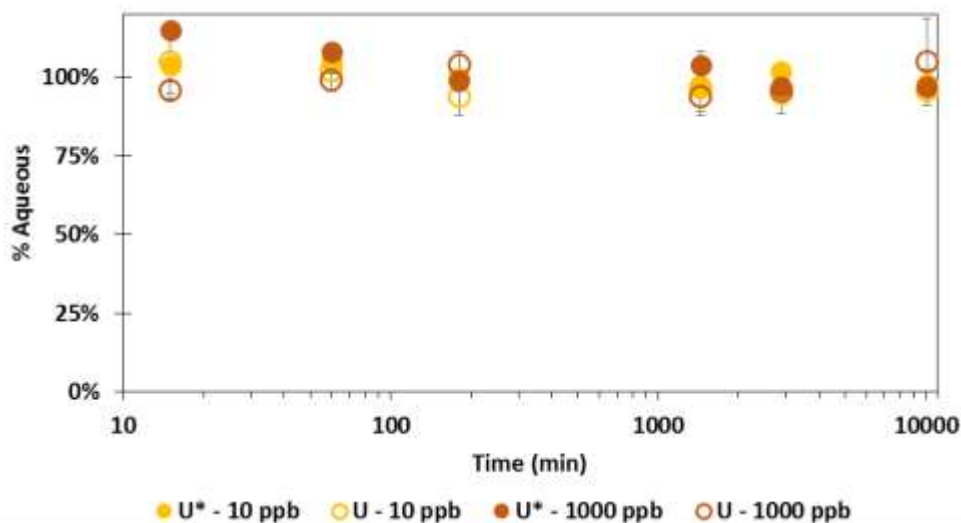
Figure 62. Aqueous fraction of U in ERDA-6 with dolomite (5 g/L) and with (U*, closed circles) and without (U, open circles) EDTA. Yellow data points denote [U]initial of 10 ppb and red data points denote [U]initial of 1,000 ppb. The 10 ppb data was collected after centrifuging (20 min, 8,000 rpm). The 1,000 ppb data was collected after filtration through 10k MWCO filters (20 min, 8,000 rpm).

The results for aqueous Nd in GWB and ERDA-6 are presented in Figure 63 and Figure 64, respectively. The aqueous Th results in GWB and ERDA-6 are presented in Figure 65 and Figure 66, respectively.

In GWB, both Nd and Th remain primarily in solution with and without EDTA, with little change after 7 days. For both metals, the aqueous fractions without EDTA are slightly lower than those with EDTA, indicating a small impact from the presence of the ligand.

In the ERDA-6 brine, the behavior of both metals varies significantly with the addition of EDTA. With EDTA, Nd remains in solution over 7 days. The aqueous fraction of Nd does not vary significantly between the 10 and 1,000 ppb systems. Without EDTA, after 24 hours (1,440 min), a significant drop in aqueous Nd is observed. The 10 ppb system consistently drops to below 25% aqueous after 7 days. However, the 1,000 ppb system shows an initial drop of Nd_{aq} after 24 hours, followed by an increase after 48 hours (2,880 min) and 7 days (10,080 min). This could be indicative of experimental errors leading to inaccurate data.

The behavior of Th in ERDA-6 is similar to Nd. Under 24 hours, Th primarily remains in solution at both concentrations (10 and 1,000 ppb) and with or without EDTA. However, after 24 hours, aqueous Th decreases in all systems. However, the data does not present a clear trend after 24 hours, with all systems showing an increase in aqueous Th. The error for the 24+ hour sampling periods is significant, preventing accurate determination of the system chemistry. Potential sources of this error include the recycling of the 10 k MWCO filters used for the 1,000 ppb systems, the GWB and ERDA-6 brine preparation, and the stock metal solutions.
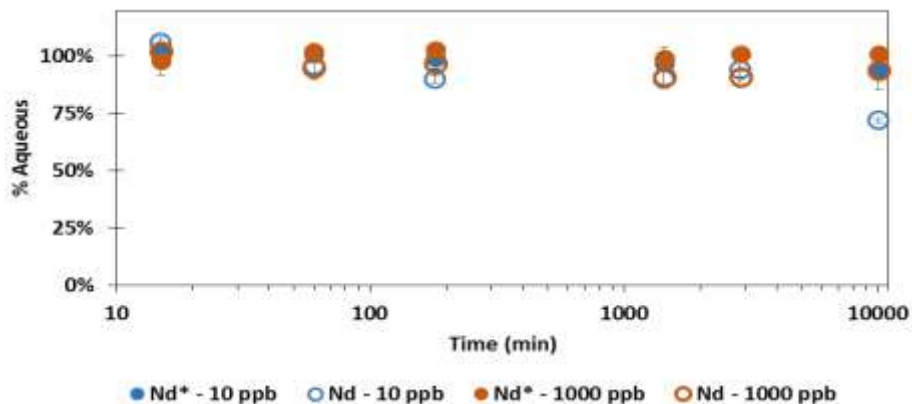
Figure 63. Aqueous fraction of Nd in GWB with dolomite (5 g/L) and with (Nd*, closed circles) and without (Nd, open circles) EDTA. Blue data points denote [Nd]initial of 10 ppb and red data points denote [Nd]initial of 1,000 ppb. The 10 ppb data was collected after centrifuging (20 min, 8000 rpm). The 1,000 ppb data was collected after filtration through 10k MWCO filters (20 min, 8,000 rpm).
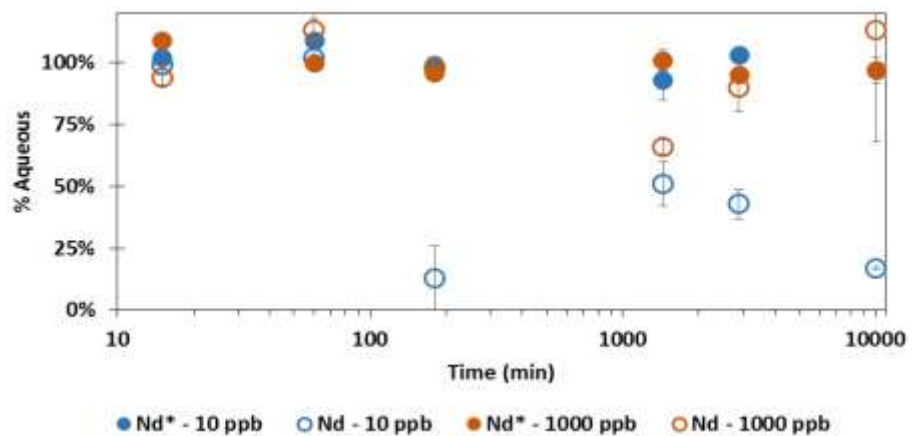
Figure 64. Aqueous fraction of Nd in ERDA-6 with dolomite (5 g/L) and with (Nd*, closed circles) and without (Nd, open circles) EDTA. Blue data points denote [Nd]initial of 10 ppb and red data points denote [Nd]initial of 1,,000 ppb. The 10 ppb data was collected after centrifuging (20 min, 8000 rpm). The 1,000 ppb

data was collected after filtration through 10k MWCO filters (20 min, 8,000 rpm).
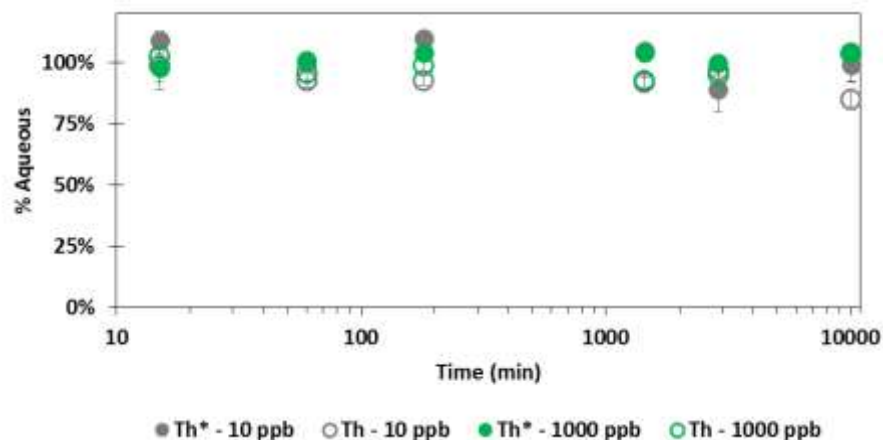
Figure 65. Aqueous fraction of Th in GWB with dolomite (5 g/L) and with (Th*, closed circles) and without (Th, open circles) EDTA. Gray data points denote [Th]initial of 10 ppb and green data points denote [Th]initial of 1,000 ppb. The 10 ppb data was collected after centrifuging (20 min, 8,000 rpm). The 1,000 ppb data was collected after filtration through 10k MWCO filters (20 min, 8,000 rpm).
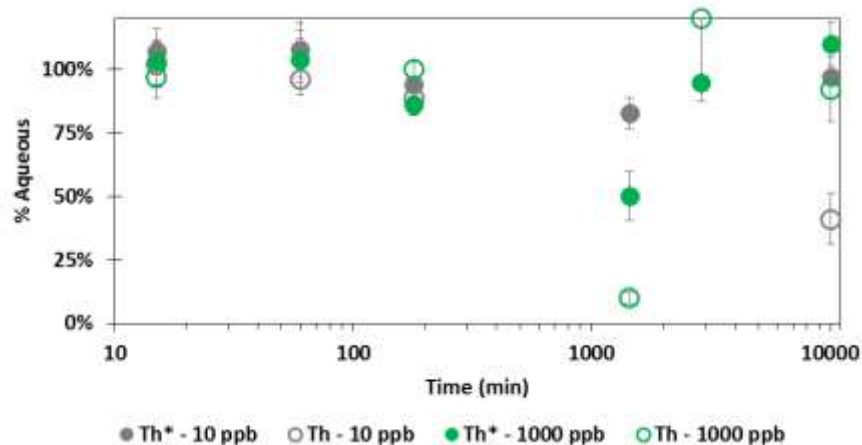
Figure 66. Aqueous fraction of Th in ERDA-6 with dolomite (5 g/L) and with (Th*, closed circles) and without (Th, open circles) EDTA. Gray data points denote [Th]initial of 10 ppb and green data points denote [Th]initial of 1,000 ppb. The 10 ppb data was collected after centrifuging (20 min, 8,000 rpm). The 1,000 ppb data was collected after filtration through 10k MWCO filters (20 min, 8,000 rpm).

This work, including conditional K_d values and methodology, can be found in the corresponding paper for the Waste Management 2020 Symposium of the same title.

Impact of ionic strength and EDTA on the dissolution behavior of dolomite

The impact of EDTA, ionic strength, and varying cations and anions on the dolomite dissolution behavior was investigated by FIU ARC during Year 9. Previous studies have investigated the dolomite surface charge and dissolution rates in the presence of various organic ligands and ionic strengths (Pokrovsky, *et al.*, 1999; Pokrovsky and Schott, 2001; Ruiz-Aguido, *et al.*, 2011; Veetil, *et al*., 2018). However, these studies did not fully cover WIPP conditions, (e.g. >1.0 M ionic strength).

Preliminary work by FIU ARC showed that over one week, less than 2% of dolomite dissolved at pH 8.5 in solutions of 0.1 and 1.0 M NaCl, CalCl$_2$, and MgCl$_2$. A higher aqueous concentration of Ca was observed in 1.0 M NaCl than 0.1 M NaCl, which was also previously observed (Emerson, *et al.*, 2018). Increased dissolution was observed in NaCl and CaCl$_2$, but not MgCl$_2$. Across the salts, dissolution followed the trend of NaCl > MgCl$_2$ > CaCl$_2$. This work was expanded to include a higher ionic strength (5.0 M) and a wider range of salts. The test matrix is presented in Table 21.

Table 21. Test matrix for investigation of dolomite dissolution in variable ionic strength and in the presence and absence of EDTA and various salts

Salt	Ionic Strength (M)	EDTA
NaCl	0.1	w/ & w/o
	1.0	w/ & w/o
	5.0	w/ & w/o
MgCl$_2$	0.1	w/ & w/o
	1.0	w/ & w/o
	4.0*	w/ & w/o
CaCl$_2$	0.1	w/ & w/o
	1.0	w/ & w/o
	5.0	w/ & w/o
CsCl	0.1	w/ & w/o
	1.0	w/ & w/o
	5.0	w/ & w/o
NaNO$_3$	0.1	w/ & w/o
	1.0	w/ & w/o
	5.0	w/ & w/o
Na$_2$SO$_4$	0.1	w/ & w/o
	1.0	w/ & w/o
Na$_2$B$_4$O$_7$	0.1	w/ & w/o
	1.0	w/ & w/o
Water		w/ & w/o

This work is being prepared for submission for publication in a peer-reviewed journal.

Subtask 5.2: Conclusions

The impact of EDTA on the sorption of Nd, Th, and U to dolomite in a wide range of ionic strength conditions was investigated. U consistently remained soluble in all conditions, with and without the presence of EDTA. The high solubility of U-carbonate species in the system most likely keeps U in solution and outcompetes the formation of U-EDTA species.

The behavior of Nd and Th followed the same general trends. Without the presence of EDTA, the aqueous concentration of both metals decreased through either sorption to the dolomite or precipitation. Aqueous Th concentrations decreased to a greater degree. The presence of EDTA significantly increased the aqueous concentrations of Nd and Th. A significant impact of high ionic strength was observed for the Th system when EDTA was present. In this case, after 48 hours, the aqueous concentration of Th began to decrease. This varied from the behavior of Th in lower ionic strength conditions where the aqueous concentration of Th in the presence of EDTA remained near 100% of the Th in the system.

Similar trends were observed in the WIPP-relevant brines, GWB and ERDA-6. U remained in solution in all systems. In GWB, Nd and Th remained in solution with and without the presence of EDTA. The behavior of Nd and Th in ERDA-6 more closely related to the behavior observed in the NaCl systems.

Work from this task is currently being prepared for submission for publication in a peer reviewed journal as two papers. One paper, tentatively titled "Impact of EDTA and ionic strength on actinide and lanthanide sorption to dolomite," will present the batch sorption data from experimnents in variable ionic strength solutions of NaCl from FIU Year 9. The dolomite dissolution work will also be prepared for publication in a peer-reviewed journal. The batch sorption experiments with GWB and ERDA-6 will be presented as a full paper and poster at the Waste Management 2020 symposium.

Task 5: Future Work

Experimental support for WIPP performance assessment models will be continued by FIU ARC. Ligands of interest for the WIPP, such as gluconate (cement additive) and isosaccharinic acid (ISA, cellulose degradation product), are potential targets for FIU research (Askarieh, *et al.*, 2008). Currently gluconate and ISA are not considered in risk assessments of the WIPP due to the expected low impact in WIPP conditions. However, previous studies have shown the ability of actinides to form complexes with gluconate in a wide pH range (Baston, *et al*., 1992; Sawyer, 1964; Tits, *et al.*, 2005). An increase in Th solubility was observed in alkaline conditions when in the presence of gluconate (Colàs 2011; Colàs 2013). Better understanding of the impact of gluconate in WIPP conditions will be supported through experimental work by FIU ARC. Future risk assessment models will be indirectly supported by experimental work to increase understanding of potential impacts from gluconate in WIPP conditions.

Task 5: Acknowledgements

Andersen Ward and Mr. Russ Patterson from the DOE Carlsbad Field Office (DOE-CBFO) and Dr. Hilary Emerson from PNNL for their input and consistent support.

Task 5: References

Askarieh, M., Chambers, A., Daniel, F., FitzGerald, P., Holtom, G., Pilkington, N., Rees, J. (2000) The chemical and microbial degradation of cellulose in the near field of a repository for radioactive wastes. *Waste Management* 20, 93-106.

Baston, G. M. N., Berry, J. A., Bond, K. A., Bronsword, M., Linklater, C. M. Effects of organic degradation products on the sorption of actinides. *Radiochimica Acta,* **1992**, *52/53*, 249-356.

Borkowski, M. (2008) Actinide (III) Solubility in WIPP Brine: Data Summary and Recommendations. LA-14360, Los Alamos National Laboratory.

Brady, P. V., Papenguth, H. W., Kelly, J. W. Metal sorption to dolomite surfaces. *Applied Geochemistry*, **1999**, *14*, 569-579.

Brush, L. H., Storz, L. J. (1996) Revised Ranges and Probability Distributions of Kds for Dissolved Pu, Am, U, Th, and Np in the Culebra for the PA Calculations to Support the WIPP CCA. Albuquerque, New Mexico.

Brush, L. H., Xiong, Y. (2003) Calculation of Organic Ligand Concentrations for the WIPP Compliance Recertification Application, S27657. Sandia National Laboratories.

Colàs, E., Grivé, M., Rojo, I., Duro, L. Solubility of $ThO_2 \cdot H_2O$(am) in the presence of gluconate. *Radiochimica Acta*, **2011**, *99*, 269-273.

Colàs, E., Grivé, M., Rojo, I., Duro, L. The Effect of Gluconate and EDTA on Thorium Solubility Under Simulated Cement Porewater Conditions. *Journal of Solution Chemistry*, **2013**, *42*, 1680-1690.

Lucchini, J. F., Borkowski, M., Khaing, H., Richmann, M. K., Swanson, J. S., Simmons, K., Reed, D. T. (2013) WIPP Actinide-Relevant Brine Chemistry, LA-UR 13-20620. Los Alamos National Laboratory - Carlsbad Operations, Carlsbad, New Mexico.

Emerson, H., Zengotita, F., Richmann, M., Katsenovich, Y., Reed, D., Dittrich, T. Retention of neodymium by dolomite at variable ionic strength as probed by batch and column experiments. *Journal of Environmental Radioactivity*, **2018**, *190*, 89-96.

Papenguth, H. W., Krumhansl, J. L., Bynum, R. V., Wang, Y., Kelly, J. W., Anderson, H. A., Nowak, E. J. (2000) Status of Research on Magnesium Oxide Backfill, SAND-98-2582C. Sandia National Laboratories.

Perkins, W. G., Lucero, D. A., Brown, G. O. (1998) Column Experiments for Radionuclide Adsorption Studies of the Culebra Dolomite: Retardation Parameter Estimation for Non-Eluted Actinide Species, SAND98-1005. Sandia National Laboratories, Albuquerque, New Mexico.

Pokrovsky, O. S.; Schott, J.; Thomas, F. Dolomite surface speciation and reactivity in aquatic systems. *Geochimica et Cosmochimica Acta*, **1999**, *63*, 3133-3142.

Pokrovsky, O. S.; Schott, J. Kinetics and Mechanism of Dolomite Dissolution in Neutral to Alkaline Solutions Revisited. *American Journal of Science*, **2001**, *301*, 597-626.

Ruiz-Agudo, E.; Urosevic, M.; Putnis, C. V.; Rodriguez-Navarro, C.; Cardell, C.; Putnis, A. Ion-specific effects on the kinetics of mineral dissolution. *Chemical Geology*, **2011**, *281*, 364-371.

Sawyer, D. Metal-gluconate complexes. *Chemical Reviews*, **1964**, *64*, 633-643.

Snider, A. C. (2003) Verification of the Definition of Generic Weep Brine and the Development

of a Recipe for this Brine, S27505. Sandia National Laboratories.

Stein, C. L. (1985) Mineralogy in the Waste Isolation Pilot Plant (WIPP) Facility Stratigraphic Horizon, SAND85-0321. Sandia National Laboratories.

Tits, J., Wieland, E., Bradbury, M. The effect of isosaccharinic acid and gluconic acid on the retention of Eu (III), Am (III) and Th (IV) by calcite. *Applied Geochemistry*, **2005**, *20*, 2082-2096.

Van Soest, G. D. (2018) Performance Assessment Inventory Report – 2018, INV-PA-18. Los Alamos National Laboratory – Carlsbad Operations.

Veetil, S. P.; Mucci, A.; Arakaki, T. Dolomite dissolution kinetics in aqueous solutions in the presence of organic and inorganic additives at 25°C and pCO$_2$ ~ 1 atm. *Chemical Geology*, **2018**, *483*, 98-110.

Wall, N. A., Mathews, S. A. Sustainability of humic acids in the presence of magnesium oxide. *Applied Geochemistry*, **2005**, *20(9)*, 1704-1715.

Xiong, Y., Lord, A. S. Experimental investigations of the reaction path in the MgO-CO$_2$-H$_2$O system in solutions with various ionic strengths, and their applications to nuclear waste isolation. *Applied Geochemistry*, **2008**, *23*, 1634-1659.

TASK 6: HYDROLOGY MODELING FOR WIPP (NEW)

Task 6: Executive Summary

This is a new task that was initiated in FIU Performance Year 9 by researchers at the Applied Research Center at FIU in collaboration with DOE personnel at Pacific Northwest National Laboratory (PNNL) and the Carsbad Field Office (CBFO) to support research and development activities at the WIPP site. Under this task FIU will develop a groundwater-basin model for the WIPP site using the DOE-developed Advanced Simulation Capability for Environmental Management (ASCEM) modeling toolset. The groundwater-basin model will be used to improve the current understanding of regional and local groundwater flow at the WIPP site, compute the water balance, and derive estimates of groundwater recharge in the post-closure phase. There is a need for an improved understanding of the regional water balance, particularly the relation between Culebra recharge and the intense, episodic precipitation events typical of the monsoon. This relationship is essential for understanding the rate of propagation of the shallow dissolution front, and the impact of land-use changes around the WIPP facility on water levels in compliance-monitoring wells. These types of analyses require a revision of the current site conceptual model to couple surface water and groundwater processes, a high resolution digital elevation model including channels and sink holes to account for surface water routing, and the development of a new mathematical model.

ASCEM is a multi-laboratory initiative to promote a state of the art scientific approach for understanding and predicting the subsurface flow and contaminant transport behavior and is ideally suited for this task. Its integrated toolset offers advanced modeling capabilities that can be used across the DOE complex. However, the hydrologic model cannot currently account for land surface hydrology, which is essential for computing the water balance. The proposed work will require the coupling of a state-of-the-art open-source land surface model (LSM) with the groundwater models (GWMs) within the ASCEM toolbox to simulate three-dimensional, unsaturated and saturated water flow. Candidate LSMs include the Community Land Model (CLM), which has been successfully coupled with the LBNL-developed ParFlow, and the UCAR-developed Noah and Noah-Multi-parameterization (Noah-MP) models. Noah-MP has been successfully coupled with the Weather Research and Forecasting (WRF) Model and used to predict the water cycle components including precipitation, soil moisture, snow pack, groundwater, streamflow, and inundation. Both the CLM and Noah-MP LSMs can be run as standalone codes, generating output that can be used to force ASCEM groundwater models while work is done within the ASCEM program to couple the LSM and GWMs.

The objective of this task is to develop a groundwater-basin model for the WIPP site using ASCEM coupled with a selected LSM to account for the surface and near-surface processes. These models will be used to compute the water balance across multiple scales and to reduce uncertainties in recharge estimates and propagation of the shallow dissolution front. This task will provide an extensible, multi-scale land-atmosphere modeling capability for conservative, coupled and uncoupled prediction of the hydrological cycle components. This will simplify the upper boundary condition for flow in Culebra that is currently externally specified without consideration of water fluxes due to surface processes like runoff, infiltration and evapotranspiration. Coupling of the LSM with the ASCEM GWMs leads to more accurate predictions of groundwater flow patterns, including horizontal flow (e.g., potentiometric surface,

flow direction, vertical flow into transmissive units, and the effect of density on flow direction). With improved estimates of the spatial and temporal patterns of recharge to force the GWM, predictions of halite dissolution and propagation of the shallow dissolution front will be made possible and the potential impact on repository performance quantified.

During this first year, FIU's aim was to initiate work on this task by: 1) determining the appropriate methodology, software, data, and processing requirements to initiate development of a high-resolution digital elevation model (DEM) for the WIPP facility and surrounding groundwater basins; 2) collecting and compiling existing information and data relevant to site hydrology, and 3) training of FIU research personnel and students on the selected LSM and ASCEM. FIU's collaboration with WIPP is projected to be a multi-year effort.

Subtask 6.1: Digital Elevation Model and Hydrologic Network

Subtask 6.1: Introduction

Development of a high resolution DEM will facilitate future creation of spatially-distributed soil and vegetation classes. This task will ensure that all features are hydrologically correct so that channels and drainage divides are in the correct places and will identify optimal monitoring and forecasting points. The outputs from this task will be geospatial and tabular data layers for use with the selected LSM, and ultimately for coupling with a regional stratigraphic model to enable groundwater modeling using the ASCEM toolbox.

Subtask 6.1: Objectives

The purpose of this task is to develop the data layers for the terrestrial overland flow, channel routing, and subsurface flow processes of the land surface model. In the first year, this task will be initiated by first determining an appropriate methodology for development of a high-resolution digital elevation model (DEM) for the WIPP site and surrounding basins to better capture the ground surface topography and local features. In FIU Year 9 the software, data and processing requirements will be defined to initiate the development of a high resolution DEM of the site, which will enable more accurate delineation and extraction of features such as drainage basins, brine lakes, channels, sink holes and discharge points in future years.

Subtask 6.1: Methodology

In FIU Performance Year 9, FIU initiated this task by conducting a literature review of methodologies for development of a high-resolution digital elevation model (DEM) for the WIPP site and surrounding basins to better capture the ground surface topography and local features which will enable more accurate delineation and extraction of features such as drainage basins, brine lakes, channels, sink holes and discharge points in future. The information gathered will also aid in determination of the software, data and processing requirements required for this task. FIU also conducted a review of methodologies for vegetation removal from UAV-based photogrammetric digital surface models (DSMs) in addition to post processing methods for extracting significant topographical features such as sink holes from high resolution DEMs.

To support this work, the DOE Fellow students were trained on the use of ArcGIS tools in order to test the first step of a methodology to extract sink holes from 1 m LiDAR-derived DEMs based on a conference paper by Doctor and Young (2013) found during FIU's detailed literature review. This involved adding the DEM to ArcMap, then using the Fill Command in ArcToolBox

followed by the Raster Calculator to subtract the DEM from the fills. This produced a layer that represents areas where there can potentially be sinkholes; however this determination requires several other spatial statistical analyses (e.g., K-function, Geographically Weighted Regression (GWR), Inverse Distance Interpolation, etc.) to calculate sinkhole density potential, and involves consideration of other factors such as geologic structure, rock type, and proximity to quarries, water bodies, streams, roads, faults, axes of synclines or anticlines, and depth to groundwater (Doctor et al, 2008). FIU conducted this procedure on a 10m DEM as well for comparison. Students were also trained on the use of ArcHydro to conduct a watershed delineation using DEM data in ArcMap. This process will be used in future to delineate hydrological features from the high-resolution DEM to be developed by FIU that will be used to create a land surface model of the WIPP site and surrounding basins.

FIU also conducted a data acquisition test in a small field beside the parking lot at ARC using an unmanned aerial vehicle (UAV) equipped with a 12 MP digital camera. The images were processed using photogrammetry software to generate a high-resolution DEM (5 mm/pixel). This method can generate sub-meter accuracy DEMs for land surface model development.

In August 2019, Dr. Yan Zhou visited the Carlsbad Environmental Monitoring & Research Center (CEMRC) in New Mexico to meet with the project collaborators and discuss details of the field work to be executed in the next year (FIU Year 10). The meeting was also beneficial in FIU establishing contact with researchers from other DOE National Labs and universities who are conducting studies of the WIPP hydrogeology and are familiar with the region's topographical and hydrological features. Dr. Zhou met with Dr. Don Reed from Los Alamos National Laboratory and Dr. Anderson Ward from the Carlsbad Field Office (CBFO) and held discussions on photogrammetric data collection and processing and future involvement of the DOE Fellows in student summer internships at the national labs next year related to this research. Dr. Ward introduced Dr. Zhou to Dr. Dennis Powers who is a consulting geologist with profound experience related to the field work conditions within and around the WIPP Land Withdrawal Act (LWA) Boundary, and Dr. Amelia Hayes from Sandia National Laboratories who may be able to assist in sharing relevant GIS data of the WIPP surrounding region that would be useful for the hydrology model development.

While in Carlsbad, Dr. Zhou was given a tour of Basin 6, a representative area of the WIPP LWA Boundary that will be used as the proposed pilot study area. This helped Dr. Zhou gain familiarity with the terrestrial features of the WIPP area and a better understanding of the terrain and vegetation cover. During the visit, most of Basin 6 was accessible on foot which will facilitate setting up ground control points (GCPs). It was also noted that vegetation removal techniques will be needed to acquire an accurate digital elevation model of the land surface if the aerial images for photogrammetry were to be collected during the summer wet season when the vegetation cover is prominent. Aerial images of Basin 6 were collected to create a DEM for the purpose of testing sinkhole detection and vegetation removal techniques. The DEM has been created with a resolution of 0.0233 m using 48 aerial images; the warping artifacts on the DEM resulted from error accumulation because of lacking GCPs. This will be minimized for the pilot test by calibration based on GCPs, and as a large-scale deviation this will not impact processing local features such as vegetation and sinkholes. As mentioned above, FIU has conducted a literature review to identify state-of-the-art sinkhole detection and vegetation removal techniques which will be tested using aerial images of Basin 6 that were collected during Dr. Zhou's visit to Carlsbad.
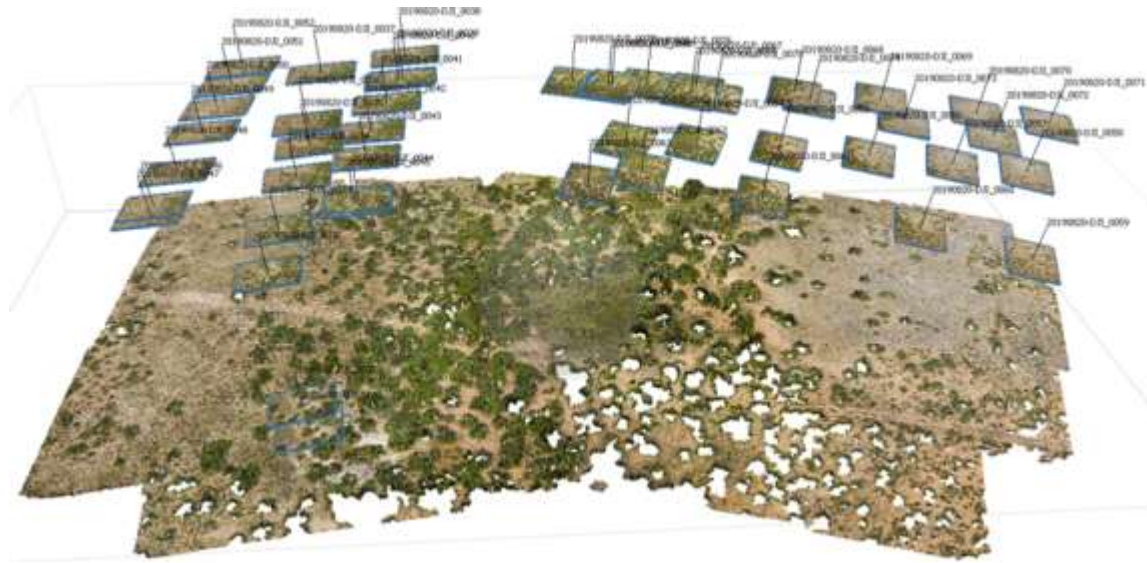
Figure 67. Aerial image locations and dense point cloud of Basin 6 created using the photogrammetry software.
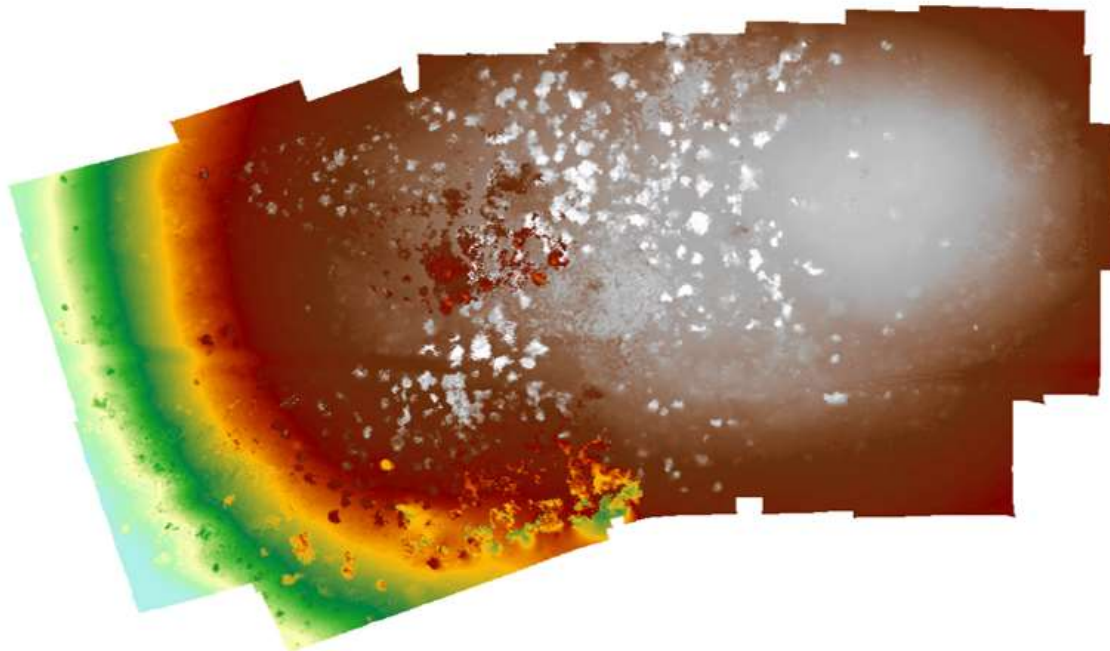
Figure 68. DEM derived after processing the aerial images of Basin 6 using photogrammetry software.

Subtask 6.1: Results and Discussion

Literature Review

In August 2019, the literature review of methodologies for development of a high resolution DEM for the WIPP (milestone 2018-P2-M12) was completed. The following is provides a brief summary of the journal articles reviewed, however the full literature review can be found in Appendix 3.

METHODOLOGIES FOR DEVELOPMENT OF A HIGH-RESOLUTION DIGITAL ELEVATION MODEL (DEM)

DEVELOPMENT AND ACCURACY ASSESSMENT OF A HIGH-RESOLUTION DIGITAL ELEVATION MODEL USING GIS APPROACHES FOR THE NILE DELTA REGION, EGYPT

El-Quilish, M., El-Ashquer, M., Dawod, G., & El Fiky, G. (2018). Development and Accuracy Assessment of High-Resolution Digital Elevation Model Using GIS Approaches for the Nile Delta Region, Egypt. American Journal of Geographic Information System, 7(4), 107-117.

This paper describes the development of a high accuracy digital elevation model (DEM) which is needed for the Nile region to investigate the impact of climate change and observing the effects of sea level rise. The first step was the digitizing process which consisted of obtaining available topographic maps of the Nile Delta region as it is covered by 220 topographic maps of scale 1:25,000 with a contour interval of 50 cm. Topographic maps of scales 1:50,000 and 1:100,000 with a contour interval of 1 m were also obtained to complete missing zones of the study areas in the case of damaged topographic maps. Once obtained, georeferencing and projection processes for the horizontal datum were conducted for each topographic map using the ArcGIS projection tool, converting from ETM red belt/GCS Egypt 1907 projection to WGS84. Note, however, that the final DEM was created using a local coordinate system for the study area. These maps were manually digitized by extracting all the available contour lines and elevation points. Once the digitizing process was completed, local DEMs were created using nine different spatial interpolation methods (SIMs).

The authors of this paper emphasized the fact that there is no single interpolation method that is considered to be standard and different methods can be employed depending on the situation and what is most appropriate. In this study, the SIMs used were the Inverse Distance Weighted (IDW), Natural Neighbor Inverse Distance Weighted (NNIDW), Global Polynomial Interpolation (GPI), Spline with Barriers (SWM), Topo to Raster (TTR), Kriging, Radial Basis Function (RBF), Empirical Bayesian Kriging (EBK) , and Local Polynomial Interpolation (LPI). Parameters were set to test each SIM to produce the most accurate DEM.

DEVELOPING A FINE-RESOLUTION DIGITAL ELEVATION MODEL TO SUPPORT HYDROLOGICAL MODELING AND ECOLOGICAL STUDIES IN THE NORTHERN EVERGLADES

Xie, Z., Pearlstine, L. & Gawlik, D. E. (2012). Developing a Fine-Resolution Digital Elevation Model to Support Hydrological Modeling and Ecological Studies in the Northern Everglades. GIScience & Remote Sensing, 49:5, 664-686, DOI: 10.2747/1548-1603.49.5.664.

This study aimed to integrate elevation survey data and vegetation data at the point and 50 m scales to develop a fine-resolution digital elevation model (DEM) for the northern Everglades. The terrain was divided into lowlands and highlands based on a 50 m scale vegetation map. The DEM in the highlands was interpolated with survey points and later adjusted to connect the

vegetation and hydro period (the number of flooded days), while the DEM in the lowlands was interpolated with elevation surveys tagged as lowland types.

The study integrates elevation and vegetation data from USGS High Accuracy Elevation Dataset (HAED) and the South Florida Water Management District (SFWMD) 2004 Vegetation Map to create a 50 m resolution ground elevation model in Water Conservation Area One (WCA1), managed by the U.S. Fish and Wildlife Services at the Arthur R. Marshall Loxahatchee Wildlife Refuge. A 50 m resolution was chosen because it was close to the scale of the slough and ridge structure in the Everglades and it matched the resolution of the SFWMD 2004 Vegetation Map.

GENERATING HIGH-RESOLUTION DIGITAL ELEVATION MODELS FOR WETLAND RESEARCH USING GOOGLE EARTH™ IMAGERY – AN EXAMPLE FROM SOUTH AFRICA

Hoffmann, E., and Winde, F. (2010) Generating high-resolution digital elevation models for wetland research using Google Earth™ imagery – an example from South Africa, Water SA, 36:1, 53-68.

The goal of this study was to design a method by which detailed relief/elevation data in Google Earth™ could be converted to a compatible GIS format that could be imported for use in ArcGIS Desktop for development of a digital elevation model for wetland research in South Africa. A procedure was developed to capture Google Earth™ elevation point data and subsequently import them into ArcGIS Desktop. A high-resolution contour map and DEM was then generated in ArcGIS Desktop using the imported elevation data from Google Earth™. An assessment of the quality and reliability of the generated contour map underlying the DEM was then conducted by comparison with the standard CDSM contour data as well as high-resolution relief data generated from airborne survey data. The airborne survey data had an elevation interval of 0.5 m, making it the highest resolution of all the data, so it was used in the assessment after being converted into a GIS-compatible format.

DEM DEVELOPMENT FROM GROUND-BASED LIDAR DATA: A METHOD TO REMOVE NON-SURFACE OBJECTS

Sharma, M., Paige, G. B., & Miller, S. N. (2010). DEM development from ground-based LiDAR data: A method to remove non-surface objects. Remote Sensing, 2(11), 2629-2642.

In this study, a method was created to remove vegetation from ground-based LiDAR data to create high-resolution DEMs. Research was conducted on intensively studied rainfall-runoff plots on the USDA-ARS Walnut Gulch Experimental Watershed in Southeast Arizona. LiDAR was used to create 1 cm digital surface models (DSM) for 5 plots. DSMs created from LiDAR data has non-surface objects like vegetation cover. A vegetation removal method was created using a slope threshold and a focal mean filter method to remove vegetation and create a bare earth DEM. It was then validated on a synthetic plot, where rocks and vegetation were added in increments.

According to the study, the removal of non-surface objects to develop DEMs from LiDAR data DSMs can be difficult and take up a lot of time. This study focuses on developing a method to

remove non-surface objects from high-resolution ground-based LiDAR DSMs to develop bare earth DEMs for small plots using single returns because of the lack in difference between the first and last returns. This was tested using ground-based LiDAR from rainfall simulator plots and validated on a synthetic laboratory plot where the placement of surface objects was controlled.

CREATING HIGH-RESOLUTION DIGITAL ELEVATION MODEL USING THIN PLATE SPLINE INTERPOLATION AND MONTE CARLO SIMULATION, WORKING REPORT

Pohjola, J., Turunen, J. and Lipping, T. (2009). Creating High-Resolution Digital Elevation Model Using Thin Plate Spline Interpolation and Monte Carlo Simulation, Working Report 2009-56.

In this report, thin plate spline interpolation was used to create a high resolution DEM. It is described as if bending a thin metal plate over the desired grid passing through the available source data points by applying the minimum energy principle. The method was implemented using the "tpaps" routine of the Spline-toolbox of the MATLAB software version 7.5 (R2007b). The routine takes the source data points (x,y,z), the x and y coordinates of the grid points of the new DEM and the relaxation parameter p as inputs. The relaxation parameter p determines how strictly the approximated surface follows the source data points and its value is between 0 and 1. If p=1 the surface passes exactly through the z values of the source data points while in the case p=0 linear interpolation by minimizing the sum of squared errors between the source data point values and the approximated surface is performed.

CREATING LOW-COST HIGH-RESOLUTION DIGITAL ELEVATION MODELS

Louhaichi, M., Borman, M. M., Johnson, A. L. and Johnson, D. E. (2003). Creating Low-Cost High-Resolution Digital Elevation Models. Journal of Range Management, 56:1, 92-96.

This research required a digital elevation model with vertical accuracy (root mean square error) of approximately 10 cm and neither a real time stop and go nor real time kinematic carrier-phase differential GPS was available. Therefore, a method was developed to efficiently generate a high accuracy elevation model for open, relatively level land using a course differential GPS (<$8000) and a low cost laser level (<$1000).

This technique was developed for measuring land with gently rolling topography, such as found in agronomic fields, wetlands, and research plots. Because the X, Y coordinates have a root mean square error of 50 to 100 cm, it is not appropriate for short, deep cut banks or short, steep escarpments where the cut face must be precisely positioned. Because the leveling rod and receiver unit have a working height from near ground level to 5 m, rugged land can require frequent repositioning of the laser level, which in turn, reduces efficiency and increases cost. Shrubs, trees, rain, fog, and/or excessive dust can limit the technique used in this study.

DEVELOPMENT OF A HIGH-RESOLUTION DIGITAL ELEVATION MODEL FOR NEW ZEALAND. LANDCARE RESEARCH CONTRACT REPORT

Barringer, J. R. F., Pairman, D., & McNeill, S. J. (2002). Development of a high-resolution digital elevation model for New Zealand. Landcare Research Contract Report: LC0102/170.

Landcare Research was tasked to develop a high resolution digital elevation model of New Zealand from the national TOPOBASE data that was supplied by the Land Information New Zealand (LINZ). The purpose of this report was to describe the methods being used to develop a national DEM with the use of GIS and LIDAR data. The DEM was created using an interpolation algorithm where data was interpolating from up to four contours or spot heights instead of two, assigning the pixel height based on interpolation within the pixel, tracking distances from the nearest contours using floating point precision for elevations. The developed DEM was then tested against a high resolution reference DEM and showed a consistent bias which overestimated elevation by a mean of six meters.

Landcare Research was able to develop a DEM with the use of interpolation methods and previously developed DEMs but continue to experience spatial inaccuracies when modeling river valleys or low elevation landforms. The paper notes that interpolation methods vary depending on the focus of the study. Different methods are available to create a DEM such as bilinear interpolation, various spline functions, radial basis functions, etc.). Although it is helpful to use GIS to develop a high resolution, DEMs generated by other organizations which use different software should be referenced as well in order to compare the accuracy of the DEM being created. It is also vital to detail the interpolation methods used in order for other users to be aware of what was used to create the DEM.

DEVELOPMENT OF AN ANTARCTIC DIGITAL ELEVATION MODEL BY INTEGRATING CARTOGRAPHIC AND REMOTELY SENSED DATA: A GEOGRAPHIC INFORMATION SYSTEM BASED APPROACH

Liu, H., Jezek, K. C., & Li, B. (1999). Development of an Antarctic digital elevation model by integrating cartographic and remotely sensed data: A geographic information system based approach. Journal of Geophysical Research: Solid Earth, 104(B10), 23199-23213.

This paper describes the development of a DEM of the Antarctic with a spatial resolution ranging from 200 m to 5 km, generated using a wide selection of topographic data sets. It relied on the availability of the most detailed cartographic data in the Antarctic Digital Database (ADD) and large-scale topographic maps from the USGS and Australian Antarctic Division for mountainous and steeply sloping areas.

Scientists at the Byrd Polar Research Center created a high resolution digital elevation model of the Antarctic developed through the use of data that falls into three categories: (1) cartographic data, (2) remotely sensed (RS) data, and (3) survey data. Cartographic maps with the most detailed data including contours, spot heights, and surface structure lines were chosen. Sources included the Antarctic Digital Database (ADD), United States Geological Survey (USGS), Australian Antarctic Division, and a digitized map from Institut fur Angewandte Geodasie of Germany. Remotely sensed data consisted of satellite radar altimetry data and radar echo sounding data. RS data sources included European Remote Sensing (ERS) satellites, SCP airborne radar sounding data, BAS airborne radar echo sounding data, and Ross Ice Shelf Geophysical and Glaciological Survey (RIGGS). Survey data included ground-based survey data

and satellite based Global Positioning System (GPS) measurements. Data was selected if it satisfied the following criteria: (1) used GPS data, airborne radar data, and large-scale topographic maps wherever available, (2) used satellite radar altimeter data if slope was less than 0.8 degrees, (3) used the ADD cartographic data for rugged and highly sloped areas, and (4) used satellite radar altimeter data for areas with surface slopes between 0.8 and 1.0 degree (Liu, H., et.al., 1999).

The use of detailed and accurate information from a combination of cartographic data, remotely sensed data, and survey data, enabled the Byrd Polar Research Center to create a DEM using interpolation and merging methods to create an accurate representation of the region. Further improvements could be made using more data sources including digitized topographic maps and radar sensing data.

METHODOLOGIES FOR VEGETATION REMOVAL FROM UNMANNED AERIAL VEHICLE (UAV)-BASED PHOTOGRAMMETRIC DIGITAL SURFACE MODELS

Due to the cost of acquiring and processing LiDAR data for DEM development, the use of unmanned aerial vehicles (UAVs) to acquire digital photos is becoming more common. However, UAV-based point clouds do not represent the bare earth surface as well as LiDAR. This literature review therefore serves to investigate various ground filtering and machine learning methodologies for vegetation identification and removal from UAV-based photogrammetric digital surface models (DSMs) in order to improve DEM accuracy.

The use of UAV-based photogrammetric methods provides a more affordable approach for DEM development. In conjunction with the appropriate ground filtering or machine learning methodology, it can provide researchers with accurate representations of the bare earth for development of land surface and hydrological models. The following provides a summary of a few noteworthy journal papers. The full literature review can be found in Appendix 4.

COMPARING FILTERING TECHNIQUES FOR REMOVING VEGETATION FROM UAV-BASED PHOTOGRAMMETRIC POINT CLOUDS

Anders, N., Valente, J., Masselink, R., & Keesstra, S. (2019). Comparing Filtering Techniques for Removing Vegetation from UAV-Based Photogrammetric Point Clouds. Drones, 3(3), 61.

There are many methods used to process LiDAR-derived point clouds and classify vegetation points, but they are not applicable to point clouds derived with photogrammetry. The use of Structure-from-Motion (SfM) to generate digital elevation models (DEM), which can contain information below dense vegetation unlike aerial images, has increased over time but there has not been a formal comparison of existing methods to determine which is best considering different settings, locations, and DTM applications. Therefore, the goal of this study was to evaluate the performance of different vegetation filtering algorithms for SfM-obtained point clouds. The filtering algorithms evaluated and compared were: color-based filtering using an excessive greenness vegetation index (VI), Triangulated Irregular Networks (TIN) densification from LAStools, the standard method in Agisoft Photoscan, Iterative Surface Lowering (ISL), and a combination of ISL and VI methods.

The study concluded that there was little to no difference between the filtering methods which can be explained by the fact that there was very little vegetation in the study area. For shrub and tree areas, the ISL, VI and TIN methods were concluded to be the best. It was determined that "off the shelf" algorithms are the best for vegetation removal and it is best to use more custom methods such as the TIN densification.

IMAGE CLASSIFICATION-BASED GROUND FILTERING OF POINT CLOUDS EXTRACTED FROM UAV-BASED AERIAL PHOTOS

Yilmaz, V., Konakoglu, B., Serifoglu, C., Gungor, O., & Gökalp, E. (2018). Image classification-based ground filtering of point clouds extracted from UAV-based aerial photos. Geocarto international, 33(3), 310-320.

Due to the cost of acquiring and processing LiDAR data, the use of unmanned aerial vehicles (UAVs) to acquire digital photos is becoming more common. However, UAV-based point clouds do not represent the bare earth surface as well as LiDAR. This study proposes a ground filtering methodology to filter UAV-based point clouds. The support vector machines (SVM) statistical learning theory separates classes with a decision surface (also known as an optimal hyperplane) maximizing the margin between the classes. Data points closest to the decision surface are 'support vectors'. If the classes are linearly separable, then two parallel planes maximizing the margin between the classes are formed and an optimal hyper plane is placed in the middle of these parallel planes. Standard quadratic programming optimization techniques are used to maximize the margin between each class. If the classes cannot be linearly separated, each vector of a class is transformed into another higher dimensional space using a nonlinear transformation to increase the possibility of separating classes with a linear hyperplane.

The ENVI software's SVM classifier was used to classify the orthophoto images taken into six classes: road, building, soil, grass, shadow, and tree; and red, green, and blue bands were used in the process. The classes road, grass, and soil were merged to generate the ground class. The classes building, shadow, and tree were merged to generate the non-ground class. The accuracy of the classified image was calculated with an error matrix and the McNemar test. Then, the classified image was overlapped with the generated point cloud to determine the points corresponding to the non-ground class. The determined non-ground points were then removed. The accuracy of the ground filtering process was determined using the Cohen's Kappa coefficient. The ground points were then interpolated to produce the DEM. To determine the vertical accuracy of the produced DEM, field measurements were conducted in four test sites.

VEGETATION REMOVAL FROM UAV DERIVED DSMS, USING COMBINATION OF RGB AND NIR IMAGERY

Skarlatos, D., & Vlachos, M. (2018). Vegetation removal from UAV derived DSMS, using combination of RGB and NIR imagery.

The focus of this study was to create a detailed Digital Terrain Model (DTM) from drone aerial imagery by automatically filtering the vegetation on the Digital Surface Model (DSM) through standard control point acquisition. The methodology consisted of using NDVI to classify DSM points as vegetation and non-vegetation points, then using the non-vegetation points to create a DTM using interpolation to fill in any gaps that were created from the exclusion of the vegetation points. The high resolution multispectral imagery with 4 channels (red, green, blue,

and near infrared) and a dense DSM were the inputs. According to the study, the most common practice for NDVI calculation is to create two orthophotomosaics, an RGB and a NIR, and calculate the NDVI using the data from each orthophotomosaic. Once this is done, a threshold is defined for the mask creation. The threshold can be defined depending on illumination differences, vegetation type, topographic variations, sensor sensitivity, epoch, leaf coverage, etc. A low NDVI threshold can mask out valid ground points whereas a high threshold will include vegetation points and therefore worsen the accuracy. This study used a threshold of 0.09. Next, an interpolation algorithm was applied to fill in any gaps caused by the removal of vegetation points.

The study concluded that incorporation of NIR imagery to eliminate vegetation from a DSM can increase the DTM's accuracy. This method can produce DTMs that describe the terrain well enough to act as an alternative option when LiDAR is not available. The quality of results depends on various factors such as morphology, density, area covered by vegetation, the NDVI threshold, and the interpolation method used.

COMPARISON OF THE PERFORMANCES OF GROUND FILTERING ALGORITHMS AND DTM GENERATION FROM A UAV-BASED POINT CLOUD

Serifoglu Yilmaz, C., & Gungor, O. (2018). Comparison of the performances of ground filtering algorithms and DTM generation from a UAV-based point cloud. Geocarto international, 33(5), 522-537.

Compared to LiDAR technology, Unmanned Aerial Vehicles (UAVs) are much less costly and easier to use. This study evaluated five widely used ground filtering algorithms: Progressive Morphological (PM) 1D/2D, Maximum Local Slope (MLS), Elevation Threshold with Expand Window, and Adaptive TIN. This study used ALDPAT v.1.0 software to test the algorithms.

The accuracy of the filtering results was tested quantitatively and qualitatively. Qualitatively, results were analyzed visually and was done by overlapping the filtered point cloud with the produced high resolution orthophoto image. Quantitatively, the test points were selected randomly from the unfiltered point cloud of each of the raw, low-density, medium-density and high-density data. Then, the filtered point cloud, test points, and orthophoto were overlapped to visually evaluate

The MLS algorithm was found to be the one most affected by increase in point density but had the worst performance when filtering medium-density and high-density data. It is better to use the MLS algorithm to filter the sparse point clouds. The PM2D algorithm performed better than the PM1D algorithm, but the performances of the algorithms are close as the point density increases. Considering the total error and chi-squared values, the ATIN algorithm was found to be the most accurate and can be used to filter the point clouds with high densities. Because the ATIN algorithm was found to be the most successful algorithm, the ATIN result was used to interpolate the DTM. The filtered point cloud contained 1,284,763 points and the study area covered 72,980 m^2 which resulted in a spatial resolution of 25 cm for the DTM.

To test the accuracy of the produced DTM, test points were established within the study area. A total of 87 test points were established for flat areas (test site 1), 163 test points for sloping areas (test site 2), and 128 test points for areas close to above ground objects (test site 3). The Real Time Kinematik (RTK) GPS technique was used to measure positions of all test points. Root

Mean Square Error (RMSE), Standard Deviation of Residuals (SDR), Mean Absolute Error (MAE), and Mean Error (ME) were calculated for each test site by using the measured elevation of the test points and their corresponding elevations on the DTM.

METHODOLOGIES FOR VEGETATION IDENTIFICATION FROM UNMANNED AERIAL VEHICLES (UAV)-BASED PHOTOGRAMMETRIC DIGITAL SURFACE MODEL USING MACHINE LEARNING

UAVs AND MACHINE LEARNIG REVOLUTIONISING INVASIVE GRASS AND VEGETATION SURVEYS IN REMOTE ARID LANDS

Sandino, J., Gonzalez, F., Mengersen, K., & Gaston, K. J. (2018). UAVs and machine learning revolutionising invasive grass and vegetation surveys in remote arid lands. Sensors, 18(2), 605.

The goal of this study was to delineate a process to detect and create a pixel-wise segmentation of invasive grasses in Cape Range National Park, Australia. It involved the use of unmanned aerial vehicles (UAVs) equipped with high-resolution RGB cameras and a data processing approach using machine learning algorithms. The accuracy and segmentation indicators served to validate the methodology to map vegetation. Any observed misclassification of buffel and spinifex grasses were the result of human error when the sample data was first labeled. The proposed methodology showed detection rates of 96.75% and 96% for single mapping of buffel grass and spinifex, respectively, and a multiclass detection rate of 96.54%. Invasive grasses were accurately detected at different spatial concentrations with a GSD of 1.015 cm per pixel. Moving forward, work will be focused on implementing unsupervised and supervised methods for labeling vegetation to reduce processing times.

MULTI-FEATURE MACHINE LEARNING MODEL FOR AUTOMATIC SEGMENTATION OF GREEN FRACTIONAL VEGETATION COVER FOT HIGH-THROUGHPUT FIELD PHENOTYPING

Sadeghi-Tehran, P., Virlet, N., Sabermanesh, K., & Hawkesford, M. J. (2017). Multi-feature machine learning model for automatic segmentation of green fractional vegetation cover for high-throughput field phenotyping. Plant methods, 13(1), 103.

Accurate vegetation segmentation from the background in digital images is a fundamental and challenging task in phenotyping. Digital RGB cameras are most commonly used for field phenotyping because they are affordable and portable in size. This study proposed a multi-feature learning method to quantify vegetation growth. The proposed machine learning method involved the acquisition of digital images in time series, extraction of multi-feature color transformation, a supervised classification model to label pixels as foreground or background, and noise reduction using median filtering. The proposed method was then compared with other state of the art methods with the following criteria: (1) comparison with ground-truth images, (2) variation along a day with changes in ambient lighting, (3) comparison with manual measurements, (4) an estimation of performance along the full life cycle of a wheat canopy.

OBJECT-BASED VEGETATION MAPPING IN THE KISSIMMEE RIVER WATERSHED USING HYMAP DATA AND MACHINE LEARNING TECHNIQUES

Zhang, C., & Xie, Z. (2013). Object-based vegetation mapping in the Kissimmee River watershed using HyMap data and machine learning techniques. Wetlands, 33(2), 233-244.

This study, based on the Kissimmee River watershed, evaluated the applicability of fine spatial resolution hyperspectral data collected from the HyMap sensor for both the community and species level vegetation mapping. Vegetation maps were produced using machine learning methods, Support Vector Machines (SVM) and Random Forest (RF), object based image analysis techniques, and Minimum Noise Fraction (MNF) data transformation. The South Florida Water Management District (SFWMD) provided the hyperspectral data and field data for the study. The accuracy of the object based vegetation maps was compared using an error matrix and calculating a Kappa statistic. The Kappa statistic serves to describe the proportion of correctly classified validation sample after random agreement is removed. The non-parametric McNemar test was used to evaluate the statistical significance of differences in accuracy between different classifications. A significant statistical difference has a 95% confidence level and a z-score larger than 1.96 which is calculated from the McNemar test. There was an overall accuracy of 90% for community-level mapping and an 85% accuracy of discriminating 55 species. By doing a minimum noise fraction (MNF) on the data, it removes inherent noise in the hyperspectral data, improves classification accuracy, and reduces the data dimensionality to decrease computational cost. This study concluded that SVM and RF were sensitive to the number of training data and can be the result of high spatial and spectral heterogeneity of the study area. It was also concluded that the number of classes decreased accuracy.

METHODS FOR EXTRACTING SIGNIFICANT TOPOGRAPHICAL FEATURES (SINK HOLES) FROM DEMS

During FIU Performance Year 9, research was also conducted on various methods of identifying sinkholes through automated processes such as the use of GIS tools. The literature findings have shown the use of statistical methods, aerial images, and a combination of both. The following provides a summary of a few noteworthy journal papers arranged in chronological order, with the more recent techniques first. The full literature review can be found in Appendix 3.

SINKHOLE SUSCEPTIBILITY HAZARD ZONES USING GIS AND ANALYTICAL HIERARCHICAL PROCESS A CASE STUDY OF KUALA LUMPUR AND AMPANG JAYA

Rosdi, M. A. H. M., Othman, A. N., Abdul, M. A. M. Z. Z., & Yusoff, Z. M. (2017). Sinkhole Susceptibility Hazard Zones Using GIS and Analytical Hierarchical Process (AHP): A Case Study of Kuala Lumpur and Ampang Jaya. International Archives of the Photogrammetry, Remote Sensing & Spatial Information Sciences, 42.

In this study, based in Kuala Lompur and Ampang Jaya, there has been an increase in sinkhole incidents that have posed a serious threat to human lives and infrastructure. A Sinkhole Hazard Model (SHM) was generated with integration of a GIS framework by applying an Analytical Hierarchical Process (AHP) technique in order to produce a sinkhole susceptibility hazard map for the area. Five consecutive parameters for main criteria each categorized by five sub classes were selected for this research: (1) Lithology (LT), (2) Groundwater Level Decline (WLD), (3)

Soil Type (ST), (4) Land Use (LU), and (5) Proximity to Groundwater Wells (PG). A set of relative weights were assigned to each inducing factor and computed through a pairwise comparison matrix derived from expert judgement. Lithology and Groundwater Level Decline were identified to give the highest impact to sinkhole development.

AUTOMATIC DELINEATION OF KARST SINKHOLES

Wu, Q., Deng, C., & Chen, Z. (2016). Automated delineation of karst sinkholes from LiDAR-derived digital elevation models. Geomorphology, 266, 1-10.

In this study, a localized contour tree method for automated extraction of sinkholes was presented. According to this study, previous methods for identification depended on visual interpretation of low resolution topographic maps provided by USGS, aerial images, and on the field research. Similar studies have used LiDAR data to identify sinkholes as well but with different processing methods, such as applying a sink filling method on LiDAR data to create a depressionless DEM and then subtracting the original DEM from the modified DEM to locate depressions. This layer was then processed with different thresholds of elevation differences to locate sinkholes. Other methods included image filtering techniques with kernel windows using focal functions and the "active" contour approach, which delineates sinkhole boundaries based on changes in the flow of the elevation gradient in the surrounding region around the local minima at potential sinkhole locations.

In this study, once the smoothed DEM was created, they generated vector contours by setting the base contour to be 39 m and the contour interval to be 0.5 m, which is slightly higher than the vertical accuracy of the LiDAR DEM. The contour tree method was then applied to the contours to identify depressions. A minimum depression area of 100 m^2 and minimum depression of 0.5 m were used in order to identify sinkholes larger than 100 m^2 and deeper than 0.5 m.

The method proposed in this study is said to have improved the sinkhole inventory by detecting non-inventoried sinkholes, identifying already inventoried sinkholes, delineating sinkhole boundaries, and characterizing sinkhole morphometric properties. Three times as many sinkholes were identified compared to the already identified sinkholes. According to the study, an ArcGIS toolbox referred to as the Sinkhole Extraction Analyst tool was created and will be freely available for the public to download in the near future.

KARST FEATURES DETECTION AND MAPPING USING AIRPHOTOS, DSMs, AND GIS TECHNIQUES

Kakavas, M. P., Nikolakopoulos, K. G., & Zagana, E. (2015, October). Karst features detection and mapping using airphotos, DSMs and GIS techniques. In Earth Resources and Environmental Remote Sensing/GIS Applications VI (Vol. 9644, p. 96440Y). International Society for Optics and Photonics.

In this study, thirty seven aerial photographs of the study area in Aitoloakarnania Prefecture, Western Greece at 1/40,000 scale from the Hellenic Military Geographical Service were obtained and processed to create a mosaic. An orthophoto mosaic with a spatial resolution of 1 m and the respective DSM were derived. Four DEMs were used to identify limestone terrain, describe exokarst features, analyze karst depressions, and detect geological structures that are

important to karst development. The first DEM used was the Aster GDEM that was developed by the Ministry of Economy, Trade, and Industry (METI) of Japan and NASA. A Shuttle Radar Topographic Mission (SRTM) DEM was also used with a resolution of 90 m at the equator and also provided in mosaiced 5 deg x 5 deg tiles for easy download and use. The third DEM used was a DSM created for the Greek Cadastral from aerial imagery with a 5 m resolution and vertical accuracy of 2-3 m. The fourth DEM used was created from digitized contours from 1/50,000 topographic maps with a 20 m pixel size and a vertical accuracy of 10 m.

Initially, the detection and mapping of geologic structures important to karst development was conducted using aerial photo stereo pairs which led to the digitization of 277 karst features that were tested via in situ observation. Next, closed karst features were identified in ArcGIS through the "cut fill" command and the points where there was a reduction of elevation were then converted to polygons and considered representative of "possible" karst features. Finally, through the intersection of data, the "possible" karst features were compared to the digitized karst characteristics from aerial photos.

KARST DEPRESSION DETECTION USING ASTER, ALOS/PRISM AND SRTM-DERIVED DIGITAL ELEVATION MODELS IN THE BAMBU iGROUP, BRAZIL

de Carvalho, O., Guimarães, R., Montgomery, D., Gillespie, A., Trancoso Gomes, R., de Souza Martins, É., & Silva, N. (2014). Karst depression detection using ASTER, ALOS/PRISM and SRTM-derived digital elevation models in the Bambuí Group, Brazil. Remote Sensing, 6(1), 330-351.

This study investigated the use of ASTER-,SRTM, and ALOS/PRISM derived DEMs to detect natural karst depressions along the Sao Francisco River near Barreiras city, northeast Brazil. Depressions were identified by the following steps: (1) acquiring DEM; (2) sink-depth calculation using the difference between the raw DEM and the corresponding DEM with sinks filled; and (3) eliminating falsely identified karst depressions using morphometric attributes. The methodology included using the Fill Sink tool in ArcMap, extracting the sink depths in the area and subtracting the maps between the sink filled "depressionless" DEM and the original DEM. The depressed areas were given a value of 1 and the remaining areas a value of 0. This binary image was then converted to vector format. The minimum area of depressions corresponded to the spatial resolution of the sensor; however, the polygons depicted natural features as well as pits from surface imperfections. The vectors created therefore had to be further analyzed by defining criteria to separate the dolines from non-depressions. The delimitation of the non-depressions were derived from threshold values of morphometric attributes, specifically depth, size, and shape. Evaluation of the appropriate threshold values was obtained by comparing maps of already identified dolines with previous mapping of dolines from field validation and interpretation of higher spatial resolution imagery (such as ALOS-PRISM and Google Earth images). Karst features in the area were easily identified through visual interpretation because the area is characterized by natural moist grassy vegetation where the water table approaches the surface for part of the year. A range of different threshold values were used for the minimum sink depth to identify the best threshold value from the maximum accuracy index between manual and automated classification. Identification of true sinkholes was assessed with the intersection of reference and classified polygons.

REMOTE SENSING AND GIS CONTRIBUTION TO THE INVESTIGATION OF KARST LANDSCAPES IN NW-MOROCCO

Theilen-Willige, B., Malek, H., Charif, A., El Bchari, F., & Chaïbi, M. (2014). Remote sensing and GIS contribution to the investigation of karst landscapes in NW-Morocco. Geosciences, 4(2), 50-72.

The goal of this study was to investigate the use of different satellite data, like Landsat, RapidEye, and IKONOS imagery, as well as ASTER- and SRTM-derived digital elevation models (DEMs) for the analysis of karst features. Dolines were identified by visual interpretations based on high resolution images and aerial photographs. Digital image processing of the satellite data was useful to identify areas with higher surface water input, where karstification processes might be more intense than in surrounding areas. ArcGIS tools were used for this purpose by aggregating morphometric, causal factors (lowest and flattest areas) influencing the susceptibility to higher surface water input. Lineament analysis based on different satellite data contributed to the detection of near surface fault and fracture zones with potential for dissolution in subterranean waterways.

When searching for areas that are susceptible to karst processes, causal factors were taken into account, including slope gradient, curvature, lithology, or groundwater table level. Some of the causal factors could be determined from height level maps, slope gradient maps, curvature maps, and the drop raster which is calculated as the difference in the z-value divided by the path between the cell centers.

To visualize these areas, the weighted overlay approach integrated in ArcGIS was used for identification of endangered lowland areas that are susceptible to increased surface water input and possibly flooding due to their disposition by aggregating the causal factors. The susceptibility is calculated by adding every layer with a weighted influence (for example, a slope degree $<10^{o}$:30%, lowest local height level: 30%, drop raster: 30%, curvature $=0$::10%) together and summing all layers. The sum, which can be included into GIS, provides some information on the susceptibility to surface water input and thus, on areas prone to more intense karstification processes. The resulting maps are divided into susceptibility classes which range from 0 to 6, where 6 is the strongest assumed susceptibility to surface water input due to aggregation and summation of causal, morphometric factors in the area. The study basically identified dolines and/or sinkholes through the use of GIS and remote sensing processing tools on satellite imagery and validation through field observation.

PREDICTING SINKHOLE SUSCEPTIBILITY IN FREDERICK VALLEY, MARYLAND USING GEOGRAPHICALLY WEIGHTED REGRESSION

Doctor, K. Z., Doctor, D. H., Kronenfeld, B., Wong, D. W. S., & Brezinski, D. K. (2008). Predicting Sinkhole Susceptibility in Frederick Valley, Maryland Using Geographically Weighted Regression. 41003(September), 243–256. https://doi.org/10.1061/41003(327)24

In this study, 556 identified sinkholes were analyzed to understand the likelihood of a sinkhole to form in a specific area. Characteristic features considered for predicting the density of sinkholes included clustering of sinkholes, geologic structure, rock type, and the sinkhole proximity to

quarries, water bodies, streams, roads, faults, axes of synclines or anticlines, and depth to groundwater. The spatial statistical analysis methods used were K-function, Geographically Weighted Regression (GWR), and Inverse Distance Interpolation. After applying these functions, it was concluded that the proximity to the groundwater table, proximity to fold axes, proximity to faults, and proximity to quarries were the significant factors that greatly influence the formation of sinkholes.

AN EVALUATION OF AUTOMATED GIS TOOLS FOR DELINEATING KARST SINKHOLES AND CLOSED DEPRESSIONS FROM 1-METER LIDAR-DERIVED DIGITAL ELEVATION DATA

Doctor, D. H., & Young, J. A. (2013). An evaluation of automated GIS tools for delineating karst sinkholes and closed depressions from 1-meter LiDAR-derived digital elevation data. 13th Multidisciplinary Conference on Sinkholes and the Engineering and Environmental Impacts of Karst, 449–458. Retrieved from

https://scholarcommons.usf.edu/cgi/viewcontent.cgi?referer=https://www.ecosia.org/&httpsredir =1&article=1156&context=sinkhole_2013

In this study, one way of identifying sinkholes was identified using tools integrated into ArcGIS. This involved three steps: 1) filling in sinks to their spill level, 2) determining the flow direction within each pixel once the sinks in the DEM are filled, and 3) determining the flow accumulation of each pixel in the elevation model. The first step in the process (which has already been tested by FIU) was to use the Fill tool in ArcMap, which results in a new elevation surface with all sinks filled to their spill elevation. The process is repeated until all the pixels within the depression are filled and depressions spill over, removing all natural depressions. Poppenga et al. (2011) suggested using a threshold area of depressions specifically for drainage greater than or equal to 1,000 square meters and depth greater than or equal to 1 meter and greater than 0.5 standard deviation of the difference grid. This threshold, however, could result in exclusion of a number of depression artifacts.

The resulting polygon layer represents the possible sinks from the fill-difference layer that was created during the geoprocessing procedure based on the accuracy of the downloaded DEM. To refine the polygons and classify the ones that are true depressions (and possible sinkholes), a training polygon feature class of known depressions that have been identified in the field and outlined from the LiDAR data is required for comparison. For FIU to employ this method, a manually delineated spatial dataset will be required. FIU has reached out to DOE collaborators to determine if this data is available. The study's results revealed that this semi-automated method using LiDAR and aerial photos captured 99.5% of the depressions delineated in the manually created dataset.

Subtask 6.1: Conclusions and Future Work

FIU has conducted a literature review to determine an appropriate methodology for development of a high resolution (1-m or sub-meter) DEM which will ultimately serve as the stepping stone for development of a regional land surface model of the WIPP site and surrounding basins. Methods to develop a high resolution DEM included the use of Geographic Information Systems

(GIS), Google Earth, LiDAR, and different interpolation algorithms. Of the methods investigated, a photogrammetric approach using Unmanned Aerial Vehicles (UAVs) is likely the most appropriate for FIU's research considering its affordability, flexibility, and ease of implementation in areas with limited site accessibility. Due to the cost of acquiring and processing LiDAR data for DEM development, the use of unmanned aerial vehicles (UAVs) to acquire digital photos will be considered. The only setback with photogrammetry is that the images acquired by UAVs do not accurately represent the bare earth surface due to the presence of vegetation. A literature review was therefore also conducted to evaluate methods to identify and remove vegetation from UAV-based photogrammetric point clouds. Machine learning, as of recent, has been used to identify vegetation for the purpose of quantifying vegetation growth as well as for the removal process. Machine learning methods included various classification algorithms such as Support Vector Machines (SVM), and Random Forest, object based image analysis techniques, and Minimum Noise Fraction (MNF) data transformation. Once vegetation has been identified, applicable vegetation removal methods can be applied which include color-based filtering using an excessive greenness vegetation index (VI), Triangulated Irregular Networks (TIN) densification from LAStools, the standard method in Agisoft Photoscan, Iterative Surface Lowering (ISL), a combination of ISL and VI methods, a normalized difference vegetation index (NDVI) and additional algorithms. FIU will determine the most appropriate method to be used based on funding resources, equipment and software availability, and site accessibility.

Once the DEM is created, post processing actions for extracting features of interest, such as sinkholes, will be implemented. The methods found in the literature for delineating and extracting sinkholes include developing an analytical hierarchical process, a localized contour tree method, GIS processes, and implementing statistical approaches. Coupling of the LSM with the ASCEM GWMs will enable more accurate predictions of groundwater flow patterns in the WIPP region. With improved estimates of the spatial and temporal patterns of recharge, predictions of halite dissolution and propagation of the shallow dissolution front will be made possible and the potential impact on repository performance quantified.

Based on the reviews conducted during FIU Performance Year 9, FIU plans to conduct a pilot study in Year 10 to: (1) capture high resolution aerial imagery of a representative basin of the WIPP site, such as Basin 6 in the Nash Draw, using a UAV equipped with a GPS and way-point tracking ability; (2) process the aerial images collected using photogrammetric techniques to build a high resolution DEM; and (3) utilize the developed DEM to delineate and extract topographical features such as drainage basins, brine lakes, channels, sink holes, discharge points and other relevant hydrological features.

The first step will be to use a UAV to capture high resolution imagery of a representative basin at the WIPP site, such as Basin 6 in the Nash Draw, which has the Laguna Cinco brine lake, sink holes, a spring, and evidence of return flow. Utilization of UAVs for aerial surveying is very cost effective in comparison to traditional methods with manned aircraft and can achieve equivalent sub-meter resolution. Equipped with a GPS and way-point tracking ability, UAV aerial surveys can also be automated to rapidly cover large land areas and infrastructure with minimal supervision. Image processing using state-of-the-art photogrammetric techniques will then be conducted to build a high resolution DEM which will enable more accurate delineation of the ground surface topography and local features and facilitate future creation of spatially-distributed

soil and vegetation classes. FIU will utilize a selected open-source LSM, the delineated features and other relevant hydrological data collected in FIU Performance Year 9 to initiate development of a LSM of Basin 6 in the Nash Draw area. In the future, this LSM will be used to force the ASCEM GWMs to predict groundwater flow patterns. The spatial distribution of recharge, and groundwater flow rates and directions will be used to estimate the rate of halite dissolution and the rate of propagation of the shallow dissolution front, both of which have the potential to affect post-closure repository performance.

The pilot study will serve as proof of concept that the proposed methodology is feasible and has practical applications at WIPP to generate high-resolution imagery for development of a DEM, which is essential for detailed delineation of hydrologic basins within and surrounding the WIPP LWA boundary. FIU will train undergraduate and graduate students (DOE Fellows) on UAV photogrammetry methods and provide mentorship and field experience through student summer internships in collaboration with CBFO and PNNL scientists.

Subtask 6.2: WIPP Hydrologic Database Development

Subtask 6.2: Introduction

Geographic Information System (GIS)-based hydrological models provide a foundation for management, storage, processing, analysis and visualization of environmental and hydrological parameters. This task involves the creation of a GIS-based hydrologic database (geodatabase) to store spatial and temporal data required for development of the land surface and groundwater models of the WIPP and surrounding region. The proposed geodatabase possesses a spatial relational database management system (RDBMS) schema and relationship structure primarily based on the ArcHydro data model that is specific to hydrologic systems. This makes it a significant tool when conducting contaminant flow and transport analyses that require large amounts of high-quality spatial and temporal data in order to ensure reliability and validity of modeling results. ArcGIS tools significantly reduce the time needed for data preparation and improve overall efficiency by automating and batch processing model-specific geospatial and timeseries data via the development and implementation of process flow models. Utilization of the ArcGIS platform will continue to provide ARC researchers with a basis for management and geoprocessing of model configuration parameters, documenting process workflows, conducting geospatial analyses and visualization of model results. In addition, the hydrologic geodatabase infrastructure makes it scalable and replicable.

Subtask 6.2: Objectives

This subtask will provide information to support the development of the selected land surface model (LSM) and ASCEM groundwater model (GWM) of the WIPP study area. FIU will develop a WIPP Hydrologic Database which will be comprised of both surface hydrologic and subsurface hydrogeologic data parameters.

Subtask 6.2: Methodology

As the first steps towards developing a comprehensive WIPP hydrologic database, FIU's goal was to:

- Perform a comprehensive literature review for existing site characterization information.

- Perform data mining to acquire existing spatial and temporal data for the site. A search of readily available data from federal, state and local online resources will be conducted. FIU will also work with the research collaborators and site contacts to acquire additional data that may be available outside of the online resources. All collected information/data will be consolidated into a central repository.
- Determine the database framework required for use with the selected LSM, identify the appropriate database platform, and perform preliminary development of the database infrastructure.
- Determine the database framework required for use with ASCEM, identify the appropriate database platform, and perform preliminary development of the database infrastructure.

Subtask 6.2: Results and Discussion

FIU initiated the development of the comprehensive WIPP hydrologic database by going through a data mining process to acquire existing spatial and temporal data for the site. A search was conducted for readily available spatial data from federal, state and local online resources including:

- USGS National Hydrography Dataset (NHD), https://www.usgs.gov/core-science-systems/ngp/national-hydrography
- USGS National Map Viewer, https://viewer.nationalmap.gov/advanced-viewer/
- USGS New Mexico geologic map data - Mineral Resources Online Spatial Data, https://mrdata.usgs.gov/mrds/
- Multi-Resolution Land Cover Characteristics (MRLC) Consortium National Land Cover Database (NLCD) 2016, https://www.mrlc.gov/national-land-cover-database-nlcd-2016
- USDA Natural Resources Conservation Service (NRCS) Web Soil Survey, https://websoilsurvey.sc.egov.usda.gov/App/WebSoilSurvey.aspx
- USDA Forest Service, Forest Inventory and Analysis National Program, FIA Data Mart, https://apps.fs.usda.gov/fia/datamart/datamart.html
- New Mexico Department of Transportation (NM DOT) Map Portal, https://nmdot.maps.arcgis.com/home/index.html
- US DOT Federal Highway Administration (FHWA) National Bridge Inventory (NBI), https://www.fhwa.dot.gov/bridge/nbi.cfm
- New Mexico Environment Department (NMED) OpenEnviroMap, https://gis.web.env.nm.gov/oem/?map=egis
- New Mexico Bureau of Geology & Mineral Resources Geologic Mapping Program Open-File Geologic Map (OF-GM) Series, https://geoinfo.nmt.edu/publications/maps/geologic/ofgm/home.cfml
- RGIS Data Portal, http://rgis.unm.edu/rgis6/

Several geospatial files were downloaded which had varying spatial extents, either encompassing Eddy and Leo counties of New Mexico, or the entire NM state and include the following:

- Populated places (cities, towns, etc.)

- Bridges and dams
- Roads
- Flowlines (rivers/streams)
- Waterbodies
- Watersheds
- State and county boundaries
- Soil Map Units
- Vegetation
- Land cove/Land use (2011)
- Geologic formations
- Statewide digital elevation model (DEM), 60m
- Digital orthophotography

Some of the downloaded GIS data and imagery can be viewed in the images below.

Figure 69. Digital orthophoto of an area in Eddy County, NM near the WIPP facility.

Figure 70. Statewide DEM (60m) zoomed into Eddy and Lea counties, NM.
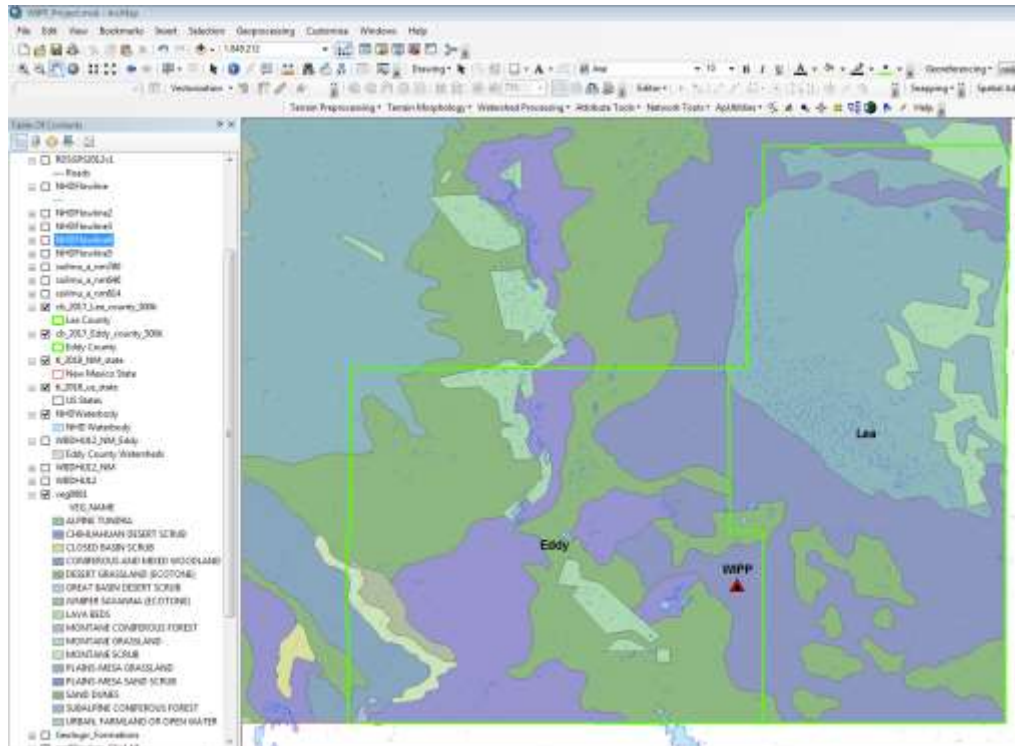
Figure 71. NM vegetation map of the area surrounding Eddy and Lea counties.
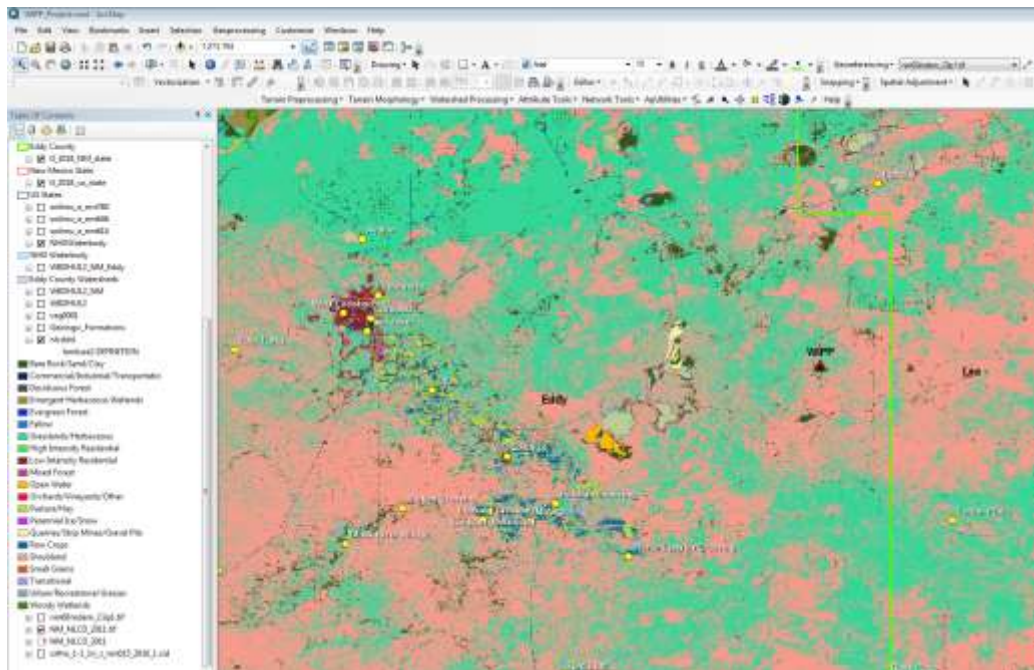
Figure 72. Land cover map of the area surrounding Eddy and Lea counties, NM.
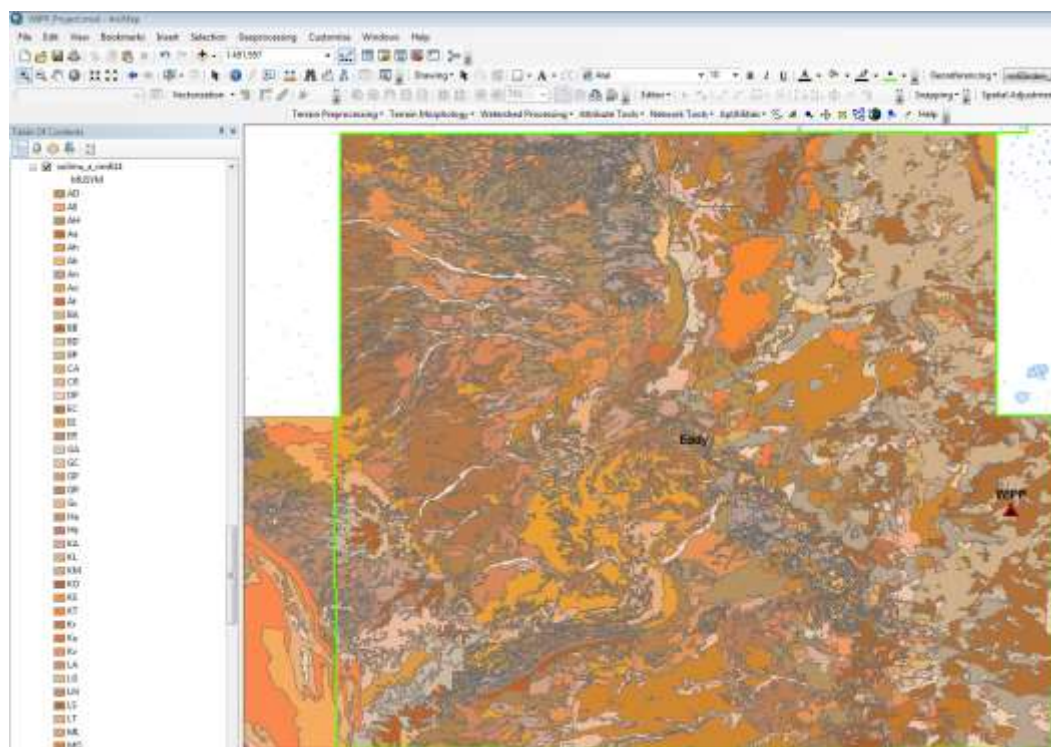
Figure 73. Soil map units in Eddy County, NM.

During FIU's preliminary search, a 60 m resolution digital elevation model (DEM) was donwloaded, however, upon further investigation, 1/3rd arc-second (approx. 10 m) DEMs were found from the publicly accessible USGS National Map 3D Elevation Program (3DEP) downloadable data collection. Currently, 1 m resolution DEMs are also available for certain parts

of the US through the 3DEP, however, data is not yet available at this resolution for the WIPP surrounding region. In May 2019, DOE Fellow Gisselle Gutierrez downloaded 1 m DEM data derived from LiDAR and 10 m DEM data derived from topography for the state of New Mexico to support the work being conducted under Subtask 6.1 which involves a method of sinkhole extraction from 1-meter LiDAR-derived digital elevation data. Gisselle was trained by Dr. Zhou on the use of Python scripts to automate the data download process and reduce the overall timeframe for this exercise. FIU is now in the process of searching for relevant geospatial data that are characteristic of areas where sinkholes tend to occur in order to conduct a geographic statistical analysis based on methods derived from FIU's literature review. The data will also be used for an evaluation of various sinkhole extraction methods using high resolution DEMs derived from recent peer reviewed journal papers. Gutierrez also downloaded updated vegetation and soil data for the New Mexico region with the latest versions released by the USGS and USDA. This data will be used in the land surface model to be developed in the next year.

Subtask 6.2: Conclusions and Future Work

FIU has created an ArcGIS file geodatabase and has imported the downloaded files to create a central repository for future use. Once a defined study area has been established, the data will be processed and clipped to the established spatial extent. FIU will also work with the research collaborators and site contacts to identify the knowledge gaps with respect to the WIPP region's land surface hydrology and gather relevant background information and additional data that may be available outside of the online resources.

Subtask 6.3: ASCEM GWM and LSM Training

Subtask 6.3: Introduction

This subtask involves training of FIU personnel and students on the use of the ASCEM modeling toolset. This task will also focus on understanding the requirements for coupling a state-of-the-art LSM with a variably saturated ASCEM GWM. In order to address the priorities of the EM Office of Technology Innovation and Development (OTID), the Groundwater and Soil Remediation (GW&S) program developed the Advanced Simulation Capability for Environmental Management (ASCEM). ASCEM is an open source processed based computational framework for prediction of contaminant fate and transport in natural and engineered systems across DOE sites. The use of this integrated program is expected to improve the remediation efficacy and decrease overall cleanup costs. FIU intends to use the ASCEM groundwater-basin model to assist DOE-EM improve the current understanding of regional and local groundwater flow at the WIPP site, compute the water balance, and derive estimates of groundwater recharge in the post-closure phase. Currently, ASCEM is unable to account for land surface hydrology, which is essential for computing the water balance. The proposed work will therefore require coupling of a state-of-the-art open-source land surface model (LSM) with the groundwater models (GWMs) within the ASCEM toolbox to simulate three-dimensional, unsaturated and saturated water flow.

Subtask 6.3: Objectives

The objective of this subtask was to provide training of FIU personnel and students on the use of the ASCEM modeling toolset so that a groundwater-basin model can be developed to assist DOE-EM improve the current understanding of regional and local groundwater flow at the WIPP

site, compute the water balance, and derive estimates of groundwater recharge in the post-closure phase.

Subtask 6.3: Methodology

The intent for the first year of this task was for FIU personnel and students to receive training on the use of the ASCEM modeling toolset. This training was to be coordinated with the DOE ASCEM team in the form of a workshop to begin learning how to use the ASCEM code as well as become familiar with the publicly available graphical user interface (GUI), and research existing case studies where ASCEM has been implemented at DOE sites to determine the best practices and lessons learned for implementing this modeling toolset. For circumstances beyond FIU's control, the training was not conducted during FIU Year 9. Based on recent notification, PNNL and Carlsbad Field Office are projecting to conduct the course during the 2nd or 3rd quarter of FIU Year 10.

Subtask 6.3: Results and Discussion

In April 2019, FIU downloaded the publicly available AKUNA graphical user interface (GUI) for accessing the ASCEM code in preparation for the training that was planned for May 2019. The training was to include research of existing case studies where ASCEM has been implemented at DOE sites to determine the best practices and lessons learned for implementing this modeling toolset. However, in May, after discussion with collaborators at PNNL, it was agreed for FIU to postpone the training on the ACSEM modeling toolset. Authorization for funding to prepare the short course was delayed, leaving insufficient time for preparation by the scheduled date of 5/17/2019. A new projected completion date for this training is still to be determined based on the availability of funding and the ASCEM development team. PNNL collaborators have indicated that moving the ASCEM training may also be of benefit to minimize the gap between the training and the actual model development/implementation in the next performance year. In the meantime, the FIU team requested credentials to access the ASCEM code through the AKUNA GUI and began familiarizing themselves with the interface by using the online tutorials provided.

FIU also began a review of candidate land surface models. The first model reviewed was the Community Land Model (CLM5) model, which was developed as a collaborative project between the Terrestrial Sciences Section (TSS) and the Climate and Global Dynamics Division (CGD) at the National Center for Atmospheric Research (NCAR) and the CESM Land Model and Biogeochemistry Working Groups. CLM5 is focused on examining the land surface that is being affected by climate change and thereby affecting society and ecosystems. This model was developed to represent many land surface aspects such as surface heterogeneity, land biogeophysics, the hydrological cycle, biogeochemistry, human dimensions, ecosystem dynamics and other processes including:

- Vegetation composition, structure, and phenology
- Absorption, reflection, and transmittance of solar radiation
- Absorption and emission of longwave radiation
- Momentum, sensible heat (ground and canopy), and latent heat (ground evaporation, canopy evaporation, transpiration) fluxes
- Heat transfer in soil and snow including phase change
- Canopy hydrology (interception, throughfall, and drip)

- Snow hydrology (snow accumulation and melt, compaction, water transfer between snow layers)
- Soil hydrology (surface runoff, infiltration, redistribution of water within the column, subsurface drainage, groundwater)
- Plant hydrodynamics
- Stomatal physiology and photosynthesis
- Lake temperatures and fluxes
- Dust deposition and fluxes
- Routing of runoff from rivers to ocean
- Volatile organic compounds emissions
- Urban energy balance and climate
- Carbon-nitrogen cycling
- Dynamic land cover change
- Land management including crops and crop management and wood harvest
- Ecosystem Demography (FATES, optional)

DOE Fellow Gisselle Gutierrez spent time reviewing various online tutorials and learning how to use GitHub and GitBash to edit and view CLM model results. Although CLM was reviewed, FIU will likely not use this model due to is strong emphasis on vegetation composition and its significant contribution to ecological climatology, which is an interdisciplinary framework to understand how natural and human changes in vegetation affect climate. The WIPP region and the proposed pilot study area, Basin 6, are very sparsely vegetated and as such it was deemed appropriate to investigate other land surface models more compatible for the terrain being studied.

In September 2019, FIU began reviewing the Weather Research and Forecasting Model Hydrological modeling system (WRF-Hydro), which is an open-source community model used for flash flood prediction, regional hydroclimate impacts assessment, seasonal forecasting of water resources, and land-atmosphere coupling studies. The WRF-Hydro system has been serving as the core model for the new National Water Model. Below is a snapshot taken from the NCAR/UCAR Research Applications Laboratory (RAL) website as an example of the WRF-Hydro output of accumulated precipitation (shaded colors) and associated gridded streamflow (points) for the Colorado flood of September 11-15, 2013, which is extremely useful in providing the locations and timing of rapid river stage increase as well as the duration of high waters and inundation during major precipitation events, and can have significant contribution to the proposed hydrology modeling efforts at the WIPP.
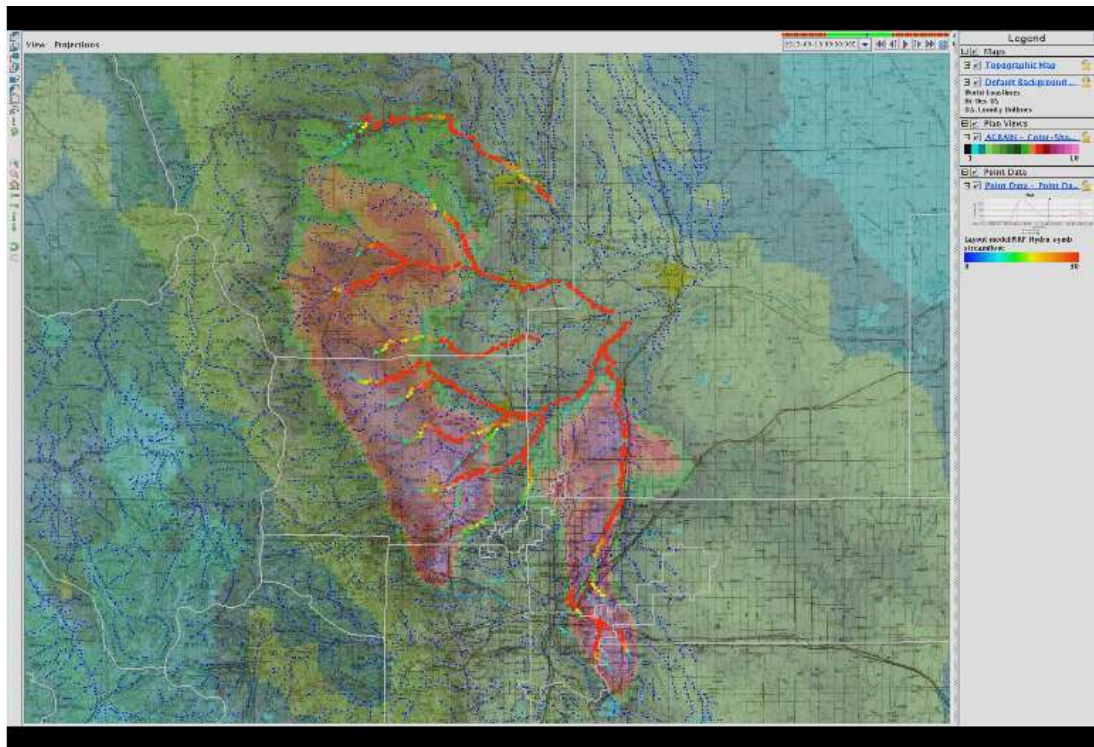
Figure 74. WRF-Hydro output for the Colorado flood of 11-15 Sept. 2013.
(https://ral.ucar.edu/projects/wrf_hydro/overview).

The WRF-Hydro modeling system also has a coupling framework designed to link multi-scale atmospheric and terrestrial hydrologic process models. This infrastructure provides multi-scale and multi-physics land-atmosphere modeling capability for conservative, coupled and uncoupled assimilation and prediction of major water cycle components such as precipitation, soil moisture, snow pack, ground water, streamflow, and inundation.
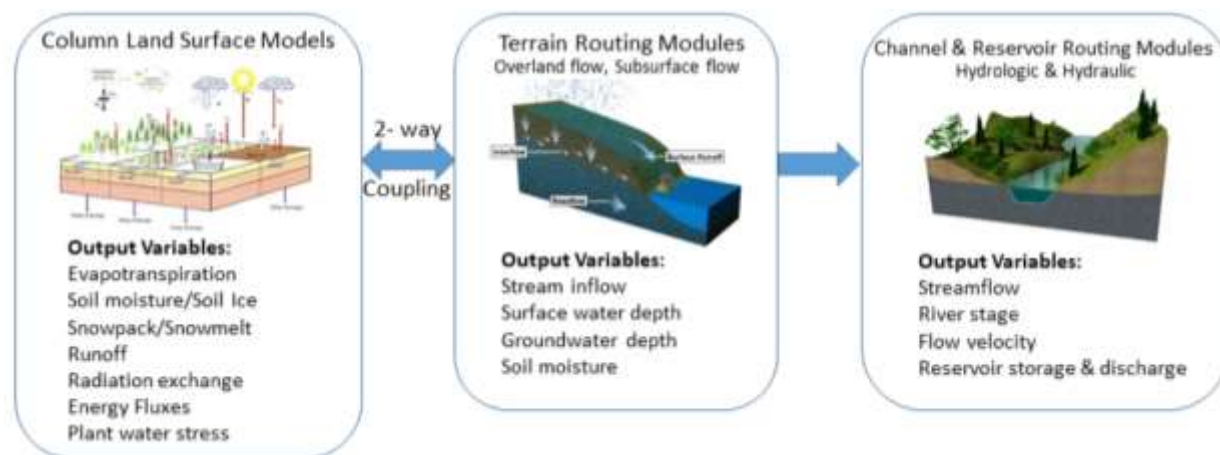

Figure 75. WRF-Hydro physics components and output variables.
(https://ral.ucar.edu/projects/wrf_hydro/overview)

The WRF-Hydro coupling framework was designed to facilitate easier coupling between the Weather Research and Forecasting model (an atmospheric model) and components of terrestrial

hydrological models. It is also fully-parallelized to enable its usage on clusters and high performance computing systems. Its multi-scale functionality permits modeling of atmospheric, land surface and hydrological processes on different spatial grids; while its architecture significantly simplifies the task of integrating, or coupling, existing and emerging hydrological models into the WRF modeling framework. Having such an extensible, portable and scalable infrastructure may someday make it possible to couple it with models (e.g. ASCEM) that account for subsurface processes as well.

Subtask 6.3: Conclusions and Future Work

In FIU Performance Year 10, FIU plans to continue their collaboration with PNNL and CBFO and select an open-source LSM, which will be used to derive parameters that account for the surface and near-surface hydrological processes and assist in computing the surface water balance across multiple scales to reduce uncertainties in recharge estimates at the WIPP site. During FIU Performance Year 10, FIU will utilize the selected open-source LSM to initiate development of a LSM of Basin 6 in the Nash Draw area. A literature review will be conducted to identify the optimal LSM based on capacity and compatibility with ASCEM. Candidate LSMs include the Community Land Model (CLM), which has been successfully coupled with the LBNL-developed ParFlow, and the UCAR-developed Noah and Noah-Multi-parameterization (Noah-MP) models. Noah-MP has been successfully coupled with the Weather Research and Forecasting (WRF) Model and used to predict the water cycle components including precipitation, soil moisture, snow pack, groundwater, streamflow, and inundation. This task will involve understanding the requirements for coupling a state-of-the-art LSM with a variably saturated ASCEM GWM, initially as a single-column model. The development of a coupling interface can be initiated in future to communicate between the chosen LSM and ASCEM. This subtask will also include training of FIU personnel and students on the use of the ASCEM modeling toolset. FIU will coordinate with the DOE ASCEM team to arrange a workshop to begin learning how to use the ASCEM code as well as become familiar with the publicly available graphical user interface (GUI), and research existing case studies where ASCEM has been implemented at DOE sites to determine the best practices and lessons learned for implementing this modeling toolset.

Task 6: Acknowledgements

Task 6: References

Anders, N., Valente, J., Masselink, R., & Keesstra, S. (2019). Comparing Filtering Techniques for Removing Vegetation from UAV-Based Photogrammetric Point Clouds. Drones, 3(3), 61.

Barringer, J. R. F., Pairman, D., & McNeill, S. J. (2002). Development of a high-resolution digital elevation model for New Zealand. Landcare Research Contract Report: LC0102/170.

Brezinski, D.K. (2004). Stratigraphy of the Frederick Valley and its Relationship to Karst. Rep. No. 75, Annapolis: Maryland Department of Natural Resources.

Chen, H., Oguchi, T., & Wu, P. (2018). Morphometric analysis of sinkholes using a semi-automatic approach in Zhijin County, China. Arabian Journal of Geosciences, 11(15). https://doi.org/10.1007/s12517-018-3764-3

de Carvalho Júnior, O. A., Guimarães, R. F., Montgomery, D. R., Gillespie, A. R., Gomes, R. A. T., Martins, É. de S., & Silva, N. C. (2014). Karst depression detection using ASTER, ALOS/PRISM and SRTM-derived digital elevation models in the Bambuí group, Brazil. Remote Sensing, 6(1), 330–351. https://doi.org/10.3390/rs6010330

Doctor, D. H., & Young, J. A. (2013). An evaluation of automated GIS tools for delineating karst sinkholes and closed depressions from 1-meter LiDAR-derived digital elevation data. 13th Multidisciplinary Conference on Sinkholes and the Engineering and Environmental Impacts of Karst, 449–458. Retrieved from

https://scholarcommons.usf.edu/cgi/viewcontent.cgi?referer=https://www.ecosia.org/&httpsredir=1&article=1156&context=sinkhole_2013

El-Quilish, M., El-Ashquer, M., Dawod, G., & El Fiky, G. (2018). Development and Accuracy Assessment of High-Resolution Digital Elevation Model Using GIS Approaches for the Nile Delta Region, Egypt. American Journal of Geographic Information System, 7(4), 107-117.

Goodale, C. L., Aber, J. D., & Ollinger, S. V. (1998). Mapping monthly precipitation, temperature, and solar radiation for Ireland with polynomial regression and a digital elevation model. Climate Research, 10(1), 35-49.

Hoffmann, E., and Winde, F. (2010) Generating high-resolution digital elevation models for wetland research using Google Earth™ imagery – an example from South Africa, Water SA, 36:1, 53-68.

Kakavas, M. P., Nikolakopoulos, K. G., & Zagana, E. (2015, October). Karst features detection and mapping using airphotos, DSMs and GIS techniques. In Earth Resources and Environmental Remote Sensing/GIS Applications VI (Vol. 9644, p. 96440Y). International Society for Optics and Photonics.

Kobal, M., Bertoncelj, I., Pirotti, F., Dakskobler, I., & Kutnar, L. (2015). Using lidar data to analyse sinkhole characteristics relevant for understory vegetation under forest cover - Case study of a high karst area in the Dinaric mountains. PLoS ONE, 10(3), 1–19. https://doi.org/10.1371/journal.pone.0122070

Launspach, J. (2013). Automated sinkhole extraction and morphological analysis in northeast Iowa using high-resolution LiDAR data. Retrieved from http://scholarworks.uni.edu/etd%0Ahttp://scholarworks.uni.edu/etd/33

Lawrence, D., Fisher, R., Koven, C., Oleson, K., Swenson, S., Bonan, G., & Zeng, X. (2019). The Community Land Model Version 5: Description of new features, benchmarking, and impact of forcing uncertainty. Journal of Advances in Modeling Earth Systems.

Lindsay, J. B., & Creed, I. F. (2006). Distinguishing actual and artefact depressions in digital elevation data. Computers and Geosciences, 32(8), 1192–1204. https://doi.org/10.1016/j.cageo.2005.11.002

Liu, H., Jezek, K. C., & Li, B. (1999). Development of an Antarctic digital elevation model by integrating cartographic and remotely sensed data: A geographic information system based approach. Journal of Geophysical Research: Solid Earth, 104(B10), 23199-23213.

Louhaichi, M., Borman, M. M., Johnson, A. L. and Johnson, D. E. (2003). Creating Low-Cost High-Resolution Digital Elevation Models. Journal of Range Management, 56:1, 92-96.

Miao, X., Qiu, X., Wu, S.-S., Luo, J., Gouzie, D. R., & Xie, H. (2013). Developing Efficient Procedures for Automated Sinkhole Extraction from Lidar DEMs. Photogrammetric Engineering & Remote Sensing, 79(6), 545–554. https://doi.org/10.14358/pers.79.6.545

Pohjola, J., Turunen, J. and Lipping, T. (2009). Creating High-Resolution Digital Elevation Model Using Thin Plate Spline Interpolation and Monte Carlo Simulation, Working Report 2009-56.

Poppenga, S.K., Worstell, B.B., Stoker, J.M., and Greenlee, S.K. (2010). Using selective drainage methods to extract continuous surface flow from 1-meter LiDAR-derived digital elevation data. U.S. Geological Survey Scientific Investigations Report 2010–5059, 12 p.Rajabi, A., Kim, Y., Kim, S.-H., Kim, Y., Kim, B., & Nam, B. H. (2018). A Preliminary Study on Use of LiDAR Data to Characterize Sinkholes in Central Florida. 23–31. https://doi.org/10.1061/9780784481585.003

Rajabi, A. (2018). Sinkhole Detection and Quantification Using LiDAR Data. 61. Retrieved from https://pdfs.semanticscholar.org/6e97/ac20592c758b335184edaf30a4ac4a889769.pdf

Rosdi, M. A. H. M., Othman, A. N., Abdul, M. A. M. Z. Z., & Yusoff, Z. M. (2017). Sinkhole Susceptibility Hazard Zones Using GIS and Analytical Hierarchical Process (AHP): A Case Study of Kuala Lumpur and Ampang Jaya. International Archives of the Photogrammetry, Remote Sensing & Spatial Information Sciences, 42.

Sadeghi-Tehran, P., Virlet, N., Sabermanesh, K., & Hawkesford, M. J. (2017). Multi-feature machine learning model for automatic segmentation of green fractional vegetation cover for high-throughput field phenotyping. Plant methods, 13(1), 103.

Sandino, J., Gonzalez, F., Mengersen, K., & Gaston, K. J. (2018). UAVs and machine learning revolutionising invasive grass and vegetation surveys in remote arid lands. Sensors, 18(2), 605.

Serifoglu Yilmaz, C., & Gungor, O. (2018). Comparison of the performances of ground filtering algorithms and DTM generation from a UAV-based point cloud. Geocarto international, 33(5), 522-537.

Sharma, M., Paige, G. B., & Miller, S. N. (2010). DEM development from ground-based LiDAR data: A method to remove non-surface objects. Remote Sensing, 2(11), 2629-2642.

Skarlatos, D., & Vlachos, M. (2018). Vegetation removal from UAV derived DSMS, using combination of RGB and NIR imagery.

Theilen-Willige, B., Malek, H., Charif, A., El Bchari, F., & Chaïbi, M. (2014). Remote sensing and GIS contribution to the investigation of karst landscapes in NW-Morocco. Geosciences, 4(2), 50-72.

Tibouo, F. N. (2016). Use and evaluation of LiDAR for mapping sinkholes in Royal Spring Groundwater Basin.

Todd, A., & Ivey-Burden, L. (2016). A Method of Mapping Sinkhole Susceptibility Using a Geographic Information System: A Case Study for Interstates in the Karst Counties of Virginia. 299–306. https://doi.org/10.5038/9780991000951.1048

Wall, J., Bohnenstiehl, D., & Levine, N. (2013). Automated sinkhole detection using a DEM subsetting technique and fill tools at Mammoth Cave National Park Methods : LiDAR Processing. 64, 2013.

Wu, Q., Deng, C., & Chen, Z. (2016). Automated delineation of karst sinkholes from LiDAR-derived digital elevation models. Geomorphology, 266 (2016), 1–10. https://doi.org/10.1016/j.geomorph.2016.05.006

Xie, Z., Pearlstine, L. & Gawlik, D. E. (2012). Developing a Fine-Resolution Digital Elevation Model to Support Hydrological Modeling and Ecological Studies in the Northern Everglades. GIScience & Remote Sensing, 49:5, 664-686, DOI: 10.2747/1548-1603.49.5.664.

Yilmaz, V., Konakoglu, B., Serifoglu, C., Gungor, O., & Gökalp, E. (2018). Image classification-based ground filtering of point clouds extracted from UAV-based aerial photos. Geocarto international, 33(3), 310-320.

Zhang, C., & Xie, Z. (2013). Object-based vegetation mapping in the Kissimmee River watershed using HyMap data and machine learning techniques. Wetlands, 33(2), 233-244.

Zhu, J., Taylor, T. P., Currens, J. C., & Crawford, M. M. (2014). Improved karst sinkhole mapping in Kentucky using LiDAR techniques: A pilot study in Floyds fork watershed. Journal of Cave and Karst Studies, 76(3), 207–216. https://doi.org/10.4311/2013ES0135

CONFERENCE PARTICIPATION, PUBLICATIONS & AWARDS

Peer-reviewed Publications

Emerson, H. P., Kaplan, D. I., Powell, B. A. (2019) Plutonium binding affinity to sediments increases with contact time. *Chemical Geology*, **505**, 100-107. DOI: 10.1016/j.chemgeo.2018.11.009

Szecsody, J., Truex, M., Qafoku, N., McKinley, J., Ivarson, K., Di Pietro, S.A., (2019). Persistence of Chromate in Vadose Zone and Aquifer Sediments in Hanford, Washington, *Science of the Total Environment*, **676**, 482-492.

Zengotita, F., Emerson, H. P., Dittrich, T., Reed, D. T., Swanson, J. (2019) Potential for biocolloid transport of Cs at high ionic strength. *Chemosphere*, **235**, 1059-1065. DOI: 10.1016/j.chemosphere.2019.06.222

Anagnostopulos, V., Katsenovich, Y., Lee, B. (2019). Biotic dissolution of autunite under anaerobic conditions: effect of bicarbonates and Shewanella oneidensis MR1 microbial activity, *Environmental Geochemistry and Health. Published 12.19.2019.* https://doi.org/10.1007/s10653-019-00480-7

Emerson, H. P., Zengotita, F., Dittrich, T., Richmann, M., Katsenovich, Y., Reed, D. (2018) Retention of neodymium by dolomite at variable ionic strength as probed by batch and column experiments. *Journal of Environmental Radioactivity*, **190-191**, 89-96. DOI: 10.1016/j.jenvrad.2018.05.007

Emerson, H., DiPietro, S., Katsenovich, Y., Szecsody, J. (2018). Potential for U Sequestration with Select Minerals and Sediments via Base Treatment. *Journal of Environmental Management*, 223, 1, 108-114.

Silvina Di Pietro, Hilary P. Emerson, Yelena Katsenovich, Nikolla P. Qafoku and Jim Szecsody. Phyllosilicate Mineral Alteration in Alkaline Conditions with Variable Redox State (Under review in the *Applied Clay Science Journal).*

In Preparation:

Garcia, A., Katsenovich, Y., Lee, B., Roguer Placencia-Gomez, E., Thomle, J., and D. Whitman. Geophysical indicators on uranium release from autunite mineral in biotic sediment systems (In preparation).

Gonzalez-Raymat, H., Gudavalli, R., Denham, M., Cai, Y, and Y. Katsenovich. *In situ* sequestration of uranium from contaminated groundwater using a low-cost unrefined humic substance (In preparation).

Oral Presentations (presenter is underlined)

Iodine Co-Precipitation with Calcium Carbonate in the Presence of Silica Ions. Katsenovich, Y., Trimino Gort, R. (DOE Fellow), Lugo, X., (DOE Fellow), Gudavalli R., Qafoku, N.P., Freedman, V., and L. Lagos.. WM2020 Conference Proceedings, March 8-12, 2020, Phoenix AZ.

Phyllosilicate mineral dissolution upon variable alkaline treatment and redox conditions, Silvina Di Pietro, Hilary P. Emerson, and Yelena Katsenovich, 258th American Chemical Society National Meeting, San Diego, CA, Aug. 26th, 2019.

Sorption behavior of Nd^{3+}, Th^{4+}, and UO_2^{2+} to dolomite in high ionic strength systems and the effect of EDTA, A. Kirstin Sockwell, Frances Zengotita, Alexis Vento, Timothy M. Dittrich, Donald T. Reed, Yelena Katsenovich, and Hilary P. Emerson, Fall 2019 American Chemical Society National Meeting and Exposition, San Diego, CA, Aug. 25-29, 2019.

Mineral Dissolution upon Alkaline Treatment and Variable Redox Conditions, Silvina Di Pietro, Hilary P. Emerson, and Yelena Katsenovich, SoFL-ACS Chapter Chemical Sciences Symposium – Miami, FL, April 13th, 2019.

Graduating Students and New Engineers - Wants and Needs – Are Companies Even Listening? Silvina Di Pietro, Ximena Lugo, Waste Management Symposia – Phoenix, AZ, March 5th, 2019.

Introduction to Honors and Leadership Seminar Discussion Di Pietro, S. (DOE Fellow). Guest Lecture, Panther Alumni Week FIU Honors College, Miami, FL. February 2019.

Isopiestic Measurements of Water Adsorption on Uranium-Bearing Solids Created after Ammonia Gas Treatment. Katsenovich, Y., C. Cardona. Waste Management 2019 Conference, Phoenix, AZ, March 2019.

An Integrated Hydrological Model for Long-Term Monitoring in Tims Branch Watershed. Mahmoudi, M., A. Lawrence, SC. Waste Management 2019 Conference, Phoenix, AZ, March 2019.

An Integrated Hydrological Model for Long-Term Monitoring in Times Branch Watershed Mahmoudi, M., SC. American Water Resources Association (AWRA), Baltimore, MD, November 2018.

Potential for transport of cesium as biocolloids in a high ionic strength system, Frances Zengotita, Hilary P. Emerson, Timothy M. Dittrich, Juliet Swanson, Donald T. Reed, and Michael Richmann, FIU McNair Scholars Conference, Miami, FL, Oct. 18-19, 2018.

Potential for Transport of Cesium and Lanthanides as Biocolloids in a High Ionic Strength System. F. Zengotita (DOE Fellow), H. Emerson, T. Dittrich, J. Swanson, M. Richmann, D. Reed. 256th American Chemical Society National Meeting, Boston, MA, August 2018.

Poster Presentations (presenter is underlined)

Culebra dolomite dissolution of relevance to the Waste Isolation Pilot Plant – 20550, Alexis Vento, Hilary P. Emerson, A. Kirstin Sockwell, and Frances Zengotita, Waste Management Symposia 2020, Phoenix, AZ, Mar. 8-12, 2020.

Impact of Free Radicals on the Fate of Tc, I, and U in Wetlands at Savannah River Site Ravi Gudavalli, Hilary Emerson, Silvia Garcia, Hansell Gonzalez Raymat, Yelena Katsenovich, Leonel Lagos. Submitted for the WM2020 Conference Proceedings, March 8-12, 2020, Phoenix, AZ.

Study of an Unrefined Humate Solution as a Possible Attenuation-based Remedy for Uranium Contamination in Acidic Groundwater. Ravi Gudavalli, Katherine Delarosa, Hansell Gonzalez

Raymat, Brian Looney, Yelena Katsenovich, Leonel Lagos. Submitted for the WM2020 Conference Proceedings, March 8-12, 2020, Phoenix, AZ.

The Impact of ethylenediaminetetraacetic acid (EDTA) on the Sorption of Nd(III), Th(IV), and U(VI) onto Dolomite in WIPP-relevant Brines, GWB and ERDA-6. A. Kirstin Sockwell, Frances Zengotita, Alexis Vento, Juliet S. Swanson, Donald T. Reed, Yelena Katsenovich, Hilary P. Emerson. Submitted for the WM2020 Conference Proceedings, March 8-12, 2020, Phoenix, AZ.

Neptunium (IV) Diffusion through Bentonite Clay Silvina Di Pietro, Claudia Joseph, Mavrik Zavarin, *DOE Fellows Poster Competition - Applied Research Center, Florida International University* – Miami, FL, November 7th, 2019.

Can We Isolate Nuclear Waste? Neptunium (IV) Diffusion Rates through Bentonite Clay Silvina Di Pietro, Claudia Joseph, Mavrik Zavarin Lawrence Livermore National Laboratory Poster Symposium – Livermore, CA, August 8th, 2019.

Impact of Photodegradation of SRS Wetland Sediments on Radionuclide. Garcia, S. (DOE Fellow), H. Emerson. Waste Management 2019 Conference, Phoenix, AZ, March 2019.

Investigation of dolomite dissolution in variable ionic strength systems relevant to the WIPP, Alexis Vento, Frances Zengotita, A. Kirstin Sockwell, and Hilary P. Emerson, Mirion Connect Annual User's Conference, Santa Anna Pueblo, NM, Jul. 29 – Aug. 2, 2019.

Remediation of Radioactive Waste-contaminated Sites, Silvina Di Pietro Persistent Toxic Substances Workshop, FIU Department of Chemistry & Chinese Academy of Sciences – Miami, FL, April 4th, 2019.

Investigating the Effect of Sorbed Humic Acid on the Mobility of Uranium. Gudavalli, R., Raubenolt, R. (DOE Fellow), Looney, B. Waste Management 2019 Conference, Phoenix, AZ, March 2019.

Mineral Dissolution Effects of Alkaline Treatment with Redox Conditions on Hanford Sediments, Silvina Di Pietro and Hilary P. Emerson, Waste Management Conference, Phoenix, AZ, Mar. 4th, 2019.

Mineral Dissolution upon Alkaline Treatment and Variable Redox Conditions. Di Pietro, S. (DOE Fellow), H. Emerson, Y. Katsenovich. SoFL-ACS Chapter Chemical Sciences Symposium, Miami, FL, April 2019.

Effect of Minerals on the Removal of U(VI) in the Presence of Humic Acid and Colloidal Silica Delarosa, K. (DOE Fellow), R. Gudavalli, Y. Katsenovich.. Waste Management 2019 Conference, Phoenix, AZ, March 2019.

Protocol Development for Monitoring Methylmercury and Mercury Speciation of Water Samples via DMA-80. Delarosa, K. (DOE Fellow). Waste Management 2019 Conference, Phoenix, AZ, March 2019.

Effect of Mineral on the Removal of Uranium (VI) in the Presence of Humic Acid and Colloidal Silica Delarosa, K. (DOE Fellow), R. Gudavalli, Y. Katsenovich., during the Life Sciences South Florida Conference in Boca Raton, FL, on April 6, 2019.

Potential for transport of cesium as biocolloids in a high ionic strength system, Frances Zengotita, Hilary P. Emerson, Timothy M. Dittrich, Juliet Swanson, Donald T. Reed, and

Michael Richmann, FIU McNair Scholars Conference, Miami, FL, Oct. 18-19, 2018. (1st Place Poster Award)

Fate of Actinides in the Presence of EDTA and Dolomite at Variable Ionic Strength, Hilary P. Emerson, Frances Zengotita, Yelena Katsenovich, and Donald T. Reed, 256th American Chemical Society National Meeting, Boston, MA, Aug. 19-23, 2018.

Quantifying Groundwater/Surface Water Interaction in the Tims Branch Stream. Hariprashad, R. (DOE Fellow)., Savannah River Site, SC. Waste Management 2019 Conference, Phoenix, AZ, March 2019.

Iodine Co-precipitation Process with Calcium Carbonate. Lugo, X. (DOE Fellow), Y. Katsenovich. Waste Management 2019 Conference, Phoenix, AZ, March 2019.

Contrast of Cultures in Interagency Radiological Management Involving Human Health Reference Dose. Morales, J. (DOE Fellow). Waste Management 2019 Conference, Phoenix, AZ, March 2019.

Student Awards

2020 WM Symposia – Roy G. Post Foundation Scholarship recipients (Gisselle Gutierrez, Amanda Yancoski and Frances Zengotita).

DOE Fellow Frances Zengotita was accepted into the Seaborg Institute Nuclear Science and Security Summer Internship Program at Lawrence Livermore National Laboratory (Summer 2019).

Fall 2019 – FIU World's Ahead Graduate (Frances Zengotita).

Young Researcher Speaker Award – SoFL-ACS Chemical Sciences Symposium (Silvina Di Pietro), 2019

APPENDIX

The following documents which are related to this report are provided as separate attachments:

1. Appendix 1: Silvina Di Pietro, Hilary P. Emerson, Yelena Katsenovich, Nikolla P. Qafoku and Jim Szecsody, *Phyllosilicate Mineral Alteration in Alkaline Conditions with Variable 1 Redox State*, Manuscript under review in the Applied Clay Science Journal. This report will be available in the FIU's DOE EM Research website once paper is published.
2. Appendix 2: Yelena Katsenovich, Rocio Trimino Gort, Ravi Gudavalli, Nikolla Qafoku, Vicky Freedman, *Incorporation and stability of iodate and chromate in calcium carbonate at variable pH and Si concentrations.* Draft manuscript prepared for the submission to the peer-reviewed journal. This report will be available in the FIU's DOE EM Research website once paper is published.
3. Appendix 3: Gisselle Gutierrez. *Literature Review of Methodologies for Development of a High Resolution DEM for the Waste Isolation Pilot Plant (WIPP)*, Report, Applied Research Center, Florida International University, August 2019.
4. Appendix 4: Gisselle Gutierrez. *Literature Review of Methodologies for Vegetation Identification and Removal from UAV-Based Photogrammetric DSMs for the Waste Isolation Pilot Plant,* Thesis, Report, Applied Research Center, Florida International University, January 2020.

The following documents are available at the DOE Research website for the Cooperative Agreement between the U.S. Department of Energy Office of Environmental Management and the Applied Research Center at Florida International University: http://doeresearch.fiu.edu

1. Florida International University, *Project Technical Plan,* Project 2: Environmental Remediation Science and Technology, December 2019.

2. Florida International University, *Impact of Alkaline pH on Mineral Dissolution*, Technical Report, March 21, 2019.

3. Florida International University, *Glass Dissolution under Environmental Conditions*, Technical Report, April 2019.

4. Florida International University, *Humic Acid Batch Sorption Experiments with SRS Soil*, Technical Report, July 2019.